The Generation and Analysis of High Energy Proton Induced X-Ray Emission Data

by

ALI AKBAR MIRZAI

A thesis submitted to the Faculty of Graduate Studies of the University of Manitoba in partial fulfillment of the requirements for the degree of

DOCTOR OF PHILOSOPHY

ISBN 0-315-76859-2

THE GENERATION AND ANALYSIS OF HIGH ENERGY PROTON INDUCED X-RAY EMISSION DATA

BY

ALI AKBAR MIRZAI

A thesis submitted to the Faculty of Graduate Studies of the University of Manitoba in partial fulfillment of the requirements of the degree of

DOCTOR OF PHILOSOPHY

ABSTRACT

Fourier transform techniques (*FTT*) have been used for investigating the information content of *PIXE* X-ray spectra. The spectra used for this purpose were obtained through high energy *PIXE* experiments which were carried out at the University of Manitoba Accelerator Centre.

The measured data were preconditioned for the purpose of obtaining the greatest benefit from a Fourier transformation. The preconditioning procedure employed the linear relationship between the square of peak width and energy in order to both perform the transformation of the energy axis of X-ray spectra and to produce peaks with constant line width.

A digital filter was designed to separate background and statistical noise from the peaks observed in a measured X-ray spectrum by making maximum use of Fourier transform techniques. The first component of the filtering function subtracted most of the background from the entire spectrum and the second component suppressed the statistical noise. In this approach no assumptions were made about the method of production or the functional form of the background.

By using the above filter function and *FTT*, it was possible to extract peaks from the background-free and smoothed data without resorting to the conventional methods for locating peaks. Establishing a minimum detection limit based on a 3σ test, small peaks present in the spectrum were easily extracted and identified.

Error analysis was performed based on comparing the error in the fitted background with that of the expectation value of the convolved background. The error in the fitted background dropped approximately 30% in all channel numbers.

A minimum number of free parameters was used as compared with conventional methods of background subtraction, data smoothing and peak extraction.

ACKNOWLEDGEMENTS

I wish to thank my supervisor, Dr. J.S.C. McKee, for his support and helpful discussions and guidance provided throughout the course of my studies.

I would also like to thank Dr. G.R. Smith for his assistance, encouragement and involvement at nearly all stages of this work as well as to thank the other members of my advisory committee, Dr. M. Mathur, Dr. N.M. Halden and Dr. C Pinsky for their help in determining the best possible ways of achieving my goals.

Thanks are extended to Dr. P. Paatero of the Department of Physics, University of Helsinki for his valuable advice and guidance during the early stage of this work.

I am grateful to the cyclotron support staff and in particular the members of the so-called "PIXE Group", Wallace Mulholland and D. Gallop, for their helpfulness during the PIXE experiments.

Thanks are also extended to the computer support manager, J.J.G. Durocher for his cooperation.

Finally, I would like to thank Dr. H. Moheb for providing technical facilities and my daughters Mahta and Bita for their support and excellent work in typing the thesis.

TABLE OF CONTENTS

LIST OF TABLES

LIST OF FIGURES

Introduction

The process of Proton Induced X-ray Emission (*PIXE*) followed by detection of the X-ray represents a highly sensitive, multielement analytical method. In the past, energies in the range 0.5-10 MeV have been extensively used for *PIXE* work, more due to the abundance of low energy Van de Graaf and Tandem accelerators than to this being the optimum energy range for such experiments. There is, however, a widely held belief that at higher energies Compton scattering can produce a high enough background to obscure the X-rays completely. It has even been stated that cyclotrons can find only limited application in particle induced X-ray analysis and that there is no significant advantage in studying X-ray fluorescence at higher energies than a few MeV. This argument is presumably based upon the study of L rather than K X-rays, which at low energies are not detected for elements with $Z > 45$. There are in principle of course advantages in using the characteristic K rather than L X-rays in the analysis in terms of heavy elements. Neighboring peaks are easily resolved and there is no overlap with L X-rays from other elements. For heavy elements the K X-ray production cross sections using low energy protons fall by 2-3 orders of magnitude over the lighter elements, therefore low energy machines are unable to measure their cross sections and have to rely on the L X-rays for trace element analysis. The peaks overlap significantly, which limits the sensitivity of the analysis.

The University of Manitoba cyclotron which is capable of producing proton beams in the energy range 20-50 MeV has been used for more than a decade for *PIXE* studies employing K X-ray analysis. The yield of K X-rays at the energy of the University of Manitoba cyclotron is quite high and the cross sections for medium to high- Z elements are expected to be comparable with those for lighter elements from an approximately 3 MeV machine.

The basic purpose of the *PIXE* analytical technique is the determination of the absolute concentrations of elemental constituents in a sample by generating and analyzing experimental X-ray spectra. However, these spectra are not simple as the features are superimposed on an energy dependent background and the data show statistical

fluctuations. The presence of this background component sets a limit to the detection of the small X-ray peaks.

The background shape in the case of X-ray fluorescence is not so predictable and one has to exploit any features which distinguish background from peaks. Some methods such as interpolating the background beneath the peaks using smooth analytical functions have been used but this may be inaccurate when carried out over the large range required. To get around this problem, coefficients for a polynomial function can be included as undetermined parameters in the least-squares analysis, thus removing the need for an explicit fit to background points. However, the function used must accurately represent the background over the whole fitting range and while regions of high curvature, such as absorption steps, can be accommodated by including higher terms in the polynomial, this may make the technique unstable with regard to small errors in the peak model functions. In addition, the process requires intensive interaction of the physicist with the data analysis at all stages.

An alternative approach of looking at the information content of an X-ray spectrum and separating the spectral components is through its Fourier transform. Conceptually, the slowly varying background spectrum, contributed by all channels, is the result of a few "low frequencies" being present. On the other hand, the noise, which is contributed channel by channel to the spectrum, is a result of "higher frequencies". If a Fourier transformation of the data from energy domain to frequency domain is made, the broad, slowly varying background component could be characterized by a set of frequencies which are different from those characteristic of the peaks (several channels associated together), and both of these are different from the set of frequencies typical of noise. The major advantages of this method over conventional techniques are that the shape of the background need not be known explicitly and there is no need to find suitable points away from peaks for background scaling. By choosing an appropriate digital filtering function, and applying it to the data transformed to the frequency domain (the power spectrum), the undesired parts of the spectrum, i.e. the noise and the background, can be eliminated. What remains in the power spectrum is transformed back to the energy (channel number) domain. The parts of the energy spectrum of interest, namely the peaks, remain and are available for further analysis.

This thesis is devoted to the study and investigation of both background subtraction and noise suppression in a digitized X-ray spectrum using Fourier transform techniques (*FTT*) and utilizing an appropriately designed digital filter, as this approach has not previously been exploited successfully.

Chapter 1 deals with the experimental considerations of high energy *PIXE* at the University of Manitoba Accelerator Centre and discusses the two main fields, i.e. "geology and mineralogy" and "biology and medicine" in which the *PIXE* analysis had had numerous applications.

Chapter 2 discusses the problems leading to the complexity of X-ray spectra and gives a brief overview of the origins and formation of continuous background and statistical noise in *PIXE* spectra. The problem of regularly varying widths of the peaks arising in applying Fourier transform techniques and the ways for preconditioning the spectra with an emphasis on the translational invariance of the system to provide peaks with constant line widths are also discussed in this chapter.

Chapter 3 gives a brief discussion of Fourier transform techniques and the related theorems. After discussing the Fourier representation of finite duration sequences applicable to the measured data, it deals with background subtraction and data smoothing using *FTT*.

The design of a digital filter to remove the disinformative parts of the data is discussed in chapter 4. The filter function $W(\nu)$ has two components $W_B(\nu)$ and $W_N(\nu)$ to subtract background and remove noise respectively. However, application of the filter function $W(\nu)$ to the measured spectrum directly recovers the sought quantity by simultaneously subtracting background and smoothing data. Although the number of low frequencies assigned for background subtraction varies under different operational parameters, assignment of proper values to the filter function and its application to the first six frequency points subtracted nearly the whole background.

To design the proper smoothing filter function $W_N(\nu)$, having the characteristic of a low-pass filter, the optimal filter proved to be a good choice for the purpose. The value of the parameters required to construct the smoothing filter were obtained from power spectrum of the data which was easily separated into a "noise model" and a "spectral model".

Chapter 5 deals with the application of the filter function to the data and the experimental results. After subtracting background and removing the noise, the same technique (*FTT*) is used to extract peaks. This chapter also gives an exposition of the sensitivity/detection limit of the system and identification of the peaks. A discussion is made of error analysis in background subtraction. Finally, the position of *PIXE* as compared with other analytical techniques and some of the currently used computer porgrammes for *PIXE* spectrum analysis are discussed.

Chapter 1
Experimental Measurements of X-ray Emission Following High Energy Proton Bombardment of Mineralogical and Biological Samples

1.1. Proton Induced X-ray Emission (*PIXE*)

If a target is bombarded by protons energetic enough to cause inner shell ionization, then the X-rays emitted when the inner shell vacancies are filled can be detected by a suitable detector and the resulting X-ray spectrum used to identify the elements in the target. The X-ray spectrum consists of a series of sharp lines, called the "characteristic spectrum", superimposed on the continuous "bremsstrahlung spectrum" (braking radiation). The line spectrum is characteristic of the target material and varies from element to element. The continuous spectrum has a sharp cutoff wavelength, λ_{min}, which is independent of the target material but depends on the energy of the bombarding particles.

As far as the characteristic X-rays are concerned, the generation of X-ray radiation from an atom is achieved through any interaction that excites or removes an electron from its normal place in the atom. The atom will subsequently seek to revert back to its original electronic configuration. This takes place when electrons from some higher shell are transferred to the vacant electron site. Such electron transitions imply a loss of energy and the requirement of energy conservation is satisfied by the emission of electromagnetic radiation (X-rays) carrying an amount of energy equivalent to the energy difference between the two shells of the electron transition. Due to the discrete energy values of the permissible shells, there will be a well defined set of energies associated with the emitted X-rays. Since the energy values of the shells are characteristic of the atomic element, the emitted X-rays will always be characteristic of the element from which it originates. Scofield has treated the emission

rates for K X-ray emission theoretically and drawn comparisons with available experimental results [Sc, 69; Sc, 74].

The process of Proton Induced X-ray Emission (*PIXE*) followed by detection of the X-ray represents a highly sensitive, multielement analytical method. The basic purpose of the method is the determination of the absolute concentrations of elemental constituents in the sample under investigation. *PIXE* is a powerful tool for a variety of reasons and the advantages of this analytical technique are as follows:

(i) Elemental identification via the characteristic X-ray spectra is simplified due to the relative simplicity of the X-ray spectra.

(ii) X-ray analysis is nondestructive. Bombardment with protons does not in general alter the composition of the specimen. It is preserved for possible re-examinations by the same or other analytical techniques.

(iii) Analysis of the characteristic X-rays results in a spectrum containing several peaks that may be interpreted in both a qualitative and quantitative sense.

(iv) The opportunity exists to scan a large proportion of the periodic table of the elements in a single measurement.

(v) $Si(Li)$ and intrinsic Ge detectors have high detection efficiency and energy resolution.

The position of *PIXE* as compared with other analytical techniques is discussed in chapter 5. For a more detailed information about the *PIXE* method reference can be made to [Jo, 76; Fo, 74].

PIXE studies applied to identification of elemental compositions of materials, have attracted a great deal of interest in recent years. The University of Manitoba cyclotron which is capable of producing proton beams in the energy range 20-50 MeV is used for *PIXE* studies. Two main goals for this purpose were identified: First, an improved understanding of the K-shell ionization process and of the X-ray emission following it. Second, the use of K X-ray fluorescence as an analytical tool in the study of the concentrations of heavy elements [Wi, 77]. K_α X-rays are emitted when K-shell vacancies are filled by radiative transitions from the L-shell and K_β X-rays result when K vacancies are filled from the M-shell.

1.2. High Energy *PIXE*

PIXE analysis has been used for more than a decade at the University of Manitoba to determine trace-element concentrations in a wide variety of materials. While the majority of *PIXE* systems rely on the detection of *K* and *L* X-rays generated using low energy, typically between 2 and 5 MeV, protons; the University of Manitoba facility employs *K* X-ray analysis using proton beams in the 20-50 MeV range to remove the inner shell electrons. Although *PIXE* analysis using higher energy protons is less sensitive in the low-Z range, the ability to excite the *K*-shell for medium to high-Z makes this the system of choice for studies involving these elements [Du, 88].

The reason why most *PIXE* work is carried out at low energies are to be found in the number of low-energy Van de Graaf generators still available to experimenters and in the low cost of new custom-made accelerators operating in this energy region. The rationale for higher energy analysis is as follows [Mc, 90a; Mc, 90b]:

(i) The 5-20 MeV proton energy region covers the compound nucleus region for most elements. In this regime, the incoming particle can be captured and form a compound system which then decays to stability through the emission of a γ-ray, often of a similar energy to the *K* X-ray from a known element. Separation of *K* X-rays from γ-rays in this energy range can be a daunting task, particularly when the sample is of unknown composition. At higher energies, however, nuclear processes become multiple-particle processes, and no simple discrete γ-ray is emitted unless a two-stage reaction process is involved, the second stage involving a simple two-body emission and recoil procedure. Not that γ-rays are not created; they contribute significantly to the background continuum, but in random fashion. The available phase space for gamma-rays is also extended, however, and in reality the ratio of X-ray peak to background may be improved with energy. For this reason, the detection limit for elements *As* (Z=33) and up is two orders of magnitude lower at 40 MeV than for low-energy *PIXE*.

(ii) *K* X-rays are detected in all cases and there is clear identification of all intermediate and heavy elements through *K* X-ray measurement. The fact that *K* X-rays are the signature for each element studied by high energy proton *PIXE* ensures that for rare earth region and above unambiguous determination is possible even when complex mixtures of elemental concentrations are present.

(iii) Self-absorption of *K* X-rays from medium and heavy elements is low for transmission targets which incidentally may be of the thickness of low-energy *PIXE* stopping

targets.

Energy loss for a 40 MeV proton in a 100 μm foil or ore slice is often negligible and self-absorption is relatively unimportant. In high-energy *PIXE* analysis the peaks appear in the raw data, and corrections needed to these data will often be slight.

(iv) The peak yield for K X-ray production lies in the region between 30 to 50 MeV for most rare-earth and medium-heavy elements [Ra, 78]. So not only is γ-ray contamination of most spectra low, but the K X-ray yield is at or near its maximum value.

(v) As K X-ray production cross section is a measure of the probability that a given atom exposed to a proton beam will emit a K X-ray, by referring to Fig. 1.1 it is noticed that low energy protons have a low cross section for ionization of the inner K electrons of heavier elements. Therefore, elemental identification must rely upon the L rather than the K X-ray series. Problems arise in that L X-rays are not only of lower energy and thus more difficult to identify quickly, but since they are more numerous than the K X-rays, the corresponding peaks in the L X-ray energy spectrum overlap each other and the K X-ray peaks of lighter elements present in the sample (see Fig. 1.2). Detailed information about K and L shell X-ray cross-sections can be found in [Co, 90; Pe, 90; Ga, 70].

(vi) A low energy proton beam measures elemental concentrations in the near-surface region of a sample. Low energy protons lose energy at a rate ten times higher than the high energy beam passing through a transmission sample. For this reason, there is more radiation and heat induced damage in the low energy case, and high energy proton analysis is therefore more truly nondestructive.

(vii) The range of 40 MeV protons in biological material may be 200 times longer than in low energy *PIXE*. The high energy beam, if well defined, yields the opportunity for depth analysis of a sample through the use of nuclear scattering information to obtain a depth profile.

(viii) In the case of low energy *PIXE*, much of the work involves thick targets, and sophisticated techniques are needed to extract elemental concentrations from the data obtained.

(ix) Finally, *PIXE* analysis at 40 MeV can measure elemental concentrations at the 1ppm level for all elements in the periodic table from *As* to *U*. This level is 100 times lower than that of low energy *PIXE*.

1.2.1. Experimental Set-Up

The *PIXE* experiments were carried out with the proton beam of the University of Manitoba cyclotron laboratory at an energy of 30-40 MeV on target samples using the "*PIXE* cube" located on the "C" line (see Fig. 1.3). The target samples were prepared by depositing small amounts of samples or homogenates on a thin mylar film cemented over an oval aperture on an aluminum target holder. The target holder, after drying the targets if this was necessary, was fixed on a remotely controlled target ladder which was mounted on top of the *PIXE* cube. Up to 10 targets could be mounted simultaneously on the ladder.

The emitted X-rays were detected using $Si(Li)$ and $Ge(Li)$ detectors to cover low energy and high energy range of X-ray spectrum respectively. The proton beam was collected in a Faraday cup at the exit from the "*PIXE* cube" and integrated to give total charge. Signals from the detectors' built-in preamplifiers were prepared for pulse height analysis by a standard spectroscopy amplifier and fed to an analog to digital converter. 1024 channel spectra were accumulated using *VAX* computer.

1.2.2. Applications

The applications of high energy proton *PIXE* to biological, medical and geological sciences should prove invaluable in future. Some of the fields in which the *PIXE* analysis of the University of Manitoba Accelerator Centre has had numerous applications are discussed below:

(a) Geology and mineralogy in which *PIXE* is well established,[An, 90]. Among the reasons for this is the fact that the samples can be irradiated directly without preparation or chemical modification. This makes the analysis fast and inexpensive. Among the numerous experiments done in the area of geology and mineralogy at the University of Manitoba Accelerator Center, here an experiment entitled "leaf analysis as an exploratory tool in mineralogy" is discussed (for detail refer to [Mi, 90]). In this experiment, it was decided to use the *PIXE* facilities in the nondestructive analysis of leaf material, and assess the results obtained in comparison with other biological methods used in mineral prospecting.

Biological methods of prospecting for minerals include geobotany (visual examination of the vegetation cover), geozoology (use of animals for mineral prospecting) and biogeochemistry (chemical analysis of vegetation) and have been used for many years [Br, 83]. Biological methods of prospecting have over the years become much more sophisticated and quantitative due to the development of statistical techniques facilitated by the advent of computers.

The Federal Department of Energy, Mines and Resources Canada, commenced the testing and development of vegetation geochemical exploration techniques in the Bissett area, Southeastern Manitoba in 1985 when samples of black spruce (Picea mariana) and dwarf birch (betula glandulosa) from a small study area east of Bissett were studied [Fe, 87]. The samples were collected during the month of January from an area of frozen peat bog. The survey was undertaken in an attempt to define vegetation geochemical anomalies related to a suspected zone or zones of mineralization overlain by a superficial deposit of peat bog.

Following the completion of the above biogeochemical prospecting project, the University of Manitoba Accelerator Centre carried out leaf analysis as an exploratory tool in mineralogy using *PIXE* technique. The Accelerator Centre group has determined trace-element concentrations for a wide variety of materials including minerals [Wi, 77; Du, 88] over the last decade.

Detailed analysis of the element composition of leaves of the species mentioned is of interest because the macronutrient and micronutrient elements present in plant tissues are already well known from chemical studies [Bi, 72]. These, having a maximum Z equal to 30, were confirmed by our analysis. Based on these available data, the main purpose of the application of the *PIXE* method to leaf analysis was therefore to determine if the technique is useful in the analysis of plant material for trace elements that are of particular interest to mineral prospectors. Samples were taken from trees located 20 Km north-east of the town of Bissett, South-eastern Manitoba [Fe, 87] and prepared in the following way:

First the leaves were washed in distilled water to remove any non-absorbed contaminants. Next the leaves were freeze-dried by storing them for at least overnight in a glass chamber evacuated to less than 50 μm by a mechanical pump. A small portion of each dried-out leaf was then sandwiched between two sheets of mylar film which were

fastened with vacuum grease onto opposite sides of a specially designed aluminum *PIXE* target holder. Since no external dopant was used in the targets, it was not possible to do a quantitative determination of trace element levels in the leaves. However, it was possible to use the results of *PIXE* analysis of the targets to determine if these trace elements are detectable, and to compare the relative amounts of the same element detected in different samples. In this experiment samples from the species Betula populifolia and Picea glauca were irradiated at an incident proton energy of 40 MeV to determine possible additional trace-element concentrations due to migration from mineral deposits present underground. Fig. 1.4 illustrates a portion of the spectrum of the leaf sample. In addition to the elements listed in ref [Bi, 72], other elements such as *Rb*, *Sr*, *Cd* and *Ba* were readily detected. In some samples the presence of *Pt* was also identified. Detailed analysis of the spectrum of the leaf sample will be discussed later when the disinformative parts of the spectrum, i.e. background and noise are removed from the data.

There is always an intrinsic interest in the ultimate capability of an analytical tool with regard to the lowest detectable concentration or amount. The minimum detection limit, being dependent both on operational parameters of the system as well as the specimen, can be improved by optimization of experimental parameters such as beam energy, acquisition time, detector area, detector resolution, etc. In general, through doping of samples it is shown that concentrations at 1 ppm are detectable using high energy *PIXE* in real samples with typical thickness of 40 μm.

As peaks in the observed spectrum indicate trace element concentrations at the part per million level or above, it is clear that low levels of elemental uptake in leaves can be identified. On the other hand the mechanisms by which foreign elements are taken up by leaf material, and by which ions migrate from an ore bed to vegetation many meters above it are little understood. Clearly the nature of the separating material, in this case sedimentary soil, and the fluctuations in the climate can both be of great importance.

(b) Biology and medicine would appear to be the most interesting areas for *PIXE* applications but at the same time it is in just these fields that the uncertainty concerning future development is the greatest. One reason is the complexity of the processes going on in living matter. The obvious task for *PIXE* in these fields is to measure trace

element concentrations, [Ma,88]. It is well known that several trace elements play important roles in living matter. However, the way in which a trace element takes part in various reactions is often not known with any certainty. The question then arises as to how meaningful it is to measure the total trace- element concentration in the body or in a certain organ. Several such measurements have been performed using *PIXE* and often interesting results have been obtained. This is especially the case when trace-element concentrations have been correlated with disease status of the patients.

For analysis of biological specimens, the high energy protons, in conjunction with a thin transmission target (often the thickness of a stopping target at 1-3 MeV), ensures that analysis is both of high resolution and simultaneously nondestructive. High energy protons have proved to be useful in identifying light elements in biological samples, and are particularly useful when it is felt that heavier trace element concentration is present.

In connection with an outbreak of atypical shellfish poisoning in Canada due to consumption of mussels from Prince Edward Island in late 1987 and early 1988, an elemental analysis of domoic acid- contaminated mussels harvested during the epidemic was undertaken using the proton induced X-ray emission technique [Mc, 90c] to estimate the concentration of metal elements in mussel tissue.

The study was inspired by the knowledge that oysters in the same vicinity were found to contain high concentrations of zinc, typically at a level sufficient to cause toxicity in mice (1000 ppm), and by the recent observation that the venomous orb weaving spider Araneus diadematus displays a very high level of zinc in its fangs. The scorpion Paruroctonus mesaenis has also been shown to display high levels of zinc in its stinger.

The choice of *PIXE* technique was prompted by the favorable turn-around time for data and the element-scanning ability of *PIXE* analysis as compared with chemical techniques. The *PIXE* system at the Accelerator Centre generated a beam of 30 MeV protons which passed through a transmission target of approximately 50 μm thickness and stimulated K X-ray emission with negligible self-absorption in the target and an excellent peak to background ratio. A $Si(Li)$ detector and an intrinsic *HpGe* detector were used to identify all trace elements present in each sample falling between phosphorus and uranium in the periodic table. Absolute measurements were not made. *Zn*

concentrations were deduced as a result of the comparison of peak height in the mussel sample with that from a *Zn* foil of the same thickness and of known concentration.

PIXE analysis is a well-established and versatile technique for the determination of elemental concentrations in biological samples. Of particular value is the ability to survey the characteristic *K* X-rays of most elements in a single measurement, as is possible with the high energy proton beam from the University of Manitoba Spiral Ridge Cyclotron. Beam energy (variable from 20 to 50 MeV) can be chosen to achieve maximum *K* X-ray yield for an element of interest. The standard millibeam probe produces a spot dimension of 2 mm diameter with which to scan a sample.

The higher velocities available from the Manitoba Cyclotron enable the proton beam to penetrate tissue sample depths some 200 times greater than is possible with conventional low energy ($\approx$ 3 MeV) *PIXE* facilities. For direct measurement of *K* X-ray intensity the resultant low self-absorption as compared with *L* X-rays from the same atoms enables direct observation of concentrations to be made directly from raw spectra with few corrections. Moreover, the amount of energy deposited from high energy protons near the surface of the transmission sample is much less than from low energy facilities. Hence heat-induced damage is low and the method is strictly nondestructive for thin samples. The foregoing factors permit greatly simplified and hence rapid procedures for the preparation of *PIXE* targets from biological tissues. *PIXE* targets were preparaed by deposition on 8C mylar film (DuPont) of aqueous extracts of pooled samples of whole mussel soft tissues or of mussel hepato-pancreas organs only.

As will be observed from the spectrum shown in Fig. 1.5 both *Zn* and *Cu* *K* X-rays are rapidly identified from the mussel samples and the resolution of K_α and K_β emissions ensures that no confusion with conflicting γ-rays is present or possible. Indeed, traces of heavier elements in such a sample are even more readily determined. Characteristic *K* X-rays from heavier elements (*As* and above) can be resolved into four components ($K_{\alpha 1}$, $K_{\alpha 2}$, $K_{\beta 1}$ and $K_{\beta 2}$) due to the high resolution of the intrinsic germanium detector used in such measurements. In practice, the lower limit for detection of concentrations of rare earth and medium heavy elements in a transmission sample (e.g. < 100 μm thick) is typically 1 ppm. This is 100 times better than that obtainable from low energy *PIXE* and 1000 times better than from scanning electron microscopy. Two high resolution detector systems are currently available for *PIXE* analysis,

specifically a lithium-drifted silicon detector for low energy emission and an intrinsic germanium detector with 0.4% resolution at 122 keV for elements in regions above *As* in the periodic table (see argument in [Mc, 90b]).

Fig. 1.5 shows a portion of the *K* X-ray spectrum from a sample of whole mussel extract as obtained by the *Si(Li)* detector. The X-ray emission was induced by 30 MeV protons and recorded via the *Si(Li)* detector. $\frac{K_\alpha}{K_\beta}$ ratios for both *Zn* and *Cu* are known, thus the $Zn(K_\alpha)$ can be calculated [Ka, 80; Sc, 69; Sc, 74]. The residual $Cu(K_\beta)$ peak then bears a known relationship to the $Cu(k_\alpha)$ line. The concentration of *Zn* in the sample is then deduced from a comparison of the *K* X-ray intensity from the mussel spectrum to that from a standard *Zn* foil of similar (50 μm) thickness. The overall error in this procedure including a correction for the difference in self- absorption is unlikely to exceed 30%. The weight of mussel tissue contributing to this sample was 15 mg, originating in tissue pooled from many specimens. Calculations from the sample shown yielded a figure of 333 ppm *Zn* per wet weight in whole mussel tissue with 80% water content. *Cu* content of same tissue, calculated from relative areas under $Cu(K_\alpha)$ and $Cu(K_\beta)$ peaks, is 533 ppm. Identical procedures were used to estimate *Zn* and *Cu* levels in hepatopancreas organ extracts. The latter is of interest because the domoic acid toxicant is concentrated by the hepatopancreas. These values of *Zn* and *Cu* levels are some 50 times greater than those generally cited in previous literature reports for similar specimens in diverse locations. The analysis of data obtained from several samples obtained using this method showed that the biological effect of the "obviously" high levels of copper also observed is not known or understood. It is worth observing, however, that a spectrum obtained simultaneously from the intrinsic germanium detector exhibited K_α and K_β peaks for *As*. Although the concentration of arsenic could not be accurately determined it is likely to be in the 100 ppm region of detectability, as only levels above 1 ppm are normally observable. It should be noted also that the use of tissues pooled from large numbers of mussels provide a representative average result in the elemental analysis.

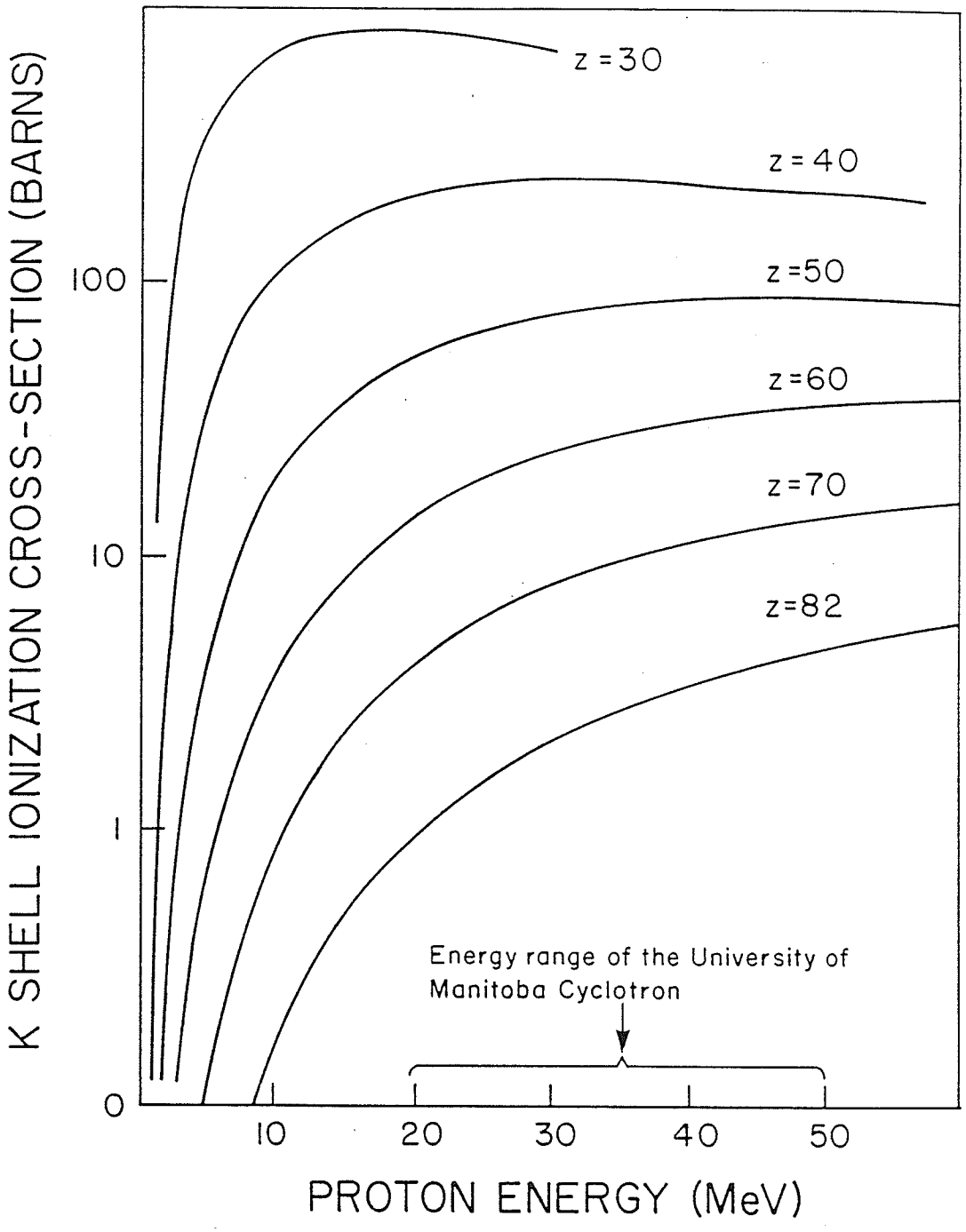

Fig. 1.1 A plot of K shell ionization cross-section vs. proton energy for different elements.

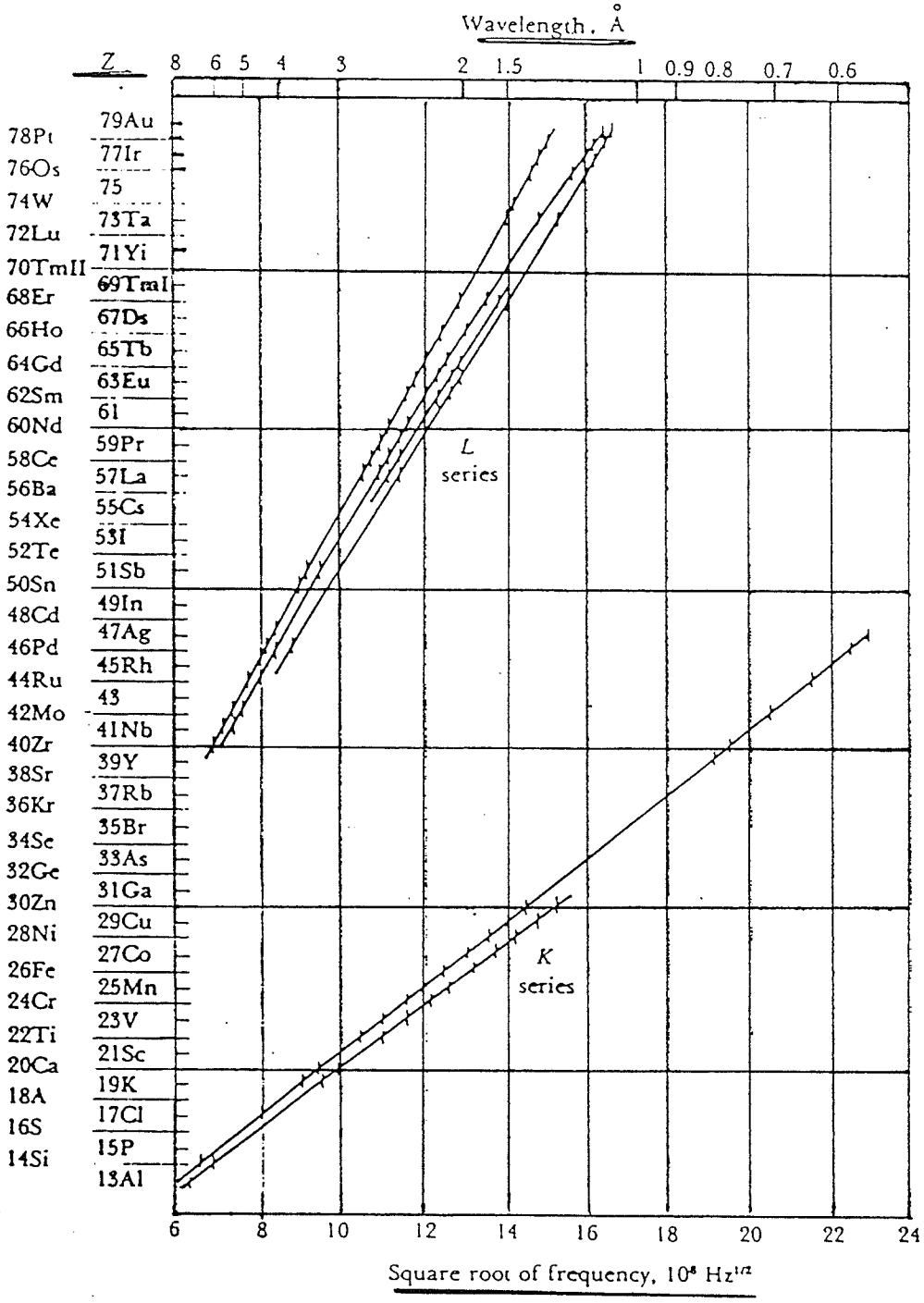

Fig. 1.2 K and L X-ray energy spectrum of elements.

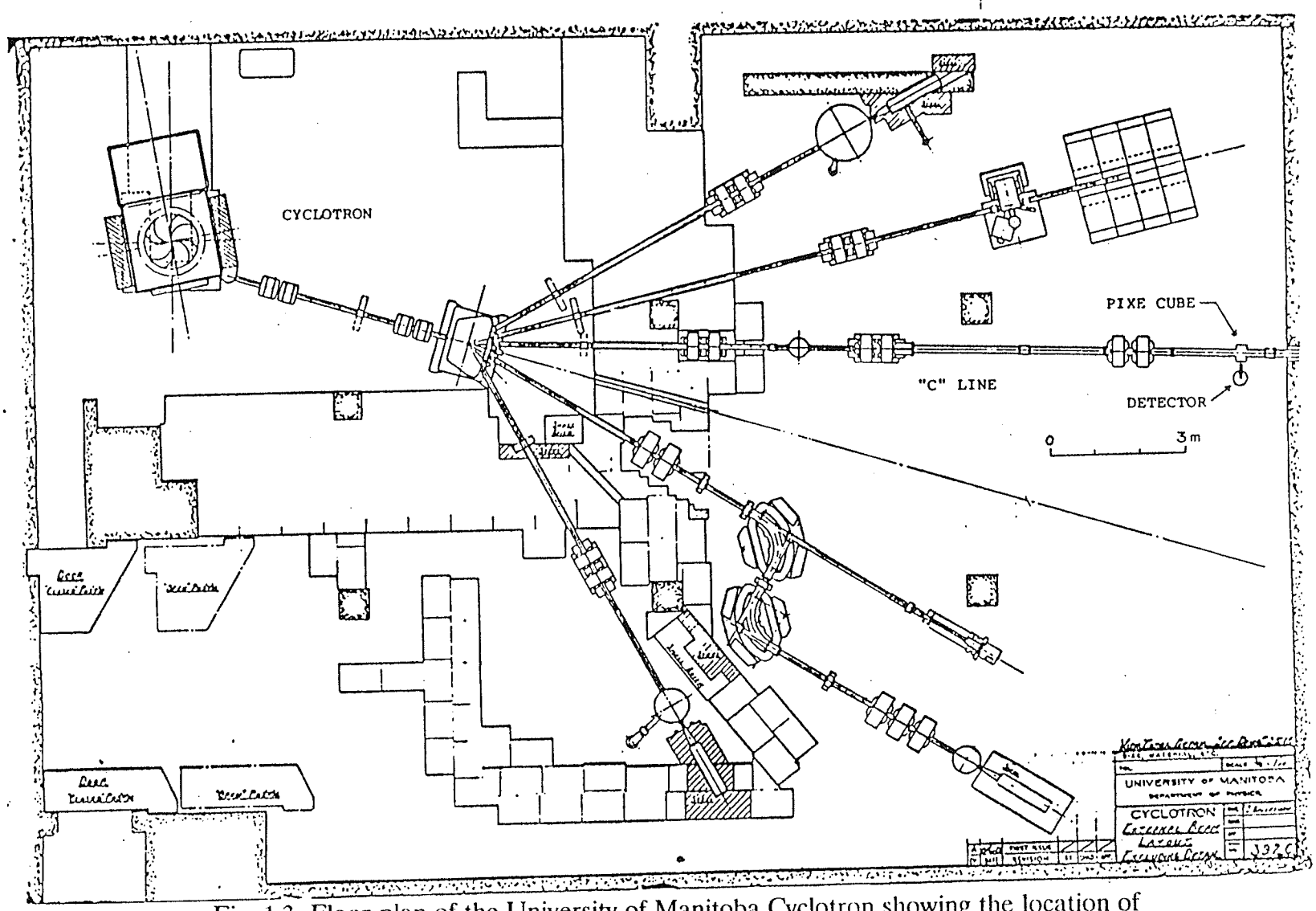

Fig. 1.3 Floor plan of the University of Manitoba Cyclotron showing the location of the "PIXE cube" on the "C" line.

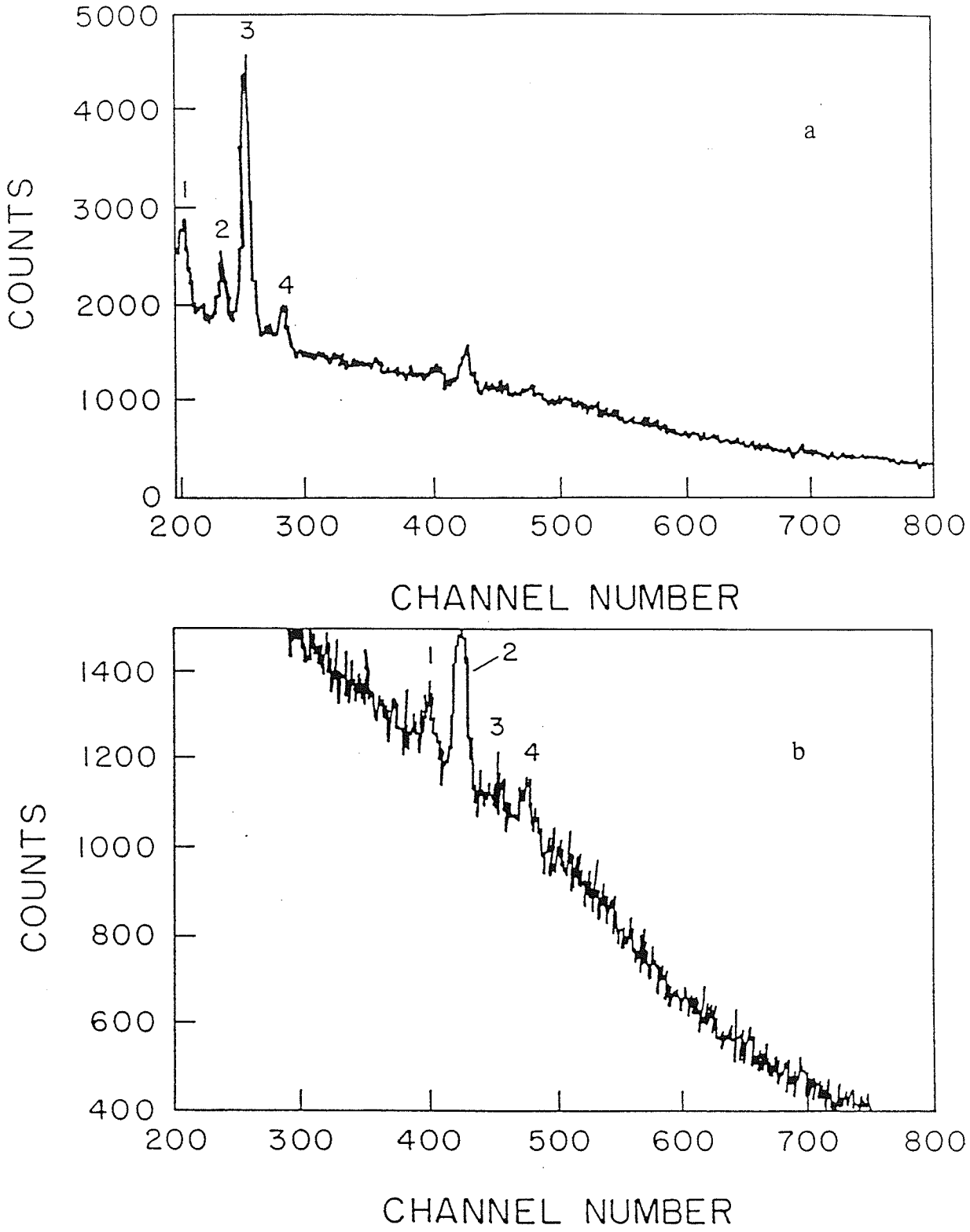

Fig. 1.4 (a) Portion of a PIXE spectrum of leaf sample taken with 40 MeV protons. Numbered peaks correspond to: 1-CoK_{α}, 2-CuK_{α}, 3-ZnK_{α}, 4-ZnK_{β}. (b) The same spectrum as in (a) expanded to make visible some of the peaks corresponding to heavier elements present in leaf sample. Numbered peaks correspond to: 1-RbK_{α}, 2-SrK_{α}, 3-RbK_{β}, 4-SrK_{β}.

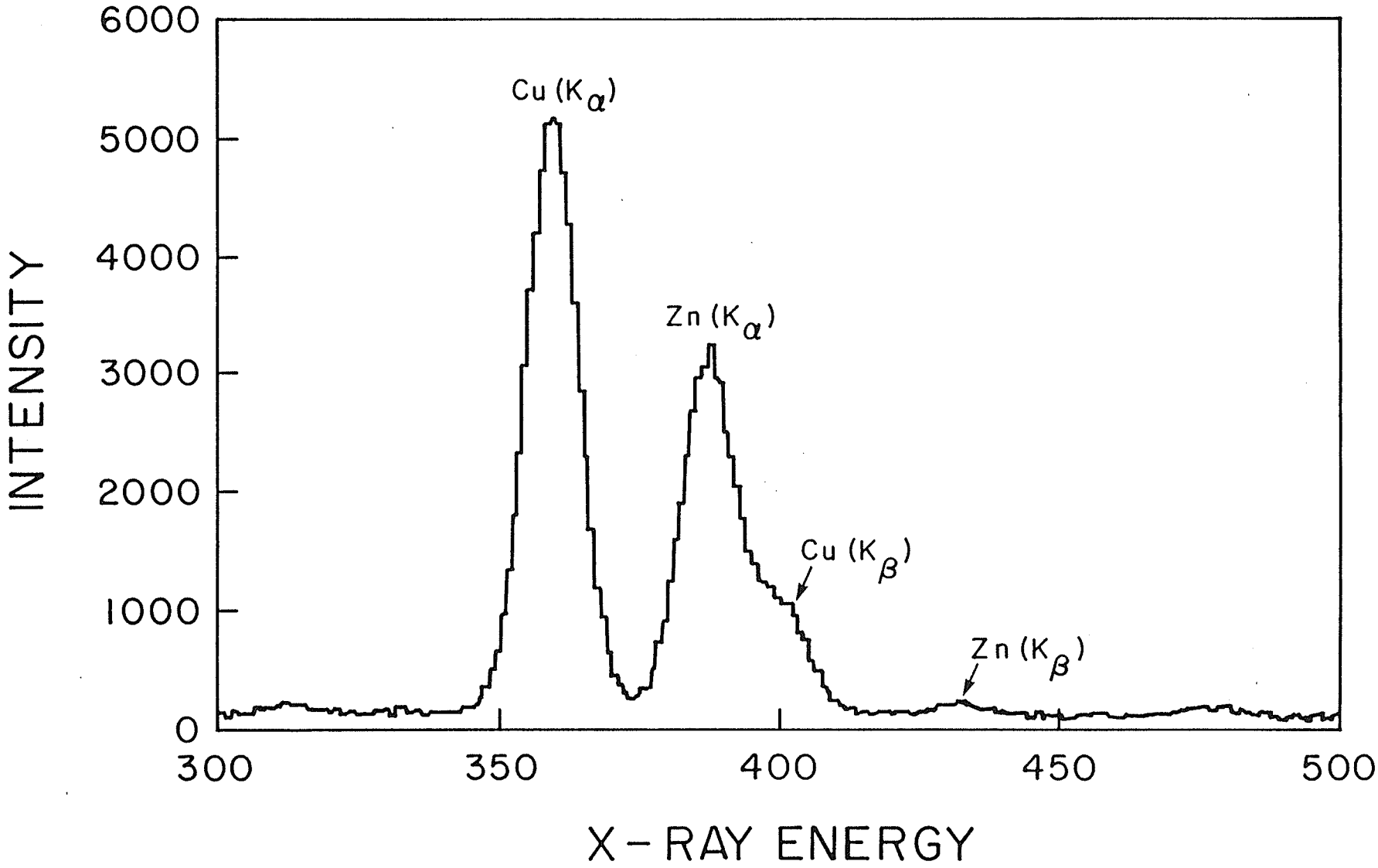

Fig. 1.5 X-ray emission spectrum induced by 30 MeV protons clearly showing K peaks corresponding to Cu and Zn from a mussel extract sample.

Chapter 2
Complexity of X-Ray Spectra

2.1. Problems Encountered in the Analysis of X-ray Spectra

The basic purpose of the *PIXE* method is the determination of the absolute concentrations of elemental constituents in the sample. After measuring an experimental *PIXE* X-ray spectrum, the first step toward an estimate of the concentrations of elements in the sample, is to evaluate the areas of all peaks in the spectrum. Investigators engaged in application of this method are aware of the difficulties inherent in the exact evaluation of peak areas and ultimately, the intensities of X-radiations from individual elements in the measured spectra. Whether one is interested in multi-element surveys, or in the measurement of trace amounts of particular elements, the X-ray spectra are not simple. They may contain overlapping peaks, and these features are superimposed on not insignificant, energy dependent background.

PIXE spectra are complicated because of the interference between K and L X-rays from light and heavy elements respectively, and between K_α and K_β peaks in neighboring elements. X-ray spectra have a multiplet structure depending on Z values. We might have a K_α and K_β doublet with both components of the doublet having a multiplet structure.

Finally, the data show statistical fluctuations. Determination of the smallest X-ray peak detectable by *PIXE* technique is complicated by the presence of the background component. The deconvolution operations in noisy spectra and in the presence of background decrease the visibility of weak peaks.

2.1.1. Continuous Background in *PIXE*

2.1.1.1. Introduction

In *PIXE* experiments when a target is bombarded with energetic protons, in addition to the characteristic X-rays of the target atoms a continuum of X-rays are also produced. This continuum of X-rays makes the background in *PIXE* spectra and determines the detection limit of *PIXE* analysis as a small characteristic X-ray peak cannot be distinguished from fluctuations in the background. While the origin of this continuum of X-rays and the processes leading to the formation of this continuum are known, the production mechanism of the continuum of X-rays is generally complicated.

In Fig. 1.4, section 1.2.2, was shown a portion of a typical *PIXE* spectrum of a leaf sample bombarded with 40 MeV protons and the X-rays produced were measured with a $Si(Li)$ detector. In this spectrum, continuous background is seen besides the characteristic X-ray peaks of the elements contained in leaf sample. Because of the fluctuation of this continuum background, the detection limit of *PIXE* is usually determined by the relation $N_P \geq 3\sqrt{N_B}$, where N_P is the number of counts of a characteristic X-ray peak and N_B is the number of counts of continuum X-rays covered by full width at half maximum (*FWHM*) of the characteristic X-ray peak. The criterion of 3σ or $N_P \geq 3\sqrt{N_B}$ yields a confidence level better than 99% for the detection of a signal. According to this relation, a characteristic X-ray peak should be larger than three times the background fluctuation to be identified as a characteristic X-ray peak.

2.1.1.2. The Origins of the Continuous Background in *PIXE*

(a) Continuous X-rays Production in Ion-Atom Collisions

The major part of the continuous background in *PIXE* is produced by the Coulomb interaction between the projectile and the target. According to Ishii et al. [Is, 87; Is, 88], concerning the origin of the continuum of X-rays induced by ion-atom collisions three main processes, namely, secondary-electron bremsstrahlung (*SEB*), quasi-free electron bremsstrahlung (*QFEB*), and atomic bremsstrahlung (*AB*) have been con-

sidered and good agreement between experiments and theoretical calculations over a wide range of projectile energy from 0.5 to 40 MeV/amu obtained [In, 90].

Before dealing with experimental and practical aspects of these bremsstrahlungs forming the continuum of X-rays and discussing the method to remove this significant component of disinformative part of the *PIXE* spectrum, the theoretical aspects of their formation are summerized below:

(1) Secondary-Electron Bremsstrahlung (*SEB*)

The secondary-electron bremsstrahlung (*SEB*) is determined by the energy distribution of the free electrons produced during the interaction of the incident protons with the target material. When a projectile ejects an electron from a target atom at point A, the electron ejected passes through the target material losing its energy and is scattered by the Coulomb field of a target nucleus at point B, and produces the so called *SEB*. The photon spectrum of *SEB* is characterized by the quantity $T_m = \frac{4m_e M_p}{(m_e + M_p)^2} E_p \approx 4m_e \frac{E_P}{M_P}$, which calculates the maximum kenetic energy that can be transferred from the projectile of mass M_P and energy E_P to a free electron at rest of mass m_e. Therefore, the bremsstrahlung of energy higher than T_m must be produced by a secondary electron ejected from an inner shell of the target atom at point A. As the number of free and outer-shell electrons is generally much larger than that of inner-shell electrons, the intensity of *SEB* rapidly decreases in the region of photon energies above T_m. A typical energy of the incident proton accelerated at the University of Manitoba Accelerator Centre is $\approx 40MeV$. Therefore the characteristic quantity of the photon spectrum of *SEB* at this energy can be calculated from the above relation as $T_m \approx 87keV$. This quantity is shown on the corresponding channel number of the leaf spectrum of Fig 2.1a.

The production cross section of bremsstrahlung σ^{SEB} by secondary electron is expressed by [In, 90]

$$\frac{d\sigma^{SEB}}{d\frac{h\omega}{2\pi}d\Omega_L}(E_p,\frac{h\omega}{2\pi},\theta_L) = \int_{\frac{h\omega}{2\pi}}^{+\infty} dE_e \int d\Omega_e \times \frac{d\sigma_e(E_p,E_e,\theta_e)}{dE_e d\Omega_e}$$

$$\times \int_{\frac{h\omega}{2\pi}}^{E_e} dE'_e (\frac{-Ndx}{dE'_e}) \frac{d\sigma^{Br}}{d\frac{h\omega}{2\pi}d\Omega_{Br}} (E'_e,\frac{h\omega}{2\pi},\theta_{Br}) \ . \qquad (2.1)$$

In the above expression, $\frac{h\omega}{2\pi}$ and θ_L are the photon energy and the angle of photon emission with respect to the direction of the projectile. Ω_L is the laboratory solid angle subtended by the detector, σ^{Br} is the production cross section of the bremsstrahlung for an electron of energy E'_e as a function of the photon energy $\frac{h\omega}{2\pi}$ and the emission angle θ_{Br} with respect to the incident direction of the electron, and σ_e is the electron-ejection cross section for the projectile as a function of the electron energy E_e and the ejection angle θ_e with respect to the projectile incident direction. The indices Br and e refer to bremsstrahlung and electron, respectively, and $\frac{-dE'_e}{Ndx}$ is the energy loss of the secondary electron in passing through the target material from point A to point B, where the energy of the electron decreases from E_e to E'_e, divided by the number of target atoms per unit volume N, and is given by the Bethe formula for energy loss [Is, 76] as:

$$-\frac{dE'_e}{Ndx} = \frac{4\pi e^4}{m_e v^2} Z \ln(1.16\frac{E'_e}{\bar{I}}) \ , \qquad (2.2)$$

where m_e, e and v are the mass, charge, and velocity of a secondary electron, respectively, and Z and $\bar{I}$ are the atomic number and mean excitation energy of the target atom, respectively.

The semiclassical calculation of the production cross section of the bremsstrahlung, σ^{Br}, has been given by Jackson [Ja, 62]. This cross section at high energy limit $E'_e = \frac{h\omega}{2\pi}$ is calculated as:

$$\frac{d\sigma^{Br}}{d\frac{h\omega}{2\pi}d\Omega_L} = \frac{2}{\pi} \frac{Z^2e^2}{\frac{hc}{2\pi}} \frac{e^2}{m_e c^2} \times (\frac{c}{v})^2 \frac{1}{\frac{h\omega}{2\pi}} \ln(4\frac{E'_e}{\frac{h\omega}{2\pi}}) \sin^2\theta_{Br} \ . \qquad (2.3)$$

The ejection cross section of an electron of energy E_e from a target atom by the projectile, $\frac{d\sigma_e(E_e, \theta_e)}{dE_e d\Omega_e}$, can be estimated from the Binary Encounter Approximation (*BEA*) [Ga, 69] or the Plane Wave Born Approximation (*PWBA*) [Ja, 70; Ra, 80] theories.

As the result of calculation, the production cross section of *SEB* is expressed by [Ya, 81; In, 90]:

$$\frac{d\sigma^{SEB}}{d\frac{h\omega}{2\pi}d\Omega_L} = \frac{1}{2\pi} Z_p^2 \left[\frac{e^2}{\frac{hc}{2\pi}}\right]^5 a_0^2 Z_T \frac{m_e c^2}{(\frac{h\omega}{2\pi})^2} (C_1 + C_2 \sin^2\theta_L), \qquad (2.4)$$

with

$$C_1 = \sum_i \int_{\frac{h\omega}{2\pi}}^{\infty} dE_e \int_0^{\infty} f_i(v_2)dv_2 \times h_1(E_e, v_2, U_i),$$

$$C_2 = \sum_i \int_{\frac{h\omega}{2\pi}}^{\infty} dE_e \int_0^{\infty} f_i(v_2)dv_2 \times h_2(E_e, v_2, U_i),$$

where Z_P and Z_T are, respectively, the projectile charge and the target atomic number, $f_i(v_2)$ and U_i are, respectively, the velocity distribution and the ionization energy of the i-shell electron, a_0 is the Bohr- atomic radius, and the functions h_1 and h_2 should be referred to [Ya, 81]. Equation 2.4 shows the angular distribution of *SEB*, which is symmetric around the maximum at $\theta_L = 90^o$. This distribution comes from the fact that secondary electrons are preferentially emitted in the forward direction and the bremsstrahlung is predominantly strong in the direction of 90^o with respect to the direction of the secondary electron.

(2) Quasifree Electron Bremsstrahlung (*QFEB*)

In a case of low energy heavy-charged particle bombardments, *SEB* is generally the predominant process for bremsstrahlung production. However, if the velocity of the projectile v_p is large enough in comparison with the velocity of the orbital electron, the orbital electron can be regarded as free and at rest. In the center of mass frame, the electron collides with the projectile with the relative kinetic energy $T_r = \frac{1}{2} m_e v_p^2$ (m_e is

the electron mass), and bremsstrahlung, called quasifree-electron bremsstrahlung (*QFEB*) is produced by the interaction between the projectile and the orbital electron. In other words, the process of *QFEB* takes place when an electron of a target atom is scattered by the Coulomb field of the projectile. T_r is the maximum energy of this bremsstrahlung and is related to the characteristic photon spectrum of *SEB* by $T_r = \frac{T_m}{4}$. However, since this process occurs in the projectile system and not in the target system; the X-ray source is the projectile and is moving with velocity v_p in the target frame. Therefore, the wavelength shift due to the doppler effect should be taken into account. The characteristic quantity of the photon spectrum of *QFEB* at the typical proton energy of $40MeV$ accelerated at the cyclotron laboratory of the University of Manitoba is calculated as $T_r = \frac{T_m}{4} \approx \frac{87}{4} = 21.7keV$. This quantity is specified on the corresponding channel number of the leaf spectrum in Fig. 2.1a.

The production cross section of the *QFEB* on the basis of *PWBA* is expressed by [Ya, 81]:

$$\frac{d\sigma^{QFEB}}{d\Omega_L \, d\frac{h\omega}{2\pi}} = \frac{N_T}{\pi} Z_p^2 \left[\frac{e^2}{\frac{hc}{2\pi}} \right]^5 a_0^2 \frac{m_e c^2}{T_r \frac{h\omega}{2\pi}}$$

$$\times \left[\sin^2\theta + \frac{1}{4}(1 + P^2)\,(3\cos^2\theta - 1) \ln\left(\frac{1+P}{1-P}\right) - \frac{1}{2} P\,(3\cos^2\theta - 1) \right], \qquad (2.5)$$

where $P^2 = \frac{1 - \frac{h\omega}{2\pi}}{T_r}$, N_T is the number of electrons of the target atom, Z_p is the atomic number of the projectile, a_0 is the Bohr radius, $\frac{h\omega}{2\pi}$ is the energy of the emitted photon, and θ is the angle between the directions of the projectile and the photon.

In the above discussion, electrons of the target atom are approximately regarded as free and at rest. However, they have a velocity distribution. Therefore, if this velocity distribution of electrons of the target atom are taken into account, the quantity T_r mentioned above and the spectrum of the emitted photons, as given by equation 2.5, should be modified (refer to [Ya, 81]).

(3) Atomic Bremsstrahlung (*AB*)

The third process for producing continuum X-rays in light-ion-atom collisions is the atomic bremsstrahlung (*AB*). In this process one of the inner-shell (bound) electrons of the target atom is excited to a continuum state by the projectile. Getting back to its original bound state, the electron emits a photon of continuum spectrum. The emission of photon in this case is due to the internal structure of the target atom.

Wave function of the final state of the electron in this process is equal to that of the initial state; $|\Psi_f> = |\Psi_i>$. If the final state is not a bound state but a continuum state, then the process is an ionization accompanied by a photon emission and is called radiative ionization (*RI*). Atomic bremsstrahlung is the most predominant component in the region of X-ray energy $\frac{h\omega}{2\pi} \geq T_m$, where T_m is the maximum energy transferred from a projectile to a free electron at rest. As compared with *QFEB* and *SEB* discussed above, each *QFEB*, *SEB*, and *AB* is the predominant process in the photon-energy region $\frac{h\omega}{2\pi} < T_r$, $T_r < \frac{h\omega}{2\pi} < T_m$, and $\frac{h\omega}{2\pi} \geq T_m$ respectively, where $T_r = \frac{1}{2} m_e v_p^2$ and v_p is the velocity of the projectile. The photon spectrum of *AB* is characterized by photon energies $\geq T_m$ in Fig. 2.1a. These three processes, i.e. *AB*, *SEB*, and *QFEB* are the main processes for continuum X-ray production in the case of light-ion-collisions.

Theoretical calculations of cross sections for the processes of *AB* and *RI* are discussed in detail in [Is, 84].

(4) Nuclear Bremsstrahlung (*NB*)

The accelerations which occur during close collisions between the projectile and the nuclei of the target atoms result in direct production of nuclear bremsstrahlung (*NB*). This is electromagnetic radiation (photons) produced by incident charged particles deflected by the nuclear charge.

The effective acceleration of the incident particle is the fundamental cause for this radiation, which is emitted with all possible energies from zero up to the energy of the incident particle beam. The total instantaneous power radiated is [Ja, 62]

$$P = \frac{2}{3}\frac{e^2}{c^3} \mid \dot{v} \mid^2 ,$$

where $\dot{v}$ is the acceleration of the particle.

For the cross section for the production of electric-dipole bremsstrahlung by this process refer to [Is, 76; Ja, 62]. Higher multipolar radiations are usually of much lower intensity.

(b) Continuous Background Induced by Other Origins

In addition to the types of bremsstrahlung mentioned above, the other types of background which are significant in *PIXE* experiments and must also be taken into consideration are the following:

(i) Rutherford background. Projectile particles, which are scattered by the target nuclei and are incident on the detector, produce large pulses and pile up with characteristic X-ray pulses, giving rise to the Rutherford background.

(ii) Compton background. Gamma rays, which are produced by the Coulomb excitation of target nuclei, are scattered by electrons in the detectors, and produce Compton background.

(iii) Response function of $Si(Li)$ detector. The tail of photo peaks and the background due to tails of the response function is an essential feature of $Si(Li)$ detectors. This tail is explained by the charge collection induced by the escape effect of Auger and photoelectrons from the intrinsic region of $Si(Li)$ detector.

(iv) Natural background. Cosmic rays and γ rays emitted from natural radio-nuclides (eg. K-40) contained in a concrete wall, make a uniform background in the X-ray spectrum. This background is not negligible in the case of a long measurement.

2.1.1.3. Conclusion

The origins of the continuum of X-rays forming the background in the *PIXE* spectra are known and it is possible to calculate the production cross section of certain types of bremsstrahlung. However, the collective production mechanism of this continuum resulting from different simultaneous processes is complicated and it is not generally possible to carry out an exact calculation of background for the whole range of a

PIXE spectrum. Conventional methods based on for example, the approximation of background by an analytical function and performing some fitting processes have not, at least in some cases, yielded satisfactory results [Ka, 87; Cl, 81a]. Some of the currently used computer progarmmes are summarized in chapter 5. Fourier transform techniques, as discussed in subsequent chapters, have been used in this thesis as an alternative approach for subtracting background in the high energy *PIXE* spectra.

2.1.2. Statistical Fluctuations

Statistical fluctuations are associated with the intrinsic random nature of the events, i.e., the X-rays, that form the fundamental information carrier in the analysis. Interrelated with the statistical fluctuations is the noise component which is a disinformative part of the measured data. Noise is due principally to statistical fluctuations in the number of counts in a channel. Unlike the spectral peaks which are spread over a number of channels, the noise results from channel to channel fluctuations. Noise, being a random process, is indeterminate in any particular single record. Large collections of records, however, show strong statistical relationships and provided sufficient resources are available the random process may be fully characterized. A random process can be defined as an ensemble or set of time functions such that the ensemble can be characterized by statistical properties.

2.2. Preconditioning The Spectra

Measurements made to investigate a phenomenon are often of an indirect nature and the acquired data frequently a linear superposition of the sought quantities. The recorded X-ray spectrum gives the response of the entire detection system to X-rays which originate as very narrow lines of many different energies. The energy and intensity of each line giving an observable peak should be calculated starting from a knowledge of the response of the system to a single narrow line.

Consider the measurement of a quantity, such as a *PIXE* X-ray spectrum, described by the function $t(E)$, using a linear system characterized by a response function $r(E,E')$. If $b(E')$ and $n(E')$ represent the background and statistical noise components respectively, the relationship between the measured data, $m(E')$, and the sought quantity, $t(E)$ may be written as:

$$m(E') = \int r(E, E')\, t(E)\, dE + b(E') + n(E')\,. \qquad (2.6)$$

The presence of $b(E')$ and $n(E')$ which are not known, make the solving of the above integral equation more complicated.

For those systems exhibiting translational invariance the response function takes the form $r(E-E')$ and the integral contained in equation 2.6 is referred to as the convolution integral. Restriction to invariant systems permits the use of Fourier transform theory which is the main topic of this thesis to remove the disinformative parts of the *PIXE* X-ray spectrum. The problem can then be framed in a more elegant manner by invoking the convolution theorem [Ke, 78a; Ke, 78b]. Position invariance is an implicit requirement in the definition of the convolution integrals and the foundation of frequency domain technique is the convolution theorem.

2.2.1. The Energy Axis Transformation

As discussed above, the greatest benefit will be obtained from a Fourier transformation incorporating a response function which is translationally invariant. This means it is required that the spectrum of interest should contain peaks having constant line widths. Clearly, this condition is not fulfilled by *Si(Li)* or *Ge* X-ray spectra because the width varies as the square root of the energy in each case. For example, the useful working energy range of a *Si(Li)* detector is from less than 1 keV up to 20 keV. From a detector with a resolution specified as 150 to 170 eV *FWHM* at 6 keV, the observed line-widths change from about 100 eV at 1 keV to 250 eV at 20 keV. However, this behavior of the line- width dependence on energy can be used to convert the observed spectrum to one containing peaks of constant width. Following the procedure of Hay [Ha, 85], the linear relationship between the square of a peak width and its energy was used to perform the transformation of the energy axis of X-ray spectra and produce peaks with constant line-widths.

The approximate linear relationship between the square of a peak width and its energy from detectors can be written as:

$$\sigma_E^2 = a + bC_E \ , \tag{2.7}$$

where the constants a and b are related to the response of the detection system.

If the channel positions, in the range, C_1 to C_2, are altered according to

$$C_H = p + q\ (a + bC_E)^{\frac{1}{2}} \ , \tag{2.8}$$

with,

$$p = C_1 - q\sigma_1 \ , \tag{2.9a}$$

$$q = \frac{C_2 - C_1}{\sigma_2 - \sigma_1} \ , \tag{2.9b}$$

$$\sigma_{1,2} = (a + bC_{1,2})^{\frac{1}{2}} \ , \tag{2.9c}$$

then the variable width, σ_E, changes to a constant width

$$\sigma_H = \frac{bq}{2} \ . \tag{2.10}$$

Using the relation expressed in equation 2.8, the functional relation between the energy

channels, C_E, and the mapped channels, C_H, is as follows;

$$C_E = \frac{1}{b}\left[\left(\frac{C_H - p}{q}\right)^2 - a\right], \tag{2.11}$$

where the values of p and q are calculated from equation 2.9a and 2.9b and the explicit values of the constants a and b are obtained from equation 2.9c as:

$$a = \sigma_1^2 - bC_1 \quad , \quad b = \frac{\sigma_2^2 - \sigma_1^2}{C_2 - C_1}. \tag{2.12}$$

C_1 and C_2 are the channel numbers which correspond to two clearly visible peaks chosen nearby in the beginning and the end of a spectrum and σ_1 and σ_2 are the widths of the corresponding peaks calculated experimentally. However, the range between C_1 and C_2 may not include the whole spectrum and consequently equations 2.8 or 2.11 above, produce peaks with constant line-widths only in the region confined between C_1 and C_2. In order to extend the range C_1C_2 so that it covers the whole spectrum it is proceeded as follows:

$$\sigma_i = (a + bC_i)^{\frac{1}{2}} \ , \ \sigma_f = (a + bC_f)^{\frac{1}{2}} \ , \ p' = C_i - q'\sigma_i \ , \ q' = \frac{C_f - C_i}{\sigma_f - \sigma_i}, \tag{2.13}$$

where the values a and b are the same as the ones calculated from equation 2.12 and C_i and C_f can have, for example, values of 1 and 1024 respectively in a 1024-channel spectrum.

Finally, the new relation between the energy channels C'_E and the mapped channels, C_H, will be the following:

$$C'_E = \frac{1}{b}\left[\left(\frac{C_H - p'}{q'}\right)^2 - a\right]. \tag{2.14}$$

It was shown above that, in a spectrum, by properly choosing two visible peaks having the centroids C_1 and C_2 and obtaining the experimental values of their widths σ_1 and σ_2 respectively, it was possible to perform the transformation of the energy axis of X-ray spectra and produce peaks with constant line-widths using relations 2.11 or 2.14. However, apart from the above experimental approach, there is another approach to serve the same purpose using the manufacturer/ rated values of the detectors and the calibration information without measuring the widths σ_1 and σ_2 from the experimental spectrum. To clarify the second approach, we use the calibration equation which was

obtained during the calibration run for the leaf experiment (refer to section 1.2.2) using $Am-241$ source and a $Si(Li)$ detector:

$$E(keV) = 0.37917 + 0.0321456\ C_E\ ,$$

where C_E represents the channel number corresponding to an energy E.

If the resolution of the detector is assumed to be 100 eV at 1 keV and 250 eV at 20 keV, then, by using the above calibration equation, the values of the centroids of the peaks sitting in the positions corresponding to 1 keV and 20 keV will be:

$$C_1(1keV) = 19.31 \text{ channels}$$
$$C_2(20keV) = 610.37 \text{ channels.}$$

From calibration equation, 1 channel is equivalent to 32 eV, then the $FWHM$ and the width, σ, of the peaks at the positions of C_1 and C_2 are calculated using: $FWHM = \frac{Resolution(eV)}{\frac{eV}{channel}}$ as follows;

$$(FWHM)_1 = \frac{100}{32} = 3.125 \text{ channel}$$
$$(FWHM)_2 = \frac{250}{32} = 7.182 \text{ channel}$$
$$\sigma_1 = \frac{(FWHM)_1}{(8\ ln2)^{\frac{1}{2}}} = 1.327 \text{ channel}$$
$$\sigma_2 = \frac{(FWHM)_2}{(8\ ln2)^{\frac{1}{2}}} = 3.317 \text{ channel.}$$

While the second approach seems to be more applicable to develop an automated system, however, due to uncertainties in the rated values of resolution for a given detector, aging effect, etc., a better result for preconditioning the data for using Fourier transform techniques and finally removing the disinformative parts of the data is obtained from the first approach as will be shown later.

Counts from the original spectrum must be redistributed to conform to the new channels. However, referring to equations 2.11 and 2.14 it can be seen that the integer energy channels C_E do not map into integer mapped constant width channels C_H.

Hence, to produce the integer C_H spectrum, counts must be transferred from fractional C_E. If data from split channels are shared in proportion to their fractions, then the resulting spectrum conserves areas without distorting the Poisson statistics of the original counts.

Figure 2.1b shows a portion of an experimental spectrum of a leaf sample (refer to section 1.2.2), taken at an incident proton energy of 40 MeV with a silicon detector and Fig. 2.2 represents the pre-conditioned version of the same spectrum. In Fig. 2.1b the standard deviations of visible peaks varied from 1.407 to 2.947 channels (refer to table 2.1). After preconditioning, all the peaks in the spectrum of Fig. 2.2 should exhibit a constant width of $\sigma_H = 2.557$ channels (refer to equation 2.10).

Referring to table 2.2 it can be noticed that all the peaks except peak number 3 have obtained a width nearly equal to the calculated value of $\sigma_H = 2.557$. By referring to elemental identification presented in chapter 5, it is noticed that peak #3 which is narrower than the other peaks both before and after preconditioning the data (refer to table 2.1 and table 2.2) corresponding to $Mn(K_\alpha)$. However, during previous *PIXE* experiments it was noticed that a spurious artefact was always present and superimposed on the $Mn(K_\alpha)$ peak. Clearly the peak #3 is an artefact, as it is generated by the detector whether or not the target is in place. Therefore, the narrow width of peak #3 can be attributed to the existence and dominance of this artefact. Unfortunately, the detector was not replaced to verify the disappearance of the artefact.

The following relations apply to the calculation of the elements in tables 2.1 and 2.2 [Fa, 84].

(i) Calculation of centroid $\overline{x}$

$$\overline{x} = \sum_i \frac{x_i\, h_i}{S},$$

where x_i is the channel number i under the peak, h_i is the corresponding number of counts and S is the total number of counts under the peak.

(ii) Calculation of standard deviation σ

$$\sigma^2 = \sum_i \frac{x_i^2 h_i}{S} - \overline{x}^2 - \frac{1}{12}.$$

iii) Calculation of *FWHM*

$$FWHM = (8\ln 2)^{\frac{1}{2}}\,\sigma\,.$$

(iv) Calculation of uncertainty in centroid

$$\delta\bar{x} = \left[\frac{\sigma^2 + \frac{1}{12}}{S}\right]^{\frac{1}{2}}.$$

(v) Calculation of uncertainty in standard deviation

$$\delta\sigma = \left[\frac{\frac{\sigma^2}{2} + \frac{1}{12} + \frac{0.09305}{\sigma^2}}{S}\right]^{\frac{1}{2}}.$$

Table 2.3 shows how the counts from the original spectrum are redistributed to conform to the new channels. Columns 1 and 2 represent the channel numbers and the corresponding counts respectively in a portion of the original data (channel number 200 to 250). Columns 3 and 4 are the output from equation 2.14 and represent how the fractional channels C_E are mapped to integer, constant-width channels, ICH. Finally, column 5 shows the calculated counts for the corresponding integer channels in column 4. Figure 2.1b corresponds to the whole range of data in columns 1 and 2 and figure 2.2 represents the preconditioned data in columns 4 and 5 for the whole spectrum.

The following are the centroids and the widths of the two experimental visible peaks, at the near and the far end of the leaf spectrum, used in equations 2.9, 2.11, and 2.12 for the energy axis transformation of the spectrum (refer to table 2.1):

$$C_1 = 85.234589 \qquad C_2 = 425.323029$$

$$\sigma_1 = 1.407343 \qquad \sigma_2 = 2.947600\,.$$

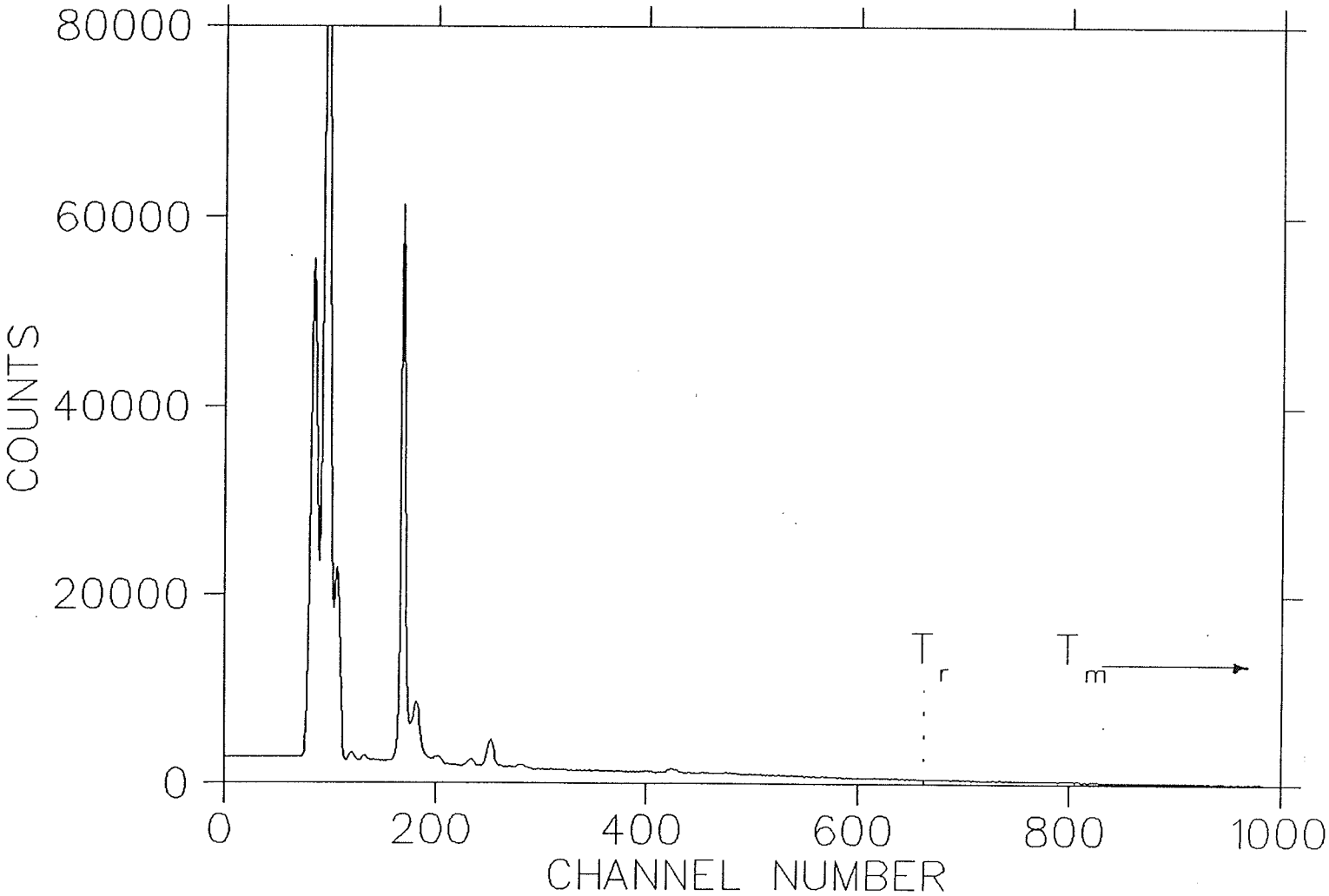

Fig. 2.1a) Typical X-ray spectrum of a leaf sample at an incident proton energy of 40 MeV (silicon detector). T_m, the characteristic quantity of the photon spectrum of SEB; and T_r, the characteristic quantity of the photon spectrum of QFEB are also specified.

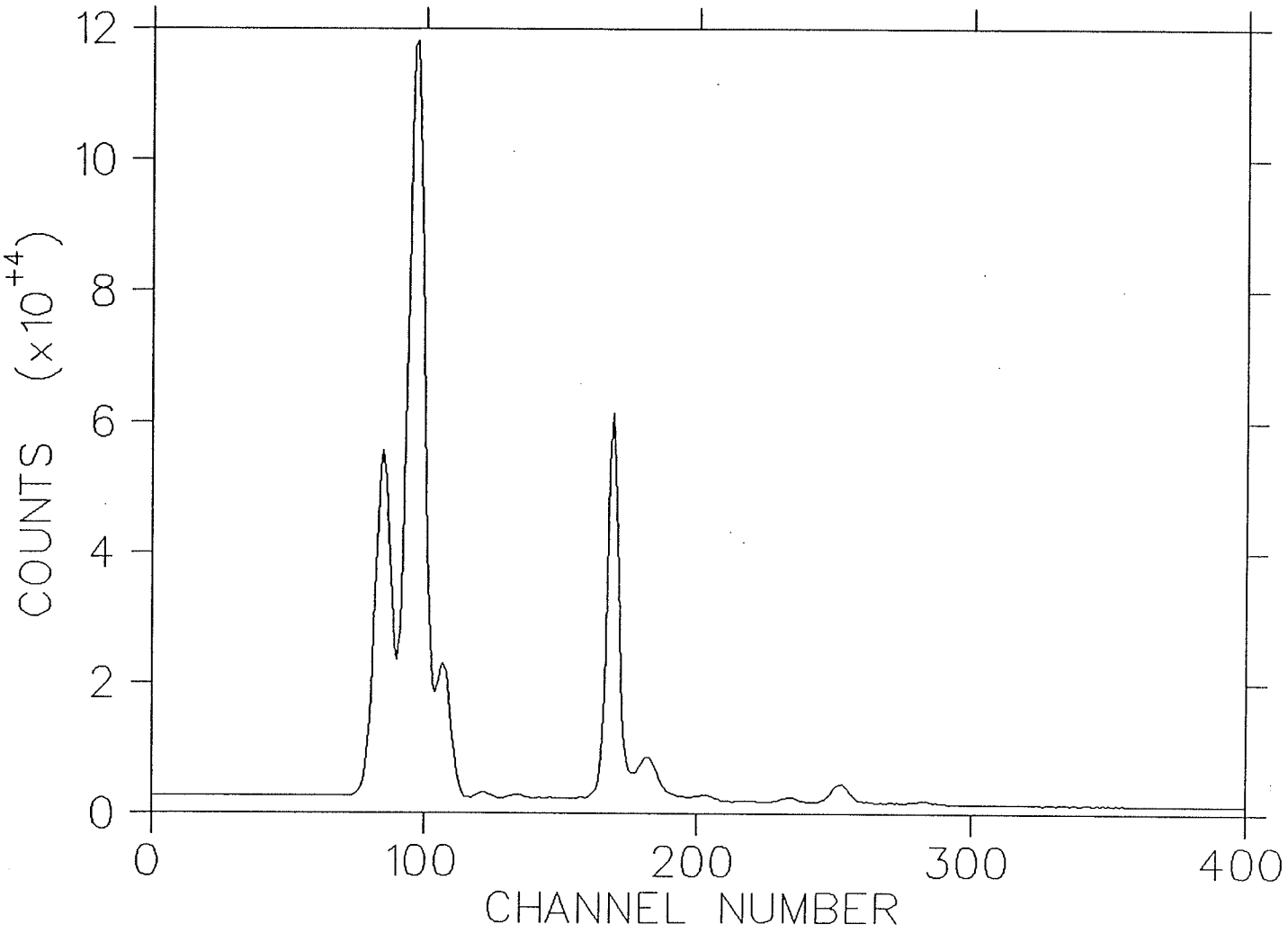

Fig. 2.1b) A portion of the X-ray spectrum of the leaf sample of Fig. 2.1a).

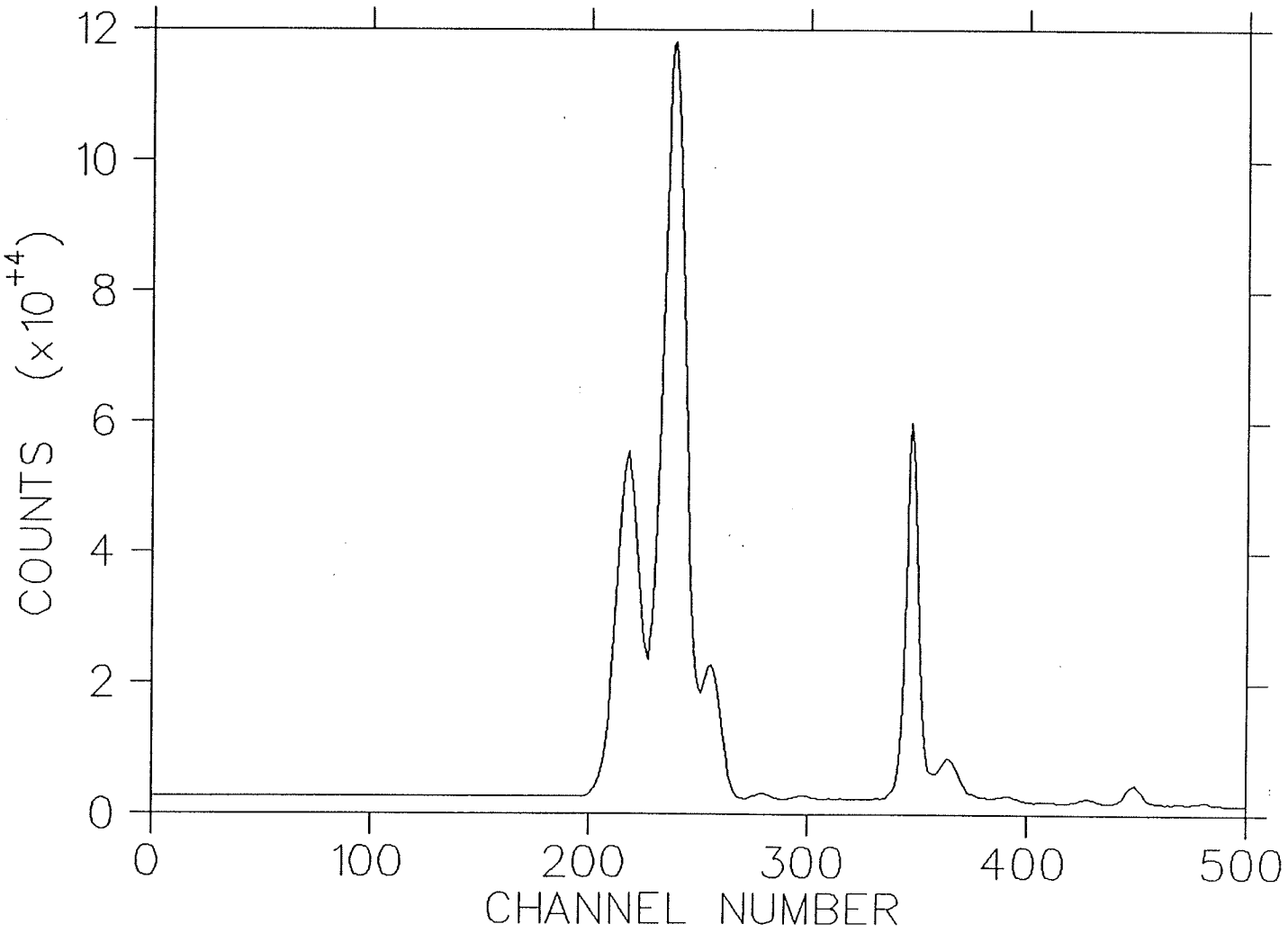

Fig. 2.2 Spectrum of the same leaf sample as Fig. 2.1 after the preconditioning to produce constant-width peaks.

Table 2.1 Centroid (Average), uncertainty in centroid (Daverage), standard deviation (Stand Devia), uncertainty in standard deviation (Dstand Devia), FWHM and uncertainty in FWHM (DFWHM) of six visible peaks of the spectrum of the leaf sample of Fig. 2.1.

PEAK (Raw)	AVERAGE	DAVERAGE	STAND DEVIA	DSTAND DEVIA	FWHM	DFWHM
1	85.234589	0.004398	1.407343	0.003183	3.314039	0.007496
2	96.552429	0.002853	1.434518	0.002061	3.378032	0.004853
3	168.981995	0.003083	0.757045	0.002729	1.782704	0.006425
4	233.250626	0.041381	2.972271	0.029296	6.999163	0.068987
5	252.476303	0.018695	2.164226	0.013276	5.096364	0.031262
6	425.323029	0.054963	2.947600	0.038913	6.941068	0.091633

Table 2.2 The same information as in Table 2.1 for the same peaks in the preconditioned spectrum of Fig. 2.2.

PEAK (Mapped)	AVERAGE	DAVERAGE	STAND DEVIA	DSTAND DEVIA	FWHM	DFWHM
1	218.177948	0.005970	2.688746	0.004229	6.331514	0.009959
2	238.193054	0.003878	2.520265	0.002749	5.934771	0.006472
3	347.035370	0.003813	1.208487	0.002811	2.845769	0.006620
4	426.971710	0.040982	2.851717	0.029019	6.715281	0.068336
5	448.423462	0.020001	2.557370	0.014173	6.022147	0.033376
6	615.967468	0.053306	2.576401	0.037773	6.066961	0.088948

Table 2.3 Original data (columns 1 and 2), energy axis transformation (columns 3 and 4) and the preconditioned data (columns 4 and 5).

ICE	COUNTS	CE	ICH	MCOUNTS
200	2790	75.279	200	3098
201	2766	75.804	201	3312
202	2841	76.331	202	3694
203	2884	76.860	203	4175
204	2798	77.390	204	4958
205	2716	77.921	205	5850
206	2529	78.454	206	7396
207	2357	78.989	207	9061
208	2286	79.525	208	12005
209	2077	80.062	209	15149
210	1958	80.601	210	19601
211	1992	81.142	211	24421
212	1992	81.684	212	30235
213	1888	82.228	213	36180
214	1917	82.773	214	42287
215	1954	83.319	215	47427
216	1974	83.868	216	51895
217	1944	84.417	217	54074
218	1974	84.969	218	55536
219	1931	85.521	219	53298
220	1964	86.076	220	50516
221	1957	86.631	221	45770
222	1828	87.189	222	40825
223	1883	87.748	223	35527
224	1794	88.308	224	30845
225	1858	88.870	225	26659
226	1854	89.433	226	24745
227	1882	89.998	227	23511
228	1970	90.565	228	26147
229	2007	91.133	229	29705
230	2115	91.702	230	36226
231	2289	92.273	231	44622
232	2347	92.846	232	55077
233	2541	93.420	233	67136
234	2501	93.995	234	79798
235	2472	94.572	235	92591
236	2302	95.151	236	104354
237	2181	95.731	237	113084
238	2031	96.313	238	117496
239	1958	96.896	239	118172
240	1827	97.481	240	112690
241	1896	98.067	241	105214
242	1850	98.655	242	92658
243	1864	99.244	243	79352
244	1787	99.835	244	64968
245	1949	100.427	245	52212
246	2082	101.021	246	40192
247	2392	101.616	247	31930
248	2700	102.213	248	25203
249	3314	102.812	249	21283
250	3884	103.412	250	19442

2.2.2. Increasing the Range of the Original Data

Another feature to be considered for preconditioning the data is increasing its range. A function that is to be submitted to Fourier transformation needs to be "periodical" in some way that allows reasonable continuity conditions at the endpoints. Then the background contribution to the spectrum can be determined without "ringing" at these points. The method selected was to increase the range of the original data, which was initially 1024 channels, to 2048 channels. Those additional channels were filled by reflecting the initial spectrum in a "mirror" located in channel 1024. The result of preconditioning and reflection is shown in Fig. 2.3. However, expanding the length of the baseline of data from 1024 to 2048 channels must not be misconstrued as doubling the data to be fitted. The Fourier transform of these data will include an infinite number of frequencies, and while this step seems to double the number of data points, care is taken throughout the application of the technique, to keep the number of frequencies used to half the number of initial data channels (Fourier transform techniques will be discussed in detail in subsequent chapters).

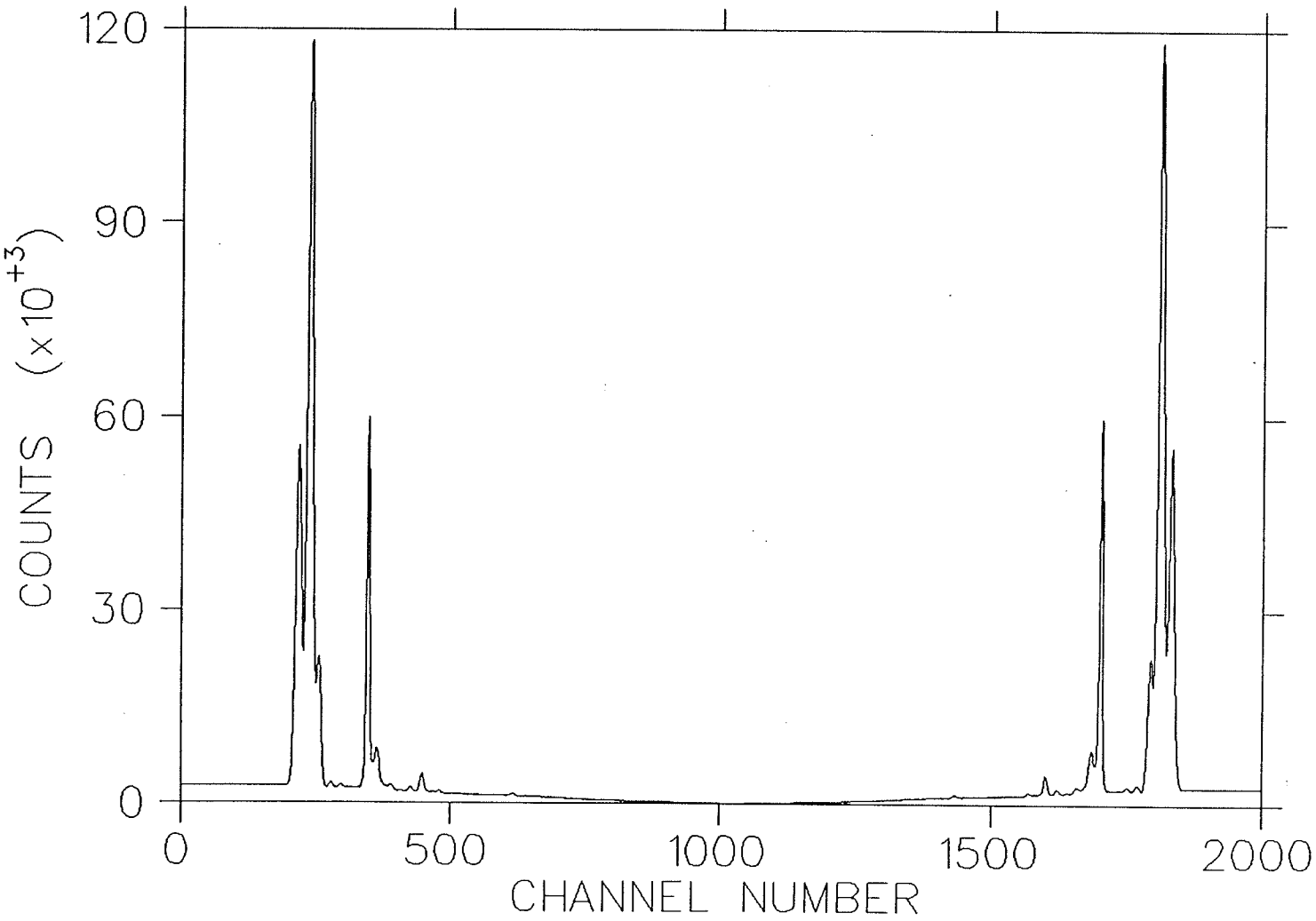

Fig. 2.3 2048-channel spectrum obtained by reflecting the initial preconditioned spectrum in a "mirror" located in channel 1024.

2.2.3. Calibration of the System

In this section the calibration of the system is discussed before and after preconditioning the spectrum and the results of energy calculations are presented. Obviously, it is expected that the energies obtained for different peaks/features in both cases should be quite consistent and any discrepancies between the two energy calculations should be far less than the resolution of the detector at the energies concerned.

The calibration source used during the *PIXE* experiments was *Am*–241. Calibration spectrum obtained during the "leaf experiment/analysis" (refer to section 1.2.2) is represented in Fig. 2.4. The five characteristic lines of *Am*–241, shown in Fig. 2.4, were used to obtain the calibration curve/equation shown in Fig. 2.5 (the channel numbers, C_E, and the corresponding energies, $E(C_E)$, of these lines are represented in columns 1 and 2 of table 2.4.

The preconditioned calibration spectrum of Fig. 2.4 is shown in Fig. 2.6. It is important to note that the preconditioning, i.e. the energy axis transformation, of the calibration spectrum and the *PIXE* X-ray spectrum to be analyzed should be performed under similar conditions. The energy axis transformation equations (2.11 and 2.14), are very sensitive to the values of the widths of the peaks. A small change in the value of σ_1 and σ_2 produces a considerable change in preconditioning the spectra. Therefore, it is not advisable to select two visible peaks in each calibration and *PIXE* X-ray spectrum and calculate the values of the four parameters (C_1, σ_1, C_2, and σ_2) independently. Otherwise, the two spectra will be preconditioned in different ways and the calibration information after preconditioning will not yield consistent results for energy calculation and the energy of a given energy channel will be different from that of the corresponding "mapped" channel.

Taking the above preconditioning remarks into consideration, the same values of C_1, σ_1, C_2, and σ_2 as used for preconditioning the leaf spectrum, given in section 2.2.1, were used for preconditioning the calibration spectrum.

The third column, C_H, in table 2.4 represents the mapped channel numbers after preconditioning the spectrum corresponding to each of the energy channels, C_E, shown in the first column before preconditioning and in the fourth column are the corresponding fitted energies of the values of column 2 for each mapped channel. Calibration curve and the calibration equation, used to calculate the energies of the preconditioned

leaf spectrum, were obtained by the least-squares fitting of the data in columns 2 and 3 of table 2.4 and are shown in Fig. 2.7. While only the five characteristic lines of Am–241 were sufficient for the fitting process, however, more data points were used to cover nearly the whole range of the spectrum. A quadratic fit was made to the data points and the total chi-square was calculated as $\chi^2 = 0.005$ and the reduced χ^2 was $\chi^2_\nu = 0.0007$. Reduced χ^2 or $\chi^2_\nu = \frac{\chi^2}{\nu}$ where ν is the number of degrees of freedom. The number of degrees of freedom is the number N values used to calculate χ^2 minus the number of parameters calculated from the data to describe the distribution. For the above case where $N = 10$ and the number of parameters for a quadratic fit is 3, then $\nu = 10 - 3 = 7$. If the fitting function is a good approximation to the parent function, then $\chi^2_\nu \approx 1$. If $\chi^2_\nu > 1$, the fitting function is not appropriate for describing the data. A value of $\chi^2_\nu < 1$, as is the case in the above quadratic fit, does not indicate an improvement of the fit, however, it is simply a consequence of the fact that the observed value χ^2_ν will fluctuate from experiment to experiment [Be, 69].

To test the quality of results, some random channel numbers from the integer preconditioned leaf spectrum, as shown in the third column of table 2.5, were chosen and their energies together with those of the corresponding fractional energy channels, C_E, were compared. The values of discrepancies between the two sets of energies are represented in column 5. It is noticed that the result is satisfactory as these values are well within the uncertainties of the detection system.

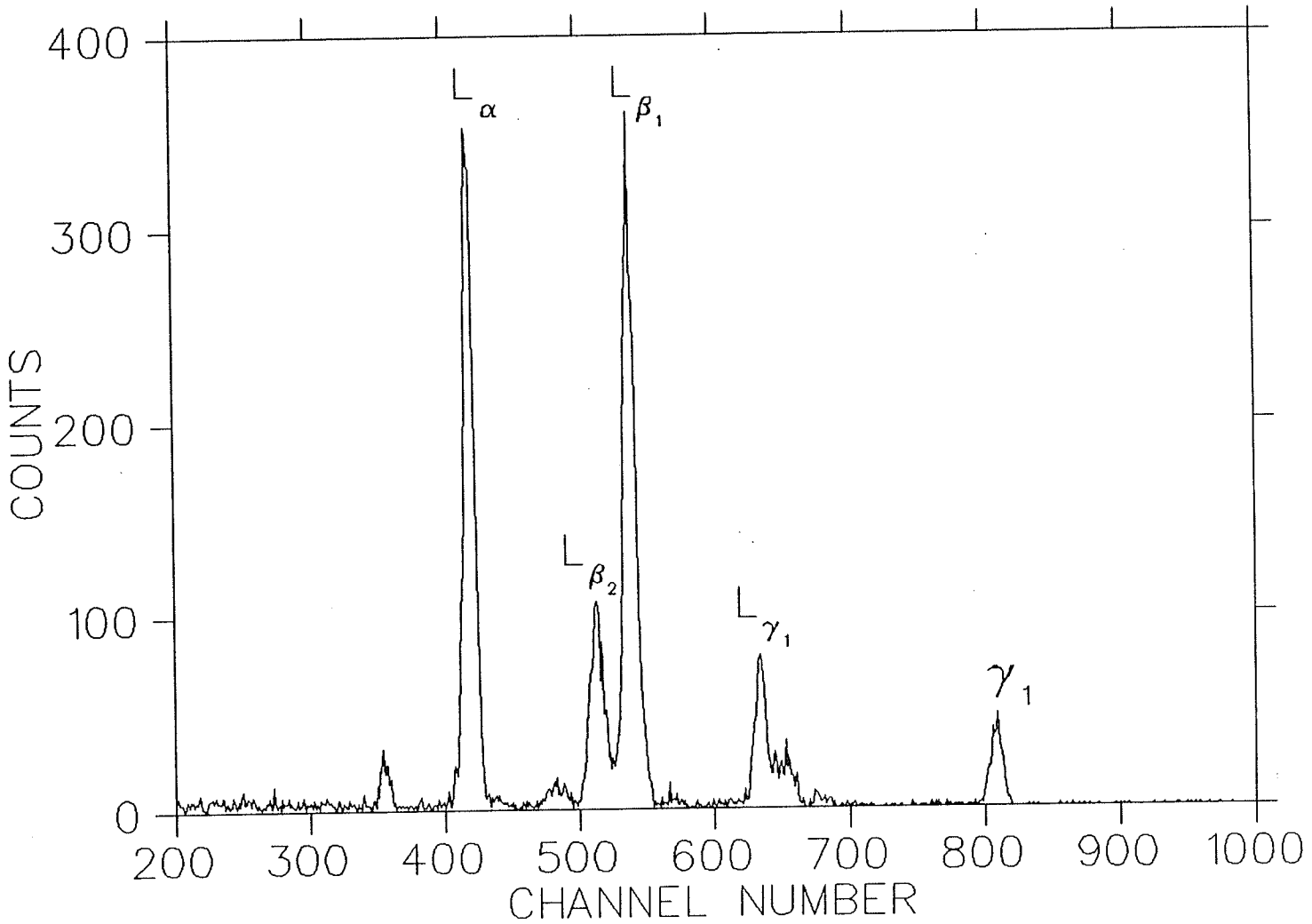

Fig. 2.4 Calibration spectrum from ^{241}Am, calibration source, during the leaf experiment (silicon detector).

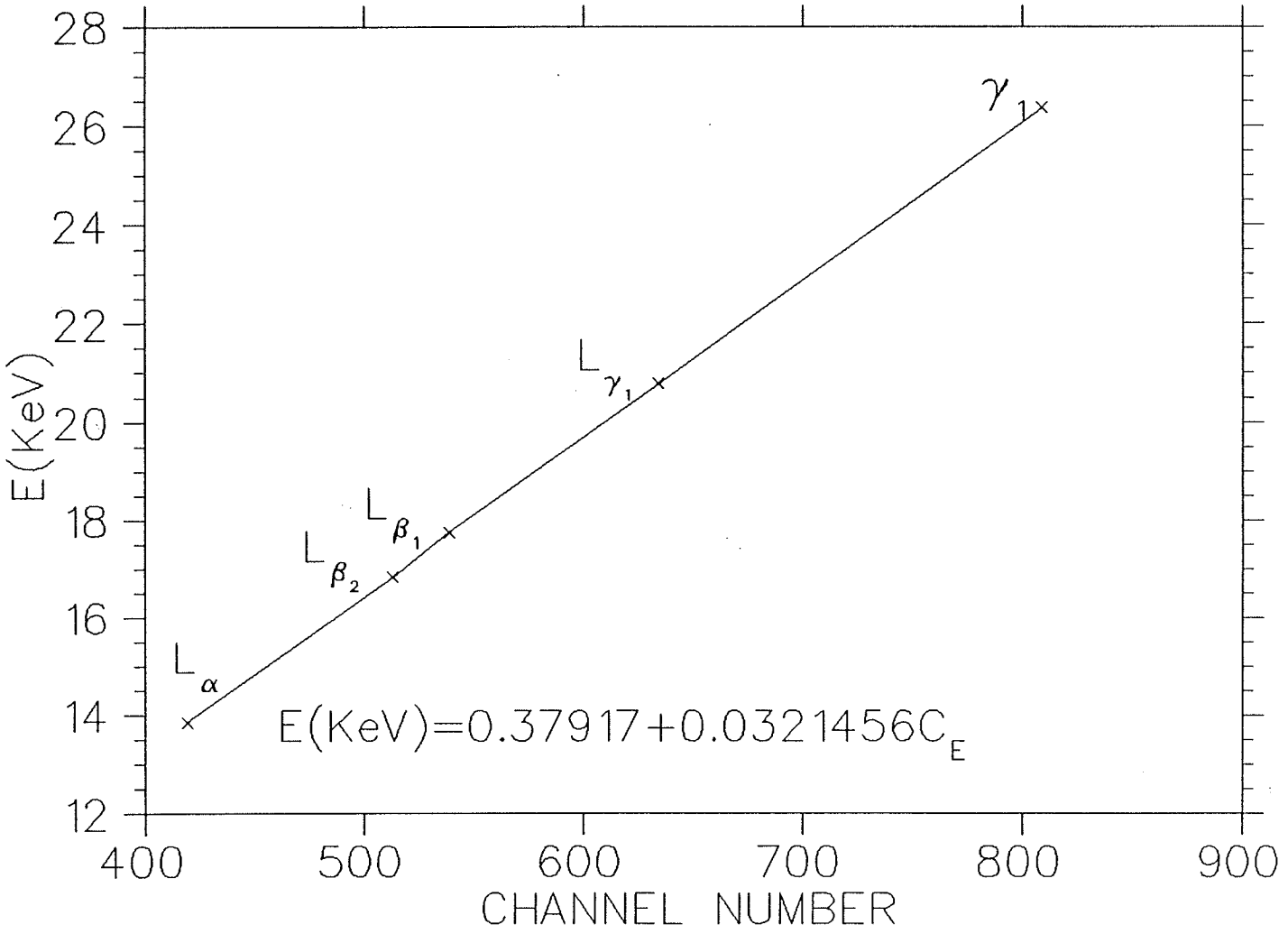

Fig. 2.5 Calibration curve obtained from Fig. 2.4.

Table 2.4 Comparison between the fitted energies after preconditioning the calibration spectrum and the corresponding energies before preconditioning.

C_E	$E(C_E)$ (keV)	C_H	$E(C_H)$ fitted (keV)	$E(C_E) - E(C_H)$ (eV)
100.000	3.594	244.279	3.591	3
200.000	6.808	387.023	6.809	-1
300.000	10.023	498.857	10.026	-3
419.249(1)	13.852	610.791	13.856	-4
513.406(2)	16.837	688.738	16.885	-48
538.880(3)	17.750	708.480	17.699	-51
634.399(4)	20.785	779.184	20.770	15
700.000	22.881	824.811	22.882	-1
808.554(5)	26.360	895.884	26.374	-14
900.000	29.310	952.048	29.308	2

(1) ^{241}Am L_α line
(2) ^{241}Am $L_{\beta 2}$ line
(3) ^{241}Am $L_{\beta 1}$ line
(4) ^{241}Am $L_{\gamma 1}$ line
(5) ^{241}Am γ_1 line

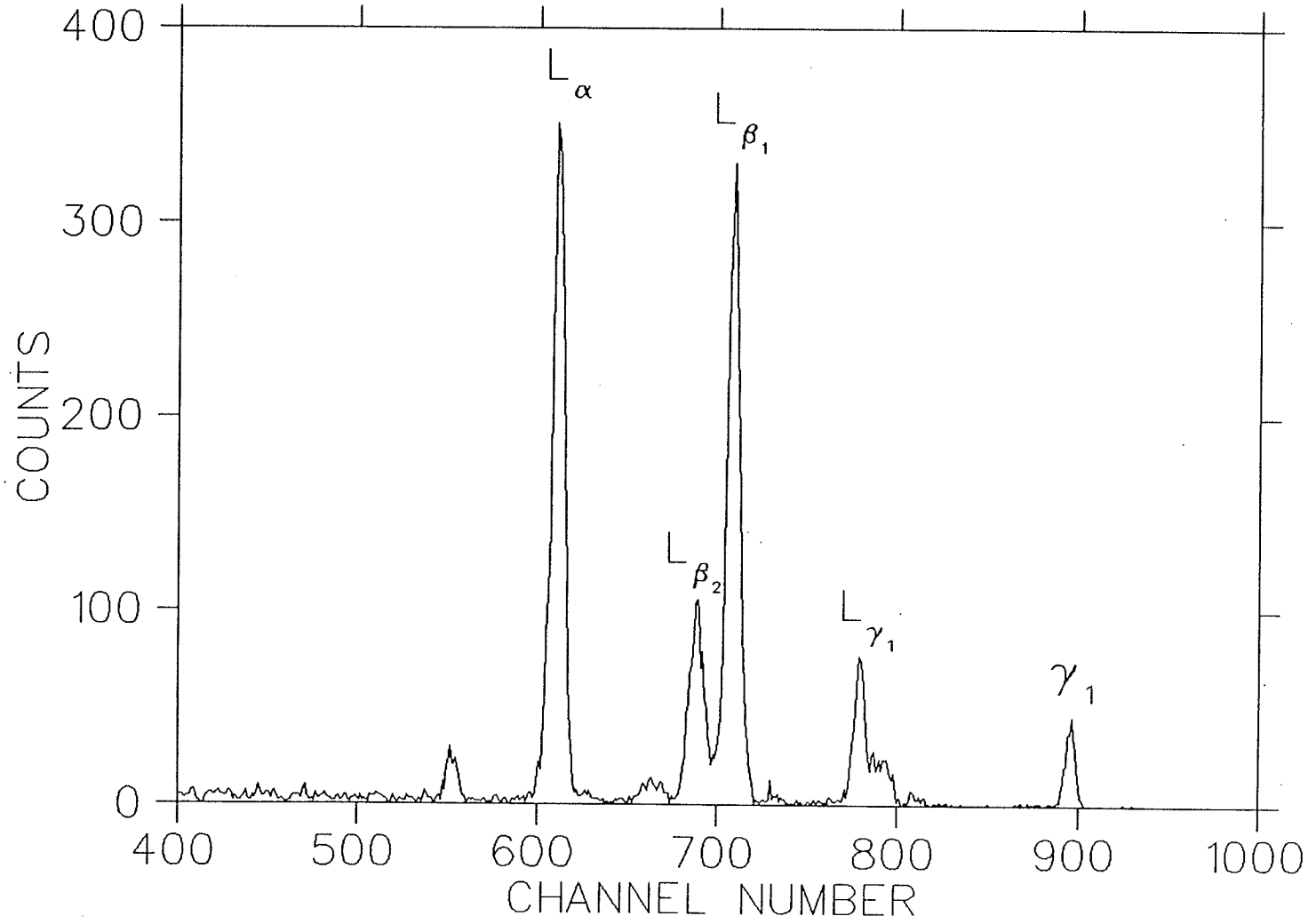

Fig. 2.6 Calibration spectrum as in Fig. 2.4 after the preconditioning.

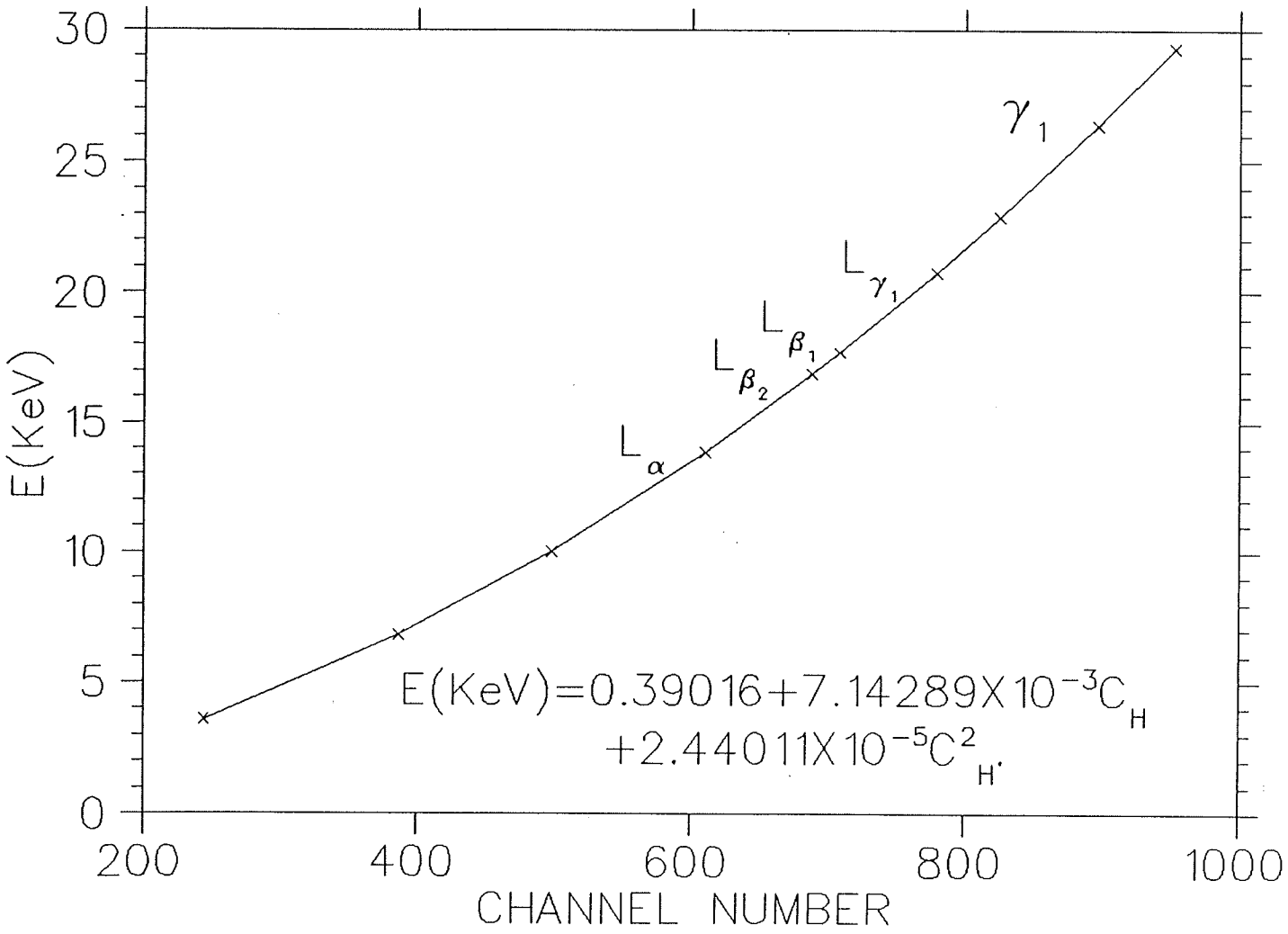

Fig. 2.7 Calibration curve obtained from the preconditioned calibration spectrum of Fig. 2.6.

Table 2.5 Test of the calibration equation after preconditioning the calibration spectrum.

C_E	$E(C_E)$ (keV)	C_H	$E(C_H)$ calc. (keV)	$E(C_E) - E(C_H)$ (eV)
171.086	5.879	350	5.879	0
253.972	8.543	450	8.545	2
352.071	11.697	550	11.700	3
465.381	15.339	650	15.342	3
593.904	19.470	750	19.473	3
737.639	24.091	850	24.091	0

Chapter 3
Fourier Transform Techniques

3.1. Introduction

The basic strategies and numerical operations required for separating the spectral components for *PIXE* X-ray spectrum analysis were established about twenty years ago. The aims are to separate the background from the peaks and to disentangle overlapping peaks. The numerical procedures which are employed include convolution (i.e. smoothing) to dampen down the statistical noise, deriving difference or second difference spectra to locate peaks, interpolations to remove background, and least-squares optimization to extract peak energies and intensities.

The most common approach to the background in *PIXE* X-ray spectra has been its approximation by an analytical function: typically a polynomial, or an exponential function multiplied by a polynomial with a certain number of free parameters, the values of which are determined by an iterative fitting process. Published results and the experience of many investigators indicate that, at least in some cases, the results obtained are unacceptable, as either an overestimation or an underestimation of some of the peak areas is observed [Ka, 87].

The traditional approach in developing processing programmes for *PIXE* analysis and some of the currently used computer programmes with corresponding references are discussed in chapter 5.

An alternative approach of looking at the information content of a spectrum is through its Fourier transform. Fourier transform techniques have played a key role in different areas of science for a number of years, and it continues to be a topic of interest in theoretical as well as applied scientific works.

The measured data, in addition to the spectral peaks or true information, has background and noise components. Clearly, each energy channel of the data spectrum contains these types of information in varying degrees. The suspicion is that if a Fourier transformation of these data to a frequency domain is made, the broad, slowly varying background component could be characterized by a set of frequencies which are different from those characteristic of the peaks (several channels associated together), and both of these are different from the set of frequencies typical of noise (a channel by channel variation).

3.2. The Fourier Integral

Let $f(x)$ be a continuous function of a real variable x. The Fourier transform of $f(x)$ is defined by the equation:

$$F(\nu) = \int_{-\infty}^{+\infty} f(x)\, e^{-i2\pi\nu x}\, dx. \tag{3.1}$$

The right hand side of equation 3.1 is a Fourier integral, and given $F(\nu)$, one may therefore apply Fourier's integral theorem with the result

$$f(x) = \int_{-\infty}^{+\infty} F(\nu)\, e^{i2\pi\nu x} d\nu. \tag{3.2}$$

Equations 3.1 and 3.2, which are called the Fourier transform pair, exist if $f(x)$ is continuous and integrable and $F(\nu)$ is integrable. These conditions are almost always satisfied in practice.

The Fourier transforms shown in the above two equations reduce to special forms when $f(x)$ or $F(\nu)$ satisfy certain conditions. If $f(x)$ is real and symmetrical, that is, if it is an even function $f_e(x)$, then,

$$F(\nu) = \int_{-\infty}^{+\infty} f_e(x) \cos 2\pi\nu x\, dx - i \int_{-\infty}^{+\infty} f_e(x) \sin 2\pi\nu x\, dx = 2\int_0^{\infty} f_e(x) \cos 2\pi\nu x\, dx \tag{3.3}$$

is real and is given by the cosine Fourier transform of $f_e(x)$. By changing the sign of ν in equation 3.3 it is noticed that $F(\nu) = F(-\nu)$ and thus $F(\nu)$ is also even. The inverse relation to 3.3 is

$$f_e(x) = \int_{-\infty}^{+\infty} F(\nu) \cos 2\pi\nu x\, d\nu = 2\int_0^{\infty} F_e(\nu) \cos 2\pi\nu x\, d\nu.$$

If $f(x)$ is real but odd, that is, $f(x) = f_o(x)$, then,

$$F(\nu) = \int_{-\infty}^{+\infty} f_o(x) \cos 2\pi\nu x\, dx - i \int_{-\infty}^{+\infty} f_o(x) \sin 2\pi\nu x\, dx = -2i \int_0^{\infty} f_o(x) \sin 2\pi\nu x\, dx \tag{3.4}$$

is pure imaginary, odd, and given by the sine Fourier transform of $f_o(x)$. By inversion of 3.4 we find that

$$f_o(x) = i \int_{-\infty}^{+\infty} F(\nu) \sin 2\pi\nu x\, d\nu = 2i \int_0^{\infty} F_o(\nu) \sin 2\pi\nu x\, d\nu.$$

More generally, if $f(x)$ is real but neither even nor odd, that is unsymmetrical, then:

$$F(\nu) = \int_{-\infty}^{+\infty} f_u(x)\, e^{-i2\pi\nu x}\, dx.$$

Since we may write an unsymmetrical function as the sum of even and odd parts, from 3.3 and 3.4 we get

$$\hat{F}(\nu) = \int_{-\infty}^{+\infty} f_e(x) \cos 2\pi\nu x\, dx - i \int_{-\infty}^{+\infty} f_o(x) \sin 2\pi\nu x\, dx \tag{3.5}$$

since the cosine transform of an odd function and the sine transform of an even function are zero. $F(\nu)$ is therefore complex and is written $\hat{F}(\nu)$ to exhibit this out explicitly.

From the relation 3.5 it is seen that the Fourier transform of a real function is generally complex; that is

$$\hat{F}(\nu) = Re(\nu) + i\ Im(\nu), \tag{3.6}$$

where $Re(\nu)$ and $Im(\nu)$ are, the real and imaginary components of $\hat{F}(\nu)$ respectively. The exponential form of equation 3.6 is

$$\hat{F}(\nu) = |\ \hat{F}(\nu)\ |\ e^{i\phi(\nu)},$$

where the magnitude function $|\hat{F}(\nu)|$ is called the Fourier spectrum of $f(x)$:

$$|\ \hat{F}(\nu)\ | = [\ \mathrm{Re}^2(\nu) + \mathrm{Im}^2(\nu)]^{\frac{1}{2}} \tag{3.7}$$

and $\phi(\nu)$ is its phase angle:

$$\phi(\nu) = \tan^{-1}\left[\frac{\mathrm{Im}(\nu)}{\mathrm{Re}(\nu)}\right]. \tag{3.8}$$

The variables ν and x in equations 3.1 and 3.2 have reciprocal dimensions, i.e., they lie in reciprocal domains.

3.3. Fourier Representation of Finite Duration Sequences

3.3.1. The Discrete Fourier Transform

The discrete Fourier transform (*DFT*) is a Fourier representation of a finite-length sequence which is itself a sequence rather than a continuous function, and it corresponds to samples equally spaced in frequency of the Fourier transform of the data.

While the Fourier representation of periodic sequences is important and a function that is to be submitted to Fourier transformation needs to be "periodical", however, the corresponding results can also be applied to the representation of finite-length sequences. This is done by constructing a periodic sequence for which each period is identical to the finite-length sequence. Therefore, one can represent a finite- duration sequence $f(x)$ of length N so that $f(x) = 0$ except in the range $0 \le x \le N-1$. The corresponding periodic sequence of period N, for which $f(x)$ is one period, will be denoted by $f_p(x)$ as given in [Op, 75]:

$$f_p(x) = \sum_{r=-\infty}^{\infty} f(x + rN) , \tag{3.9}$$

where N is the period of the sequence.

Thus, the resulting periodic sequence is formed from the aperiodic sequence by overlapping successive repetitions of the aperiodic sequence. From equation 3.9 it is noted that if the aperiodic sequence $f(x)$ is of finite duration less than N, then each period of $f_p(x)$ will be a replica of $f(x)$; if it is of duration greater than N, there will be an overlap of nonzero samples, resulting in aliasing. As a result, it follows that if $f(x)$ is of duration less than N, it can be recovered exactly from $f_p(x)$ by simply extracting one period of $f_p(x)$.

Considering the above, it is always important to remember that where *DFT* relations are concerned, a finite-length sequence is represented as one period of a periodic sequence.

Suppose that a continuous function $f(x)$ is discretized into a sequence $\left\{f(x_0), f(x_0+\Delta x),..., f(x_0 + [N-1])\Delta x\right\}$ by taking N samples Δx units apart:

$$f(x) = f(x_0 + x\ \Delta x) \qquad x = 0, 1, 2, ..., N-1$$

The discrete Fourier transform pair that applies to sampled functions is given by:

$$F(\nu) = \frac{1}{N} \sum_{x=0}^{N-1} f(x)\, e^{\frac{-i2\pi\nu x}{N}} \qquad \text{for } \nu = 0, 1, 2, ..., N-1, \tag{3.10}$$

and

$$f(x) = \sum_{\nu=0}^{N-1} F(\nu)\, e^{\frac{i2\pi\nu x}{N}} \qquad \text{for } x = 0, 1, 2, ..., N-1. \tag{3.11}$$

The values of ν=0,1,2,...,$N-1$ in the discrete Fourier transform given in equation 3.10 correspond to samples of the continuous transform at values 0, $\Delta\nu$, $2\Delta\nu$, ..., $(N-1)\Delta\nu$. In other words $F(\nu)$ represents $F(\nu\Delta\nu)$ here. It can be shown that $\Delta\nu$ and Δx are related by the expression

$$\Delta\nu = \frac{1}{N\ \Delta x}.$$

Unlike the continuous case, one need not be concerned about the existence of the discrete Fourier transform since $F(\nu)$ always exists in the discrete case.

Many Fourier spectra decrease rather rapidly as a function of increasing frequency. A useful processing technique consists of displaying the function $F'(\nu) = \log(1 + |F(\nu)|)$ instead of $|F(\nu)|$. Use of this equation preserves the zero values in the frequency plane. Also, $F'(\nu)$ is a nonnegative function.

3.3.1.1. Periodicity and Symmetry Properties of Fourier Transform

The discrete Fourier transform and its inverse are "periodic" with period N:

$$F(\nu) = F(\nu + N). \tag{3.12}$$

Although equation 3.12 points out that $F(\nu)$ repeats itself for an infinite number of values of ν, only N values of ν in any one period are required to obtain $f(x)$ from $F(\nu)$. In other words, only one period of the transform is necessary to completely specify $F(\nu)$ in the frequency domain. Similar comments hold for $f(x)$ in the spatial domain.

The Fourier transform also exhibits conjugate symmetry. Considering a general case where the input data, $f(x)$, is real but neither even nor odd, the Fourier transform of such a function is complex as was shown in equation 3.5. If the cosine transform of equation 3.5 is written as $p(\nu)$ and the sine transform as $q(\nu)$ so that

$$\hat{F}(\nu) = p(\nu) + iq(\nu) \ , \tag{3.13}$$

from a comparison of equation 3.5 and 3.13 it follows that

$$p(\nu) = p(-\nu) \quad \text{and} \quad q(\nu) = -q(-\nu)$$

and

$$\hat{F}(-\nu) = p(\nu) - iq(\nu)$$

and the complex conjugate is

$$\hat{F}^*(-\nu) = p(\nu) + iq(\nu) = \hat{F}(\nu). \tag{3.14}$$

Therefore, $\hat{F}(\nu) = \hat{F}^*(-\nu)$ which represents a Hermitian function. Also,

$$| \hat{F}(\nu) | = | \hat{F}(-\nu) | . \tag{3.15}$$

Equation 3.15 represents the symmetry property of Fourier transforms. The symmetry property shows that the magnitude of the transform is centered about the origin. In other words, the magnitudes of the transform values from $(\frac{N}{2} + 1)$ to $(N - 1)$ are images of the values in the half period on the left side of the origin.

Considering the above, the Fourier transform of an input real data of period N samples, i.e. $\hat{F}(\nu)$, satisfies the following symmetry conditions:

$$\mathrm{Re}[\hat{F}(\nu)] = \mathrm{Re}[\hat{F}(N + 1 - \nu)], \tag{3.16.a}$$

$$\mathrm{Im}[\hat{F}(\nu)] = -Im[\hat{F}(N + 1 - \nu)], \tag{3.16.b}$$

$$| \hat{F}(\nu) | = | \hat{F}(N + 1 - \nu) | \tag{3.16.c}$$

$$\measuredangle \hat{F}(\nu) = - \measuredangle \hat{F}(-\nu). \tag{3.16.d}$$

Real and imaginary components of the Fourier transform of the leaf data (refer to chapter 1) of the first and last 40 frequency points are shown in tables 3.1 and 3.2 respectively. A comparison of the values of the Fourier components in these two tables clarifies the content of equation 3.16.

3.3.1.2. Power Spectrum of the Data

The total power in a spectrum is the same whether one computes it in the channel number (energy) domain or in the frequency domain. This result is known as Paresval's theorem:

$$Total\ Power = \int_{-\infty}^{+\infty} |f(x)|^2\, dx = \int_{-\infty}^{+\infty} |F(\nu)|^2\, d\nu. \qquad (3.17)$$

The actual Fourier transformation gives one ν-point for each energy point. Therefore, the square of the Fourier spectrum or magnitude function, $|\hat{F}(\nu)|$, as defined in equation 3.7 is commonly referred to as the energy spectrum and this can easily be deduced from equation 3.17. Hence,

$$Power\ Spectrum = |\hat{F}(\nu)|^2 = Re^2(\nu) + Im^2(\nu). \qquad (3.18)$$

Tables 3.1 and 3.2 show the real components, imaginary components, Fourier spectrum (eqn. 3.7), and power spectrum (eqn. 3.18) of the first and the last 40 frequency-points of the leaf data. Figure 3.1 depicts the power spectrum of the preconditioned, 1024-channel original data of figure 2.2 and figure 3.2 represents the same for the 2048-channel spectrum of figure 2.3. The usefulness of power spectra for filtering out the background and noise components of the measured data will be discussed in the next chapters.

Table 3.1 Real components, imaginary components, Fourier spectra and power spectra of the first 40 frequency points of the leaf data.

v-point	Real component	Imaginary component	Fourier spectrum	Power spectrum
1	0.8941198E+07	0.0000000E+00	0.8941198E+07	0.7994502E+14
2	0.5396845E+07	-0.8278740E+04	0.5396852E+07	0.2912601E+14
3	-0.2099191E+04	0.6404039E+01	0.2099201E+04	0.4406644E+07
4	-0.3603581E+07	0.1658355E+05	0.3603619E+07	0.1298607E+14
5	-0.4937127E+07	0.3029434E+05	0.4937220E+07	0.2437614E+14
6	-0.3590211E+07	0.2753706E+05	0.3590317E+07	0.1289037E+14
7	-0.8999314E+06	0.8283174E+04	0.8999695E+06	0.8099451E+12
8	0.1649006E+07	-0.1770740E+05	0.1649101E+07	0.2719534E+13
9	0.3172728E+07	-0.3893713E+05	0.3172967E+07	0.1006772E+14
10	0.3549054E+07	-0.4900071E+05	0.3549392E+07	0.1259819E+14
11	0.2575796E+07	-0.3951535E+05	0.2576099E+07	0.6636286E+13
12	0.5008169E+06	-0.8451478E+04	0.5008882E+06	0.2508890E+12
13	-0.2065403E+07	0.3802379E+05	0.2065753E+07	0.4267335E+13
14	-0.3938923E+07	0.7855930E+05	0.3939706E+07	0.1552129E+14
15	-0.3995948E+07	0.8582915E+05	0.3996870E+07	0.1597497E+14
16	-0.1785131E+07	0.4108273E+05	0.1785604E+07	0.3188380E+13
17	0.1635245E+07	-0.4014302E+05	0.1635738E+07	0.2675637E+13
18	0.4250309E+07	-0.1108635E+06	0.4251755E+07	0.1807742E+14
19	0.4287334E+07	-0.1184105E+06	0.4288969E+07	0.1839525E+14
20	0.1807774E+07	-0.5270373E+05	0.1808542E+07	0.3270825E+13
21	-0.1487582E+07	0.4565281E+05	0.1488282E+07	0.2214984E+13
22	-0.3449094E+07	0.1111462E+06	0.3450885E+07	0.1190860E+14
23	-0.3206187E+07	0.1082420E+06	0.3208014E+07	0.1029135E+14
24	-0.1406628E+07	0.4964861E+05	0.1407504E+07	0.1981067E+13
25	0.5083090E+06	-0.1872212E+05	0.5086537E+06	0.2587286E+12
26	0.1681738E+07	-0.6452540E+05	0.1682976E+07	0.2832406E+13
27	0.1996480E+07	-0.7966874E+05	0.1998069E+07	0.3992279E+13
28	0.1708089E+07	-0.7078510E+05	0.1709555E+07	0.2922579E+13
29	0.9033595E+06	-0.3882454E+05	0.9041934E+06	0.8175658E+12
30	-0.2980431E+06	0.1326733E+05	0.2983383E+06	0.8900571E+11
31	-0.1576707E+07	0.7261042E+05	0.1578378E+07	0.2491277E+13
32	-0.2249968E+07	0.1070744E+06	0.2252515E+07	0.5073822E+13
33	-0.1752892E+07	0.8611411E+05	0.1755006E+07	0.3080046E+13
34	-0.1403361E+06	0.7110127E+04	0.1405161E+06	0.1974477E+11
35	0.1648247E+07	-0.8604293E+05	0.1650491E+07	0.2724121E+13
36	0.2441152E+07	-0.1311899E+06	0.2444675E+07	0.5976433E+13
37	0.1661205E+07	-0.9183062E+05	0.1663741E+07	0.2768035E+13
38	-0.1488723E+06	0.8458714E+04	0.1491124E+06	0.2223451E+11
39	-0.1702872E+07	0.9937521E+05	0.1705769E+07	0.2909648E+13
40	-0.1915980E+07	0.1147609E+06	0.1919414E+07	0.3684149E+13

Table 3.2 Real components, imaginary components, Fourier spectra and power spectra of the last 40 frequency points of the leaf data.

v-point	Real component	Imaginary component	Fourier spectrum	Power spectrum
2009	-0.1915980E+07	-0.1147609E+06	0.1919414E+07	0.3684149E+13
2010	-0.1702872E+07	-0.9937521E+05	0.1705769E+07	0.2909648E+13
2011	-0.1488723E+06	-0.8458714E+04	0.1491124E+06	0.2223451E+11
2012	0.1661205E+07	0.9183062E+05	0.1663741E+07	0.2768035E+13
2013	0.2441152E+07	0.1311899E+06	0.2444675E+07	0.5976433E+13
2014	0.1648247E+07	0.8604293E+05	0.1650491E+07	0.2724121E+13
2015	-0.1403361E+06	-0.7110127E+04	0.1405161E+06	0.1974477E+11
2016	-0.1752892E+07	-0.8611411E+05	0.1755006E+07	0.3080046E+13
2017	-0.2249968E+07	-0.1070744E+06	0.2252515E+07	0.5073822E+13
2018	-0.1576707E+07	-0.7261042E+05	0.1578378E+07	0.2491277E+13
2019	-0.2980431E+06	-0.1326733E+05	0.2983383E+06	0.8900571E+11
2020	0.9033595E+06	0.3882454E+05	0.9041934E+06	0.8175658E+12
2021	0.1708089E+07	0.7078510E+05	0.1709555E+07	0.2922579E+13
2022	0.1996480E+07	0.7966874E+05	0.1998069E+07	0.3992279E+13
2023	0.1681738E+07	0.6452540E+05	0.1682976E+07	0.2832406E+13
2024	0.5083090E+06	0.1872212E+05	0.5086537E+06	0.2587286E+12
2025	-0.1406628E+07	-0.4964861E+05	0.1407504E+07	0.1981067E+13
2026	-0.3206187E+07	-0.1082420E+06	0.3208014E+07	0.1029135E+14
2027	-0.3449094E+07	-0.1111462E+06	0.3450885E+07	0.1190860E+14
2028	-0.1487582E+07	-0.4565281E+05	0.1488282E+07	0.2214984E+13
2029	0.1807774E+07	0.5270373E+05	0.1808542E+07	0.3270825E+13
2030	0.4287334E+07	0.1184105E+06	0.4288969E+07	0.1839525E+14
2031	0.4250309E+07	0.1108635E+06	0.4251755E+07	0.1807742E+14
2032	0.1635245E+07	0.4014302E+05	0.1635738E+07	0.2675637E+13
2033	-0.1785131E+07	-0.4108273E+05	0.1785604E+07	0.3188380E+13
2034	-0.3995948E+07	-0.8582915E+05	0.3996870E+07	0.1597497E+14
2035	-0.3938923E+07	-0.7855930E+05	0.3939706E+07	0.1552129E+14
2036	-0.2065403E+07	-0.3802379E+05	0.2065753E+07	0.4267335E+13
2037	0.5008169E+06	0.8451478E+04	0.5008882E+06	0.2508890E+12
2038	0.2575796E+07	0.3951535E+05	0.2576099E+07	0.6636286E+13
2039	0.3549054E+07	0.4900071E+05	0.3549392E+07	0.1259819E+14
2040	0.3172728E+07	0.3893713E+05	0.3172967E+07	0.1006772E+14
2041	0.1649006E+07	0.1770740E+05	0.1649101E+07	0.2719534E+13
2042	-0.8999314E+06	-0.8283174E+04	0.8999695E+06	0.8099451E+12
2043	-0.3590211E+07	-0.2753706E+05	0.3590317E+07	0.1289037E+14
2044	-0.4937127E+07	-0.3029434E+05	0.4937220E+07	0.2437614E+14
2045	-0.3603581E+07	-0.1658355E+05	0.3603619E+07	0.1298607E+14
2046	-0.2099191E+04	-0.6404039E+01	0.2099201E+04	0.4406644E+07
2047	0.5396845E+07	0.8278740E+04	0.5396852E+07	0.2912601E+14
2048	0.8941198E+07	0.0000000E+00	0.8941198E+07	0.7994502E+14

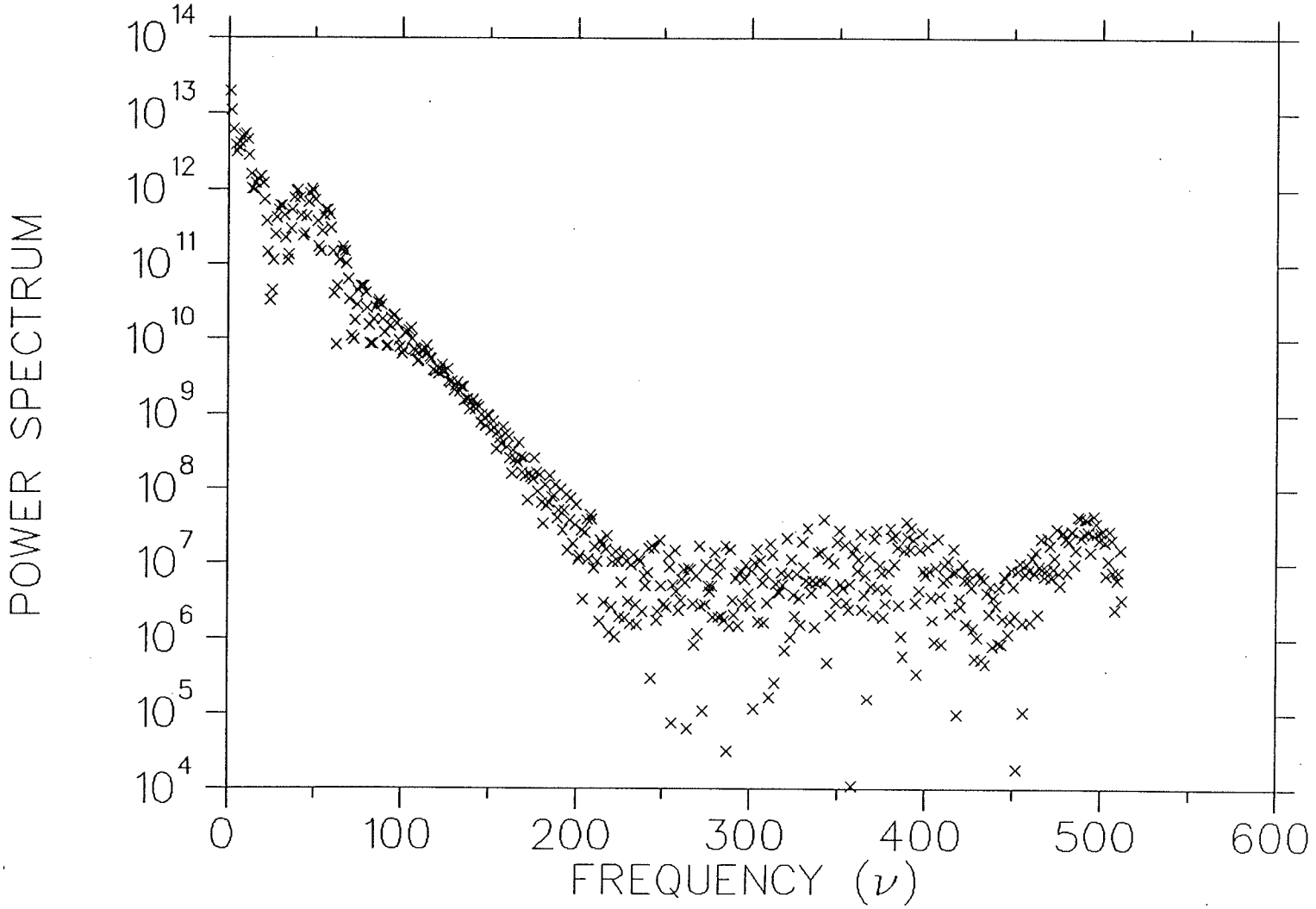

Fig. 3.1 Power spectrum of the preconditioned 1024-channel original data (only positive frequencies are shown).

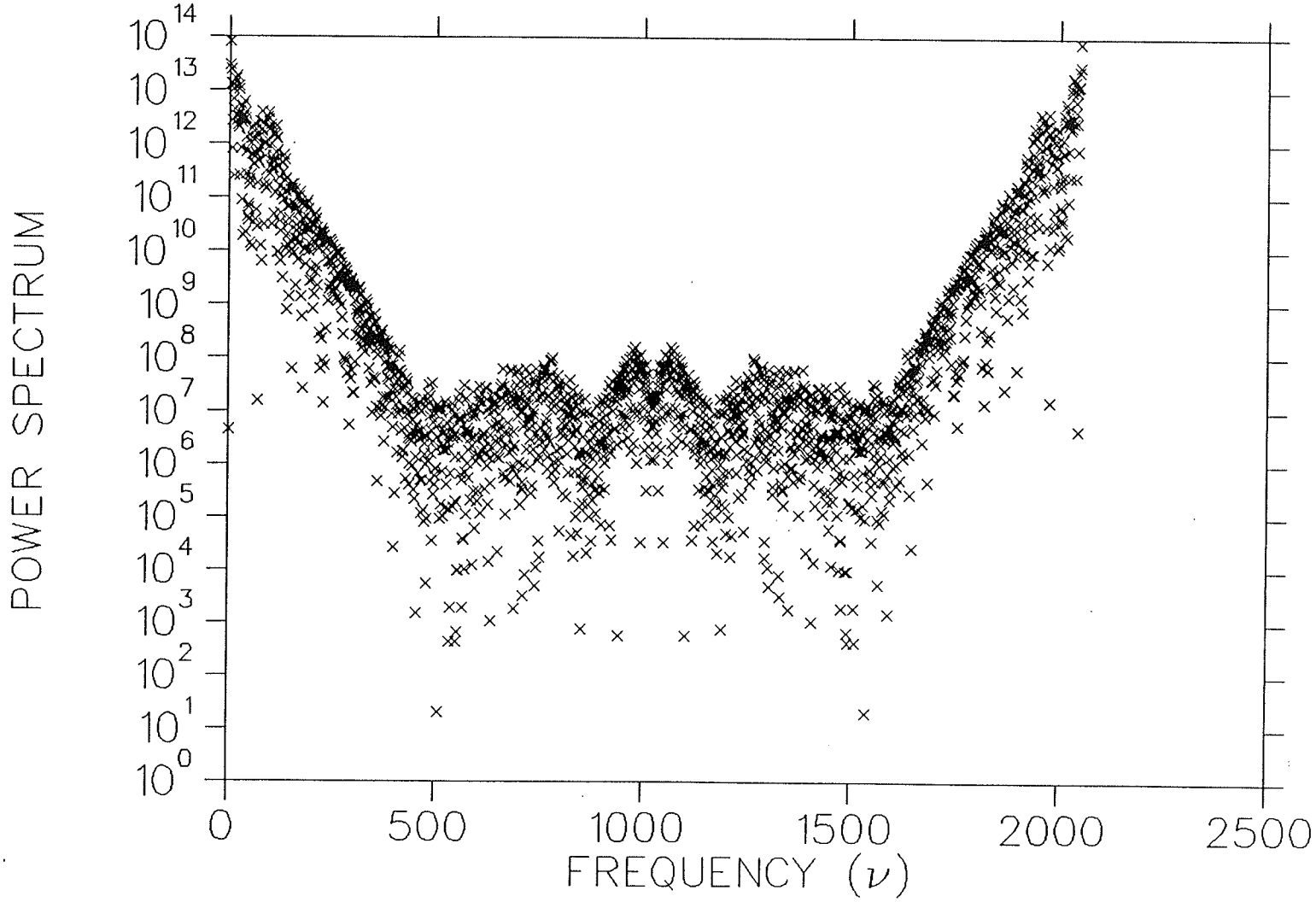

Fig. 3.2 Power spectrum of the 2048-channel spectrum (both positive and negative frequencies are shown).

3.3.2. Fast Fourier Transform as an Efficient Computational Algorithm

The Fast Fourier Transform (*FFT*) [Si, 69: Pr, 89; Ra, 75] is an efficient algorithm for the rapid computation of the finite discrete Fourier transform of a sequence of numbers. Its discovery caused a revolution in many industrial and scientific disciplines, but its potential usefulness for X-ray spectrum analysis has hardly been explored. Since all computations employing Fourier transform and the related theorems involving convolution and correlation, discussed in the subsequent chapters, have been performed using *FFT*; in the following a brief discussion is made regarding to the structure and function of this algorithm.

Since the discrete Fourier transform (*DFT*) is the central computation in most spectrum analysis problems, it follows that the *FFT* implementation of the *DFT*, which, in some practical cases can improve performance by a factor of 100 or more over direct evaluation of the *DFT*, is crucially important and must be understood as part of any serious effort to utilize the digital processing techniques of spectral analysis.

The *DFT* of a finite duration sequence {f(x)}, $0 \le x \le N-1$, was defined in section 3.3.1 (eqn. 3.10) as

$$F(\nu) = \frac{1}{N} \sum_{x=0}^{N-1} f(x)\, e^{\frac{-i2\pi\nu x}{N}} \qquad \text{for } 0 \le \nu \le N-1 \tag{3.19}$$

The number of complex multiplications and additions required to implement equation 3.19 is proportional to N^2. This can be seen by noting that, for "each" of the N values of ν, expansion of the summation sign requires N complex multiplications of $f(x)$ by $e^{\frac{-i2\pi\nu x}{N}}$ and $(N-1)$ additions of the results. By properly decomposing equation 3.19, the number of multiply and add operations can be made proportional to $N \log_2 N$. The decomposition procedure is called *FFT* algorithm. Equation 3.19 may conveniently be written in the form

$$F(\nu) = \frac{1}{N} \sum_{x=0}^{N-1} f(x)\, W_N^{\nu x}, \tag{3.20}$$

where

$$W_N = e^{\frac{-i2\pi}{N}}$$

and N is assumed to be of the form $N = 2^n$ where n is a positive integer. Based on this N can be expressed as

$$N = 2M, \tag{3.21}$$

where M is also a positive integer.

Substitution of equation 3.21 into equation 3.20 and defining

$$F_{even}(v) = \frac{1}{M}\sum_{x=0}^{M-1} f(2x)\, W_M^{vx} \qquad \text{for } v = 0, 1, 2, ..., M-1 \tag{3.22}$$

and

$$F_{odd}(v) = \frac{1}{M}\sum_{x=0}^{M-1} f(2x+1)\, W_M^{vx} \qquad \text{for } v = 0, 1, 2, ..., M-1 \tag{3.23}$$

one can obtain;

$$F(v) = \frac{1}{2}\left\{F_{even}(v) + F_{odd}(v)\, W_{2M}^{v}\right\}. \tag{3.24}$$

The following relation can be used to get the values of $F(v)$ in the range $M = \frac{N}{2} \le v \le N-1$

$$F(v+M) = \frac{1}{2}\left\{F_{even}(v) - F_{odd}(v)\, W_{2M}^{v}\right\}. \tag{3.25}$$

From the analysis of equations 3.20 through 3.25 it is noted that an N-point transform can be computed by dividing the original expression into two parts, as indicated in equations 3.24 and 3.25. Computation of the first half of $F(v)$ requires the evaluation of the two $(\frac{N}{2})$-point transforms given in equations 3.22 and 3.23. The resulting values of $F_{even}(v)$ and $F_{odd}(v)$ are then substituted into equation 3.24 to obtain $F(v)$ for $v = 0, 1, 2, ..., (\frac{N}{2} - 1)$. The other half then follows directly from equation 3.25 without additional transform evaluations.

The above approach can be used recursively. Having reduced the problem of computing $F(v)$ to that of computing $F_{even}(v)$ and $F_{odd}(v)$, one can do the same reduction of $F_{even}(v)$ to the problem of computing the transform of its $\frac{N}{4}$ even-numbered in-

put data and $\frac{N}{4}$ odd-numbered data. In other words, one can define $F_{ee}(\nu)$ and $F_{eo}(\nu)$ to be the discrete Fourier transforms of the points which are respectively even-even and even-odd on the successive subdivisions of the data. With the restriction of $N = 2^n$, it is evident that one can continue the above approach until the data are subdivided all the way down to transform of length 1.

As far as the implementation of the *FFT* algorithm is concerned, the input data must be arranged in the order required for successive applications of equations 3.22 and 3.23. The procedure for recording an input array follows a "bit reversal" rule (for details refer to [Ra, 75; Pr, 89]).

The *FFT* algorithm can be used to compute an inverse *DFT* without any changes in the algorithm. To see this, consider equations 3.10 and 3.11 . Taking the complex conjugate of equation 3.11 and dividing both sides by N yields:

$$\frac{1}{N} f^*(x) = \frac{1}{N} \sum_{\nu=0}^{N-1} F^*(\nu)\, e^{\frac{-i2\pi\nu x}{N}} \tag{3.26}$$

by comparing this result with equation 3.10, it is seen that the right side of equation 3.26 is in the form of the forward Fourier transform. Thus, if $F^*(\nu)$ is introduced as input into an algorithm designed to compute the forward transform the result will be the quantity $\frac{f^*(x)}{N}$. Taking the complex conjugate and multiplying by N yields the desired inverse $f(x)$.

3.3.3. Convolution Theorem

Convolution is known by several alternative names such as "smoothing", "blurring", "scanning", and "smearing". If $f(x)$ and $g(x)$ are two continuous functions, the convolution of the two functions, denoted by $f(x) * g(x)$, is defined by

$$y(x) = f(x) * g(x) = \int_{-\infty}^{+\infty} f(x')\, g(x - x')\, dx'. \tag{3.27}$$

One aspect of equation 3.27 involves the convolution of a function $f(x)$ with the impulse function $\delta(x - x_0)$:

$$\int_{-\infty}^{+\infty} f(x)\delta(x - x_0)\, dx = f(x_0).$$

Referring to equation 3.27, convolution is equivalent to first displacing one function, $g(x')$, over the other, $f(x')$, until the new origin of g, namely $x' = x$ is reached: g is then reflected about the origin $x' = x$. The transposed and reflected ordinates of g, at each value of x', are multiplied by the unaffected ordinates of f and the resulting function integrated over the entire range of x'. The operation of convolution is commutative:

$$f(x) * g(x) = g(x) * f(x)\,.$$

It is also associative:

$$f(x) * [g(x) * h(x)] = [f(x) * g(x)] * h(x)\,.$$

Finally, convolution is distributive over addition:

$$f(x) * [g(x) + h(x)] = f(x) * g(x) + f(x) * h(x)\,.$$

According to the "convolution theorem", the Fourier transform of the convolution of two functions is equal to the product of their individual Fourier transforms:

$$f(x) * g(x) <=> F(\nu)\, G(\nu)\,, \tag{3.28}$$

where the "<=>" symbol is used to indicate transform pairs. Also,

$$f(x)\, g(x) <=> F(\nu) * G(\nu). \tag{3.29}$$

Now, suppose that instead of being continuous, $f(x)$ and $g(x)$ are discretized into sampled arrays of size N_1 and N_2 respectively. Therefore, the duration of $f(x)$ is N_1 sam-

ples; i.e., $f(x)$ is nonzero only in the interval $0 \le x \le N_1 - 1$. The duration of $g(x)$ is N_2 samples, i.e., $g(x)$ is nonzero only in the interval $0 \le x \le N_2 - 1$.

As discussed before, the discrete Fourier transform and its inverse are periodic functions. In order to formulate a discrete convolution theorem that is consistent with this periodicity property, one may "assume" that the discrete functions $f(x)$ and $g(x)$ are periodic with some period N. The resulting convolution will then be periodic with the same period.

Unless $N \ge (N_1 + N_2 - 1)$ the individual periods of the convolution will overlap (wraparound error). If $N = (N_1 + N_2 - 1)$, then periods will be adjacent; if $N > (N_1 + N_2 - 1)$, the periods will be spaced apart.

Since the assumed period must be greater than either N_1 or N_2, the length of the sampled sequences must be increased so that both are of length N. This can be done by appending zeros to the given samples to form the following "extended" sequences:

$$f_e(x) = \begin{cases} f(x) & 0 \le x \le N_1 - 1 \\ 0 & N_1 \le x \le N - 1 \end{cases}$$

and

$$g_e(x) = \begin{cases} g(x) & 0 \le x \le N_2 - 1 \\ 0 & N_2 \le x \le N - 1 \end{cases}$$

Based on this, the discrete convolution of $f_e(x)$ and $g_e(x)$ is defined by the expression:

$$f_e(x) * g_e(x) = \sum_{m=0}^{N-1} f_e(m)\, g_e(x - m) \qquad \text{for } x = 0, 1, 2, \ldots, N-1. \quad (3.30)$$

The convolution function is a discrete, periodic array of length N, with the values $x = 0, 1, 2, \ldots, N-1$ describing a full period of $f_e(x)*g_e(x)$.

From the practical point of view, it is more efficient to compute the discrete convolution in the frequency domain, using equation 3.28, as the foundation of frequency domain technique in the convolution theorem. In situations involving convolution operations during the execution of this project and also in many other practical cases, one is interested in computing the convolution of two finite duration sequences where one sequence is much longer than the other sequence; i.e., $N_1 \gg N_2$ or $N_2 \gg N_1$.

As discussed in chapter 1, the *PIXE* X-ray spectra were recorded originally in 1024 channels and this range was increased to 2048 channels to provide periodicity to the data. Therefore, during convolution operations, to be discussed, one of the functions, say $m(E)$ was the measured data in energy domain with an increased range of N=2048 channels and the other function say $w(E)$, was a "filter function" or a "response function", as the case may be, typically a sequence M much shorter than the measured input data ($M \ll N$). The period of the convolution function was N, the length of the data set. Therefore, the other function was extended to length N by padding it with zeros, i.e. defining $w(E) = 0$ for $\frac{M}{2} \le E \le \frac{N}{2}$ and also for $\frac{-N}{2} + 1 \le E \le \frac{-M}{2} + 1$.

Another operation performed on the second function, after zero padding out to duration N, was to arrange it in wrap-around order. Generally this means that a large section of the $w(E)$'s, in the middle of that array, is zero, with nonzero values clustered at the two extreme ends of the array. To demonstrate this, consider Fig. 3.3 which represents the second derivative of a Gaussian curve, namely

$$y'' = \frac{1}{\sigma^2}[(1 - \frac{x^2}{\sigma^2})\, e^{-\frac{x^2}{2\sigma^2}}], \qquad (3.31)$$

centered at $x = 50$.

The convolution of this function with a spectrum can generally be used to smooth the data and to make a second-difference spectrum. Assuming the length of the data is 100 channels, the function represented by equation 3.31 is arranged in a wrap-around order as shown in Fig. 3.4.

After the above operations, the two functions, both of length N, are ready to compute the discrete convolution. To do this, the *FFT* algorithm was used to compute the discrete Fourier transforms of the two functions $m(E)$ and $w(E)$. The two transforms were multiplied together component by component, remembering that the transforms consist of complex numbers. Then the *FFT* algorithm was used to take the inverse discrete Fourier transform of the products. The answer was the convolution $m(E)*w(E)$ as seen from the following relation;

$$m(E) * w(E) = \sum_{m=0}^{N-1} f(m)\, w(E-m) <=> M(\nu)\, W(\nu), \qquad (3.32)$$

where $m(E)$ and $w(E)$ are the two functions in energy domain and $M(\nu)$ and $W(\nu)$ are their Fourier transforms respectively in Frequency domain.

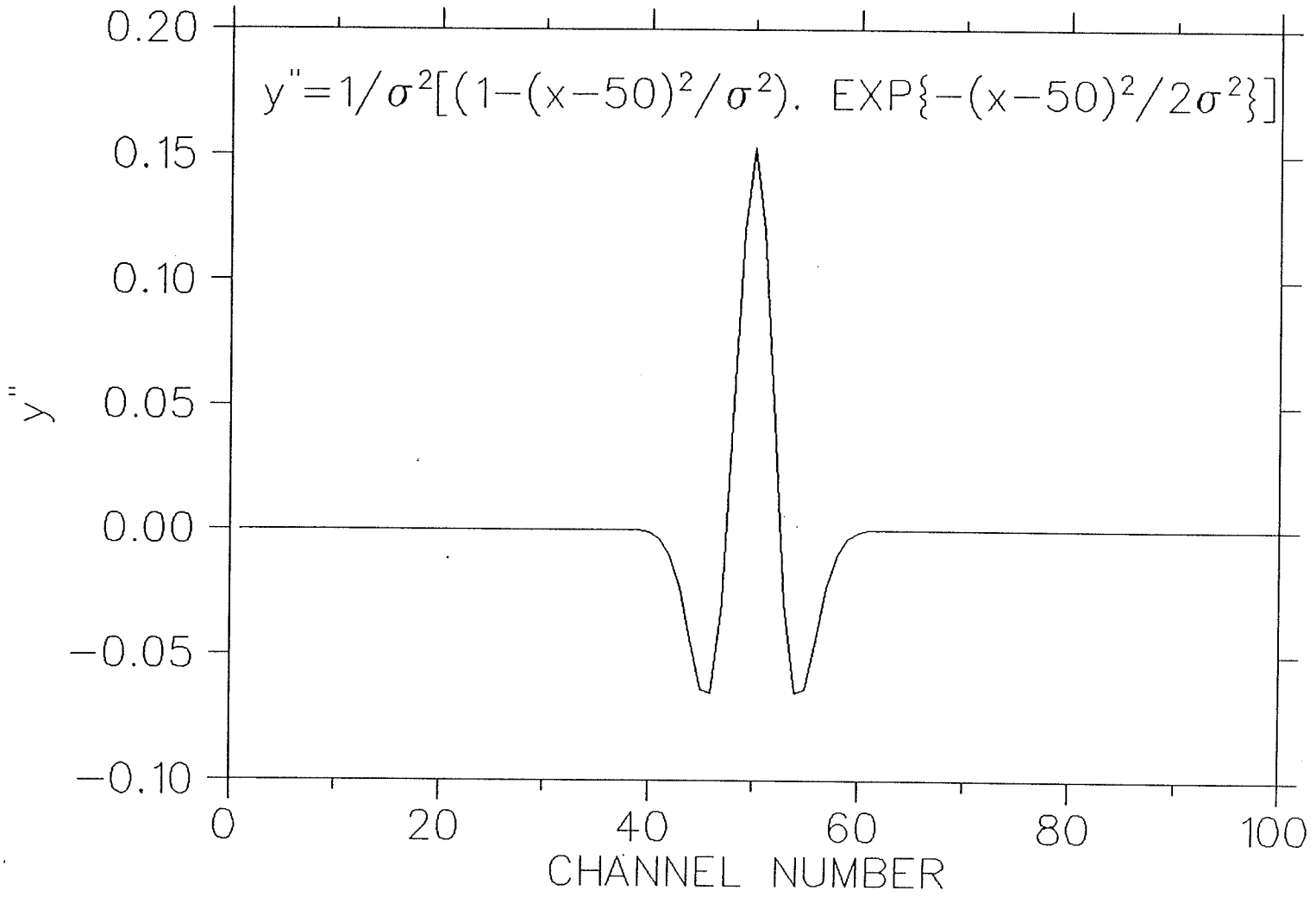

Fig. 3.3 Second derivative of a Gaussian function.

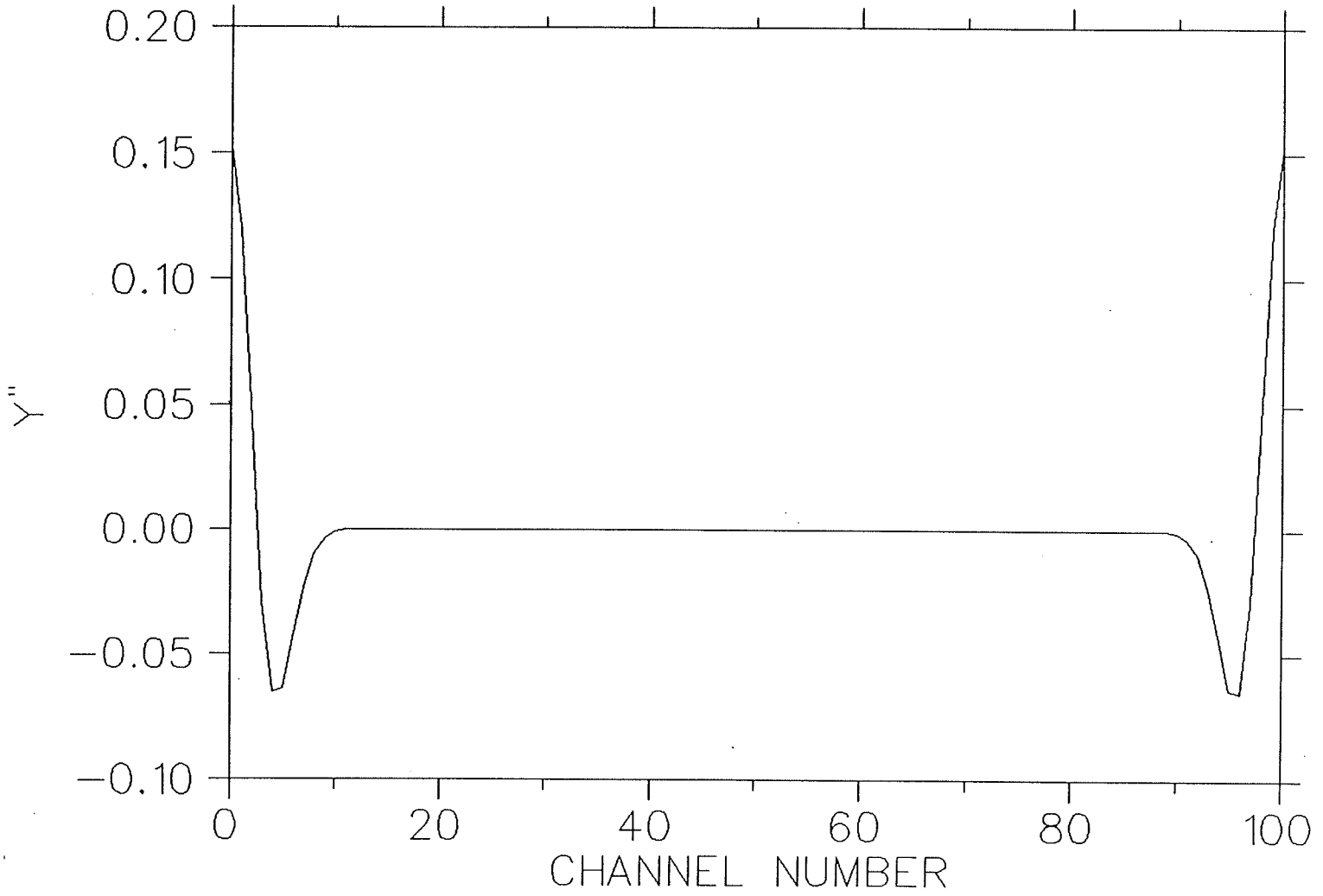

Fig. 3.4 The function of Fig. 3.3 arranged in a wraparound order.

3.4. Background Subtraction and Noise Removal

3.4.1. Previous Approach

While Fourier transform techniques have been previously applied to the examination of X-ray fluorescence and *PIXE* data, only partial success has resulted.

Inouye et al. [In, 69] employed Fourier transform techniques only for data smoothing. They represented the observed data as the sum of two components, i.e. the true spectral information and the noise component due to random fluctuations in the number of counts in a channel. The filter function chosen eliminated only part of the noise. Background was represented as a slowly varying function connecting all the minima in the smoothed data and was handled by a different approach.

Hnatowicz [Hn, 76] has shown that a symmetric, zero-area weighting function, consisting of the sum of a positive Gaussian peak and a negative constant, represents the best of the linear filters for detecting Gaussian peaks on a linear background. The positive part of this filter is apparently identical with the spectral peak shape and the general transformation, obtained by the use of the filter, has a tendency to emphasize such structures of the spectrum which resemble the filter shape.

The method used by Statham [St, 77] involves suppressing the background with a digital "top-hat" filter. He then proceeds to a conventional least-squares fit to the data remaining in the peaks. In this method, a background which is linear over the range of each peak can be suppressed by the convolution with a "top-hat" weighting function. The "top-hat" filter produces a result similar to the negative of the smoothed second derivative of the data so a single peak is transformed into a central positive lobe with negative lobes on either side and a background which is linear is suppressed. This prefiltering technique, according to Statham, is as effective as subtracting a piece-wise linear approximation of the background from the spectrum.

In the method used by M.J. Nass et al. [Na, 78], the spectra were convoluted with Gaussians of varying widths, based on detector resolution, to smooth the data. Although this convolution did not shift the location of the peaks, it, however, broadened them. The half-width of the broadened peak was the sum of that of the original peak (assumed to be Gaussian in shape) and that of the Gaussian used for the

convolution added in quadrature. Thus, if σ_m is the variance of the original measured peak and σ_g is the variance of the smoothing Gaussian function, σ_c, the variance of the function resulting from the convolution will be

$$\sigma_c^2 = \sigma_m^2 + \sigma_g^2. \tag{3.33}$$

After the initial smoothing, the background fit was made by conventional methods, i.e., locating several spectrum minima and fitting the best line through them.

Kaisla et al. [Ka, 81] represented the spectrum as the sum of components due to peaks, background, and statistical noise. The components of the background and true information in Fourier transform space could be partly separated by means of a filtering window. The selected frequency filtering window, $W(\nu)$ had lower and upper limits with shapes inversely proportional to the standard deviation of the background (upper) and the full width at half maximum ($FWHM$) of the peaks (lower). Thus, the shape of the filter was determined by characteristic frequencies of the background and peaks. The small difference between these limiting frequencies made the success of the technique very sensitive to the functional form of the window.

3.4.2. Background Subtraction

Let the measured data be represented as

$$m(E) = t(E) + n(E) + b(E), \tag{3.34}$$

where $m(E)$ is the measured translationally invariant reflected data, $t(E)$ is the true sought quantity, $n(E)$ is the noise component and $b(E)$ is the background component. If we introduce the background-free data, $s(E)$, as

$$s(E) = t(E) + n(E), \tag{3.35}$$

equation 3.34 can be written as follows

$$m(E) = s(E) + b(E). \tag{3.36}$$

The most obvious feature which distinguishes background from peaks is the slow variation of the background with energy compared with the faster variation of structure in the peaks. Using Fourier transforms $M(\nu)$, $S(\nu)$, and $B(\nu)$ of $m(E)$, $s(E)$, and $b(E)$ respectively, the following relation in frequency domain which is in fact the counter-

part of equation 3.36 in energy (channel number) domain, is obtained

$$M(\nu) = S(\nu) + B(\nu), \tag{3.37}$$

where ν is the variable in the frequency/conjugate domain and, by analogy, can be related to inverse channel number.

The components $S(\nu)$ and $B(\nu)$ can be separated by means of a filtering function $W_B(\nu)$ so that

$$S(\nu) = W_B(\nu) \times M(\nu). \tag{3.38a}$$

Here in fact, the filter function, $W_B(\nu)$ is convolved with the measured data, $M(\nu)$, in frequency domain. Note that the Fourier transform of the convolution of two functions is equal to the product of their individual Fourier transforms. Relation 3.38a in frequency space is equivalent to the following relation in energy space:

$$s(E) = w_b(E) * m(E) = \sum_k m(k)\, w_b(E - k), \tag{3.38b}$$

where k spans the width of the filter function, $w_b(E)$, to subtract background.

3.4.3. Data Smoothing

After subtracting the background component, $b(E)$ or $B(\nu)$, by using the filter function $W_B(\nu)$, the attempt was to smooth the data and to recover the true spectrum, $t(E)$, from equation 3.35 repeated below:

$$s(E) = t(E) + n(E).$$

The noise component, $n(E)$, is of random origin and is due principally to statistical fluctuations in the number of counts in a channel. Using Fourier transforms $S(\nu)$, $T(\nu)$, and $N(\nu)$ of $s(E)$, $t(E)$, and $n(E)$ respectively in equation 3.35 one has, symbolically,

$$S(\nu) = T(\nu) + N(\nu). \tag{3.39}$$

Now, the problem reduces to devising a second filter function, $W_N(\nu)$ so that when applied to $S(\nu)$ recovers the sought quantity $T(\nu)$,

$$T(\nu) = W_N(\nu) \times S(\nu). \tag{3.40}$$

Chapter 4
Filter Design

Replacing for the values of $S(\nu)$ in equation 3.40 from equation 3.38a we get

$$T(\nu) = W_N(\nu) \times [W_B(\nu) \times M(\nu)], \tag{4.1}$$

or

$$T(\nu) = W(\nu) \times M(\nu), \tag{4.2}$$

where $W(\nu)$ replaces $W_N(\nu) \times W_B(\nu)$.

From equations 4.1 and 4.2 it can be seen that $W(\nu)$ is the filter function with two components $W_B(\nu)$ and $W_N(\nu)$, which when convolved with the transformed measured spectrum, $M(\nu)$, produces the true spectrum $T(\nu)$. Finally, the inverse transform of $T(\nu)$ will produce the noise/background free spectrum $t(E)$, in channel number (energy) domain.

Using the Fourier transforms $M(\nu)$, $T(\nu)$, $N(\nu)$, and $B(\nu)$ of $m(E)$, $t(E)$, $n(E)$, and $b(E)$ respectively in equation 3.34 we have,

$$M(\nu) = T(\nu) + N(\nu) + B(\nu)\ . \tag{4.3}$$

The success of the method depends upon the components $T(\nu)$, $N(\nu)$, and $B(\nu)$ being different functions so that a filter function, $W(\nu)$, can be chosen which will eliminate the major part of the disinformative parts without seriously affecting the true spectral information $T(\nu)$. Fortunately this is true in most spectra since the spectral peaks are spread over a number of channels and so $T(\nu)$ is made up of low frequencies. The noise on the other hand is channel to channel fluctuations and $N(\nu)$ contains many higher frequencies. Finally, the background is a slow varying function of energy and is characterized by the first few frequencies.

To determine proper filter function $W(\nu)$ it is useful to plot the power spectrum $|M(\nu)|^2$ vs ν. Such a plot for the preconditioned, symmetrical (refer to section 2.2.2) leaf spectrum is shown in Fig. 4.1.

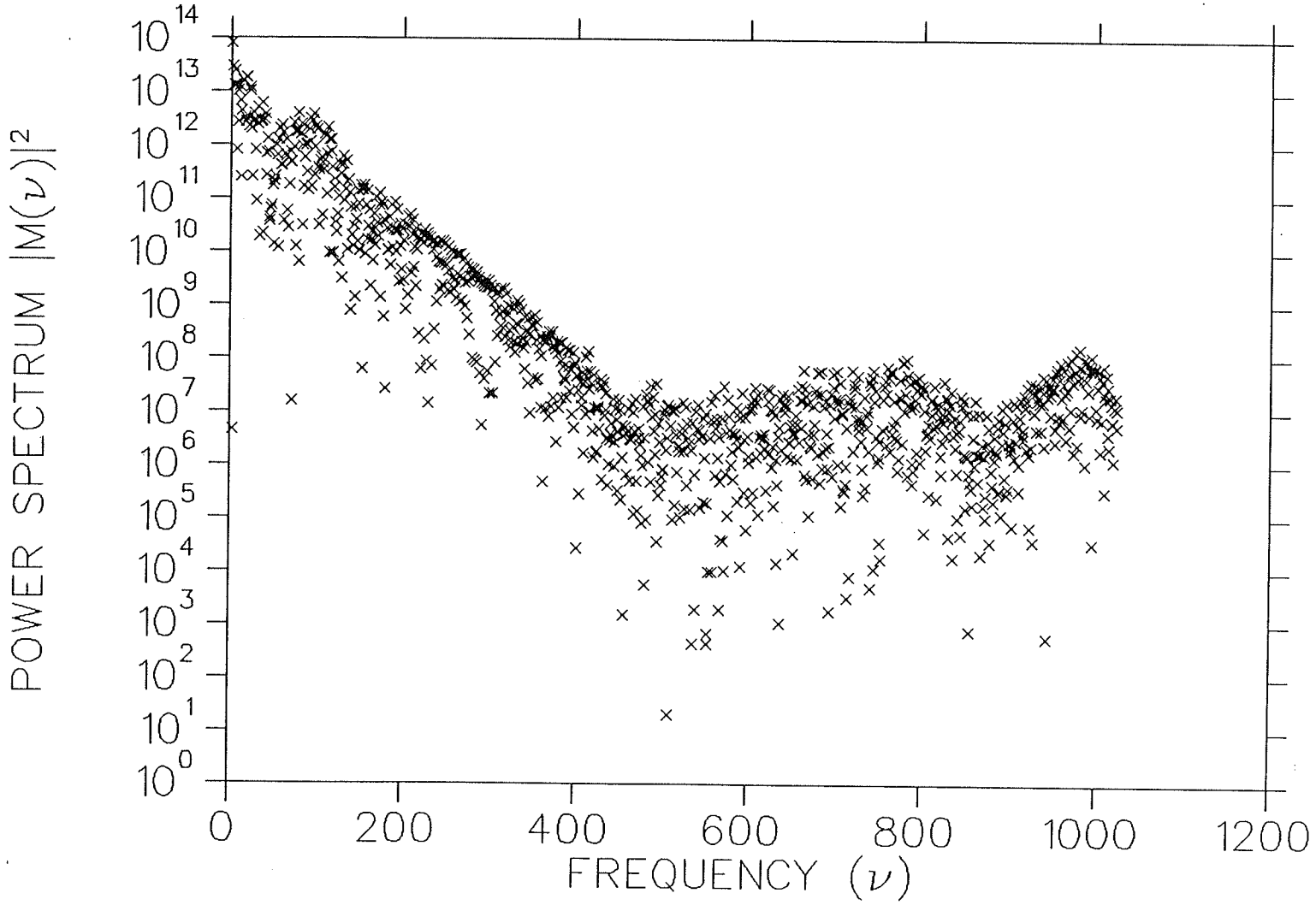

Fig. 4.1 Power spectrum of the preconditioned, symmetrical leaf data (only positive frequencies are shown).

4.1. Design Criteria for a Filter Function to Subtract Background

As discussed previously, because the background varies smoothly over the whole spectrum, it is anticipated it is characterized by lower frequencies than those associated with the spectral peaks. Therefore, the component $B(\nu)$ in equation 3.37 has significant values only at low frequencies ($\nu < \nu_{P_1}$) and background component of filter function, $W_B(\nu)$ (refer to eqn. 3.38a) will operate only in the frequency range $\nu_b \leq \nu \leq \nu_{P_1}$. Note that ν_b is the frequency point corresponding to the beginning of the frequency range to subtract background (ν_b is in general assumed to be equal to 1), and ν_{P_1} is the end of this range and the beginning of the range corresponding to the spectral peaks. Therefore, the frequencies characteristic of the background is confined between the values ν_b and ν_{P_1} where the filter function $W_B(\nu)$ operates. Then the values of filter function $W_B(\nu)$ to subtract background can be stated as,

$$W_B(\nu)_i = \sum_{i=\nu_b}^{\nu_{P_1}} f_i \ . \tag{4.4}$$

Although the number of frequencies, ($\nu_b \leq \nu \leq \nu_{P_1}$), assigned for background subtraction might be varying under different circumstances, in fact only first few low frequencies have major contributions. As discussed in detail in section 2.1.1, the production mechanism of the continuum of X-rays making the background in *PIXE* spectra is complicated and there are numerous processes responsible for the formation of this continuum. It is due to this complexity in the formation of background and its energy dependence that the upper limit of the frequencies characteristic of background, that is ν_{P_1}, as well as the values of filter function, f_i, in equation 4.4 cannot be fixed universally for all *PIXE* labs having different operating and environmental parameters.

Fig. 4.2 represents the effects of different single-valued filter functions in subtracting background when applied to the first few low frequencies, (one frequency-point at a time), of the Fourier transform of the leaf data. Note that in each case all the values of filter function are set equal to zero except one which is assigned the values specified in the figure. The application of filter function to the data is performed in frequency space and the result is obtained in channel number domain by inverse Fourier transformation. In Fig. 4.2a the filter function is applied to the first frequency-point of the data and is assigned the values of 0.1, 0.5, and 0.9 at different trials while the rest

of its values, [(N = 1024) – 1] have been set to zero.

Figures 4.2b, 4.2c, and 4.2d show the background subtractions when the single-valued filter function has values corresponding to the second, third, and fourth frequency-point of the data respectively and the rest of its values are set to zero.

As it is noticed from Fig. 4.2, the frequencies of the oscillations of the background function resulting from the application of the filter function to different frequency-points of the data vary accordingly. Applying the filter function to ν-point = 1 subtracts a uniform background for all channel numbers (refer to Fig. 4.2a). Application of the filter function to ν-point = 2 results in a background function having fundamental frequency (refer to Fig. 4.2b). Finally, when the filter is applied to ν-point > 2, successive harmonics are produced. It is also seen from Fig. 4.2 that the amplitude of the oscillations of the subtracted background generally reduces in a rather non-linear manner and it was verified in leaf data that at ν-point ≈ 200 it becomes negligible. Note that the background subtracted by filter function when applied to ν-point = 3 (refer to Fig. 4.2c) is also negligible and this, while being related to the random aspect of the data, can be verified by referring to the values of the components of Fourier transform corresponding to the third frequency-point in table 3.1.

For the purpose of further illustration, the results of the application of the single-valued filter function to ν-points equal to 10, 20, and 200 with the value of filter function in each case equal to 0.9 are shown in Fig. 4.3.

If the filter function $W_B(\nu)$, instead of being a single-valued, has more values corresponding to few low frequencies of the Fourier transform of the data, its application to the data will have the cumulative effect of the individual values of the filter function, which means the application of a multi-valued filter function is equivalent to the simultaneous application of corresponding single-valued filters.

Different types of filter functions, $W_B(\nu)$, were investigated which are able to subtract nearly the whole background from the leaf spectrum without making any assumptions about the functional form of the background or resorting to the conventional fitting methods. It was verified that by properly choosing the frequency range, $\nu_b \leq \nu \leq \nu_{P_1}$, and assigning proper values to the filter function in this range (refer to eqn. 4.4) it was possible to remove nearly the whole background by using Fourier transform techniques (*FTT*). For the leaf spectrum, it will be shown that the following

filter having the specified values proved to give the best result:

$$W_B(\nu)_i = \sum_{i=1}^{6} f_i \ , \tag{4.5}$$

with filter values,

$$f_1 = 0.655, \quad f_2 = 0.755, \quad f_3 = 1.0, \quad f_4 = 1.0, \quad f_5 = 0.987, \quad f_6 = 0.990 \tag{4.6}$$

The sketch of the above filter function is represented in Fig. 4.4 where its first six values are shown in eqn. 4.6 above and the remaining values [$(N = 1024) - 6$] are set to one.

The application of the filter function $W_B(\nu)$ to the measured data $M(\nu)$ is performed according to eqn. 3.38a. However, it is to be remembered that the filter function is a real-valued function and it is already constructed in frequency domain. It is obvious from eqns. 3.37 and 3.38a that the application of the filter function $W_B(\nu)$ produces the background-free data $S(\nu)$ in frequency space. However, it is sometimes preferable to have a filter function, say $W_B'(\nu)$, which when applied to the measured data $M(\nu)$ yields directly the subtracted background. The filter $W_B'(\nu)$ is obtained as follows. From eqn. 3.37 we have

$$B(\nu) = M(\nu) - S(\nu) \ . \tag{4.7}$$

But from eqn. 3.38a

$$S(\nu) = W_B(\nu) \times M(\nu) \ . \tag{4.8}$$

By substituting for $S(\nu)$ from eqn. 4.8 into eqn. 4.7 we get

$$B(\nu) = M(\nu) - [W_B(\nu) \times M(\nu)],$$

or

$$B(\nu) = [1 - W_B(\nu)] \times M(\nu) \ .$$

If we introduce

$$W_B'(\nu) = 1 - W_B(\nu) \ , \tag{4.9}$$

$$B(\nu) = W_B'(\nu) \times M(\nu) \ . \tag{4.10}$$

By having the values of the filter function $W_B(\nu)$ from eqn. 4.6, the values of $W_B'(\nu)$ are simply calculated from eqn. 4.9 as follows:

$$W_B'(\nu)_i = \sum_{i=1}^{6} f_i'$$

with

$$f_1' = 1.0 - 0.655 = 0.345, \quad f_2' = 1.0 - 0.755 = 0.245, \quad f_3' = 1.0 - 1.0 = 0.0,$$

$$f_4' = 1.0 - 1.0 = 0.0, \quad f_5' = 1.0 - 0.987 = 0.013, \quad f_6' = 1.0 - 0.990 = 0.010, \qquad (4.11)$$

and the remaining of the values are equal to zero. Fig. 4.5 represents the above filter $W_B'(\nu)$. From comparison of Fig. 4.4 and Fig. 4.5 it can be deduced that $W_B(\nu)$and $W_B'(\nu)$ are the two versions of the same filter. The first is a high-pass filter to produce the background-free data and the latter is a low-pass filter to yield directly the subtracted background.

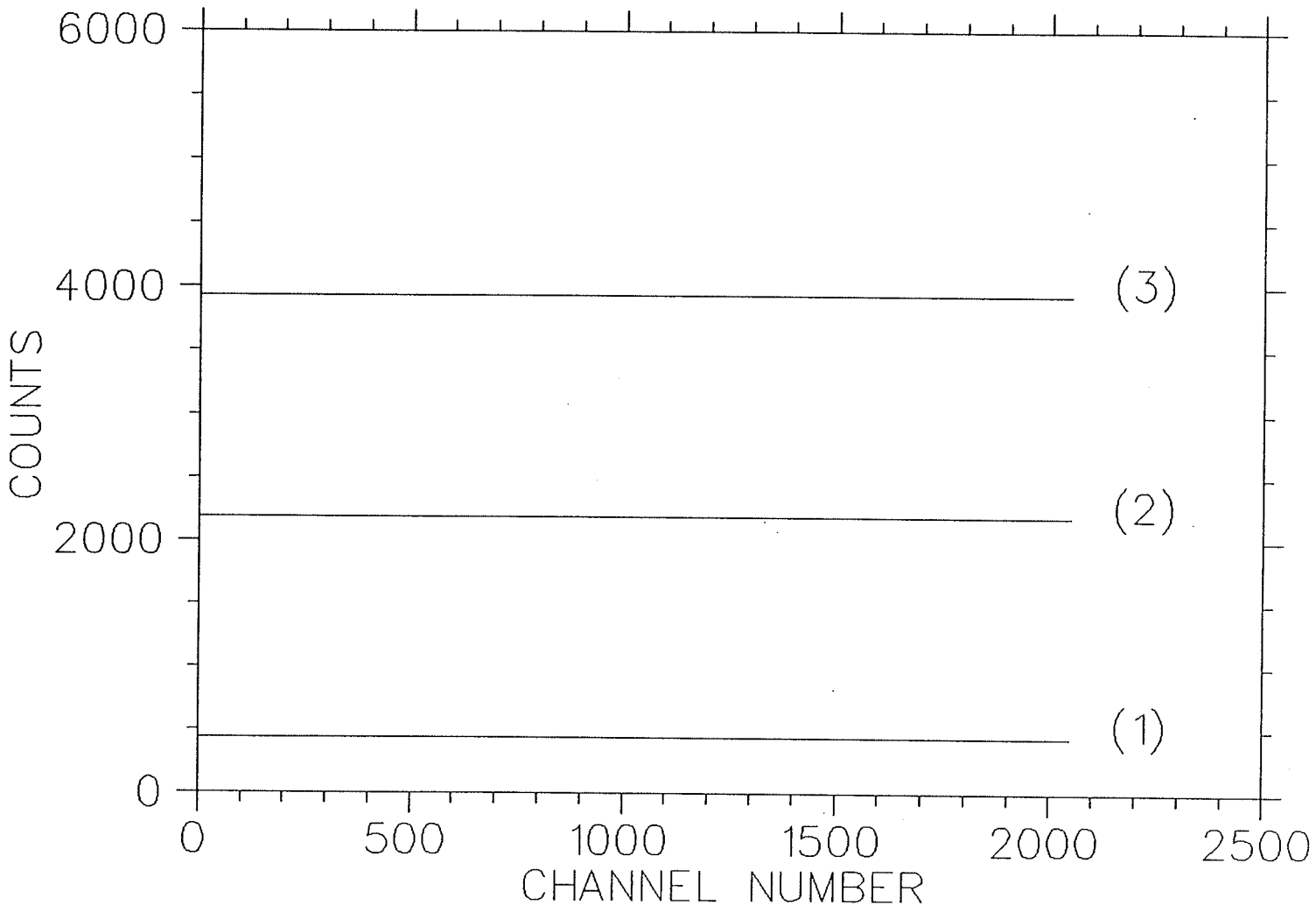

Fig. 4.2a) Background subtracted by filter function $W_B(v)$, having values corresponding only to v-point=1: *(1)* $W_B(1)=0.1$, *(2)* $W_B(1)=0.5$, *(3)* $W_B(1)=0.9$.

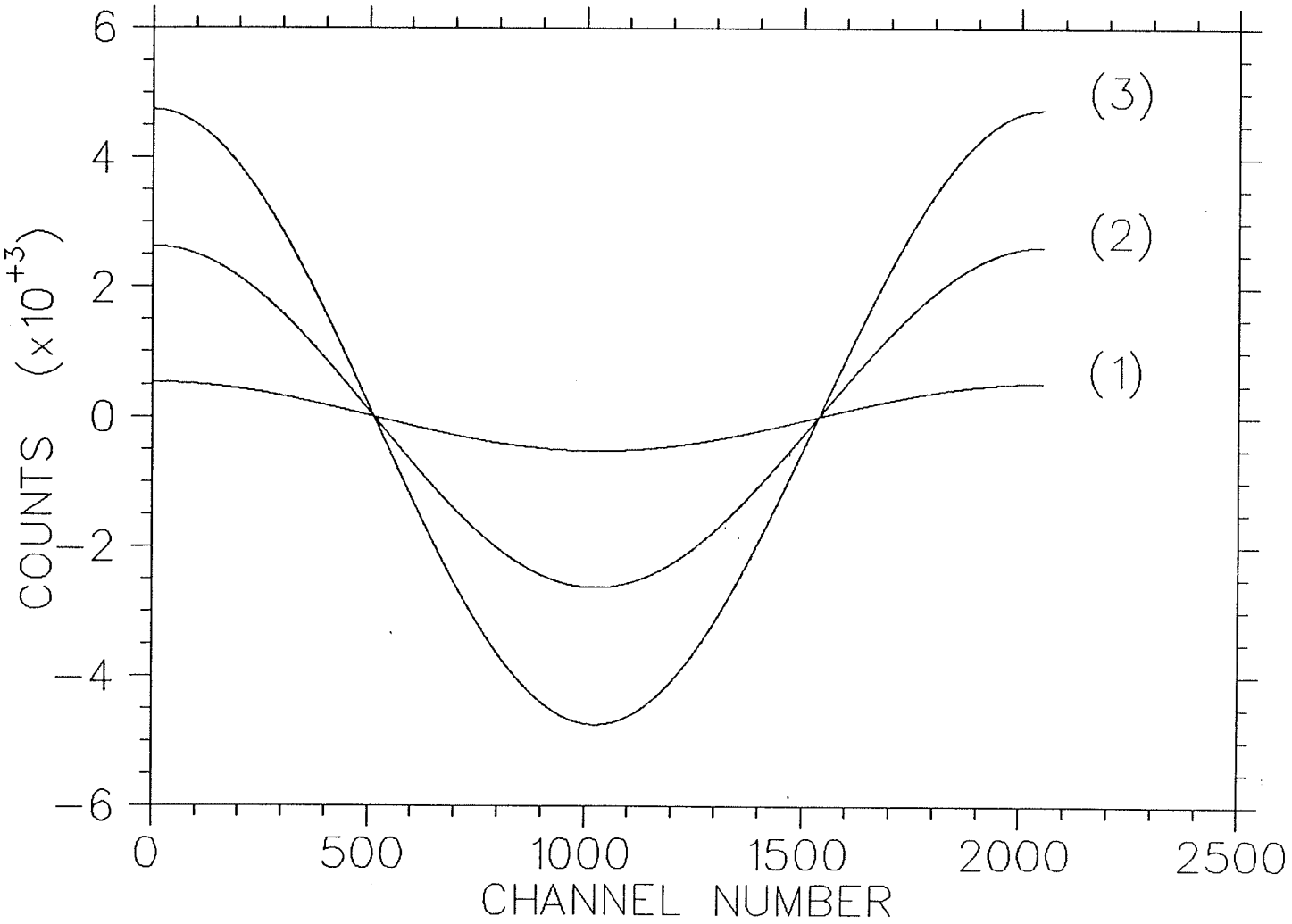

Fig. 4.2b) Background subtracted by filter function $W_B(v)$, having values corresponding only to v-point=2: *(1)* $W_B(2)=0.1$, *(2)* $W_B(2)=0.5$, *(3)* $W_B(2)=0.9$.

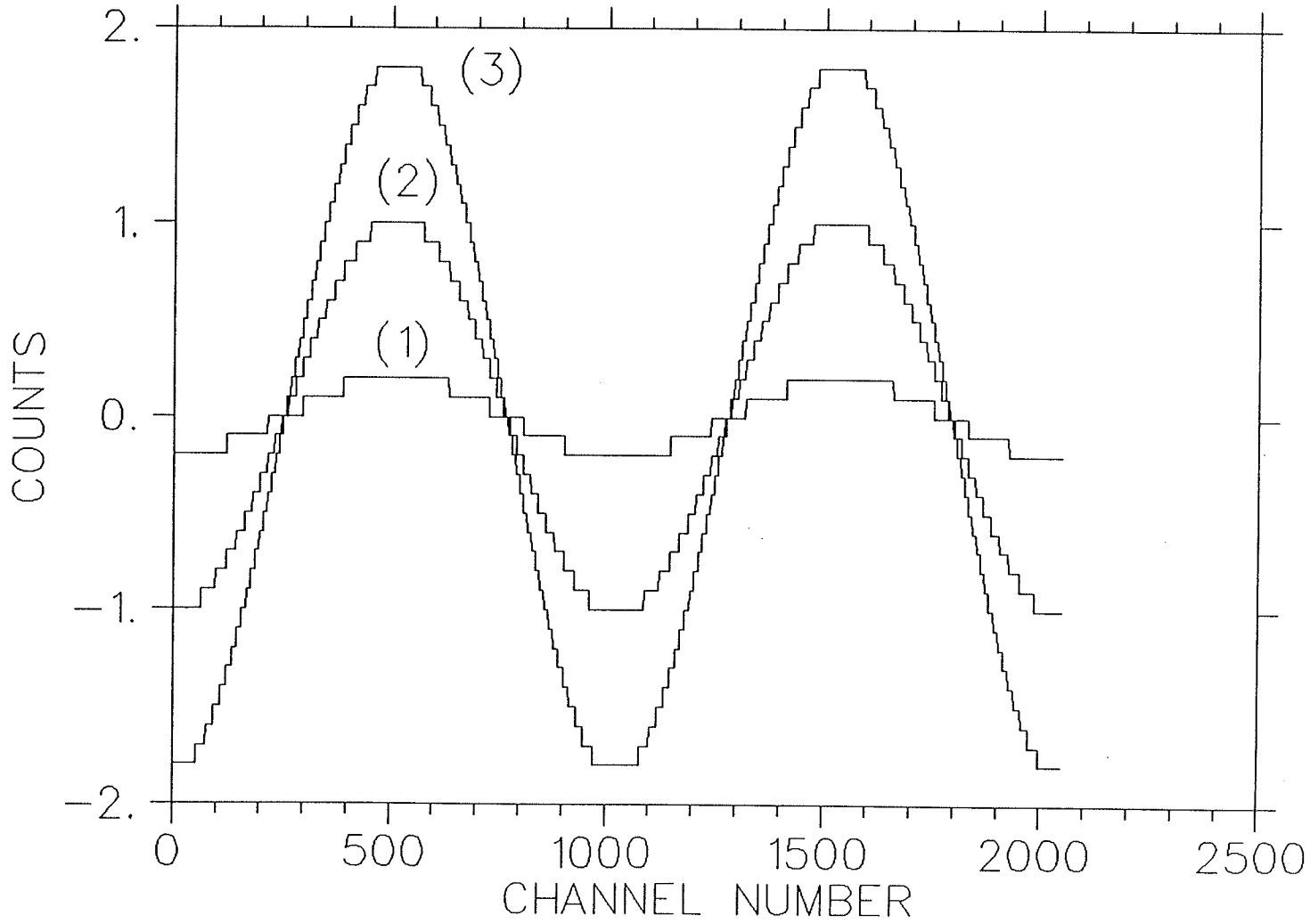

Fig. 4.2c) Background subtracted by filter function $W_B(v)$, having values corresponding only to v-point=3: *(1)* $W_B(3)=0.1$, *(2)* $W_B(3)=0.5$, *(3)* $W_B(3)=0.9$.

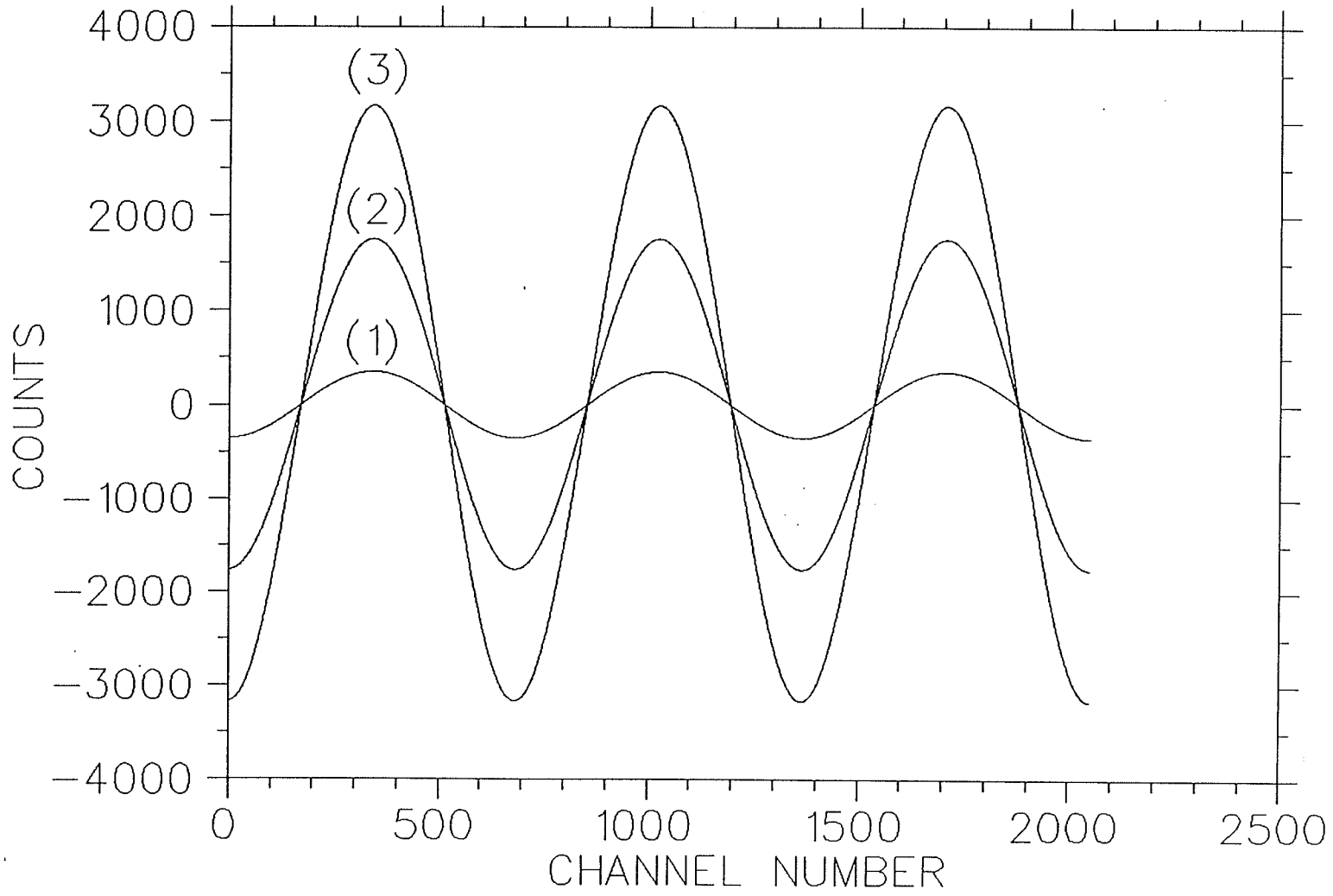

Fig. 4.2d) Background subtracted by filter function $W_B(v)$, having values corresponding only to v-point=4: *(1)* $W_B(4)=0.1$, *(2)* $W_B(4)=0.5$, *(3)* $W_B(4)=0.9$.

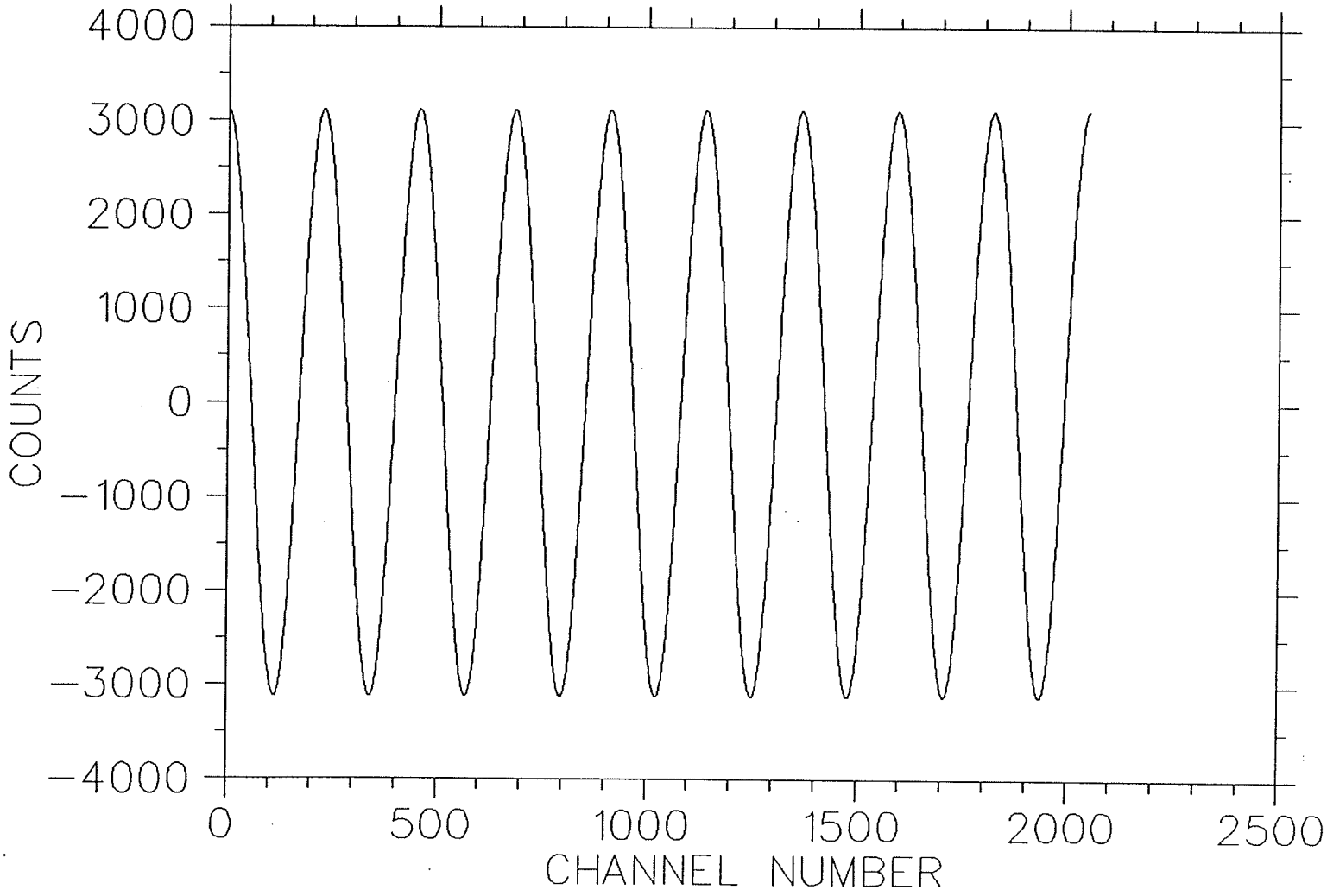

Fig. 4.3a) Background subtracted by single-valued filter function, $W_B(10)=0.9$, applied to ν-point=10.

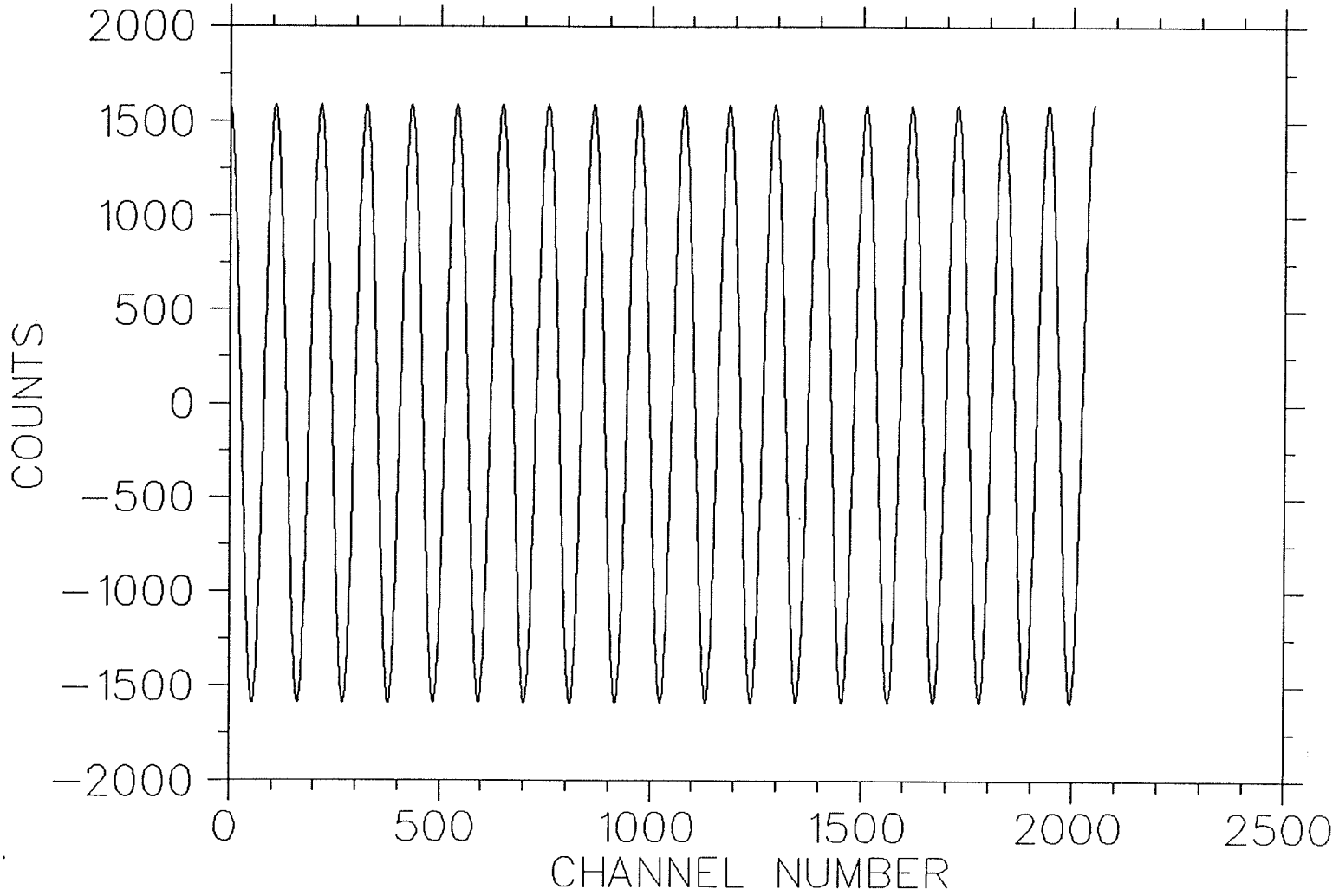

Fig. 4.3b) Background subtracted by single-valued filter function, $W_B(20)=0.9$, applied to v-point=20.

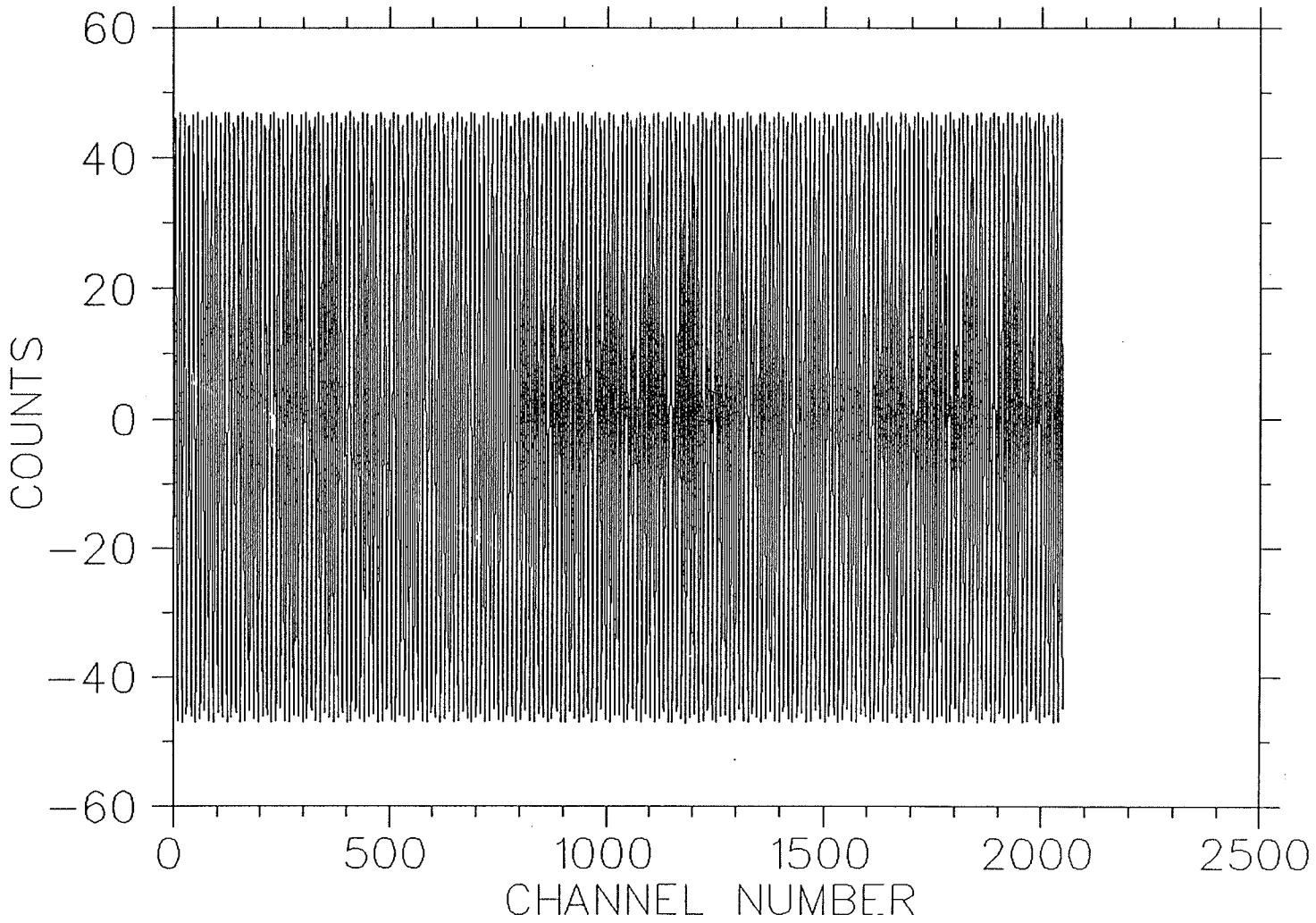

Fig. 4.3c) Background subtracted by single-valued filter function, $W_B(200)=0.9$, applied to ν-point=200.

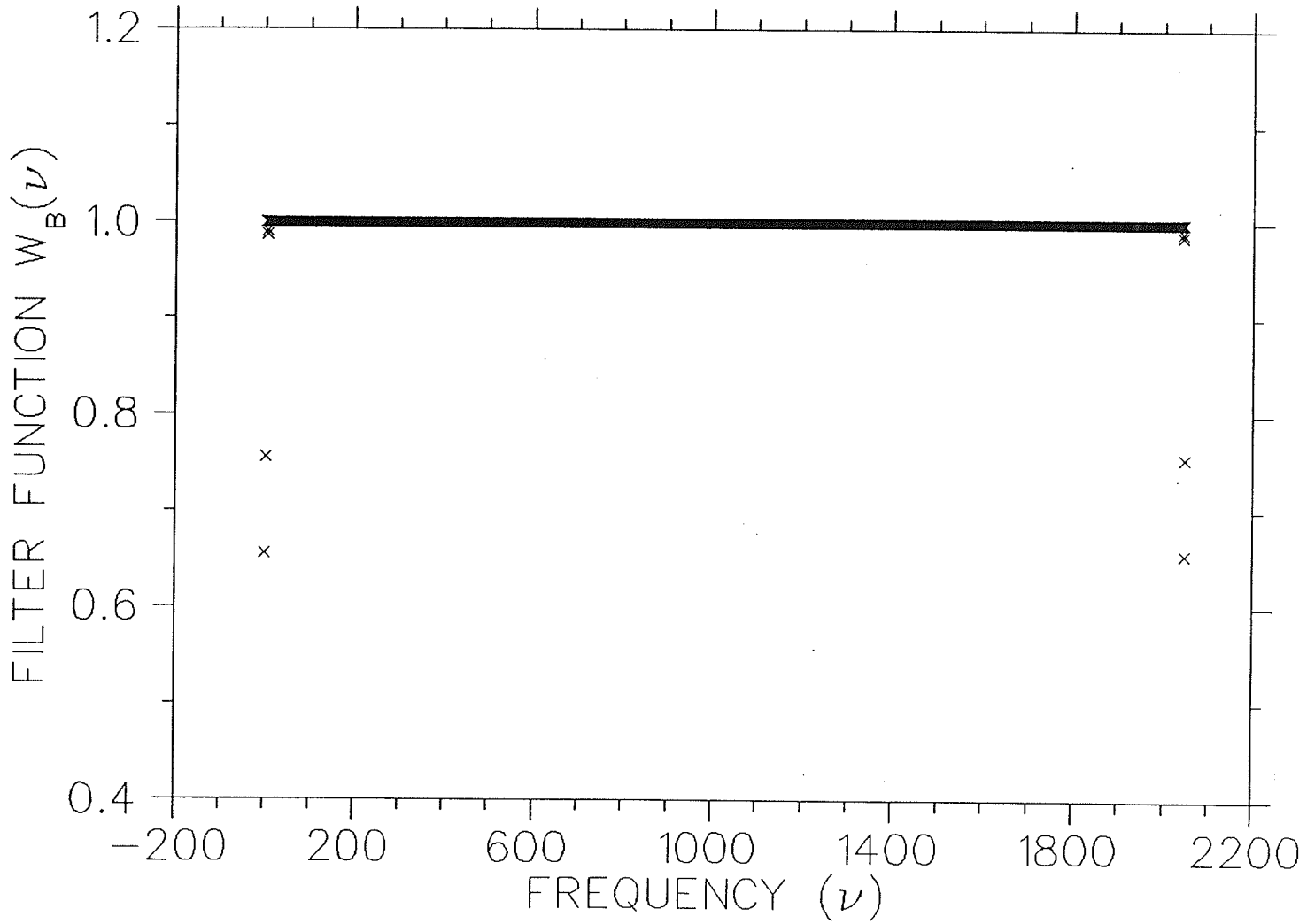

Fig. 4.4 Filter function $W_B(\nu)$ when applied to the measured leaf spectrum $M(\nu)$, subtracts background and produces background-free data $S(\nu)$.

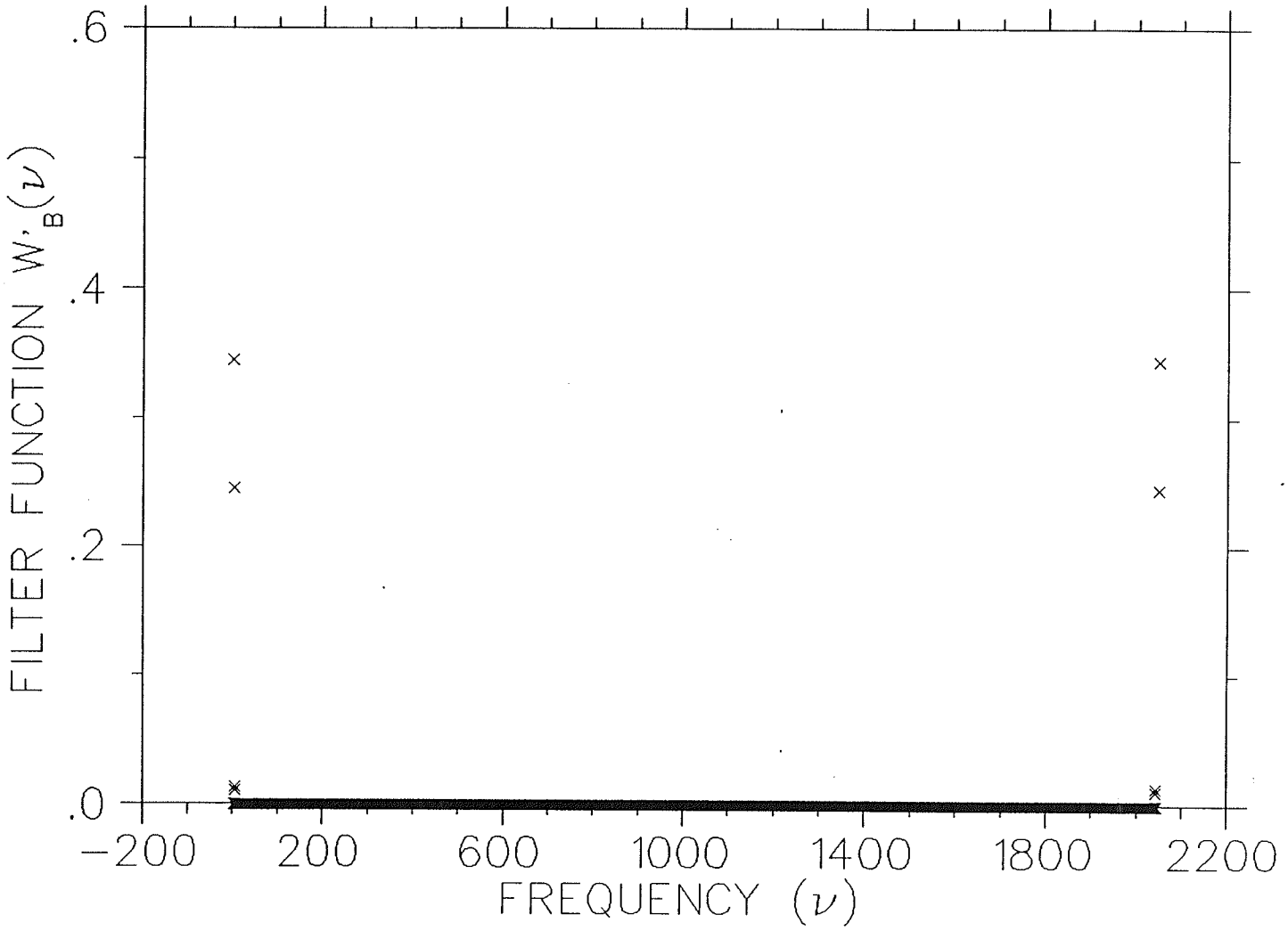

Fig. 4.5 Filter function $W'_B(\nu)$ when applied to the measured leaf spectrum $M(\nu)$, produces background function.

4.2. Design Criteria for a Filter Function to Remove Noise

The smoothing operations are used primarily for diminishing spurious effects and for eliminating most of the random fluctuations without effecting the spectral resolution. The statistical nature of the spectra, however, results in a non-zero probability of committing two kinds of errors. On one hand strong statistical fluctuations lead to detection of fraudulent peaks, on the other hand small true peaks can be missed by the procedure.

The noise component of the filter function, $W_N(\nu)$ (refer to eqn. 3.40), should produce considerable smoothing action without decreasing the peak to valley ratio in the unresolved peaks. Peak centers should not be shifted by the smoothing process.

Because the statistical fluctuations, forming the noise component, are uncorrelated channel to channel, they are attributed to high-frequencies, i.e., noise contributes heavily to the high-frequency content of its Fourier transform.

To determine the proper smoothing filter function, $W_N(\nu)$, it is useful to plot the power spectrum of the background-free data, $S(\nu)$, in eqn. 3.39, i.e. $|S(\nu)|^2$, vs ν. Such a plot for the leaf spectrum is represented in Fig. 4.6 where actual transformation gives one ν-point for each energy point. Although Fig. 4.6 and the power spectrum of the measured data, $|M(\nu)|^2$, in Fig. 4.1 seem to be similar, however, a careful study of the few low frequencies confirm the subtraction of background in the power spectrum of Fig. 4.6. For the purpose of a better comparison, the power spectrum of the first 10 ν-points of both $|M(\nu)|^2$ and $|S(\nu)|^2$ are represented in Fig. 4.7 where the difference between the two is visible only in the first two ν-points due to the corresponding larger values of filter function applied to these points. Notice that the power spectrum in Fig. 4.6 divides nicely into contributions from the peaks, $|T(\nu)|^2$, and the noise (statistical fluctuations), $|N(\nu)|^2$. The cutoff frequency, characteristic of the signal, is also identified.

The filter function $W_N(\nu)$, must be of a form that passes frequencies below the cutoff frequency but eliminates those frequencies above the cutoff where the noise component, $N(\nu)$, dominates. A function with the higher cutoff does not produce as much smoothing and the very low cutoff produces so much smoothing that considerable information is lost.

From the above discussion and by referring to the power spectrum of Fig. 4.6, it is seen that the smoothing filter function, $W_N(\nu)$, should have the characteristics of a low-pass filter which will remove noise. But the shape of the cutoff is very important as it can remove genuine detail or can introduce spurious oscillations. Note that the filter function $W_N(\nu)$, is a function which affects corresponding real and imaginary components of the Fourier transform in exactly the same manner. Such filter is also referred to as "zero-phase-shift-filter".

There are various versions of low-pass filters among which "Ideal low-pass filter", "Butterworth low-pass filter", "Exponential low-pass filter", and "Trapezoidal low-pass filter" can be mentioned (for detailed description of these filters refer to [Go, 77]).

If we designate the lower and upper limit of the frequencies characteristic of the peaks as ν_{P_1} and ν_{P_2} respectively, the high frequencies ($\nu \gg \nu_{P_{1,2}}$) contribute to $N(\nu)$ in eqn. 3.39, i.e. they belong to statistical noise, and are more easily separated than the background component. As far as the design of the noise component of the filter function, $W_N(\nu)$, is concerned, the optimal filter proved to be a good choice for this purpose.

Here eqns. 3.39 and 3.40 have been represented as,

$$S(\nu) = T(\nu) + N(\nu), \tag{4.12}$$

and

$$\tilde{T}(\nu) = W_N(\nu) \times S(\nu), \tag{4.13}$$

where $T(\nu)$ in eqn. 4.13 has changed to an estimated value of $\tilde{T}(\nu)$. It can be shown that in what sense the estimated $\tilde{T}(\nu)$ is close to the true quantity $T(\nu)$. If it is asked that they be close in the least-square sense

$$\int_{-\infty}^{+\infty} |\tilde{t}(E) - t(E)|^2 \, dE = \int_{-\infty}^{+\infty} |\tilde{T}(\nu) - T(\nu)|^2 \, d\nu \tag{4.14}$$

is minimized.

Substituting equations 4.12 and 4.13, the right-hand side of equation 4.14 becomes:

$$\int_{-\infty}^{+\infty} | [T(\nu) + N(\nu)] W_N(\nu) - T(\nu) |^2 d\nu =$$

$$\int_{-\infty}^{+\infty} [| T(\nu) |^2 \times | 1 - W_N(\nu) |^2 + | N(\nu) |^2 \times | W_N(\nu) |^2] d\nu. \qquad (4.15)$$

In view of the statistical nature of the radiation and the way in which this radiation is registered an important assumption was made, namely that the count numbers in different channels are statistically independent. Based on this assumption the true quantity $T(\nu)$ and the noise component $N(\nu)$ are "uncorrelated" therefore, their cross product when integrated over frequency ν gives zero and eqn. 4.15 is obtained from eqn. 4.14.

Obviously eqn. 4.15 will be a minimum if the integrand is minimized with respect to $W_N(\nu)$ at every value of ν. Such a solution, where $W_N(\nu)$ is a real function, can be obtained by differentiating eqn. 4.15 with respect to $W_N(\nu)$, and setting the result equal to zero. If we introduce the solution as $g(\nu)$,

$$g(\nu) = \frac{| T(\nu) |^2}{| T(\nu) |^2 + | N(\nu) |^2}. \qquad (4.16)$$

Equation 4.16 represents the formula used for the optimal filter. Note that the solution has been deliberately introduced as $g(\nu)$ rather than $W_N(\nu)$, the reason for which will be explained later.

Equation 4.16 involves the sought quantity $T(\nu)$, and the noise component $N(\nu)$. These two quantities add up to the background-free data, $S(\nu)$ (refer to eqn. 4.12).

To determine the optimal filter $g(\nu)$ from eqn. 4.16 the components $| T(\nu) |^2$ and $| N(\nu) |^2$ should be separated from the $| S(\nu) |^2$. Although there is no way for this separation alone, the power spectrum of Fig. 4.6, as discussed before, clearly shows a peak region added to a noise tail. The tail is extrapolated back into the region dominated by spectral peaks as a "noise model". The noise spectrum may be flat, or tilted, or smoothly varying. Note that a flat model is used for this case. Now a straight line is drawn through the power spectrum of the background-free data. The difference between these two curves will be the model of the signal power. The optimal filter $g(\nu)$ can be extended to negative values of ν by the formula $g(-\nu) = g(\nu)$. Notice that $g(\nu)$ will be close to unity where the noise is negligible, and close to zero where the

noise is dominant. The intermediate dependence given by eqn. 4.16 turns out to be the optimal way of interpolating between these two extremes.

It might seem logical to assign the range of frequencies between ν_{p_1} (characteristic frequency denoting the beginning of the spectral peaks) and the cutoff frequency ν_c in Fig. 4.6 to be operated upon by the optimal filter, i.e. to set $\nu_{p_1} \leq \nu \leq \nu_c$ in formula 4.16. However, it is important that the filter function be a smoothly varying function of frequency so that oscillations are not introduced in the inverse transformation. A sharp cutoff in one domain implies damped oscillatory behavior in the other [OP, 75; Ch, 79]. An extreme case for this statement is " ideal low-pass filter " whose transfer function satisfies the relation

$$H(\nu) = \begin{cases} 1 & \text{if } \nu \leq \nu_c \\ 0 & \text{if } \nu > \nu_c, \end{cases}$$

where ν_c is the cutoff frequency. Ideal low-pass filters have strong oscillatory properties which can be easily explained by resorting to the convolution theorem.

Based on the above argument the filter function should provide smooth transition between low and high frequencies. To illustrate the oscillatory behavior of the optimal filter, $g(\nu)$, if it is assigned the range of frequencies $\nu_{p_1} \leq \nu \leq \nu_c$, such a filter is shown as represented in Fig. 4.8. Note that the values in the range $\nu_c \leq \nu \leq \nu_t$ are equal to zero to remove the high frequencies characteristic of noise where ν_t is the terminal frequency, i.e. $\nu_t = 1024$ for leaf sample.

When this filter is applied to the original preconditioned data of Fig. 4.9, the spectrum as shown in Fig. 4.10 is produced. The oscillations and the spurious peaks appearing in the spectrum are attributed to the non-smooth transition of the filter between low and high frequencies.

In order to eliminate this problem of oscillatory behavior, a smooth Gaussian was fitted between the characteristic frequency-point ν_{p_2} and the cutoff frequency ν_c. ν_{p_2} is, in general, the frequency at which the values of the filter function calculated from eqn. 4.16 vary sharply. The standard deviation of the Gaussian was calculated according to

$$\sigma = \left[\frac{1}{D-1} \sum_{i=\nu_{p_2}+1}^{\nu_c} (\nu_i - \nu_{p_2})^2 \right]^{\frac{1}{2}},$$

where $D = \nu_c - \nu_{p_2}$ and the values of the Gaussian function were obtained from the relation

$$h_i = \frac{1}{\sigma\sqrt{2\pi}}\, e^{\frac{-(\nu_i - \nu_{p_2})^2}{2\sigma^2}} \qquad i = \nu_{p_2} + 1, \ldots, \nu_c \ . \tag{4.17}$$

Finally, the values of the filter function in the last portion between the cutoff frequency ν_c and the terminal frequency $\nu_t = 1024$, i.e. high frequency region, were made equal to zero in order to remove that portion of the noise completely.

Based on the above discussion the relation for the filter function $W_N(\nu)$, to remove noise component can be expressed as follows

$$W_N(\nu)_{i,j,k} = \sum_{i=\nu_{p_1}+1}^{\nu_{p_2}} g_i + \sum_{j=\nu_{p_2}+1}^{\nu_c} h_j + \sum_{k=\nu_c+1}^{\nu_t} z_k \ , \tag{4.18}$$

where g_i represents those values of the filter function obtained from the formula of optimal filter (eqn. 4.16), h_j corresponds to the smooth Gaussian fitted to the far tail of the filter function, and finally the values corresponding to z_k are equal to zero.

Fig. 4.11 represents the required filter function $W_N(\nu)$ of equation 4.18, with the frequencies characteristic of the peaks ν_{P_1} and ν_{P_2}; the cutoff frequency ν_c and the terminal frequency ν_t identified. The application of this filter function to the original data of Fig. 4.9 produces the smoothed data of Fig. 4.12.

The free parameters of the filter function $W_N(\nu)$ were assigned the following values to remove the noise component from the spectrum of the leaf sample:

(i) The noise level, i.e. the power spectrum of the noise component used in the formula 4.16 was assigned as $|N(\nu)|^2 = 10^8$. It is to be noted that variation in the noise level up to about one order of magnitude has little effect on the performance of the filter function if the difference between the power spectrum of the data and that of the noise is several orders of magnitude. However, if these two values are rather close, care should be taken in assigning a value to the noise level.

(ii) As seen from equation 4.5, the filter function to remove background, i.e. $W_B(\nu)$, operates between ν-point = 1 and ν-point = 6. Therefore, the lower limit of the first summation of equation 4.18 should be assigned $i = 7$. However, since the first few values of the filter $W_N(\nu)$ are very close to unity it is convenient if it operates from the

very first ν-point.

(iii) ν_{p_2}, which is nominally the end of the frequencies characteristic of the peaks, was assigned the value 70. However, as long as the values of the optimal filter, g_i, obtained from equation 4.16 do not fall sharply, higher values can also be assigned to ν_{p_2} with little effect or improvement in the results.

(iv) Cutoff frequency was assigned as $\nu_c = 350$. This can be decided by visual inspection of the power spectrum of the 1024-channel original data of Fig. 3.1. Variation of up to about 10-20% in the location of the cutoff frequency has a small effect on the smoothing action. Note that cutoff-frequency should be obtained from the power spectrum of the 1024-channel original data and not from that of the symmetrical 2048-channel data of Fig. 4.6. The cutoff frequency obtained from the latter, assigns much higher value to ν_c, $\approx$ 850, and hence the filter function does not produce as much smoothing as necessary.

(v) Smooth Gaussian fitted to the far tail of the filter function $W_N(\nu)$, is not considered as a free parameter as this is decided by the appropriate determination of ν_{p_2} and ν_c between which it is fitted. However, the Gaussian fitted to $W_N(\nu)$ in Fig. 4.11 has a standard derivation $\sigma = 162.38$. Note that the frequency ν is in fact in units of $\frac{2\pi}{2048}\frac{rad}{ch}$ in the 2048-channel symmetrical spectrum, therefore $\sigma = 162.38$ means $162.38 \times \frac{2\pi}{2048} = 0.499\ \frac{rad}{ch}$.

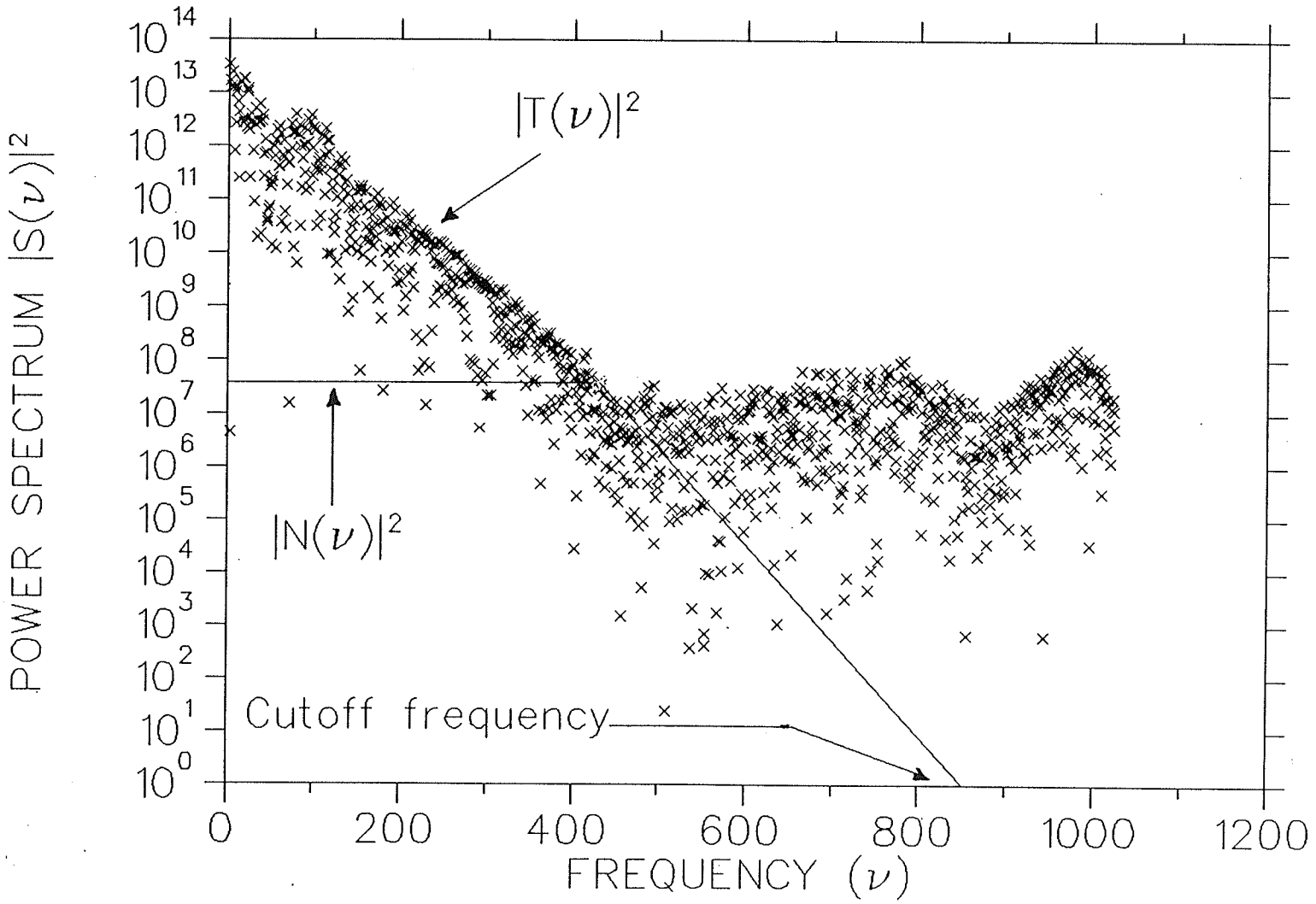

Fig. 4.6 Power spectrum of the preconditioned, background-free leaf data.

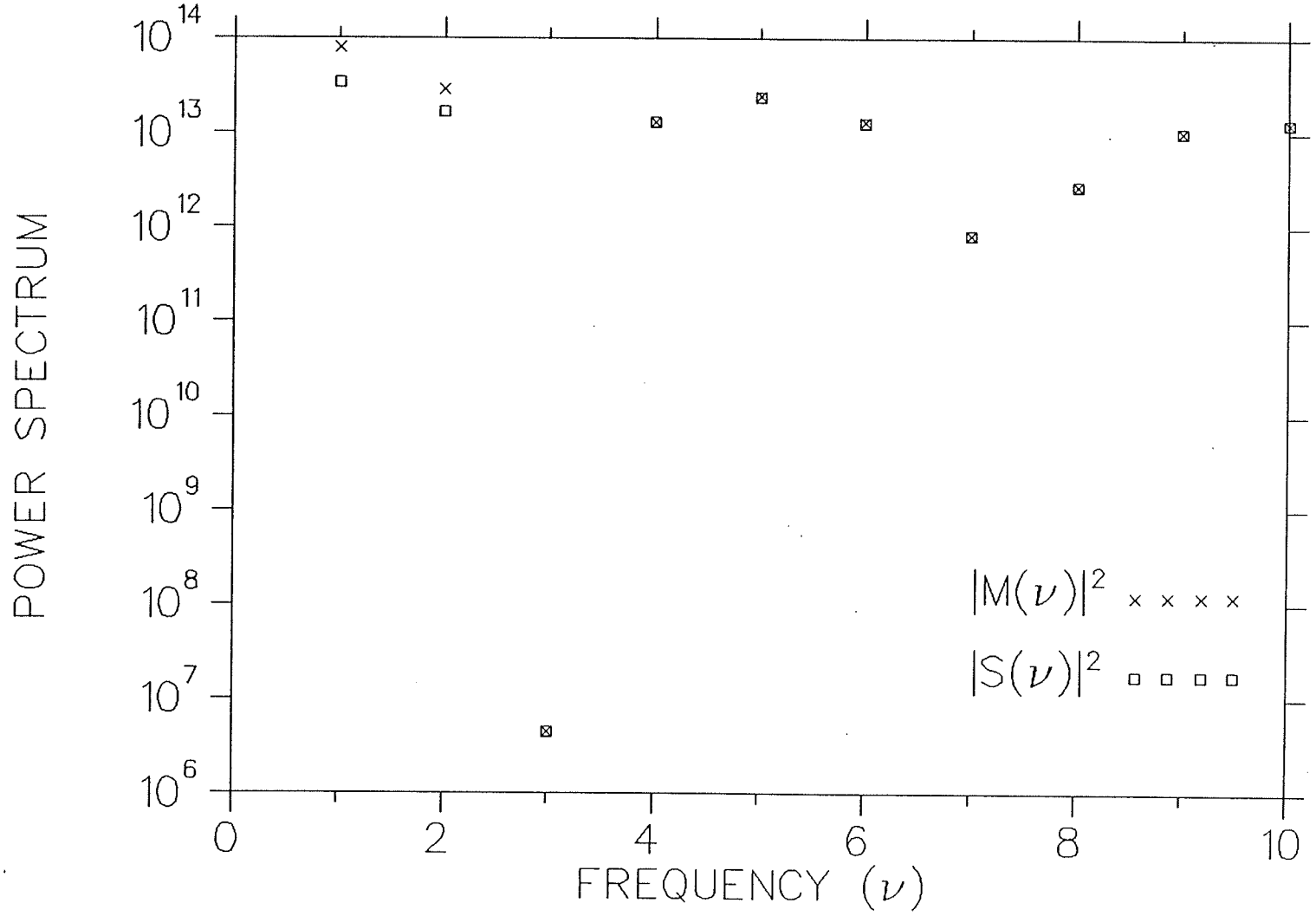

Fig. 4.7 Power spectrum of the leaf sample (only the first 10 ν-points are shown).

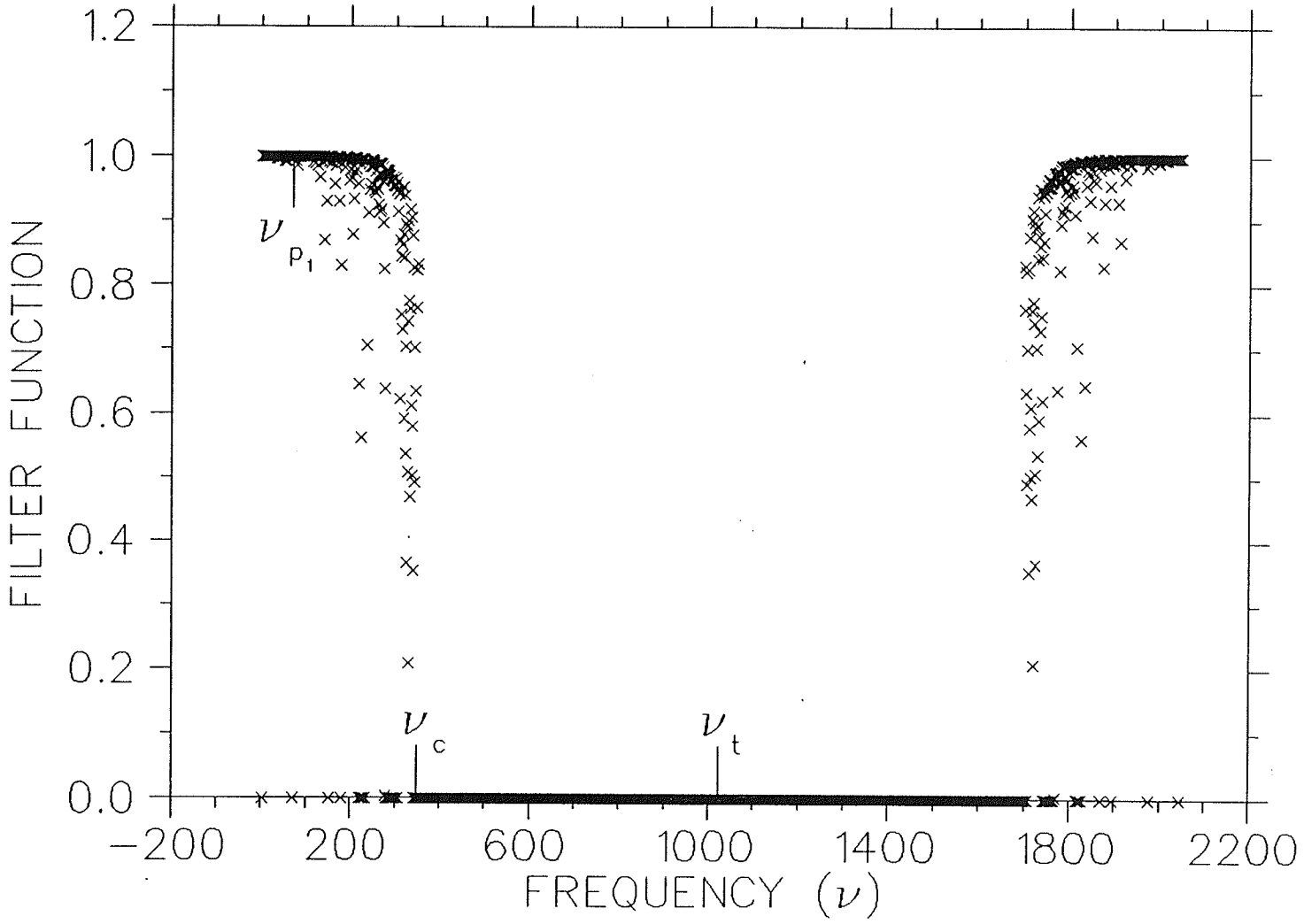

Fig. 4.8 Optimal filter function to remove the noise component. Note that no Gaussian is fitted to the tail of the filter function.

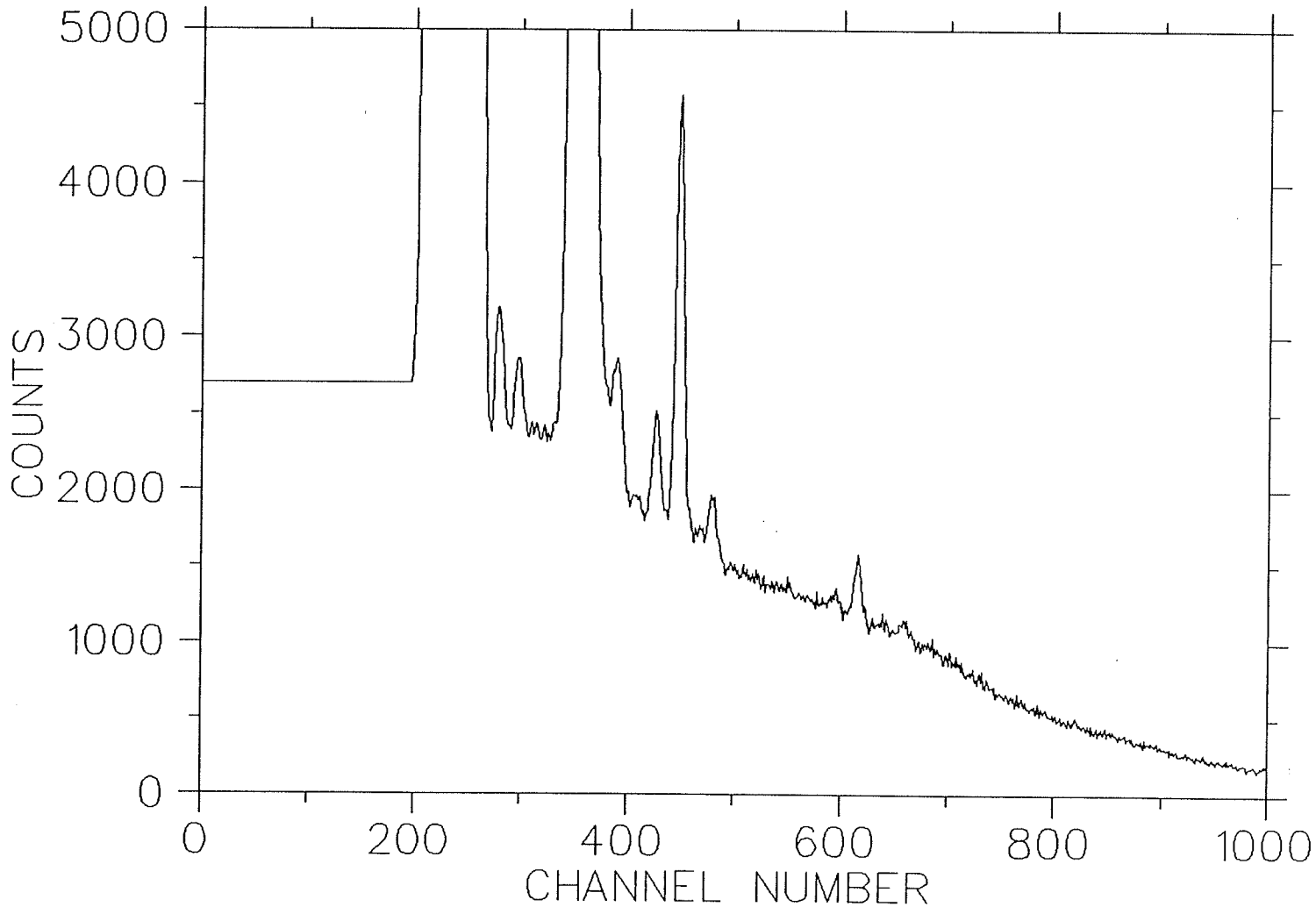

Fig. 4.9 Original, preconditioned spectrum of the leaf sample.

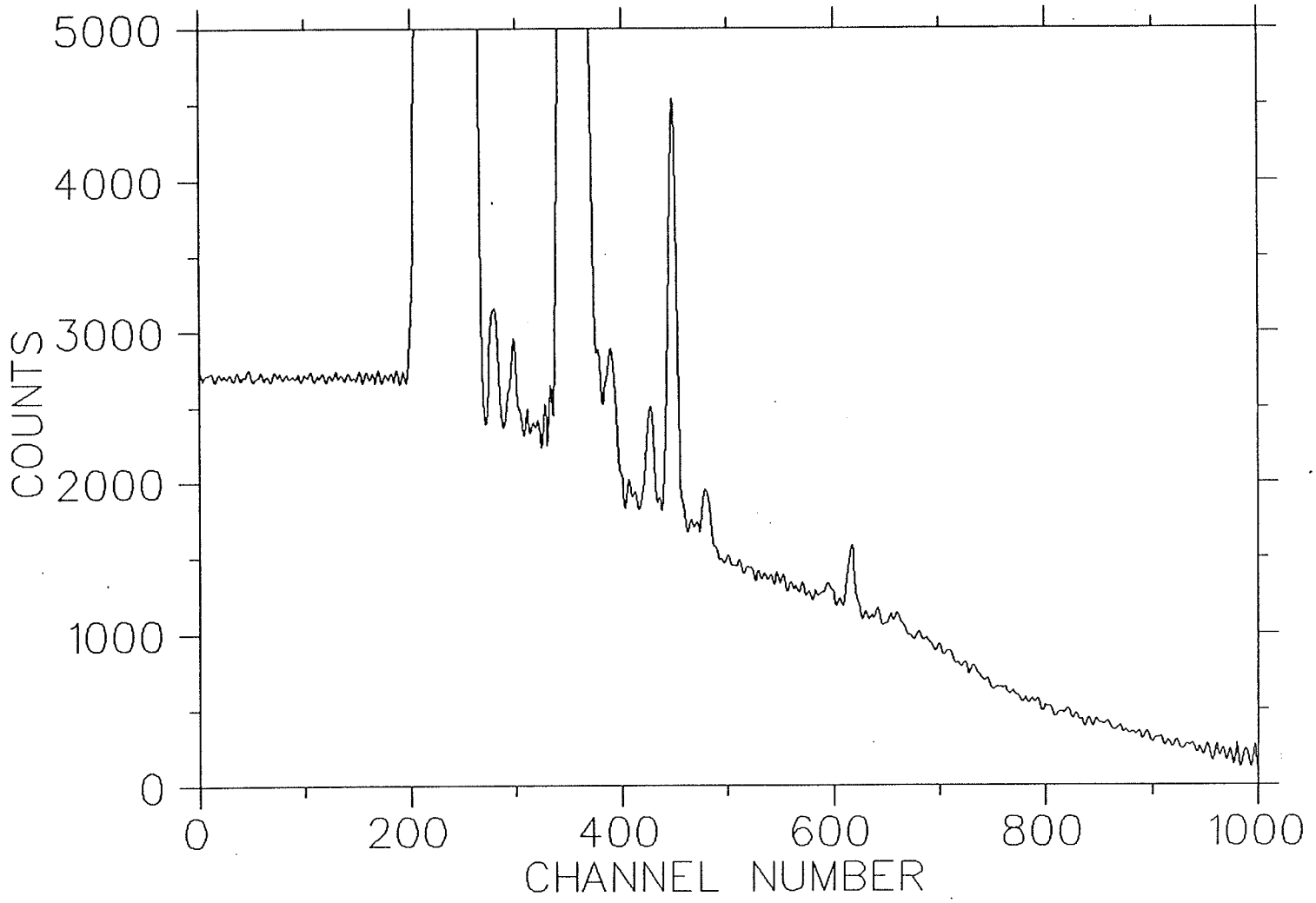

Fig. 4.10 Oscillatory behaviour introduced to the spectrum by applying improper smoothing filter function.

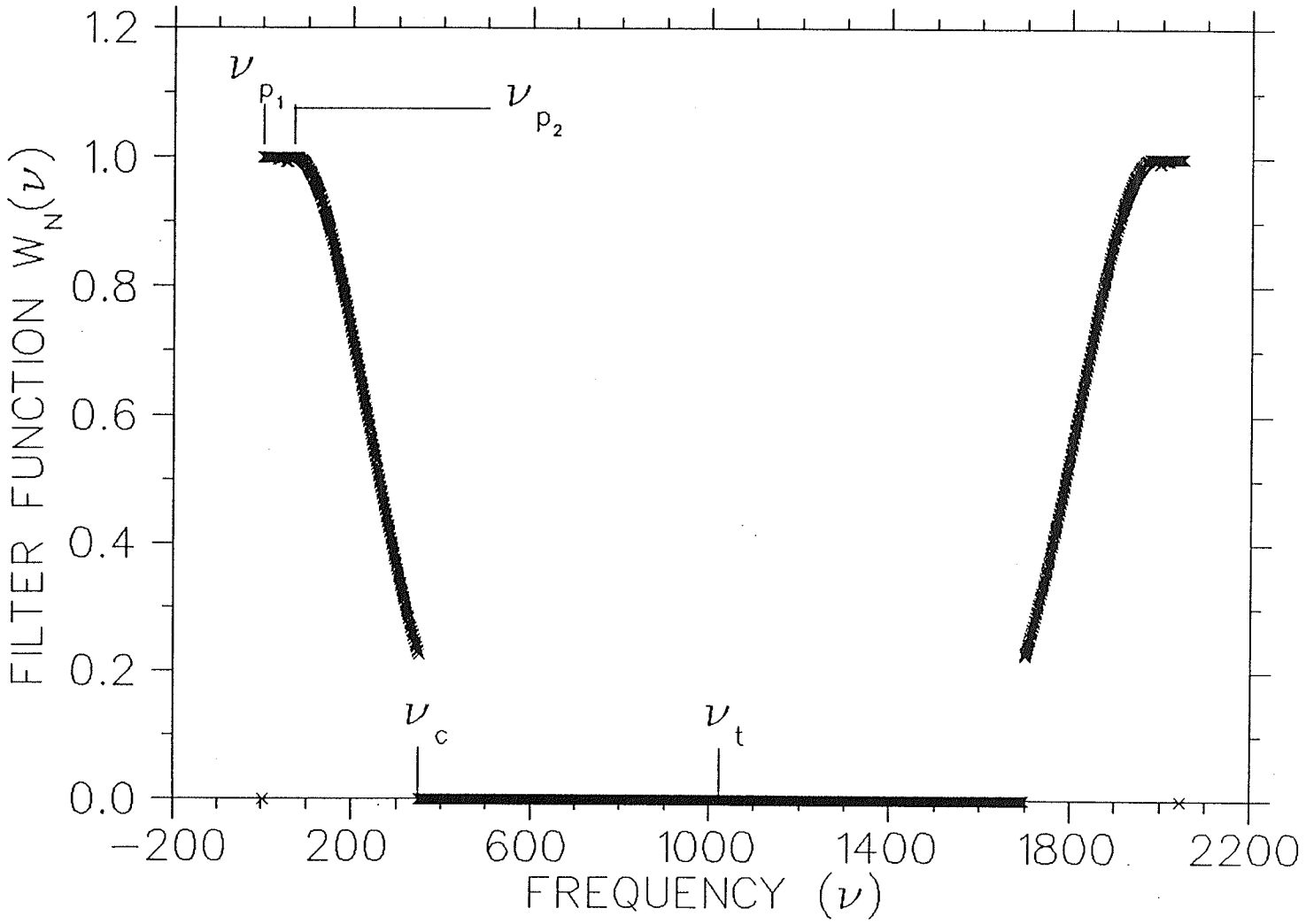

Fig. 4.11 Filter function $W_N(\nu)$ with the frequencies characteristic of the peaks ν_{p1} and ν_{p2}, the cutoff frequency ν_c and the terminal frequency ν_t.

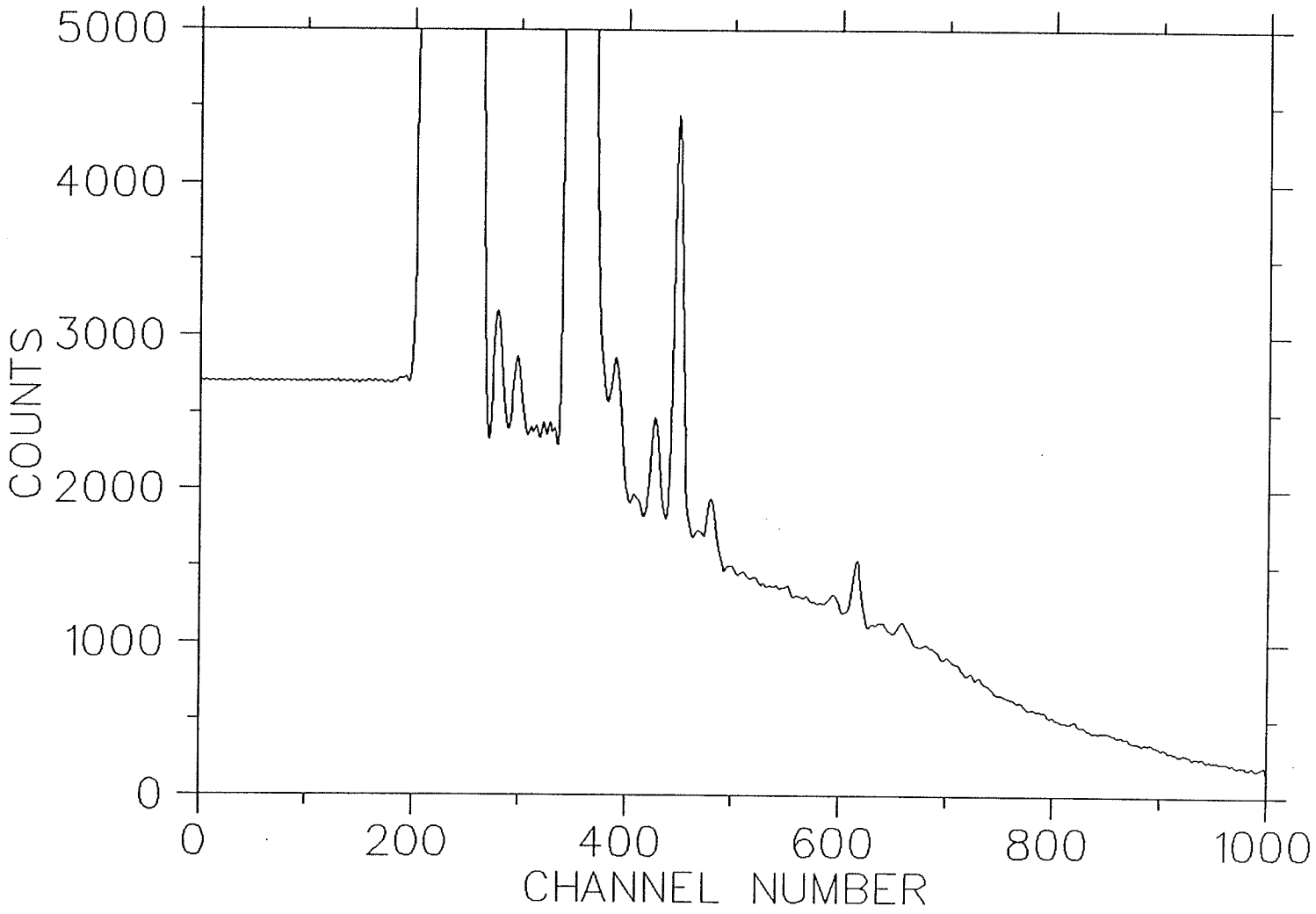

Fig. 4.12 Smoothed data produced by applying the filter function $W_N(v)$ to the data of Fig. 4.9.

4.3. Design Criteria for a Filter Function to Simultaneously Subtract Background and Remove Noise"

In sections 4.1 and 4.2 the design of the filter functions $W_B(\nu)$ and $W_N(\nu)$ to subtract respectively background and to remove noise were discussed. From equations 4.1 and 4.2 it can be deduced that the following is the relation of the filter function, $W(\nu)$, which when applied to the measured data, will simultaneously subtract background and remove noise.

$$W(\nu) = W_B(\nu) \times W_N(\nu) \; . \tag{4.19}$$

Substituting for $W_B(\nu)$ and $W_N(\nu)$ from equations 4.4 and 4.18 respectively, we have,

$$W(\nu)_{i,j,k,l} = \sum_{i=\nu_b}^{\nu_{p_1}} f_i + \sum_{j=\nu_{p_1}+1}^{\nu_{p_2}} g_j + \sum_{k=\nu_{p_2}+1}^{\nu_c} h_k + \sum_{l=\nu_c+1}^{\nu_t} z_l . \tag{4.20}$$

Fig. 4.13 represents the filter function $W(\nu)$ of equation 4.20 which has the combined effect of the filter functions of Fig. 4.4 and 4.11.

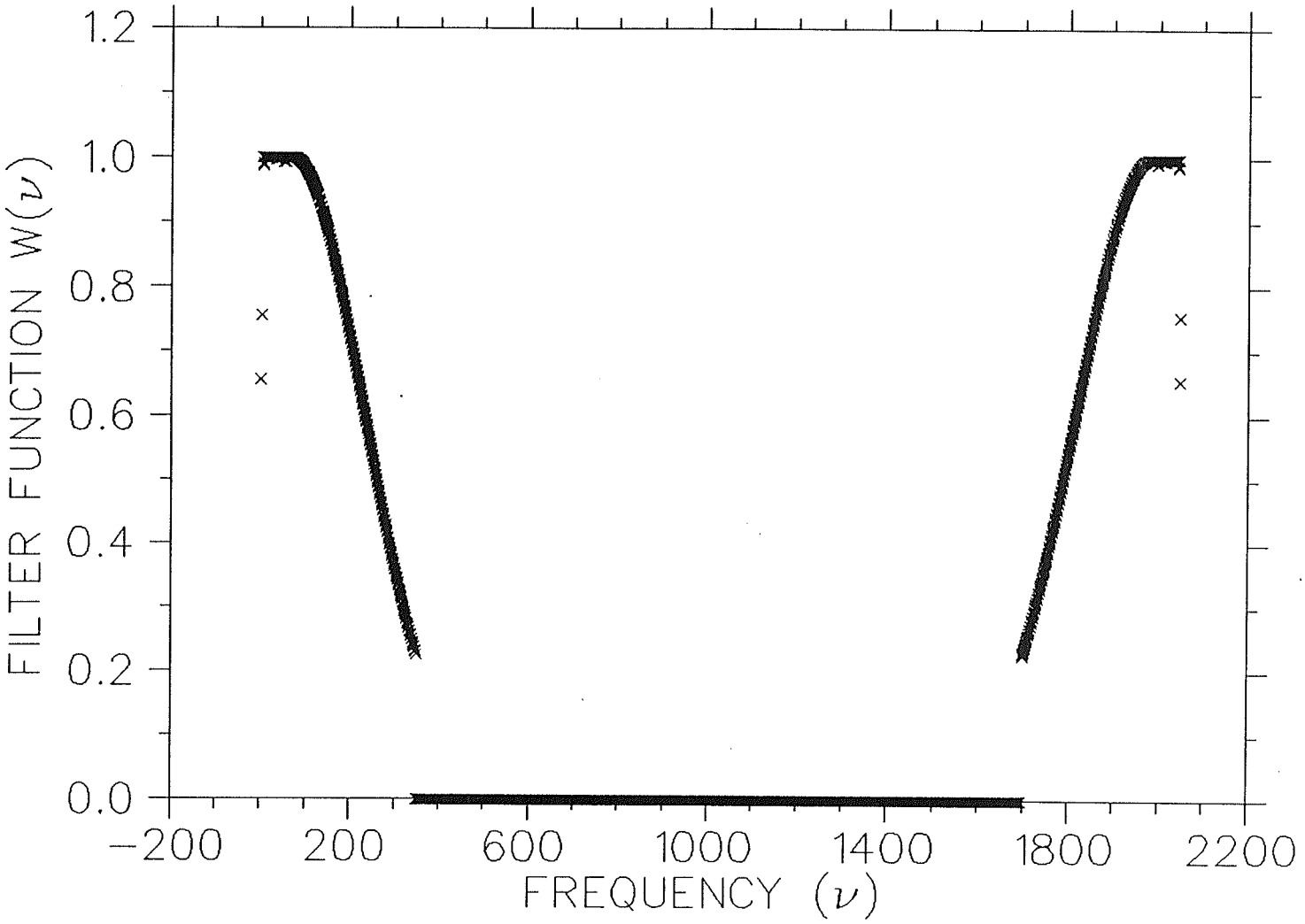

Fig. 4.13 Filter function, $W(\nu) = W_B(\nu) \cdot W_N(\nu)$, when applied to the measured data $M(\nu)$, simultaneously subtracts background and smooths the data.

Chapter 5
Results of Analysis

In chapter 4 the filter design was discussed and the filter function was constructed according to

$$W(\nu) = W_B(\nu) \times W_N(\nu) \,, \tag{5.1}$$

where $W_B(\nu)$ and $W_N(\nu)$ are the background and noise components of the filter function. By applying this filter function to the Fourier transformed measured data $M(\nu)$, the true function (peaks only), $T(\nu)$, in frequency space will be obtained

$$T(\nu) = W(\nu) \times M(\nu) \,. \tag{5.2}$$

An inverse transform of $T(\nu)$ will provide the background and noise-free spectrum, $t(E)$, in channel number domain which is the sought quantity.

Some of the experimental results obtained during the above process are discussed in the sections which follow.

5.1. Fitting Background Function to the Data

As discussed previously, only the first few low frequencies contribute to the background subtraction. However, the number of ν-points assigned for this purpose and the values of filter function at these frequencies will vary under different experimental conditions. For the conditions under which the *PIXE* experiment of the leaf sample was performed, the filter function $W_B'(\nu)$ of equation 4.10 with the filter values of equation 4.11 removed nearly the whole background. Figure 5.1 illustrates the fit of this background function to the X-ray spectrum of the leaf specimen. Figure 5.2 shows the corresponding background-subtracted spectrum, $s(E)$, of equation 4.8 which can be obtained directly by the application of the filter function $W_B(\nu)$ of equation 4.5 having the values listed in 4.6.

As can be noticed from 4.11, the values assigned to v-point= 5 and v-point= 6 of the filter function are very small. However, these optimized small values have considerable effect in removing small values of background remaining in certain regions of the spectrum. To illustrate the effect of the values $f_5' = 0.013$ and $f_6' = 0.010$ in 4.11, Fig. 5.3 depicts the background function fitted when $f_5' = 0.013$ and $f_6' = 0.0$ and Fig. 5.4 represents the same when $f_5' = f_6' = 0.0$. If the fits of the background in Fig. 5.3 and Fig. 5.4 are compared with the fit of Fig. 5.1, it can be noticed that some oscillations have appeared in the fits of the former resulting in over estimating or under estimating of background subtraction in certain regions.

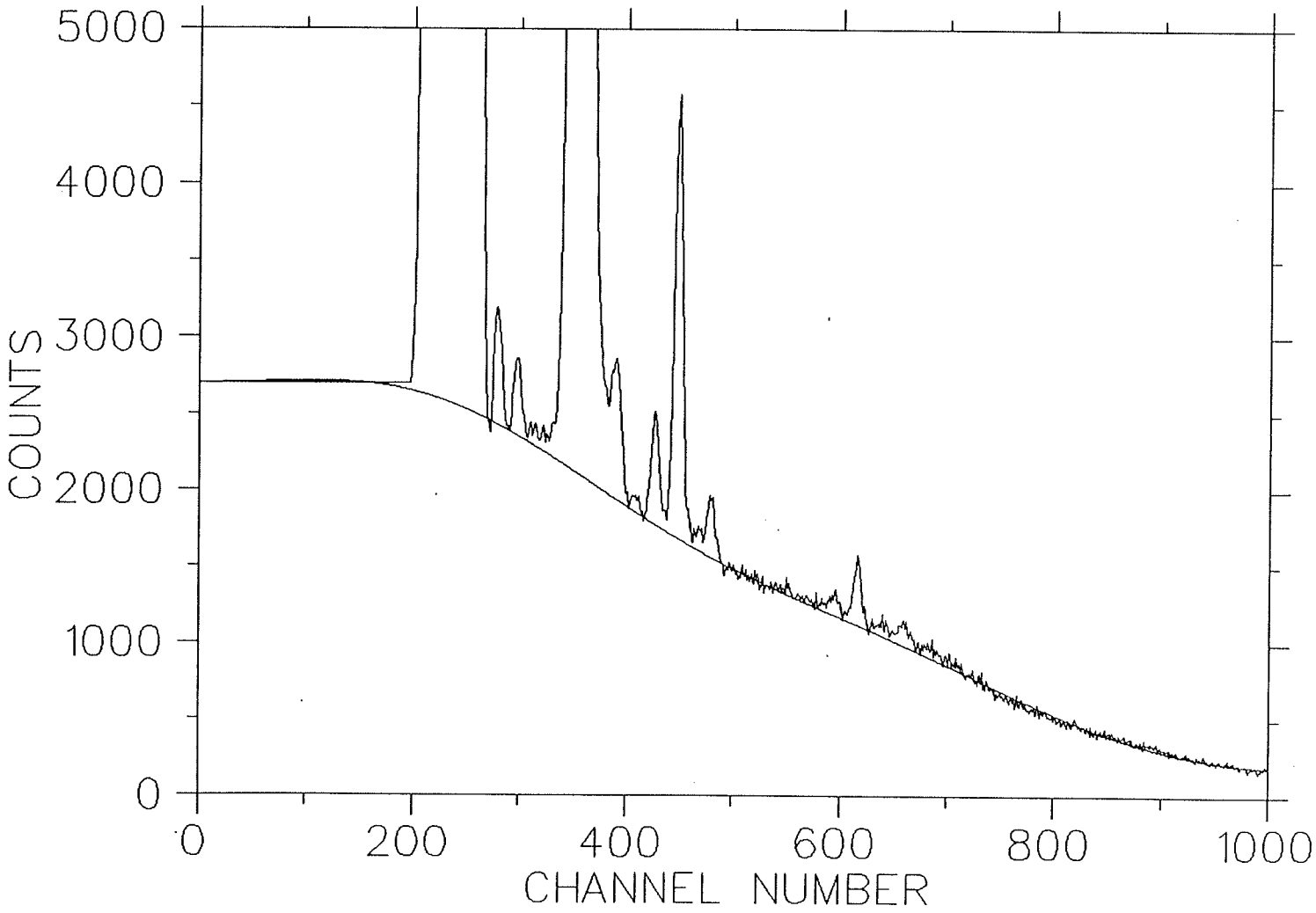

Fig. 5.1 Background function fitted to the preconditioned X-ray spectrum of the leaf sample.

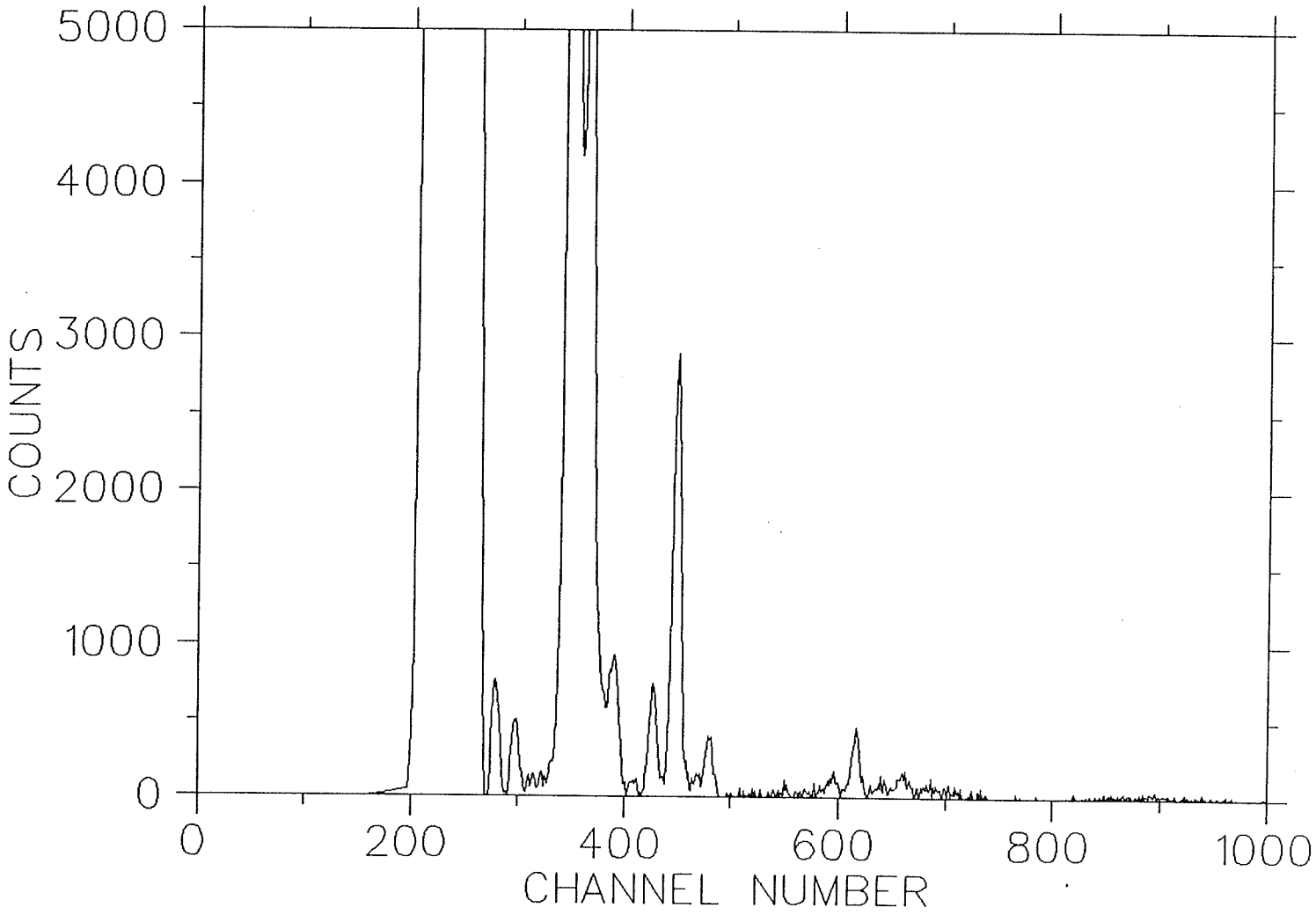

Fig. 5.2 Background-free spectrum of the leaf sample (data is not smoothed).

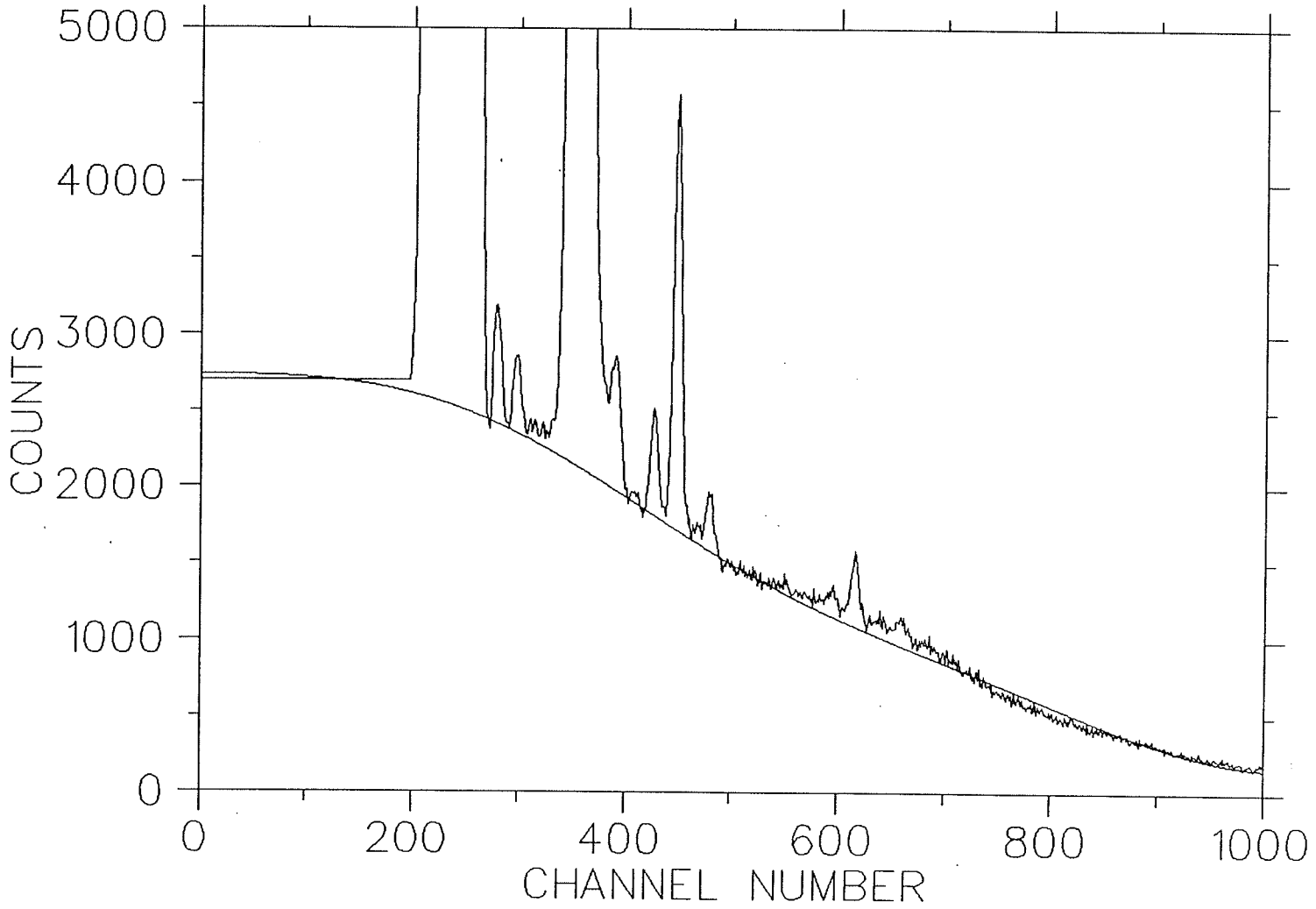

Fig. 5.3 Background function fitted to the preconditioned X-ray spectrum of the leaf sample. Note the oscillations appearing in the fit when $f'_6 = 0.0$.

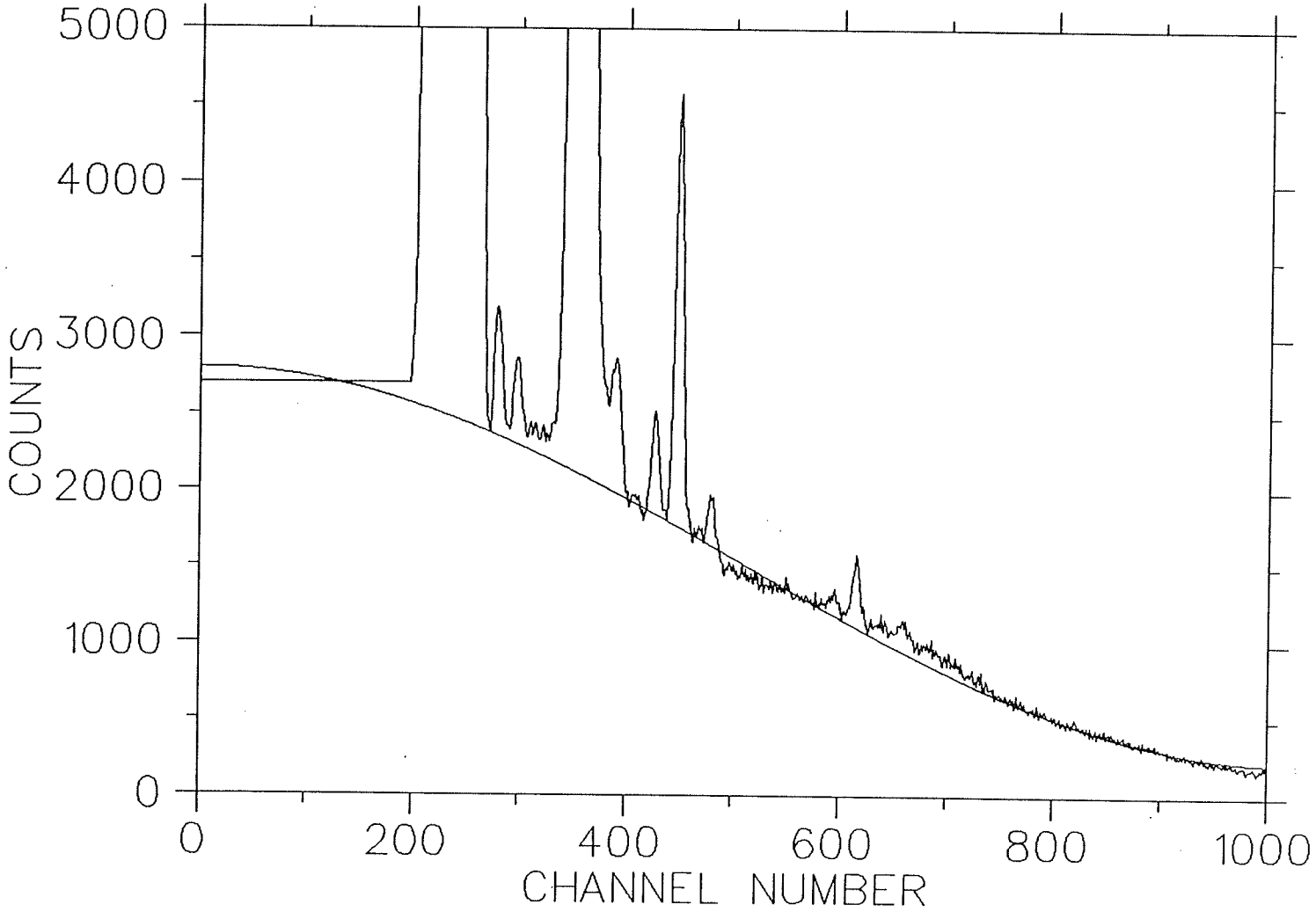

Fig. 5.4 Background function fitted to the preconditioned X-ray spectrum of the leaf sample. Note the oscillations appearing in the fit when $f'_5 = f'_6 = 0.0$.

5.2. Smoothing Operations

The background-free spectrum of Fig. 5.2 represents $s(E)$ in channel number domain the Fourier transform of which is $S(\nu)$. Fig. 5.5 shows the smoothed spectrum $t(E)$ of $s(E)$ of Fig. 5.2. The smoothing function $W_N(\nu)$ was constructed based on equation 4.18 and was applied to the background subtracted data according to equation 4.13. The free parameters of the filter function were assigned the values as discussed in section 4.2. Figures 5.6 and 5.7 illustrate the background-free/smoothed spectrum of the leaf sample in different scales for the purpose of further clarification of the results.

Figures 5.8 and 5.9 exemplify the results obtained by the application of improper smoothing functions. In Fig. 5.8 no smooth Gaussian was fitted to the tail of the filter and consequently some oscillations have appeared in the inverse Fourier transform. Figure 5.9 does not provide sufficient smoothing because the cutoff frequency was assigned an arbitrary high value of $\nu_c = 850$ instead of 350 discussed before.

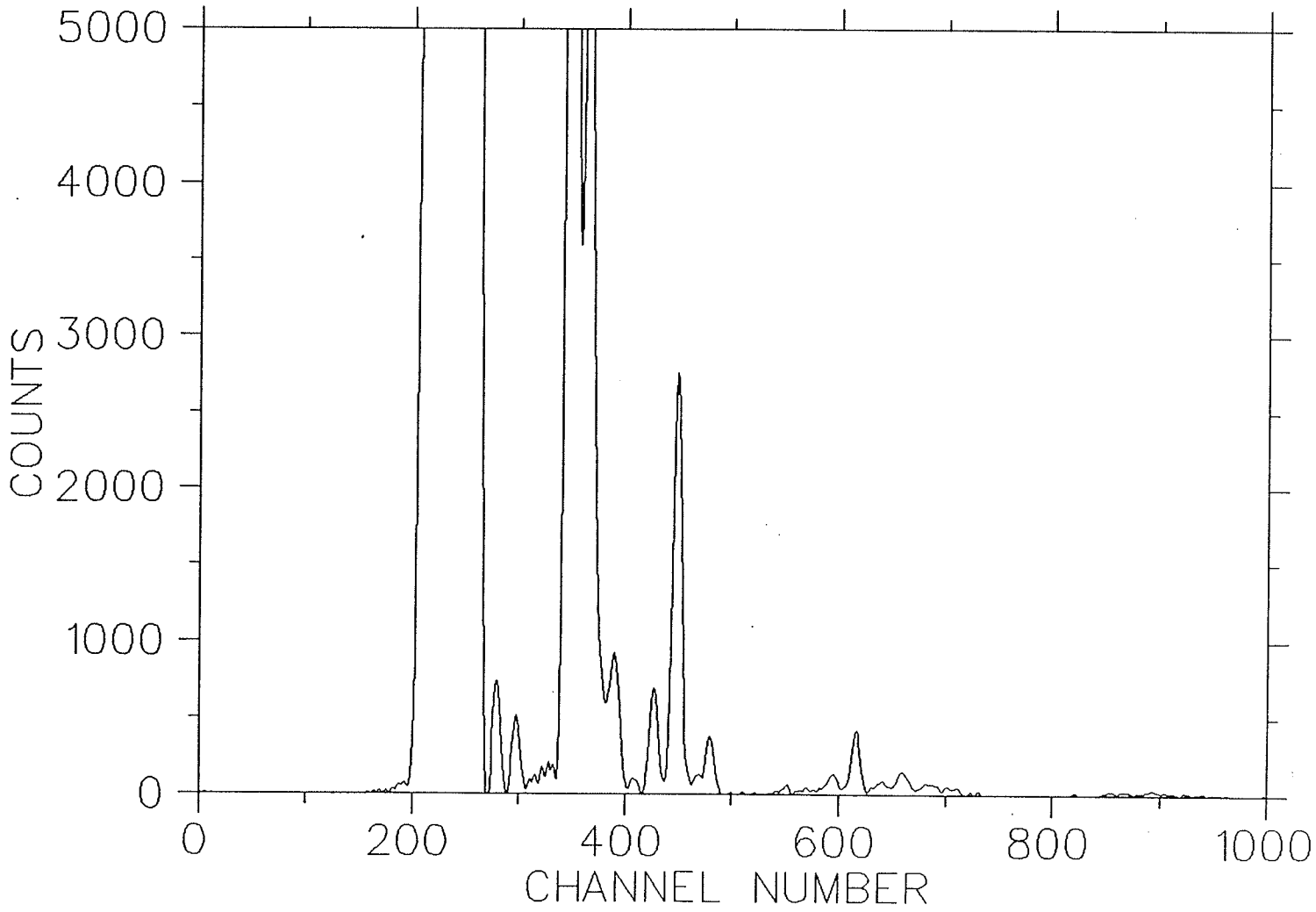

Fig. 5.5 Background-free and smoothed spectrum of the leaf sample.

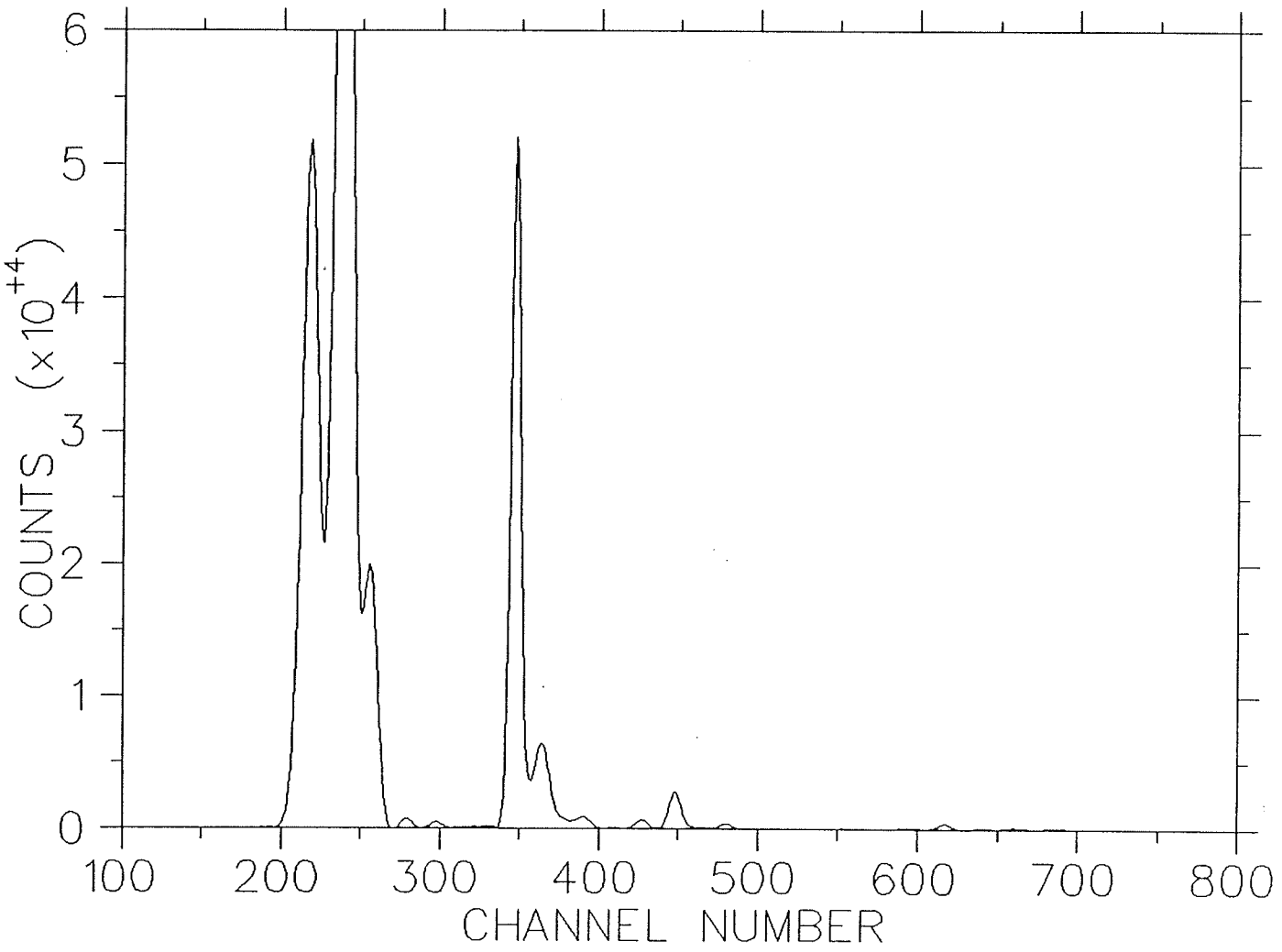

Fig. 5.6 Background-free and smoothed spectrum of the leaf sample.

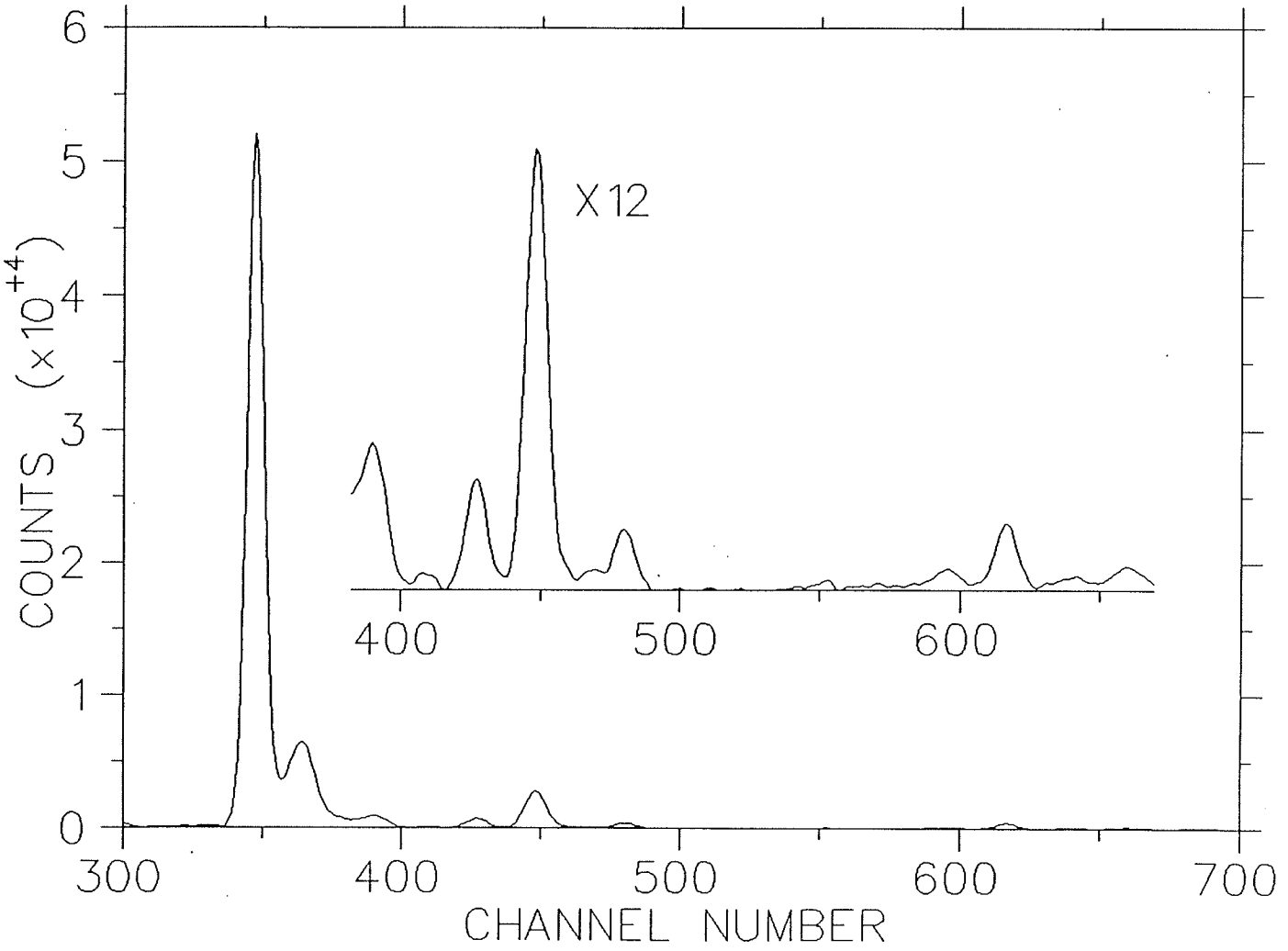

Fig. 5.7 Background-free and smoothed spectrum of the leaf sample.

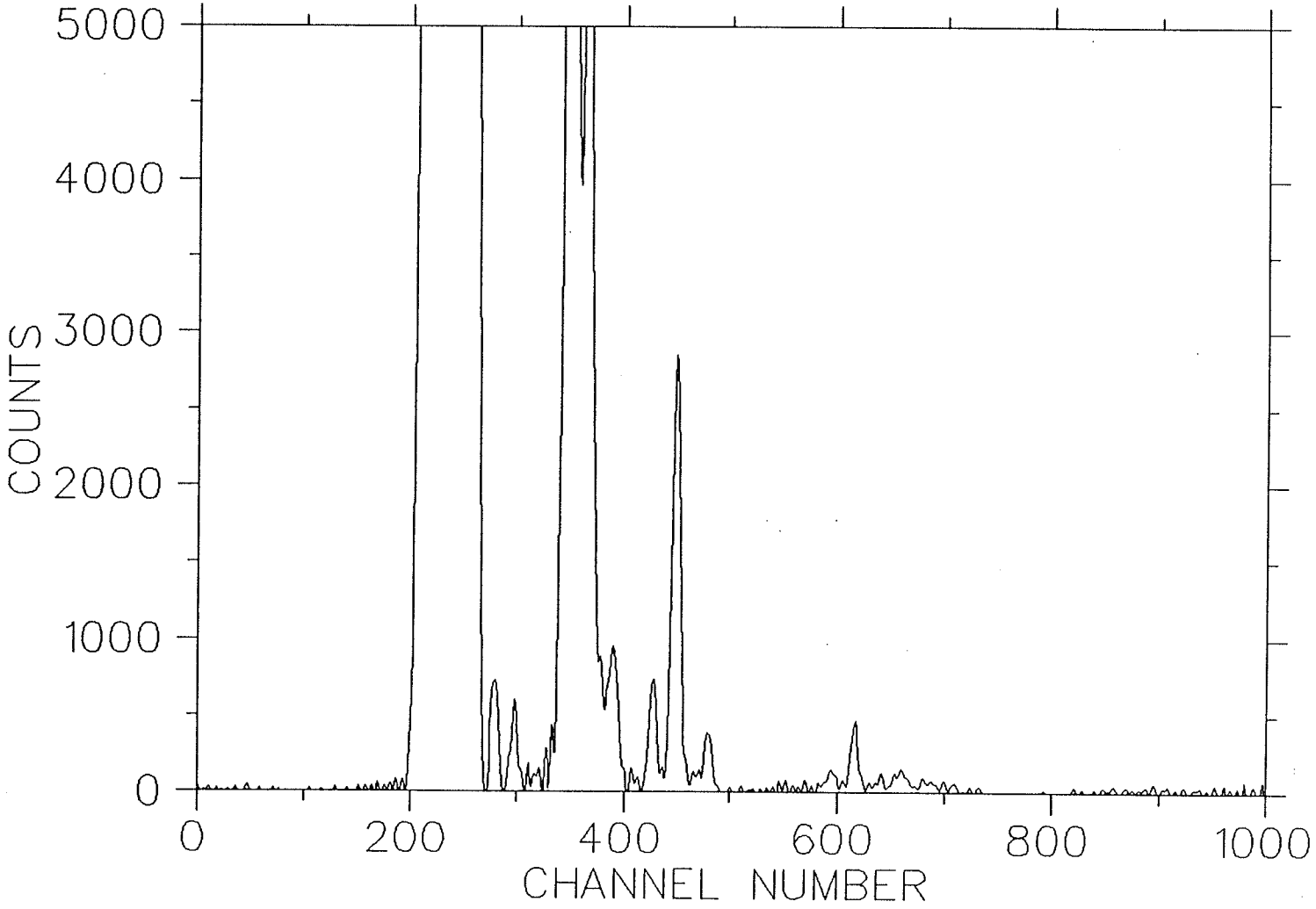

Fig. 5.8 Background-free and smoothed spectrum of the leaf sample. Note that smoothing is not satisfactory and there are oscillations introduced to the spectrum.

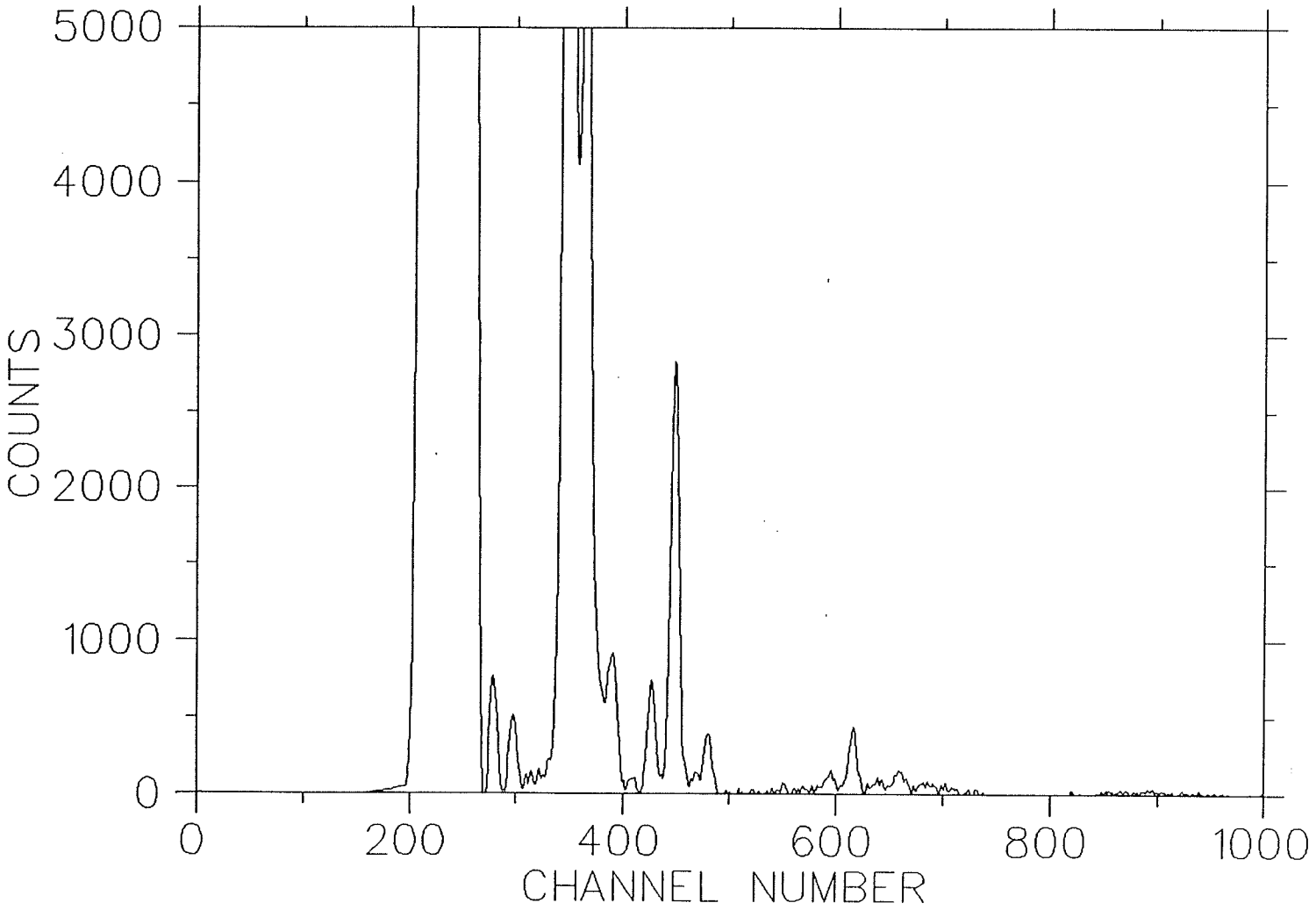

Fig. 5.9 Background-free and smoothed spectrum of the leaf sample. Note that smoothing is not satisfactory because of assigning an improper value to the cutoff frequency.

5.3. Simultaneous Removal of Disinformative Parts

According to equation 5.2, the application of the filter function $W(\nu)$ of Fig. 4.13 to the measured data should simultaneously subtract background and remove noise in one step. Figure 5.10 depicts the corresponding result which is equivalent and similar to the result of Fig. 5.5 obtained by the application of the filter functions $W_B(\nu)$ and $W_N(\nu)$ in two distinct operations.

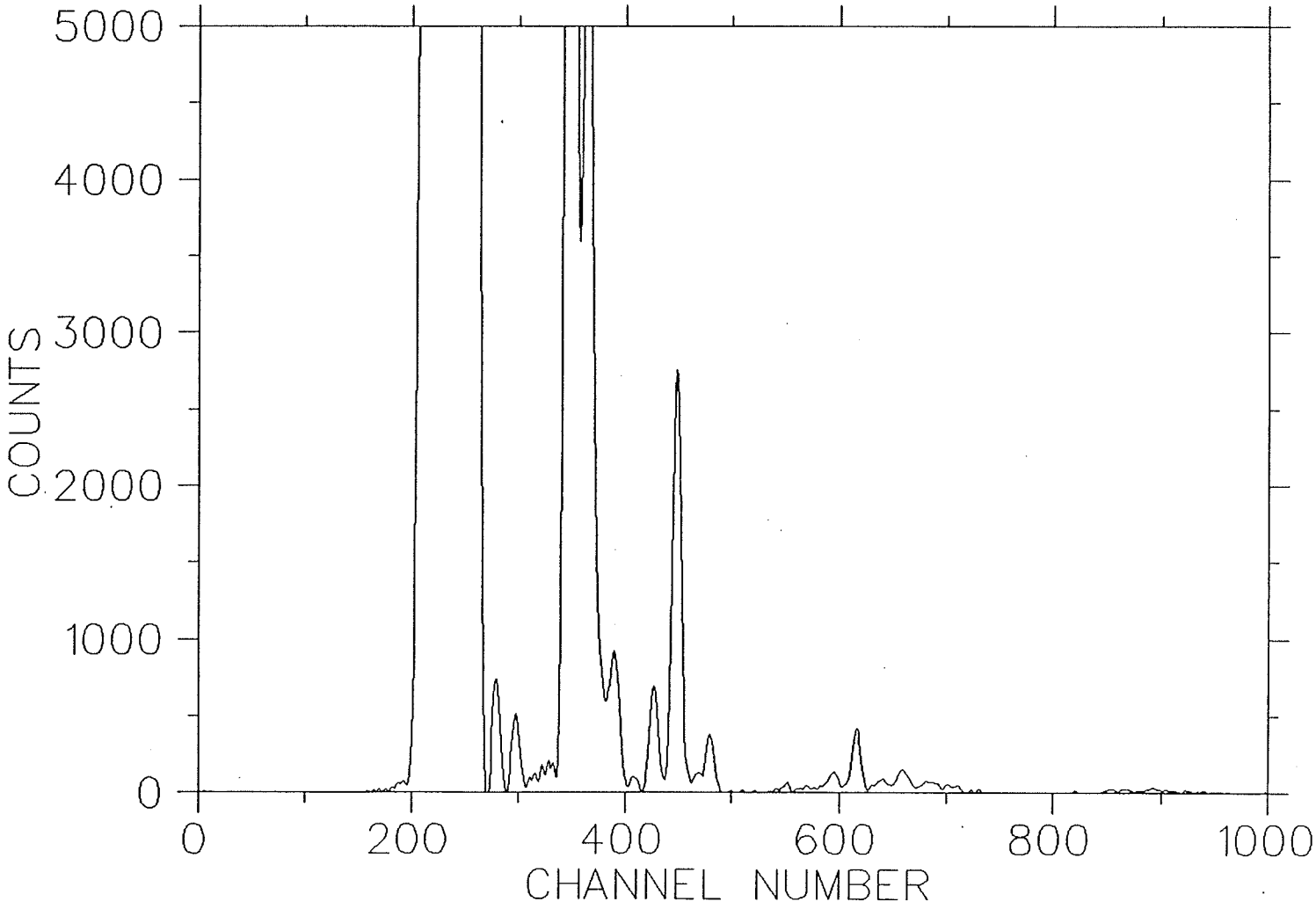

Fig. 5.10 Background and noise removed simultaneouly by $W(\nu) = W_B(\nu) \cdot W_N(\nu)$.

5.4. Peak Extraction Technique

In the usual linear least-squares procedure, the sum of a number of functions is fitted to the specimen data to find the contribution from each peak. Each function must exactly model the peak, or series of peaks (for example, $K_\alpha$and K_β peaks for a given chemical element) it is meant to represent, and the procedure is only applicable when the specimen data can be represented by a linear sum of the model functions plus statistical "noise" [Ro, 69; Bo, 87].

In another approach, the specimen spectrum has been convolved with Gaussians of varying widths to bring out peaks and also has been convolved with an offset Gaussian to establish peaks and half-width crossings [Bl, 69; Co, 70; Na, 78].

In the following, discussion is made with regard to the problem of finding peaks, i.e. peak extraction technique, in a background-free/smoothed X-ray spectrum using the filter function designed in chapter 4 employing Fourier transform techniques.

Let y_i represent the count accumulated in channel i of the histogram representing the X-ray spectrum from the specimen and w_i represent the filter function, after filtering,

$$y_i' = (w * y)_i = \sum_k w(k)\, y(i-k), \tag{5.3}$$

where k indicates the extent of non-zero values of w_i. Each count y_i is distributed statistically according to Poisson distribution and for practical purposes the variance can be approximated by y_i. Since y_i' is a linear sum of independent random variables, the variance is

$$\sigma_i'^2 \approx \sum_k [w(k)]^2\, y(i-k). \tag{5.4}$$

Now the data are weighted according to equation 5.3 and if the filtered result, y_i', exceeds some multiple of σ_i' (eqn. 5.4) then it is assumed that a peak is present in the vicinity of channel i [St, 77].

Relating equations 5.3 and 5.4 to the previous notations and equations, it can be seen that y and the filtered quantity y'in equation 5.3 are equivalent to the measured quantity $m(E)$ and the true spectral quantity $t(E)$ respectively discussed before. The quantity $t(E)$ has already been calculated and the related spectrum for the leaf sample is shown in Fig. 5.5. The quantity σ'^2 is in fact the convolution of the "square" of the

filter function with the measured data. The filter function used to calculate σ^2 in equation 5.4 is $W_B(\nu)$ which was used to subtract background. It will be shown that the application of $W_B(\nu)$ in this calculation provides satisfactory results and that it is not necessary to use the whole filter function, i.e. $W(\nu) = W_B(\nu) \times W_N(\nu)$, for this purpose.

Considering the above discussion, equation 5.4 can be written in the following form

$$\sigma^2(E) \approx [w_b(E)]^2 * m(E) = \sum_k m(k)\,[w_b(E-k)]^2. \qquad (5.5)$$

The filter function $W_B(\nu)$, being a real function, was constructed in frequency domain. For the purpose of the convolution operation of eqn. 5.5, the following steps were followed remembering that the symbol "< = >" stands to denote Fourier transform pair:

(i) Calculate the inverse Fourier transform of $W_B(\nu)$,

$$W_B(\nu) <=> w_b(E),$$

where $W_B(\nu)$ was made complex by assigning zero values as its imaginary components in order to get $w_b(E)$ as a real-valued function in conjugate domain.

(ii) Square $w_b(E)$ to obtain $[w_b(E)]^2$.

(iii) Calculate the Fourier transform of $[w_b(E)]^2$,

$$[w_b(E)]^2 <=> W_B'(\nu),$$

where $W_B'(\nu)$ is in complex form.

(iv) Perform the convolution operation of equation 5.5 in frequency domain as

$$\sum(\nu) = [W_B'(\nu)]\, M(\nu).$$

(v) Calculate the inverse of $\sum(\nu)$,

$$\sum(\nu) <=> \sigma^2(E).$$

(vi) Finally, the square root of $\sigma^2(E)$ yields the value $\sigma(E)$ to be compared with the spectral data $t(E)$.

The spectrum of Fig. 5.11 represents the quantity $\sigma(E)$ for the leaf sample. Having calculated the spectral quantity $t(E)$ (Fig. 5.5) and the quantity $\sigma(E)$, it seems the only free parameter necessary to extract peaks is the lower limit of the ratio $\frac{t(E)}{\sigma(E)}$,

which should be assigned a proper value to identify the proper peaks.

Table 5.1 shows the background-free and smoothed data of the leaf specimen $t(E)$, (filtered data); the quantity $\sigma(E)$, and their ratio (Ratio $(E) = \frac{t(E)}{\sigma(E)}$) with the corresponding channel numbers with the condition that "Ratio > 1.5". If the lower limit of 1.5 assigned to the quantity "Ratio" happens to be an optimized value, then the maxima of this "Ratio function" would yield the maxima of the legitimate peaks in the spectrum. The maxima, *PMAX*, and the minima, *PMIN*, of the "Ratio function" are calculated and shown in table 5.2 where 22 peaks have been detected. These peaks are depicted in the spectrum of Fig. 5.12a and 5.12b. Obviously, assigning lower values to the lower limit of Ratio $(E) = \frac{t(E)}{\sigma(E)}$ will erroneously introduce statistical fluctuations as peaks and on the other hand, assigning higher values might ignore the presence of legitimate small peaks. For the purpose of illustration, tables 5.3 and 5.4 represent similar results as of table 5.2 when Ratio > 1.0 and Ratio > 2.0 respectively. The peaks corresponding to tables 5.3 and 5.4 are shown in the spectra of Figs. 5.13 and 5.14 respectively. From a comparison of the results it is noticed that by having Ratio > 1.0 seven more peaks and by having Ratio > 2.0 four less peaks are extracted. The additional peaks introduced when having Ratio > 1.0 are simply statistical fluctuations. This was verified by considering the resolution of the detector as discussed in chapter 2 and the X-ray energy dispersion in the regions where these fluctuations appear. On the other hand, by increasing the optimized value of Ratio > 1.0 to Ratio > 2.0, four peaks in the spectrum have disappeared. However, the validity of the peaks of Fig. 5.12 will be verified in the next section when the detection limit of the system is taken into consideration.

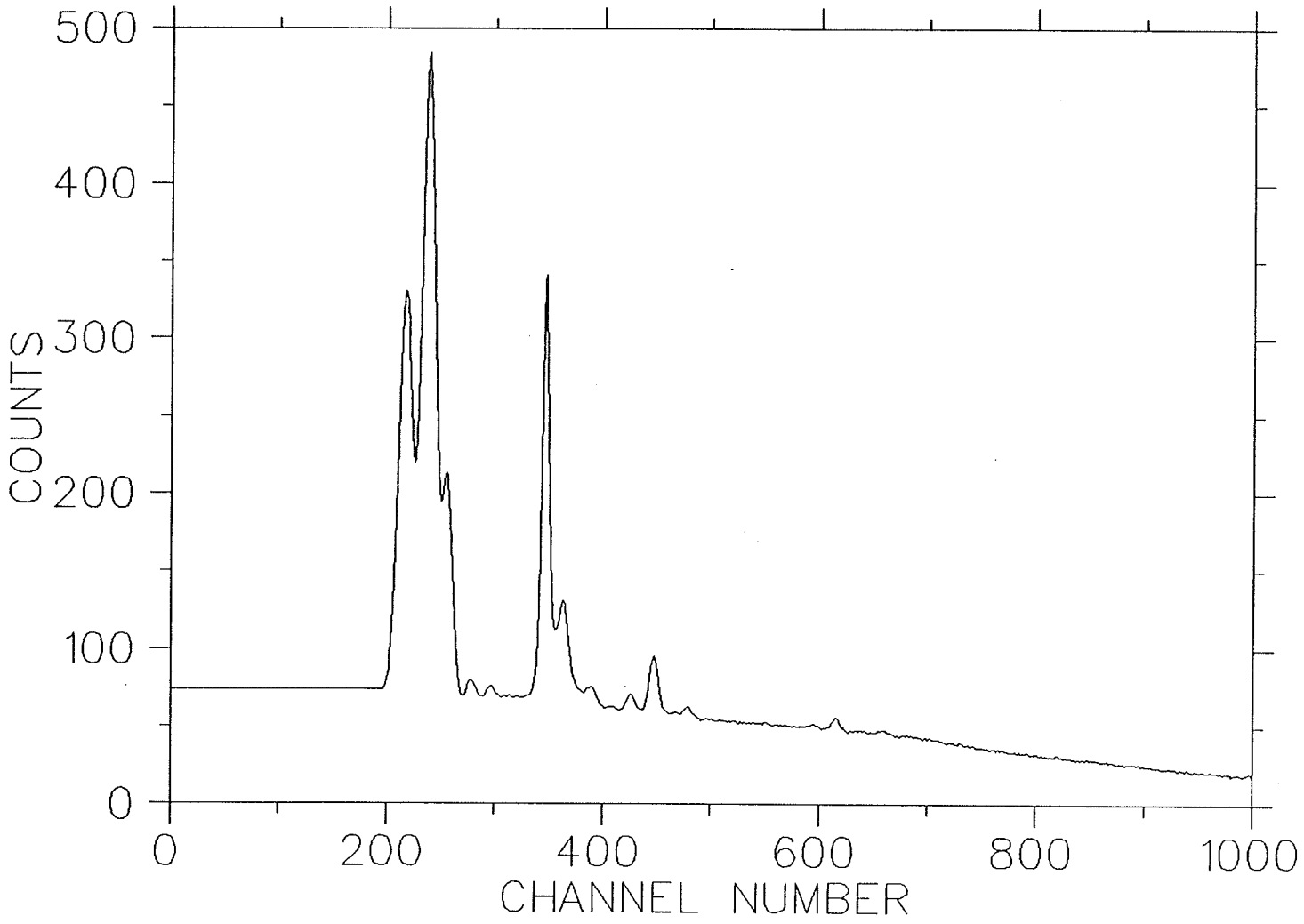

Fig. 5.11 Spectrum of $\sigma(E)$ as defined by equation 5.5.

Table 5.1 Background-free and smoothed data of the leaf specimen (filtered data), $\sigma(E)$ and their ratio when "RATIO > 1.5" with the corresponding channel numbers.

CHANNEL NUMBER	FILTERED DATA	SIGMA	RATIO
198	123.00	75.32	1.63
199	220.70	77.49	2.85
200	364.70	80.01	4.56
201	577.30	83.64	6.90
202	899.50	88.64	10.15
203	1386.40	95.50	14.52
204	2104.20	103.88	20.26
205	3136.90	115.00	27.28
206	4596.50	128.18	35.86
207	6620.40	145.02	45.65
208	9347.40	164.64	56.77
209	12877.50	186.25	69.14
210	17232.90	209.63	82.21
211	22335.10	233.58	95.62
212	27997.40	257.48	108.74
213	33923.10	279.87	121.21
214	39709.30	299.25	132.69
215	44867.00	314.87	142.49
216	48879.50	325.23	150.29
217	51298.10	330.77	155.08
218	51848.00	329.60	157.31
219	50499.00	321.91	156.87
220	47469.90	310.02	153.12
221	43172.90	294.01	146.84
222	38132.70	276.07	138.13
223	32922.10	257.40	127.90
224	28123.00	239.59	117.38
225	24301.90	226.52	107.28
226	21974.50	219.48	100.12
227	21560.60	222.64	96.84
228	23344.70	236.12	98.87
229	27463.70	256.54	107.05
230	33918.80	284.08	119.40
231	42583.60	315.47	134.99
232	53180.10	349.27	152.26
233	65221.20	382.97	170.30
234	77954.90	414.82	187.92
235	90362.80	443.38	203.80
236	101248.20	465.88	217.33

237	109408.80	479.75	228.05
238	113848.40	485.01	234.73
239	113967.70	480.04	237.41
240	109683.00	466.38	235.18
241	101446.10	444.42	228.26
242	90165.50	414.36	217.60
243	77048.50	379.55	203.00
244	63401.30	342.01	185.38
245	50428.40	303.71	166.04
246	39075.60	268.31	145.63
247	29942.50	238.81	125.38
248	23270.50	215.41	108.03
249	18989.50	201.63	94.18
250	16795.50	194.86	86.19
251	16234.50	195.44	83.07
252	16777.20	201.10	83.43
253	17879.80	207.25	86.27
254	19036.40	211.80	89.88
255	19825.60	213.52	92.85
256	19951.00	211.98	94.12
257	19269.80	206.40	93.36
258	17800.00	196.77	90.46
259	15697.20	183.40	85.59
260	13204.30	167.96	78.62
261	10588.20	151.74	69.78
262	8082.20	135.58	59.61
263	5852.90	119.31	49.05
264	3993.80	105.17	37.97
265	2536.50	93.99	26.99
266	1466.20	84.30	17.39
267	735.30	77.23	9.52
268	276.00	72.47	3.81
274	189.40	73.85	2.56
275	353.80	75.86	4.66
276	503.00	77.68	6.47
277	620.40	79.14	7.84
278	700.10	79.79	8.77
279	739.30	79.63	9.28
280	732.80	78.86	9.29
281	676.40	77.83	8.69
282	574.80	76.80	7.48
283	446.20	75.03	5.95
284	315.70	72.79	4.34
285	203.30	71.00	2.86
286	115.90	69.92	1.66
292	149.90	71.50	2.10
293	227.30	72.53	3.13
294	300.20	73.46	4.09
295	370.20	74.45	4.97
296	437.80	75.28	5.82
297	492.20	75.56	6.51

298	512.70	75.57	6.78
299	484.80	75.16	6.45
300	414.30	73.83	5.61
301	325.70	72.16	4.51
302	245.20	71.03	3.45
303	182.90	70.60	2.59
304	132.30	69.89	1.89
315	121.60	69.58	1.75
316	130.90	69.03	1.90
317	108.60	68.41	1.59
321	153.60	69.40	2.21
322	181.50	69.30	2.62
323	165.60	68.50	2.42
324	128.90	68.38	1.88
325	114.70	68.73	1.67
326	142.60	68.32	2.09
327	188.10	68.32	2.75
328	209.00	68.86	3.04
329	189.80	69.32	2.74
330	158.80	69.68	2.28
331	154.90	69.84	2.22
332	180.70	69.78	2.59
333	195.90	69.86	2.80
334	164.50	70.79	2.32
337	215.40	79.39	2.71
338	519.20	84.28	6.16
339	1150.20	92.26	12.47
340	2507.90	106.93	23.45
341	5331.90	129.91	41.04
342	10486.50	164.70	63.67
343	18429.00	212.38	86.78
344	28621.50	263.10	108.79
345	39305.30	308.02	127.61
346	47923.80	337.18	142.13
347	52094.60	340.92	152.81
348	50647.00	322.06	157.26
349	44145.70	287.24	153.69
350	34600.90	241.53	143.26
351	24548.70	197.07	124.57
352	16032.60	162.58	98.62
353	10013.50	137.36	72.90
354	6407.80	122.14	52.46
355	4561.90	115.09	39.64
356	3777.10	112.52	33.57
357	3593.20	112.30	32.00
358	3786.70	113.33	33.41
359	4234.40	115.91	36.53
360	4812.50	120.02	40.10
361	5392.30	124.51	43.31
362	5879.80	128.61	45.72
363	6226.30	130.71	47.64

364	6399.60	130.45	49.06
365	6355.80	128.60	49.42
366	6052.90	125.00	48.42
367	5493.30	119.64	45.92
368	4750.10	112.58	42.19
369	3943.60	104.89	37.60
370	3185.80	97.89	32.54
371	2537.60	91.32	27.79
372	2009.10	85.83	23.41
373	1590.20	82.45	19.29
374	1275.70	80.33	15.88
375	1063.40	78.44	13.56
376	936.30	76.55	12.23
377	857.50	74.92	11.45
378	787.90	73.81	10.67
379	711.10	73.28	9.70
380	639.90	73.05	8.76
381	597.20	72.23	8.27
382	592.00	71.61	8.27
383	611.80	71.53	8.55
384	638.60	71.67	8.91
385	667.60	72.93	9.15
386	709.20	74.24	9.55
387	771.70	74.51	10.36
388	845.00	74.66	11.32
389	902.30	75.24	11.99
390	919.30	75.59	12.16
391	891.70	75.17	11.86
392	833.30	74.25	11.22
393	759.10	72.86	10.42
394	671.20	70.88	9.47
395	562.40	69.06	8.14
396	432.90	67.69	6.40
397	300.30	65.82	4.56
398	191.60	63.70	3.01
399	123.30	62.89	1.96
407	101.00	62.51	1.62
408	104.20	62.57	1.67
409	96.00	62.40	1.54
420	118.90	62.49	1.90
421	172.50	63.32	2.72
422	253.70	64.48	3.93
423	363.20	66.38	5.47
424	484.30	67.91	7.13
425	591.40	69.36	8.53
426	664.40	70.66	9.40
427	694.80	70.71	9.83
428	682.30	70.01	9.75
429	629.10	68.51	9.18
430	539.40	66.69	8.09
431	425.00	64.88	6.55

432	307.50	63.31	4.86
433	210.40	61.92	3.40
434	147.00	61.06	2.41
435	113.30	61.13	1.85
436	94.40	61.03	1.55
439	114.00	61.22	1.86
440	210.10	63.33	3.32
441	387.50	66.22	5.85
442	653.20	70.12	9.32
443	1002.60	75.10	13.35
444	1418.10	81.36	17.43
445	1863.70	87.18	21.38
446	2281.50	91.42	24.96
447	2600.70	93.93	27.69
448	2757.90	95.19	28.97
449	2721.80	93.38	29.15
450	2503.70	89.45	27.99
451	2151.00	85.19	25.25
452	1728.30	79.19	21.82
453	1298.20	73.16	17.75
454	911.60	68.38	13.33
455	603.00	64.69	9.32
456	388.40	62.53	6.21
457	262.00	61.52	4.26
458	198.60	61.24	3.24
459	164.80	60.30	2.73
460	134.60	59.52	2.26
461	100.90	58.83	1.72
465	92.90	58.40	1.59
466	110.80	58.50	1.89
467	120.10	59.11	2.03
468	123.30	59.19	2.08
469	125.00	58.90	2.12
470	125.20	58.99	2.12
471	120.70	58.36	2.07
472	111.80	57.81	1.93
473	107.40	58.21	1.85
474	121.10	58.54	2.07
475	160.60	59.39	2.70
476	220.70	60.48	3.65
477	285.20	61.22	4.66
478	337.70	62.10	5.44
479	369.00	62.43	5.91
480	378.20	62.25	6.08
481	366.90	62.37	5.88
482	335.40	61.34	5.47
483	284.60	59.20	4.81
484	221.30	58.16	3.81
485	158.50	58.08	2.73
486	108.90	57.45	1.90
590	78.20	50.93	1.54

591	88.10	50.88	1.73
592	101.90	50.96	2.00
593	118.00	51.10	2.31
594	130.90	51.12	2.56
595	135.50	51.86	2.61
596	131.30	51.50	2.55
597	122.00	50.53	2.41
598	111.60	50.40	2.21
599	100.40	50.46	1.99
600	86.30	49.97	1.73
609	86.50	49.68	1.74
610	123.50	50.25	2.46
611	174.90	51.59	3.39
612	233.70	52.93	4.42
613	292.20	53.73	5.44
614	345.70	54.36	6.36
615	389.60	55.51	7.02
616	417.30	55.92	7.46
617	420.00	55.09	7.62
618	392.70	54.33	7.23
619	339.50	53.57	6.34
620	273.90	51.84	5.28
621	211.30	49.85	4.24
622	160.40	49.51	3.24
623	120.20	49.62	2.42
624	84.90	48.32	1.76
637	72.80	47.38	1.54
638	74.80	47.40	1.58
639	78.30	47.98	1.63
640	84.30	47.95	1.76
641	89.70	46.72	1.92
642	89.60	47.31	1.89
643	82.10	47.77	1.72
653	77.50	46.37	1.67
654	89.80	46.91	1.91
655	101.50	47.41	2.14
656	114.00	47.31	2.41
657	128.50	47.14	2.73
658	142.70	47.54	3.00
659	151.90	47.99	3.17
660	152.20	47.44	3.21
661	144.00	47.47	3.03
662	131.30	47.31	2.78
663	119.20	46.08	2.59
664	109.70	45.88	2.39
665	101.30	46.37	2.18
666	90.70	46.04	1.97
667	76.80	45.38	1.69
680	67.50	44.26	1.53
681	72.10	44.51	1.62
682	72.80	44.54	1.63

683	70.50	43.85	1.61
684	67.80	43.71	1.55
686	67.30	44.10	1.53
687	67.20	43.46	1.55

Table 5.2 Maxima (PMAX) and minima (PMIN) of the peaks extracted from table 5.1 when "RATIO > 1.5".

PEAK	CHANNEL NUMBER	PMAX	PMIN
1	218	157.31	
	227		96.84
2	239	237.41	
	251		83.07
3	256	94.12	
	274		2.56
4	280	9.29	
	286		1.66
5	298	6.78	
	315		1.75
6	316	1.90	
	317		1.59
7	322	2.62	
	325		1.67
8	328	3.04	
	331		2.22
9	333	2.80	
	334		2.32
10	348	157.26	
	357		32.00
11	365	49.42	
	382		8.27
12	390	12.16	
	407		1.62
13	408	1.67	
	409		1.54
14	427	9.83	
	436		1.55
15	449	29.15	
	465		1.59
16	470	2.12	
	473		1.85
17	480	6.08	
	590		1.54
18	595	2.61	
	600		1.73
19	617	7.62	
	637		1.54
20	641	1.92	
	653		1.67
21	660	3.21	
	680		1.53
22	682	1.63	
	686		1.53

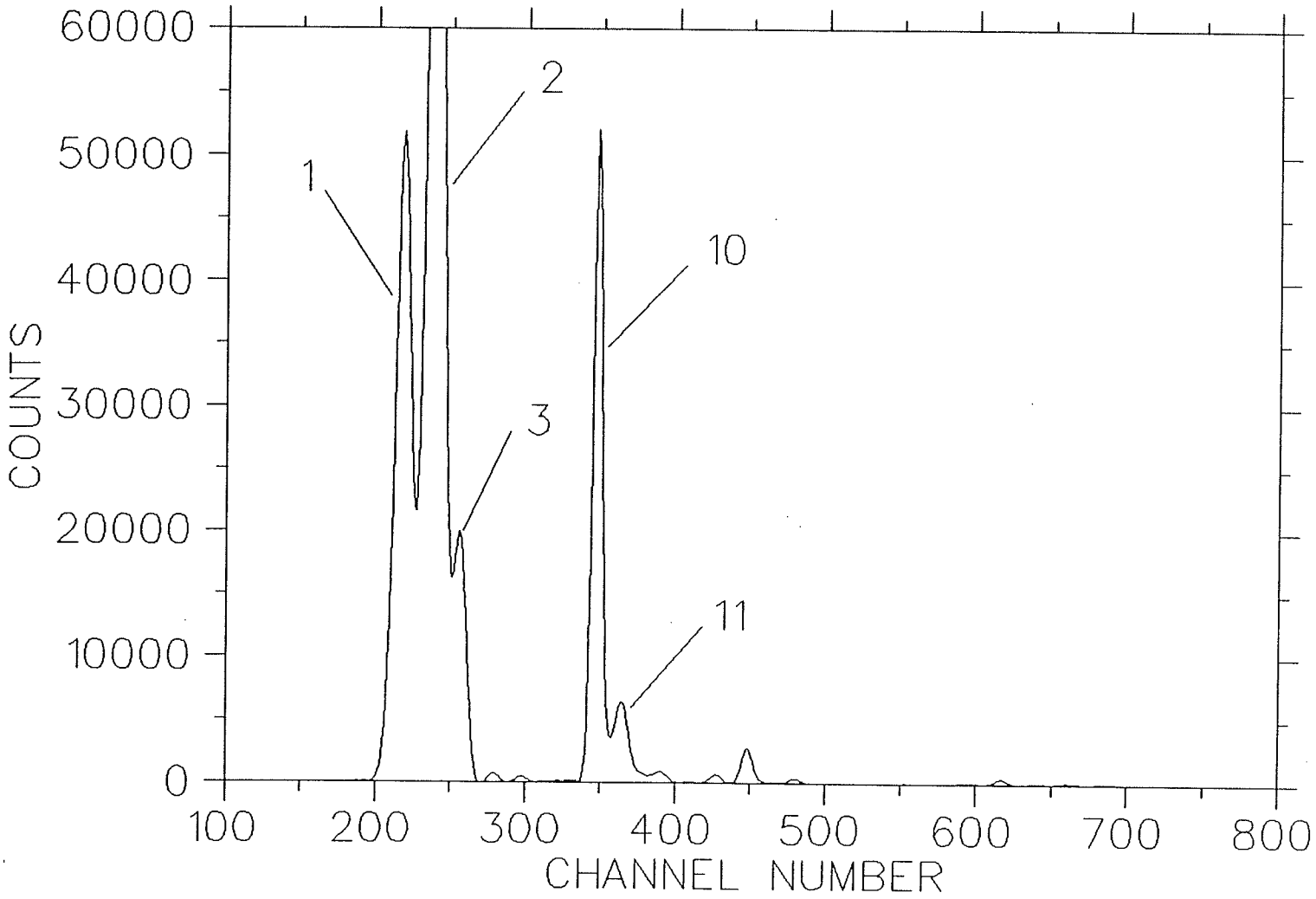

Fig. 5.12a) Peaks extracted from leaf spectrum when "RATIO > 1.5".

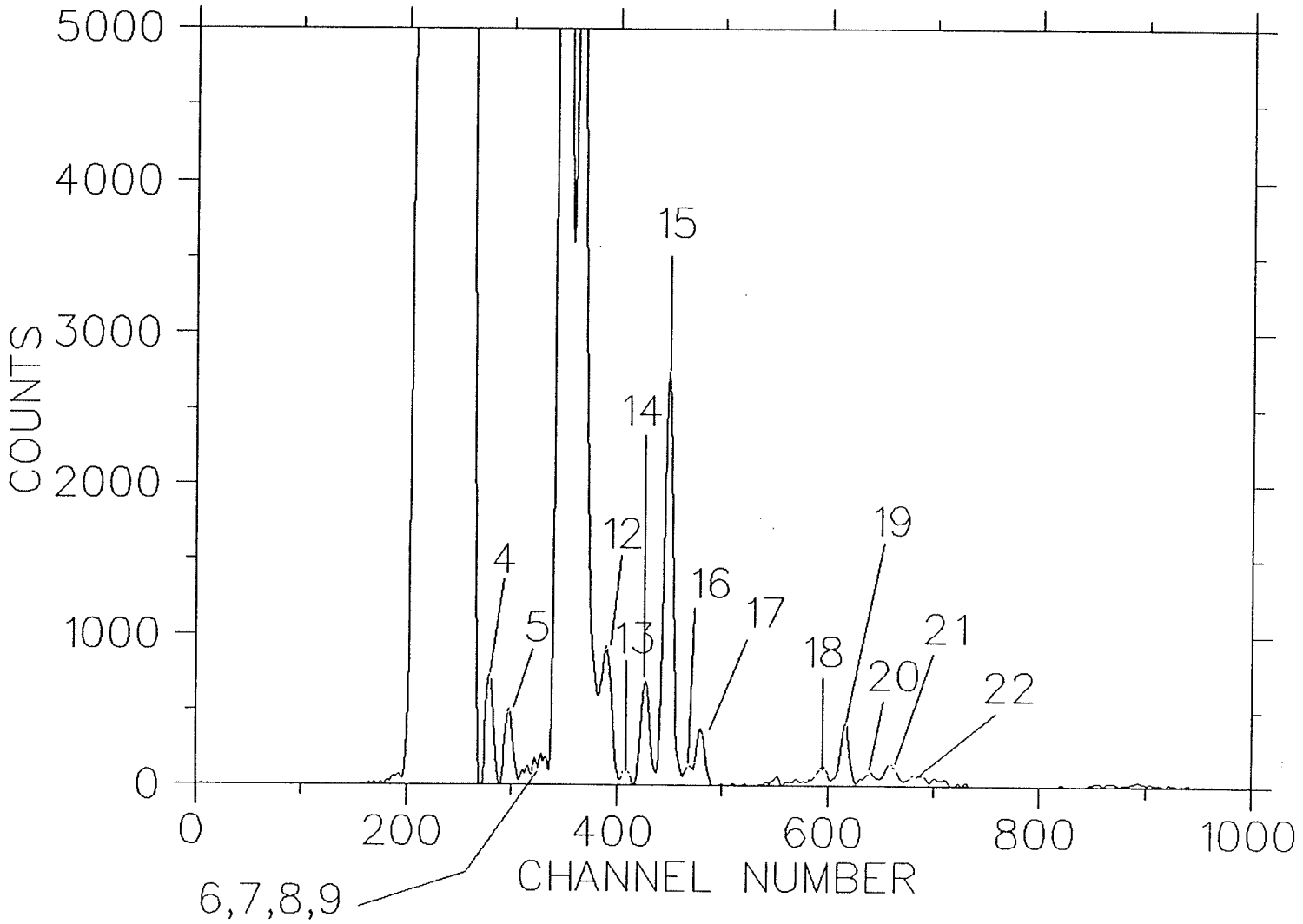

Fig. 5.12b) Peaks extracted from leaf spectrum when "RATIO > 1.5".

Table 5.3 Maxima (PMAX) and minima (PMIN) of the peaks extracted when "RATIO >1.O".

PEAK	CHANNEL NUMBER	PMAX	PMIN
1	218	157.31	
	227		96.84
2	239	237.41	
	251		83.07
3	256	94.12	
	274		2.56
4	280	9.29	
	291		1.08
5	298	6.78	
	309		1.12
6	310	1.44	
	313		1.07
7	316	1.90	
	318		1.11
8	322	2.62	
	325		1.67
9	328	3.04	
	331		2.22
10	333	2.80	
	336		1.30
11	348	157.26	
	357		32.00
12	365	49.42	
	382		8.27
13	390	12.16	
	401		1.14
14	408	1.67	
	413		1.12
15	427	9.83	
	438		1.32
16	449	29.15	
	463		1.08
17	470	2.12	
	473		1.85
18	480	6.08	
	552		1.21
19	553	1.24	
	588		1.19
20	595	2.61	
	606		1.05
21	617	7.62	
	633		1.02
22	641	1.92	
	649		1.05

23	660	3.21	
	677		1.06
24	682	1.63	
	685		1.50
25	687	1.55	
	691		1.37
26	692	1.40	
	699		1.05
27	701	1.32	
	710		1.05
28	711	1.10	
	712		1.04
29	893	1.35	
	897		1.03

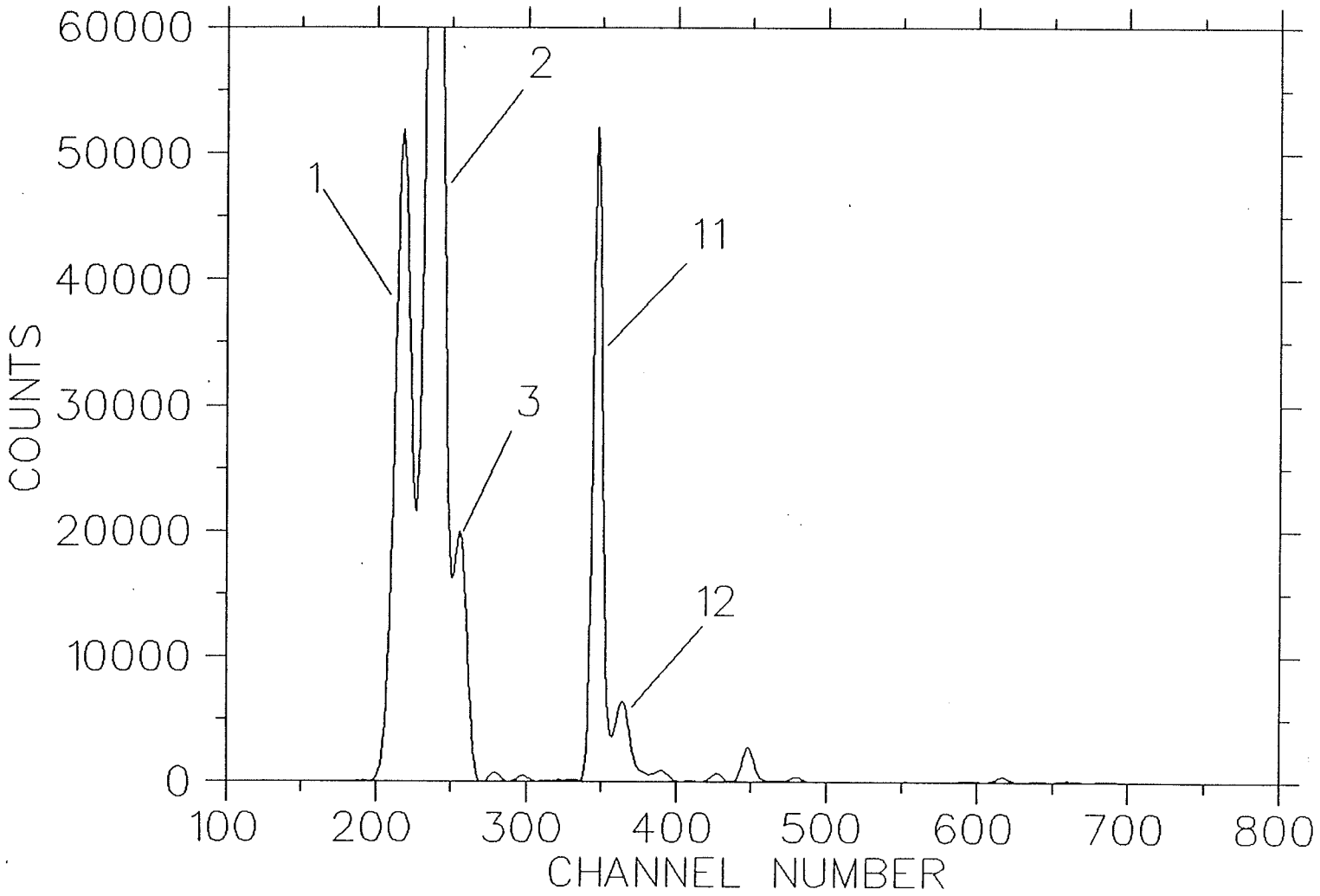

Fig. 5.13a) Peaks extracted from leaf spectrum when "RATIO > 1.0".

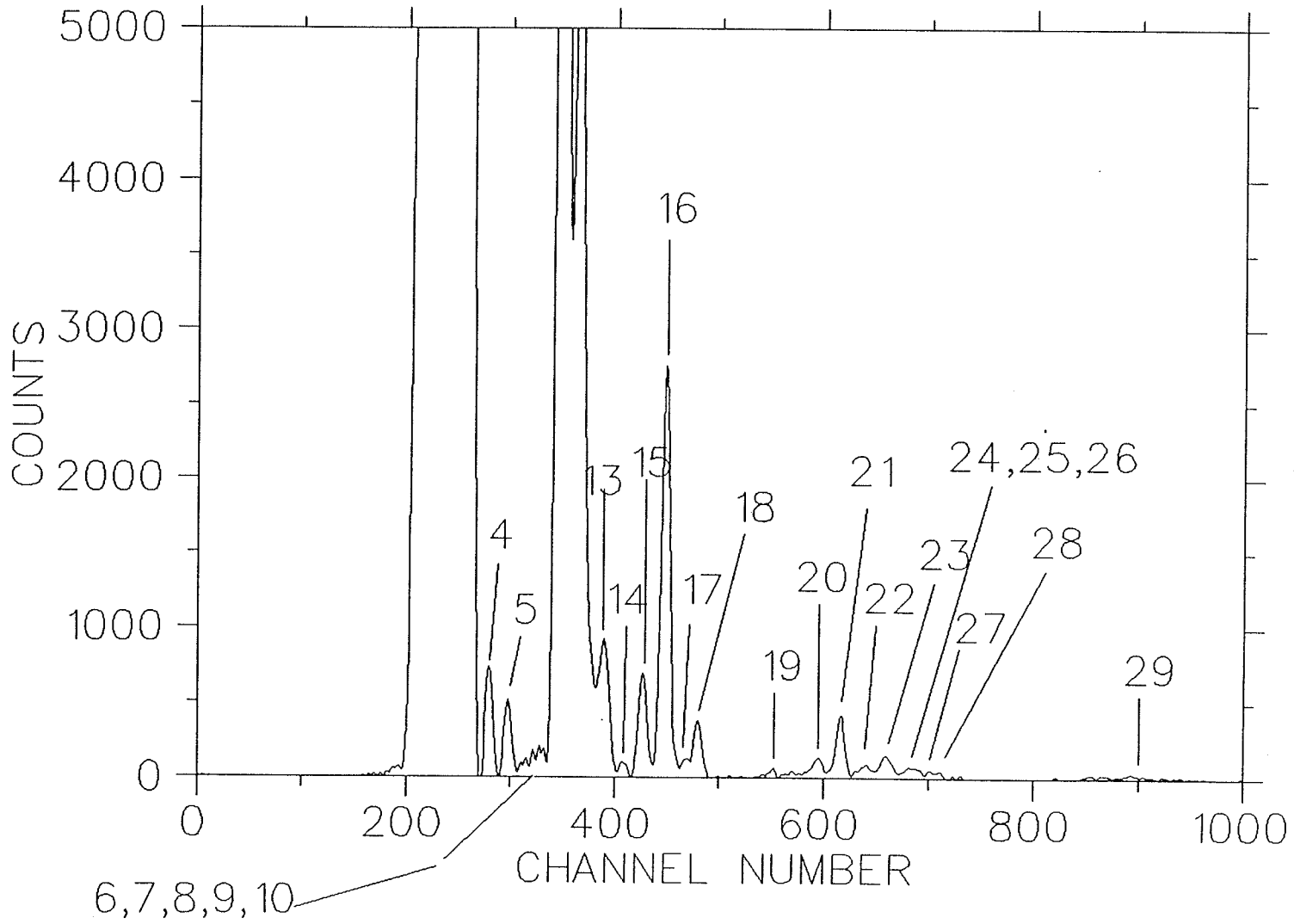

Fig. 5.13b) Peaks extracted from leaf spectrum when "RATIO > 1.0".

Table 5.4 Maxima (PMAX) and minima (PMIN) of the peaks extracted when "RATIO > 2.0".

PEAK	CHANNEL NUMBER	PMAX	PMIN
1	218	157.31	
	227		96.84
2	239	237.41	
	251		83.07
3	256	94.12	
	274		2.56
4	280	9.29	
	292		2.10
5	298	6.78	
	321		2.21
6	322	2.62	
	326		2.09
7	328	3.04	
	331		2.22
8	333	2.80	
	334		2.32
9	348	157.26	
	357		32.00
10	365	49.42	
	382		8.27
11	390	12.16	
	421		2.72
12	427	9.83	
	434		2.41
13	449	29.15	
	467		2.03
14	470	2.12	
	474		2.07
15	480	6.08	
	593		2.31
16	595	2.61	
	598		2.21
17	617	7.62	
	655		2.14
18	660	3.21	
	665		2.18

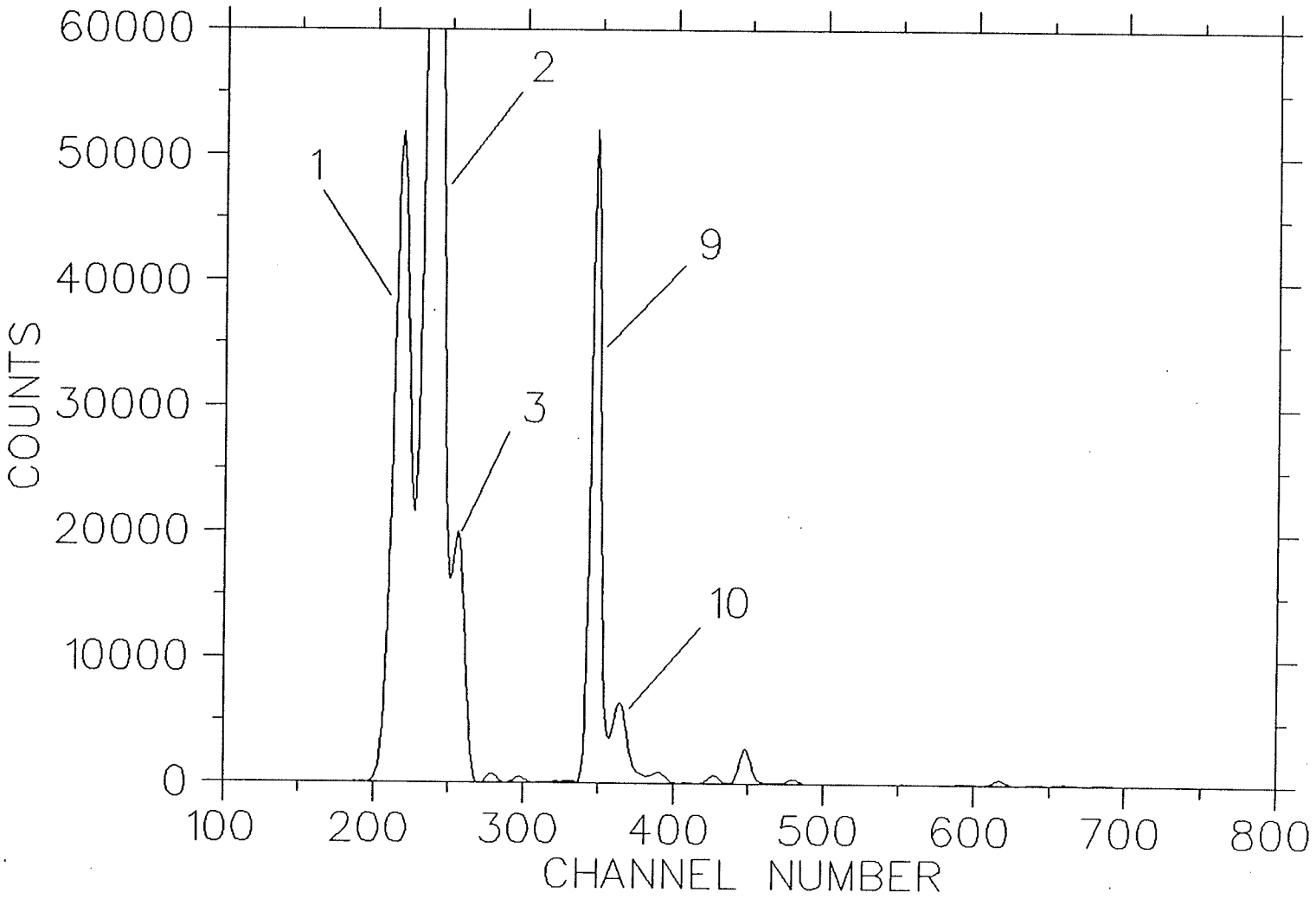

Fig. 5.14a) Peaks extracted from leaf spectrum when "RATIO > 2.0".

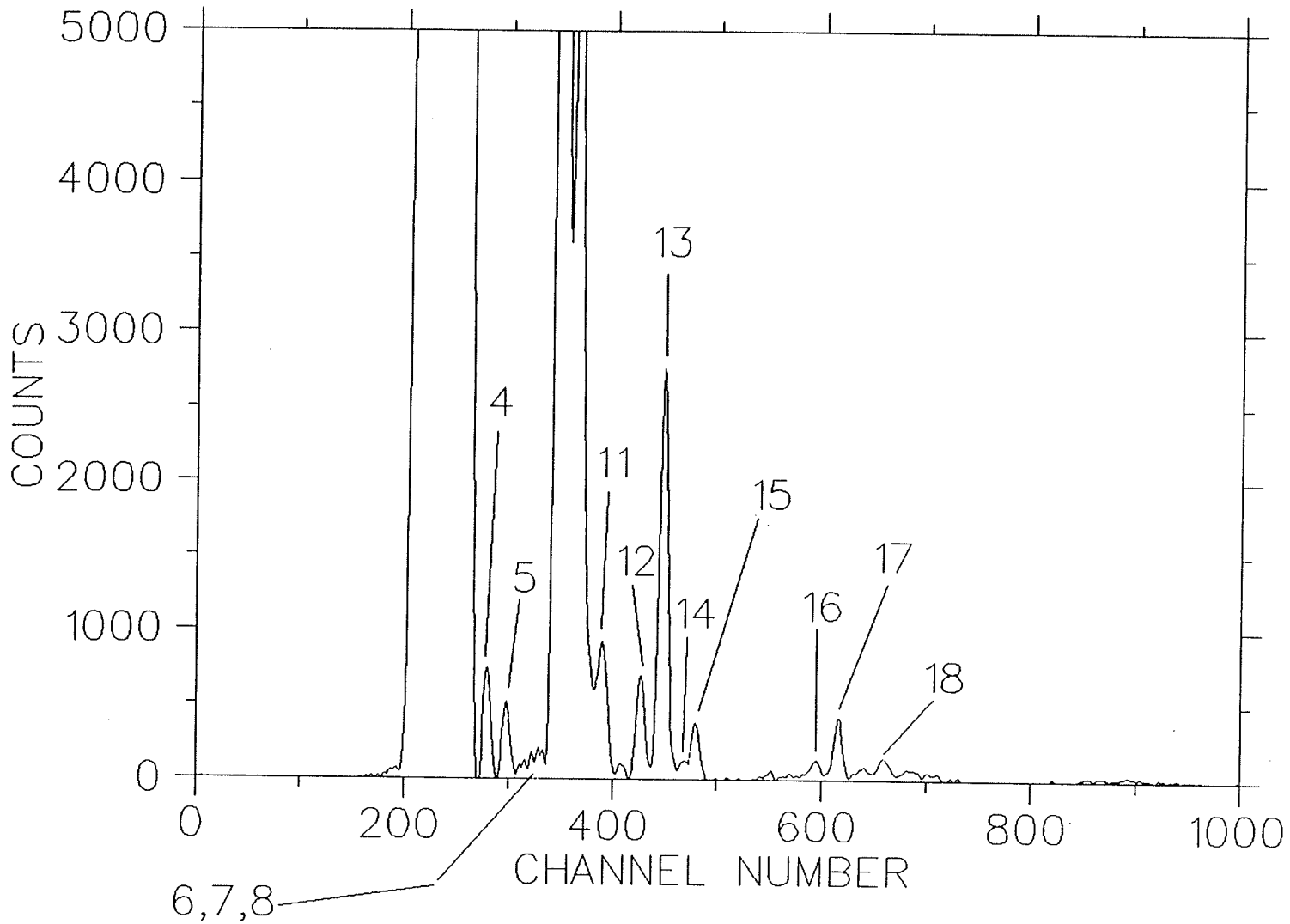

Fig. 5.14b) Peaks extracted from leaf spectrum when "RATIO > 2.0".

5.5. Sensitivity/Detection Limit

There are several ways of defining the sensitivity of an analytical method. In the present context, the problem is to find small amounts of various trace elements in a certain matrix (the so-called matrix is the bulk of the material in the sample with which the trace elements to be determined are always mixed). The most basic definition of the sensitivity is therefore the minimum detectable concentration. Once it is known one can calculate the minimum detectable absolute amounts of various elements knowing the weight of that part of the sample which is irradiated by the particle beam.

If one calculates the number of X-ray pulses registered by a silicon detector in a normal geometry when a small amount of trace element is bombarded with protons in the MeV range one finds that a sufficient number for a convenient registration is obtained even with extremely small amounts of matter, of the order of $10^{-16}\ g$. The trace elements to be measured are, however, always contained in some matrix. As discussed in chapter 2, a background arises inevitably in the interaction of the incident particles with the matrix atoms. This background sets a limit to the sensitivity which can be obtained since, in order for a characteristic X-ray peak to be discerned, it must rise above the background in a statistically significant way. The detection limit is approached when the statistical uncertainty in the "background" is of the same approximate magnitude as the "information" being detected. A positive statement as to the detection of a signal (the statement that a peak is indeed present) requires that the net counts N_s ("total" less "background") is equal to or greater than 2σ or better 3σ of the "no peak", background.

The number of pulses in the peak, N_S, must then satisfy the following relation [Wo, 73; Jo, 76] to yield a confidence level better than 99%

$$N_S \geq 3\sqrt{N_B}, \tag{5.6}$$

where N_B is the number of pulses in the background under the peak in an interval having a width equal to the *FWHM* of the peak for a similar region of channel numbers.

Defining the detection limit by relation 5.6, the value of the detection limit is expressed by [Is, 88]

$$\frac{n_Z}{n_M} = \frac{3}{\left\{ Q\ d\Omega\ n_M\ [\frac{d\sigma_x(Z)}{d\Omega}]\ \varepsilon_f(Z)\ ab(Z) \right\}^{\frac{1}{2}}} \times \left\{ \frac{\Delta E_D\ [\frac{d\sigma_B(Z)}{d(\frac{h\omega}{2\pi})d\Omega}]}{\frac{d\sigma_x(Z)}{d\Omega}} \right\}^{\frac{1}{2}} \tag{5.7}$$

where n_M is the atomic concentration of the matrix element, n_Z is that of a trace element Z, Q is the number of projectiles, $d\Omega$ is the solid angle subtended by a detector, and $\frac{d\sigma_x(Z)}{d\Omega}$, $\varepsilon_f(Z)$, $ab(Z)$, $[\frac{d\sigma_B(Z)}{d(h\frac{\omega}{2\pi})\ d\Omega}]$ are, respectively, the production cross section of K or L X-rays for the trace element, the detector efficiency, absorption of X-rays by windows and others, and the production cross section of the background. The energy resolution of the detector ($FWHM$) is denoted by ΔE_D.

Since the background depends on the composition of the matrix as well as other experimental conditions it is nearly impossible to give a general expression for the sensitivity. The following parameters have an influence on the sensitivity: the solid angle of the detector Ω, detector resolution ΔE, collected charge j, and target thickness t. The sensitivity scales as [Jo, 76]

$$\Delta E_D^{\frac{1}{2}}\ (\Omega\ j\ t)^{\frac{-1}{2}}\ . \tag{5.8}$$

Increasing the target thickness, the solid angle subtended by the detector and the collected charge about one order of magnitude, which should be within the reach of the experimental possibilities, gives according to eqn. 5.8 an improvement in sensitivity by a factor of 30.

At the low energy end of the spectrum there is a cutoff. This is due to the absorption of the X-rays in the windows of the irradiation chamber and the detector. With a standard arrangement, this effect sets a lower limit to the detectable elements. With a standard silicon detector a reasonable sensitivity can be maintained down to sulphur or aluminum.

For the given matrix elements and the experimental conditions and parameters applied to the *PIXE* experiment of the leaf sample, relation 5.6 determines the detection limit. Some information about peaks extracted from the leaf spectrum of Fig. 5.12 are given in table 5.5. In this table the columns 6 and 7 both represent the uncertainties in the background counts under the peaks with the following definitions:
In column 6,

$$\sigma_B(calculated) = \sqrt{\sigma_M^2 + \sigma_S^2} = \sqrt{N_M + N_S}, \tag{5.9}$$

where σ_B is the statistical (calculated) uncertainty in the background, σ_M and σ_S are the uncertainties respectively in the total number of counts N_M and the net counts N_S under a peak, and in column 7,

$$\sigma_B(fitted) = \sqrt{N_B}\ , \tag{5.10}$$

where σ_B is the fitted uncertainty in the background counts N_B under a peak.
Column 8 of table 5.5 represents the ratio of the number of net pulses present in a peak (column 4) to the uncertainty in the fitted background (column 7). Applying the definition expressed by eqn. 5.6 for the minimum detection limit, it is noticed that all the peaks extracted meet the requirement and can be considered as legitimate peaks. Table 5.6 represents the energies and elemental identification of the peaks shown in Fig. 5.12. For the purpose of illustrating the peaks more clearly, Fig. 5.15 shows the peaks of Fig. 5.12 with its y-axis in log scale.

Table 5.5 Peaks extracted from the leaf spectrum. "RATIO" represents the ratio of the number of net pulses in the peak (column 4) to the uncertainty in the fitted background under the peak (column 7).

PEAK	CENTROID	TOTAL COUNTS	NET COUNTS	BACKGROUND COUNTS	SIGMAB (CALC.)	SIGMAB (FIT.)	RATIO
1	217.975	358516	340241	18274	835	135	2520.3
2	238.926	763668	745757	17910	1228	133	5607.2
3	255.911	149579	132021	17557	530	132	1000.2
4	279.800	21597	4617	16979	161	130	35.5
5	297.955	19586	3095	16490	150	128	24.2
6	315.813	7207	365	6841	87	82	4.5
7	322.217	16568	786	15781	131	125	6.3
8	328.500	16655	1059	15595	133	124	8.5
9	333.029	7330	712	6617	89	81	8.8
10	347.658	317391	302429	14961	787	122	2478.9
11	364.854	56060	41649	14410	312	120	347.1
12	390.008	19613	6015	13597	160	116	51.9
13	408.057	5879	298	5580	78	74	4.0
14	427.067	16804	4372	12431	145	111	39.4
15	448.821	28871	17092	11778	214	108	158.3
16	469.741	12068	878	11189	113	105	8.4
17	480.029	13365	2443	10921	125	104	23.5
18	595.074	9133	851	8281	99	91	9.4
19	616.915	10450	2634	7815	114	88	29.9
20	641.041	7912	611	7300	92	85	7.2
21	660.038	7869	984	6884	94	82	12.0
22	681.871	4896	329	4566	72	67	4.9

Table 5.6 Elemental identification of the peaks shown in Fig. 5.12

Peak	Energy(KeV)	Element
1	3.106	$K(K_\alpha)$
2	3.490	$Ca(K_\alpha)+K(K_\beta)$
3	3.816	$Ca(K_\beta)$
4	4.299	$Ti(K_\alpha)$
5	4.684	$V(K_\alpha)$
6	5.080	$Ti(K_\beta)$
7	5.225	$V(K_\beta)$
8	5.370	$Cr(K_\alpha)$
9	5.475	Spurious peak
10	5.823	$Mn(K_\alpha)$
11	6.244	$Fe(K_\alpha)+Mn(K_\beta)$
12	6.887	$Co(K_\alpha)+Fe(K_\beta)$
13	7.368	$Ni(K_\alpha)$
14	7.891	$Cu(K_\alpha)$
15	8.511	$Zn(K_\alpha)$
16	9.130	$Cu(K_\beta)$
17	9.442	$Zn(K_\beta)$
18	13.281	$Rb(K_\alpha)$
19	14.083	$Sr(K_\alpha)$
20	14.996	$Rb(K_\beta)$
21	15.735	$Sr(K_\beta)$
22	16.606	$Nb(K_\alpha)$

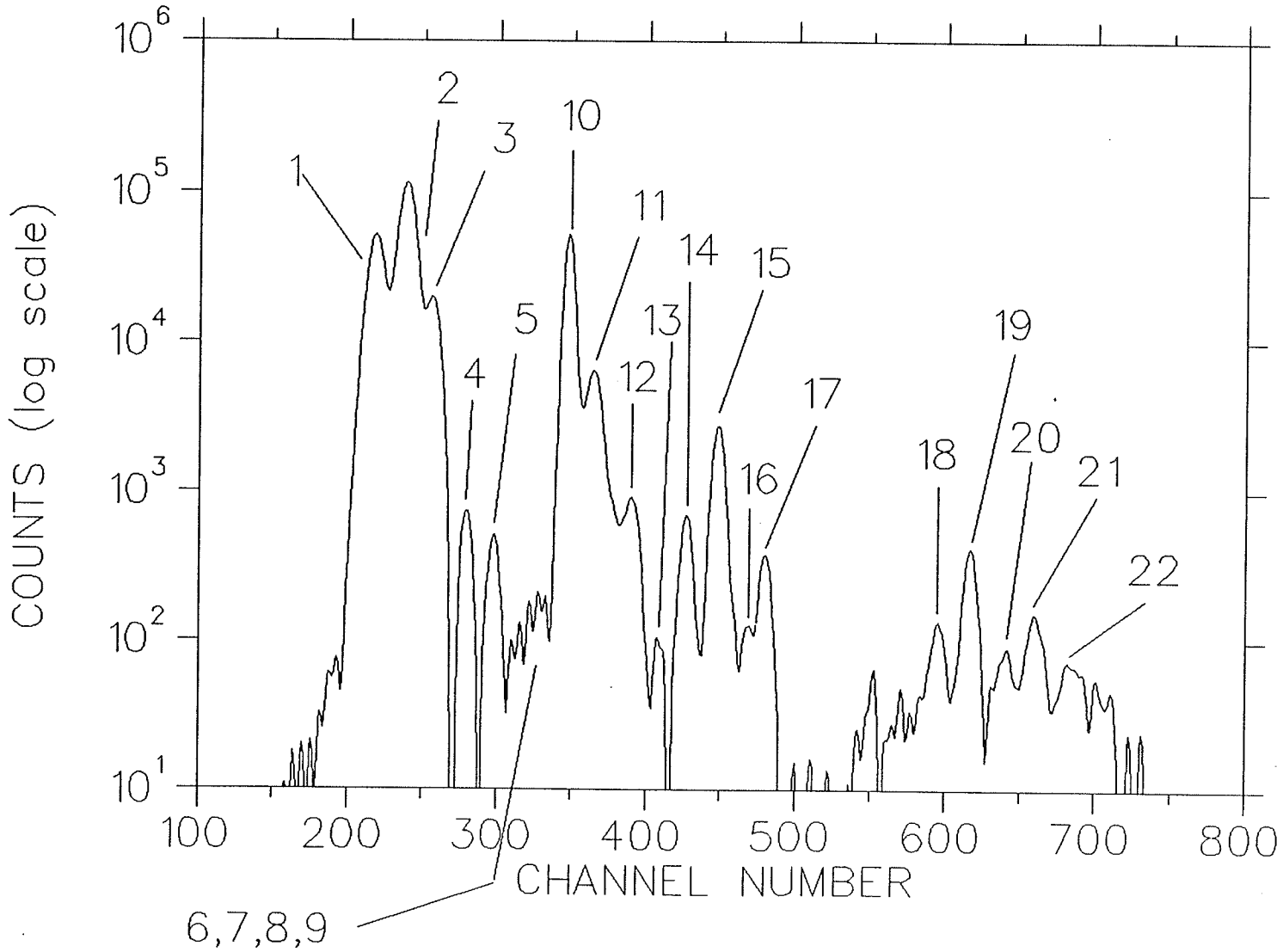

Fig. 5.15 Peaks extracted from the leaf spectrum. Note that the y-axis is in log scale.

5.6. Error Analysis of Background Subtraction

The relation between the measured quantity $m(E)$, the background-free data $s(E)$ and the background component $b(E)$ was expressed as follows

$$m(E) = s(E) + b(E). \tag{5.11}$$

If it is assumed that the application of the filter function $w_b(E)$ is sufficient to zero all background content, then the convolution spectrum reduces to

$$c(E) = w_b(E) * m(E) = \sum_k [s(k) + b(k)]\, w_b(E-k) = \sum_k s(k)\, w_b(E-k), \tag{5.12}$$

where the quantity in equation 5.11 was used for $m(E)$.

The cancellation of the signal background will in fact be subject to statistical fluctuations which mask the convolution. The resulting non-zero expectation value of the convolution background $b'(E)$ can be examined as follows

$$b'(E) = \sum_k b(k)\, w_b(E-k).$$

Therefore, the variance in $b'(E)$ is given by [Ro, 72; Be, 69]

$$\sigma^2_{b'(E)} = \sum_k \left(\frac{\partial b'(E)}{\partial b(k)}\right)^2 \sigma^2_{b(k)} = \sum_k w_b^2\,(E-k)\, b(k)$$

$$\approx \bar{b} \sum_k w_b^2(E-k). \tag{5.13}$$

The uncertainty in the fitted background function can be calculated by relation 5.10. It is expected that this uncertainty should fall drastically as compared with the uncertainty obtained from the square root of eqn. 5.13, i.e. $\sigma'_{b'}$. The two results are illustrated in Fig. 5.16 where $\sigma_b(fit) = \sqrt{N_B}$ is the uncertainty in the subtracted background and $\sigma'_{b'}$ is the uncertainty in the non-zero expectation value of the convolution background $b'(E)$ obtained from eqn. 5.13. The ratio of these two uncertainties, i.e. "$\frac{\sigma_b(fit)}{\sigma'_{b'}}$" is shown in Fig. 5.17. It is noticed that the average error ascribed to the fitted background has dropped approximately by 30% in all channel numbers.

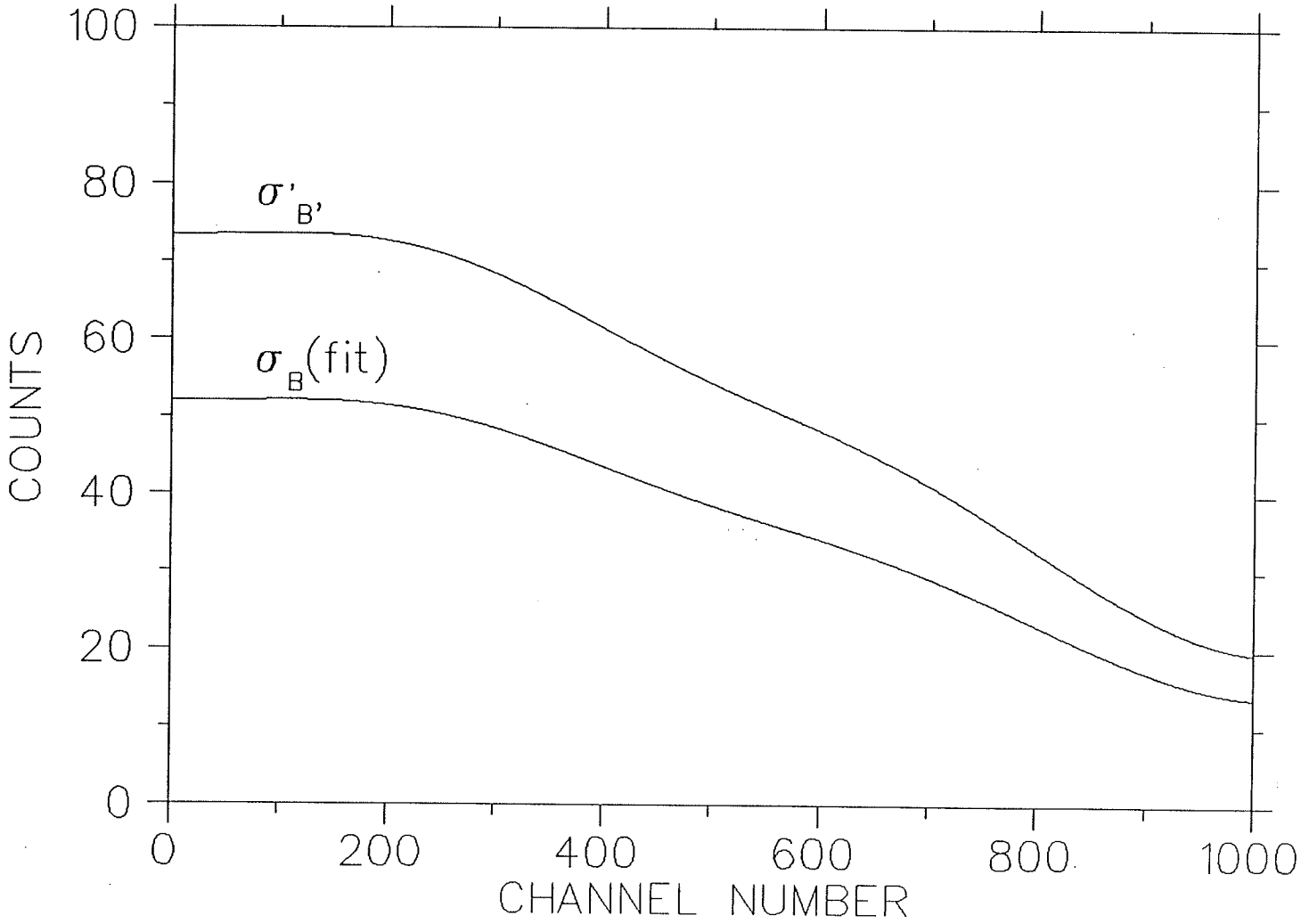

Fig. 5.16 Comparison between uncertainty in the fitted background σ_B (fit) = $\sqrt{N_B}$, and the uncertainty $\sigma'_{B'}$ calculated from eq. 5.13.

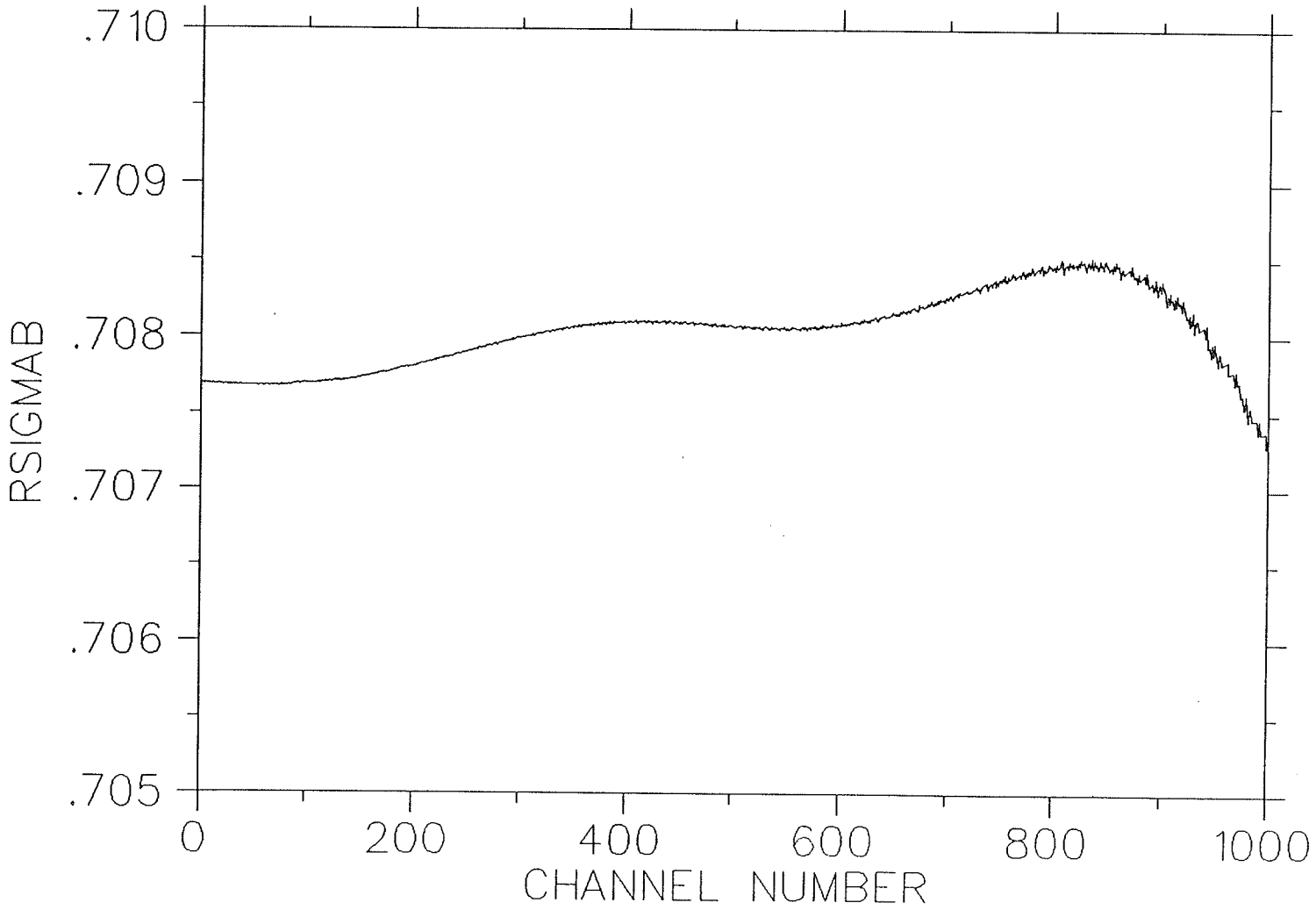

Fig. 5.17 Ratio of the two uncertainties illustrated in Fig. 5.16 plotted as RSIGMAB = σ_B (fit)/$\sigma'_{B'}$.

5.7. The Position of PIXE as Compared With Other Analytical Techniques

5.7.1. Introduction

The number and sophistication of techniques for trace element analysis is steadily growing. Despite these growths and developments, no technique can by itself tackle all sample types and determine all elements, so that the selection of the appropriate technique or techniques for a particular analytical problem has become a difficult task. In order to aid in assessing for what sample types or problems *PIXE* may be more suitable than other techniques, the principles and methodological aspects of several analytical techniques are described. The various techniques are intercompared with each other and with low and high energy *PIXE* and this is done from a number of viewpoints with an emphasis on accuracy and detection limits.

5.7.2. Nuclear Activation Analysis

Nuclear activation analysis uses the production of artificial radionuclides from stable elements for their identification and quantitative determination. The particles used for the activation may be neutrons, charged particles or energetic photons, but for the vast majority of analyses, thermalized neutrons from a fission-type reactor are employed (neutron activation analysis). Whenever possible, neutron activation analysis (NAA) is carried out in a purely instrumental way (INAA), that is by subjecting the activated sample to high-resolution gamma ray spectrometry without performing any postirradiation radiochemical separations.

The sensitivity and detection limits in neutron activation analysis are determined by several factors, including nuclear constants (e.g. cross sections), experimental parameters (e.g. neutron fluence) and presence of readily activatable elements in the sample. In very favorable cases, detection limits down to better than ng/g may be obtained in INAA. However, the sensitivities and detection limits vary in a rather irregular way as a function of atomic number, and various elements (e.g. Li, Be, B, C, N, O, Si, P, S, Ag, Sn, Tl and Pb) are difficult or impossible to measure by NAA. Besides excellent detection limits, NAA also has the benefit of being able to provide very ac-

curate results. Since both neutrons and gamma rays are not strongly absorbed by matter, corrections for absorption effects are small and often negligible.

Because of its various favorable characteristics, including accuracy, multielemental capability, high sensitivity for many elements, NAA plays a very important role in the certification of reference materials. Perhaps the most important drawbacks of NAA are that it is slow, expensive, and that one needs to have access to a nuclear reactor with proper facilities for performing the irradiations [Ma,90; En,90; Sw,90].

5.7.3. X-Ray Fluorescence

5.7.3.1. Conventional X-Ray Fluorescence

Of all techniques discussed here, X-ray fluorescence (XRF) shows most resemblance to *PIXE*, and it is also *PIXE*'s strongest competitor. Whereas heavy charged particles (generally protons) are used for the excitation in *PIXE*, XRF employs electromagnetic radiation for producing the characteristic X-rays of the elements in the sample. XRF can be used for the nondestructive analysis of a variety of sample types, including geological, environmental and biomedical samples (mostly solids, but also liquids). It is sensitive to all elements from Na to U, and in special cases even the low-Z elements down to B can be measured. In general, XRF is a sensitive tool, provided the excitation source is energy-tunable in some way. The detection limits depend to a large extent on the instrumentation used and on the sample matrix, but are in the 1-10 $\mu g/g$ range in favorable cases. As both the exciting and characteristic radiation interact significantly with matter, one generally has to correct for matrix effects in XRF. The matrix effects include absorption, enhancement and sometimes also particle size effects. However, in contrast to most other atomic spectrometric techniques, XRF has the advantage that the physics of the matrix effects are well understood. Besides matrix effects, also spectral interferences have to be taken into consideration [Ma,90; Wo,73].

5.7.3.2. Total Reflection X-Ray Fluorescence

As in any spectrometric technique, the detection limits in XRF are to a large extent determined by the peak to background ratio. In XRF of thin sample layers which are deposited on a substrate film (e.g. Mylar) most of the background originates from the scattering of the incident radiation by the substrate. When an optically flat material (e.g. quartz) is used as support and the incident radiation impinges with an angle of incidence which is smaller than a critical angle (typically a few mrad), total reflection occurs and the background originating from the support is virtually eliminated. This phenomenon forms the basis for total reflection X-ray fluorescence (TRXF). Interference free absolute detection limits, as obtained from pipetting dilute aqueous solutions on total reflectors and performing a TXRF measurement on the dried, very low mass residues, are very low, i.e. below 20 pg for over 60 elements. Assuming a pipetted volume of 100 μl, this corresponds to a relative detection limit of 0.2 ng/ml (without preconcentration) [Ma,90].

5.7.3.3. Synchrotron Radiation X-Ray Fluorescence

Very large electron storage rings are needed in synchrotron radiation XRF(SR-XRF). The synchrotron radiation (SR) in such devices is produced as the relativistic electron beam of some GeV is diverted from its straight path by bending magnets. Major characteristics of SR are its wide and continuous spectral range of very high intensity which extends up to 100 keV in some storage rings, the high degree of polarization in the plane of the electron orbit, and its natural collimation. The brightness of the radiation is larger than that of conventional X-ray tubes by several orders of magnitude, so that the storage ring is an excellent source of primary radiation of XRF. As far as its applications to bulk analysis are concerned, experimental detection limits in the range of 0.1-1 $\mu g/g$ have been reported [Bo,84; Jo,84]. By improving on the experimental conditions, detection limits down to 20 ng/g have been obtained [Gi,86].

5.7.4. Optical Atomic Spectrometry

5.7.4.1. General Characteristics

There is a wide variety of analytical techniques based on optical spectrometry. They can be classified into atomic absorption spectrometry (AAS), atomic fluorescence spectrometry (AFS) and atomic emission spectrometry (AES) techniques, but within each of these groups many variants exist. The variants derive from differences in excitation or light sources employed, from the various approaches to generate the atom (and ion) cloud, including the use of flames, electrothermal devices, plasmas, glow discharges and sputtering cells, and from the differences in detection systems.

A common aspect of all optical atomic spectrometric techniques is that the sample has to be converted into an atomic vapor, so that they are inherently destructive. Also, in most of the techniques, sample introduction occurs in the liquid form, thus implying that solid samples have to be brought into solution. Another limitation of several optical spectrometric techniques is their high consumption rate of sample solution, so that they cannot be applied when only mg amounts of sample are available. Finally, all optical spectrometric techniques primarily address metallic elements, and are not really suitable for measuring nonmetals [Ma,90].

5.7.4.2. Atomic Emission Spectrometry (AES)

Optical atomic emission spectrometry, the oldest of all multielement atomic spectrometric methods, received a new impulse in the mid- sixties when it was realized that the inductively coupled plasma (ICP) source offered significant advantages over the flame for the spectrochemical analysis of liquid samples.

In ICP-AES, the sample to be analyzed is atomized and/or ionized, and excited in an inductively coupled plasma (generally an argon plasma). The excited atomic and ionic species relax almost immediately to their ground state, thereby emitting radiation which is characteristic for the element excited. By measuring the intensity of one or more emission lines for each analyte a quantitative multielement analysis is performed.

As in many of the other techniques, the accuracy in ICP-AES is ultimately determined by the ability to overcome matrix effects and interferences. Under properly op-

timized conditions, accuracies down to a few percent may be expected. Precisions typically claimed in the literature are in the 1-2% range. Instrumental detection limits, as obtained from blank solutions, are typically in the 1-30 ng/ml range and vary in an irregular way with atomic number of the analyte element.

5.7.4.3. Atomic Absorption Spectrometry (AAS)

In AAS one utilizes the fact that atoms in the gaseous state are able to absorb optical radiation of well-defined frequencies. By supplying thermal energy to the sample in an atomizer, the analyte element is converted into a population of free atoms (atomic vapor), which will virtually all be present in the ground state. These atoms can absorb a quantum of energy and undergo a transition into an excited state, after which the excited atoms can release the same energy quantum and return to the ground state. Transitions from and to the ground state are called resonance transitions. The passing through the atomic vapor of optical radiation with a frequency corresponding to one of those resonance transitions and the measurement of the transmitted radiation intensity form the basis of quantitative AAS.

Detection limits are generally in the range of 1-30 ng/ml in flame AAS, and about two orders of magnitude lower, i.e. typically between 0.01 and 0.2 ng/ml, in electrothermal atomization AAS (ETA-AAS). These low detection limits, together with the fact that AAS is a simple to use and relatively inexpensive technique, have been the major reasons of its success.

AAS is inherently a single-element technique. Several attempts towards multielement AAS have already been made, and in recent years, simultaneous multielement atomic absorption with a continuous source has been introduced. However, the relatively low intensity of continuum sources, the low dynamic range of AAS, and the fact that furnace atomizers require separate optimization for each element and for each sample type are serious obstacles on the road to successful multielement AAS.

5.7.4.4. Atomic Fluorescence Spectrometry

Atomic fluorescence spectrometry (AFS) is based on the absorption of photons of a given frequency followed by spontaneous isotropic emission of photons at the same frequency (resonance fluorescence) or at a different frequency (nonresonance fluorescence). AFS thus shows much relation to AAS, the difference being that not the absorbence of the incident radiation but the intensity of the isotropically emitted fluoresced radiation is measured. Consequently, whereas AAS requires a straight-line geometry of light source, atom reservoir and detection optics, much more flexibility is possible in AFS setups and several radiation sources and detectors can be arranged around the same atomizer. This has for effect that AFS lends itself much more easily to multielement analysis than AAS.

Although AFS has already existed for about 25 years and exhibits multielement capability, it has never reached the popularity of AAS and ICP-AES. No multielement source has yet been identified that would make AFS significantly superior to ICP-AES for simultaneous multielement analysis. In electrothermal-atomization-laser- induced-atomic fluorescence spectrometry (LIF-ETA), absolute detection limits below a femtogram and relative detection limits down to the 0.1 pg/ml may be obtained. However, the detection limits vary in a very irregular way with atomic number, and are up to three orders of magnitude higher for certain elements.

Because fluorescence spectra are simpler than either absorption or emission spectra, especially with conventional excitation sources (i.e. not lasers), AFS is virtually free from spectral interferences. With lasers, the onset of saturation results in broadening of the fluorescence excitation profile, so that the spectral selectivity is somewhat degraded. However, no systematic investigation of the possible occurrence of spectral interferences in laser-induced-atomic fluorescence spectrometry (LIF) has been made. A much more important source of concern when making AFS measurements is scattering radiation. Therefore, much effort has been directed over the years in overcoming or correcting this problem, and many different correction procedures have been proposed, including similar ones as those used for background correction in AAS.

Although LIF and particularly LIF-ETA have the advantage of extremely low detection limits, the argument continues whether LIF will make it into the analytical laboratory for the routine analysis of complex samples. At present, pulsed dye lasers

are still very expensive and, in addition, it requires a lot of skill and patience to optimize their operation. It therefore looks that LIF will only be used for difficult analytical problems requiring extreme sensitivities.

5.7.5. Atomic Mass Spectrometry

Because of the diversification in powerful ionization sources and the commercial availability of instruments employing such sources, there has been a remarkable revival of interest in atomic (or inorganic) mass spectrometry in recent years. The many variants of atomic mass spectrometry for bulk analysis now include thermal ionization, spark source, glow discharge, inductively coupled plasma, microwave induced plasma and accelerator mass spectrometry (TIMS, SSMS, GDMS, ICP-MS, MIP-MS and AMS respectively). Of these variants, ICP-MS clearly experienced the most explosive growth, and, furthermore, many applications of ICP-MS focus on the analysis of similar sample types (i.e. biomedical and environmental) as are most popular in *PIXE*.

In ICP-MS, an inductively coupled plasma (ICP) is used as an efficient means to convert the sample into singly charged, monatomic, positive ions. The ions are sampled and focused into a mass spectrometer, where they are analysed according to their m/z value and detected.

Although mainly monatomic, singly charged, positive ions are formed in the ICP source, other ions, including polyatomic (e.g., oxide, hydroxide) and doubly charged ions, also appear to some extent in ICP-MS spectra. As a consequence, spectral overlap may occur between a peak from a monopositive analyte and that from a polyatomic and/or doubly charged ion with the same m/z value. Much more troublesome than the problems arising from spectral overlap are those arising from matrix interferences. The extent of matrix interferences depends upon the total solute concentration of the sample solution. A high concentration of a matrix element generally suppresses the signal of a trace analyte in ICP-MS, but enhancements of analyte signal have also been observed.

The major advantages of ICP-MS are the excellent sensitivity, the almost complete elemental coverage across the periodic table, the broad linear dynamic range (up to 6 orders of magnitude), and the ability to provide information about the isotopic

composition of the sample. Detection limits in ICP-MS are typically 0.03-0.1 ng/ml, and thus of the same order as those observed in ETA-AAS. However, ICP-MS has the distinct advantage that it is a multielemental technique and that the detection limits are very similar for most elements [Ma,90].

5.7.6. Electron Micro-Probe/Scanning Electron Microscope

Electrons are widely used as an easy means of exciting X-rays. They have found a fruitful application in the determination of small quantities of elements via the electron micro-probe or scanning electron microscopes (SEM). The continuous background radiation, however, is much more intense for electrons and this is mainly due to the greater charge-to-mass ratio of the electron. The concentration found, for a signal-to-noise ratio equal to 1, is at least three orders of magnitude higher than for proton bombardment under the same optimum conditions [Fo,74].

In electron microprobes the sample is analyzed nondestructively, and quantitative analysis can be obtained in many cases with an accuracy of the order of 1%-2% of the amount present for a given element (5%-10% in biological material). In the case of some biological and organic substances, there can be a substantial, i.e., up to 90% mass loss during the period of analysis. Elemental losses can also occur, particularly in the case of light elements in an organic matrix. [Go,81].

The X-ray microanalysis of biological material is beset by the same problems associated with the examination of the sample in the SEM. The experimenter has to be very careful that the elements being measured remain in the specimen and are not removed or relocated by the preparative procedure.

5.7.7. Evaluation of the Present Position of *PIXE*

It is interesting to compare *PIXE* with other competing methods such as the ones outlined in the preceding sections. The major advantages of *PIXE* are its multielement character (all elements from Na to U can in principle be measured), its high sensitivity (absolute detection limits down to $10^{-12}g$, and relative detection limits down to 0.1 $\mu g/g$), the smooth variation of the relative detection limit with atomic number of the

analyte element, the ability to analyze tiny samples (1 mg or less), the speed of the analysis (1-10 min bombardment time per specimen), the possibility for automation, and the fact that it is often nondestructive. Compared to conventional XRF, *PIXE* offers detection limits which are often one order of magnitude better, it allows one to analyze smaller sample masses, and it is faster. Another favorable feature of *PIXE* is that it can be complemented with other ion beam analysis (IBA) techniques, such as elastic (and nonelastic) scattering, and proton-induced gamma-ray emission (PIGE), and in this way a simultaneous measurement of the light element (e.g. Li, B, C, N, O and F) becomes feasible. Finally, and certainly not least, the microbeam variant of *PIXE*, which experiences an intensive research activity at present, offers the possibility of spatially resolved analyses with high resolution (down to 1 μm or better) and high sensitivity (down to the $\mu g/g$ level). The major drawback of *PIXE* is that it requires a MeV particle accelerator. Other limitations of the technique, which are also shared by XRF, are that it suffers from spectral interferences, that matrix effects have to be accounted for, and that it does not allow the direct measurement of ultra-trace elements that are present at ng per g levels. Furthermore, the sub-$\mu g/g$ detection limits in *PIXE* are only obtained when the sample matrix consists of light elements, as is for instance the case in biomedical samples. For heavier element matrices, the detection limits are worsened because of the increased continuum background and the presence of intense X-ray lines from the matrix elements in the *PIXE* spectrum.

The low mass requirement of 1 mg or less is always considered as a significant advantage of *PIXE*, and it appears that *PIXE* is still the only technique that allows a nondestructive multielement analysis of mg-sized solid samples with sub-$\mu g/g$ detection limits. For certain applications, such as for the multielement analysis of atmospheric aerosol samples which are collected with small compact samplers that provide good time and/or size resolution, there is simply no alternative yet to *PIXE*.

The values usually quoted for the accuracy and precision of *PIXE* analysis are about 5-10%. This might seem to be a rather poor performance when other methods in some cases claim values as low as 1% or less. However, it is important to keep in mind that in order to make a fair comparison one must take into account the difficulty of the analytical problem. *PIXE* is often used in cases when other methods simply do not work. For example, in analyzing trace elements in water, very good results can be obtained by atomic absorption provided the concentrations are relatively high, no dis-

turbing matrix effects occur, and the analysis is limited to elements for which this method is suitable. It is a different situation if one wants, for example, to analyze low-concentration elements in sea-water. It is obvious that in such a situation an accuracy or precision of 10% is satisfactory [Jo,87].

The accuracy which can be obtained with an analytical technique largely depends on the extent of spectral interferences and matrix effects, and on how well these can be controlled or corrected for. Spectral interferences occur in all techniques presented, but are probably least troublesome in NAA, XRF and AFS. All techniques are also subject to nonspectral interferences or matrix effects. However, these effects are often entirely negligible in NAA. Matrix effects in *PIXE* and XRF depend upon the sample thickness and are small for thin sample layers ($< 1\ mg/cm^2$). In addition, the X-ray emission techniques have the advantage over the optical spectrometric techniques and ICP-MS that the physics of their matrix effects are very well understood. Within the AAS techniques, matrix effects are much more pronounced in ETA-AAS than in flame AAS, and of the two ICP based techniques ICP-AES and ICP-MS, the latter is by far most prone to matrix effects.

Considering that NAA is the only technique other than high-energy *PIXE* (HEPP) in which matrix effects are often entirely negligible, it is evident that accurate results are more easily obtained with NAA than with any other technique. Therefore, NAA will continue to play an important role wherever the accuracy of the concentration measurement is the primary objective.

In addition to spectral and nonspectral interferences, several other factors determine the accuracy of a trace element analysis. In determinations at the $\mu g/g$ level, and particularly in ultra-trace element measurements, the control of extraneous additions and of losses before or during the measurement is very important. The fact that *PIXE*, conventional XRF and NAA require no dissolution or decomposition of solid samples presents a clear advantage in this respect over the optical spectrometric techniques and ICP-MS. When careful attention is given to all stages of the analysis, *PIXE* can provide results with an accuracy of better than 5% and a precision of a few percent down to the $\mu g/g$ level [Ma,87].

There obviously exists a wide variety of sensitive techniques for trace element analysis of bulk samples and several techniques are quite competitive with each other.

Many analytical problems that were tackled in the past by *PIXE* can now be better and more cheaply handled by other analytical techniques. However, a strong point in favor of *PIXE* is that it allows the nondestructive, multielement analysis of solids with little or no sample preparation, high sensitivity in absolute terms, low cost and high turnover. When only mg amounts or less of a solid sample are available, or when one is interested in measuring the composition of mm-sized areas on a large sample or of thin superficial layers on a bulk sample, *PIXE* is virtually the only nondestructive technique available. The analysis of small aerosol deposits, as collected by compact samplers which provide good time or size resolution or both, remains an application area where *PIXE* has virtually no competition. Other areas where *PIXE* can advantageously be applied are in the field of art and archeology, and, despite the increasing competition from other techniques, in the field of biology and medicine. A review of the wide range of *PIXE* applications in the latter field , with emphasis on applications where the unique capabilities of *PIXE* were advantageously used, was recently presented [Ma,88].

In principle, *PIXE* can detect all elements with $z>10$, but for light elements such as Na, Al and Si the accuracy is rather poor because of the self-absorption corrections, which strongly depend on the sample matrix and morphology. Moreover, very light elements in practice are not detectable at all. In this context, proton induced gamma ray emission (PIGE) is well suited for the analysis of the light elements. Thus the simultaneous use of *PIXE* and *PIGE* is a remarkable method for the detection of both light and heavy elements [Bo,90].

Besides solving bulk analytical problems, *PIXE* can also be applied to spatially resolved analyses with high resolution and high sensitivity, and ample evidence has already been presented of the enormous potential of the μ*PIXE* variant. A proton microprobe is a device for the microanalysis of a sample in which a beam of particles is focussed onto an area less than a micrometer in diameter. Electron microprobe and proton microprobe are very similar as both employ focussed beams of charged particles to excite characteristic X-rays. However, unlike electron microprobe techniques which permit determination of trace element concentrations of the order of hundreds of ppm, *PIXE* and micro-*PIXE* make it possible to achieve detection limits for K X-rays at the ppm level. Much of the improvement in detection may be ascribed to the reduction of the bremsstrahlung levels obtained when the more massive protons are used to induce the X-ray emission. Indeed micro-*PIXE* can be regarded as complementary to

electron microscopy since it frequently offers lower limits of detection, and often the two techniques can be deployed in partnership [Du,88; Ca,90]. For detailed information about "Proton Microprobes and Their Applications" refer to [Mc,90d].

The above discussion and evaluation of the *PIXE* technique is a general one and covers both low-energy and high-energy *PIXE*. The rationale for high-energy *PIXE* (*HEPP*) was discussed in chapter 1. However, when comparing different analytical techniques, it is necessary to make a distinction between low- and high-energy *PIXE* particularly in the areas of minimum detection limits. Spectral as well as nonspectral interferences are critical factors in the analysis of all trace element concentrations.

At higher energies (say 30 to 60 MeV) the yield of K X-rays is high for all medium Z elements and good for both high ad low Z materials. The fact that K X-rays are the signature for each element studied by high-energy proton *PIXE* ensures that for medium and high Z elements, spectral interferences are minimized. HEPP yields data of high resolution in a region of study where ambiguity is a feature of low-energy *PIXE* experiments. When using low-energy protons, elemental identification must rely upon the L rather than K X-ray series. Problems arise in that L X-rays are not only more difficult to identify quickly, but the corresponding peaks in the L X-ray energy spectrum overlap each other and also overlap the K X-ray peaks of lighter elements present in the sample.

Another important factor to be considered are the matrix effects. Matrix effects depend upon the sample thickness and are small for thin sample layers. Transmission targets are used for HEPP experiments in order to reduce the self-absorption of K X-rays from medium and heavy elements. These thin samples which incidentally may be of the thickness of low-energy *PIXE* stopping targets, while minimizing damage to both biological and mineral samples, they also reduce the matrix effects which can be quite high for low-energy *PIXE*.

As far as detection limits are concerned, 1 ppm is attainable for *HEPP* for all elements above Ge [Mc,90b]. Although similar sensitivities might be reached in certain selected low-energy *PIXE* experiments where particular elements and experimental conditions are involved [Jo, 76], however, the universal capabilities of *HEPP* are not attainable in low-energy analysis and the minimum detection limit of 1 ppm attained in *HEPP* is about two orders of magnitude better than low- energy *PIXE* results for ele-

ments above germanium.

Detection limits of low-energy *PIXE* for biological samples under the experimental conditions mentioned in [In,90] are calculated by Ishii et al. and these values are typically about 50 ppm for high Z elements. Campbell and Cookson [Ca,84] concluded that limits no worse than 100 ppm are possible for elements of $Z > 20$ in many matrices, while the limit can be about 1 ppm for the most favoured element, somewhere in the range $Z = 25 - 40$ (depending on beam energy) for matrices of very low atomic number.

According to Teesdale et al. [Te,88], sensitivities of 1 ppm are attainable in the analysis of thick samples in low-energy *PIXE*, but the element under consideration, the matrix in which it is found, the absorber, and the beam energy are important factors in achieving such a minimum detection limit. Detection of many rare earth and higher Z elements is shown in this reference to be at the 100 ppm, rather than the 1 ppm level. Table 5.7 summarizes the above discussion in which several characteristics of the various techniques are intercompared.

5.8. Processing Programmes for *PIXE* Spectrum Analysis

5.8.1. Introduction

PIXE has now come to a stage where full, quantitative knowledge of all parts of the system from the proton beam to the final spectrum is available. However, out of different stages of the analysis, spectral data processing now seems to be a principal determinant of *PIXE*'s accuracy, especially in the case of elements of low concentration in a multielement specimen. In the following sections, the traditional approach in developing existing computer programmes for *PIXE* analysis is discussed and a comparison is made with the recent approach to the analysis of *PIXE* spectra using Fourier transform techniques.

5.8.2. Traditional Approach

Several programmes/codes now exist for the purpose of processing *PIXE* spectra. Most of these programmes follow the traditional path of modelling the measured spectrum and of fitting some kind of function to the slowly varying background. The basic philosophy behind this traditional approach is to construct a numerical model of a spectrum and then vary its parameters to achieve a best fit to the measured spectrum.

Modelling the spectrum of an element

In constructing the model pulse height spectrum for a given element, the characteristic lines are generally represented by a Gaussian or quasi-Gaussian peak. Tailing on the low-energy side of peaks, due to incomplete charge collection are catered for by adding a flat step, exponential tails, or other artefacts to the left hand side of the Gaussian. In addition each of these peaks is accompanied by a silicon K X-ray escape peak whose energy is normally 1.742 keV less than its parent [Mu,75; Ca,86; Bo,87].

Fitting the background

Various approaches have been tried to deal with the continuum background. The first is to use a suitable analytical function with some number of free parameters to model the background. A different approach to deal with the continuum background is to have the free parameters of background function determined at the outset by fitting the function to a set of minima in the experimental spectrum. Furthermore, an iterative procedure can be used to remove peaks and progressively reduce the spectrum to the background continuum [Ca,86; Cl,87; Bo,87].

Table 5.8 lists some of the currently used computer programmes for *PIXE* analysis.

5.8.3. Spectrum Analysis Using Fourier Transform Techniques Presented in This Thesis

It is noticed from table 5.8 that nearly all the traditional techniques employ linear/nonlinear least-squares procedures for fitting purposes. The sum of a number of functions is fitted to the measured data to model the peaks and the continuum back-

ground is represented by some analytical function. The lineshape (resolution function) of the detector, which is quite strongly energy dependent, is required for modelling or least-squares fitting of *PIXE* spectra and hence extracting peak intensities. The process requires intensive interaction of the physicist with the data analysis procedure at all stages.

In the analysis approach using Fourier transform techniques, as presented in this thesis, the application of a single mathematical filtering operation effectively removes low-frequency components, i.e. the continuum background from the data. No assumption has to be made about the shape of the peaks or the functional form of the background. Because the CPU time needed is proportional to the number of fitting parameters, a decrease in the amount of interactive involvement by the physicist during the process is assured by requiring a small number of free parameters in this approach.

While the analysis approach using Fourier transform techniques was successfully tested on high-energy *PIXE* spectrum, the approach can be adapted to low-energy *PIXE* spectrum analysis as well in so far as the "broad spectral features" which contain many interfering K and L X-ray peaks, common to low-energy *PIXE* spectra, are not reconstructed out of the few low frequencies associated with the background events [Mc, 90b].

Table 5.7 Summary of some characteristics of analytical techniques for bulk trace element analysis.

Technique	Detec. limit [a] [µg/g] or [ng/ml]	Spectral interf.	Matrix effects	Multi-element	Preferred sample type	Destructive
INAA	0.001-1	low	low	yes	solid	no
XRF [b]	1-10	high/low	medium	yes	solid	no
SR-XRF	0.1-1	high	medium	yes	solid	no
TXRF	~0.2	high	medium	yes	liquid [c]	yes
PIXE (low-energy)	100 [d]	high	medium	yes	solid	no
PIXE (high-energy)	1 [d]	low	low (transmission target)	yes	solid	no
ICP-AES	1-30	high	medium	yes	liquid	yes
ETA-AAS	0.01-0.2	medium	high	no	liquid	yes
LIF-ETA	~0.001	low	high	no	liquid	yes
ICP-MS	0.03-0.1	high	high	yes	liquid	yes
SEM	500	high	medium	yes	solid	no

a) Detection limits are in µg/g for INAA, XRF, SR-XRF, PIXE and SEM and in ng/ml for the other techniques, including TXRF. However, if it is assumed that the total concentration of dissolved solids in the sample solution is 0.1% ng/mℓ would become µg/g.

b) The indications on this line before each slash apply to energy dispersive XRF , those after each slash to wavelength dispersive XRF.

c) The dried residue of the liquid on a totally reflecting substrate is subjected to analysis.

d) Particularly for elements with $z > 31$ and assuming that the operational parameters such as bombarding time, beam current, target thickness, detector efficiency, etc. are the same for both low- and high- energy PIXE.

Table 5.8 Some of the currently used computer programmes for *PIXE* analysis in other labs.

Programme name	Fitting procedure	Background model	Peak shape model	Other peaks in spectrum model	References
AXIL	Nonlinear least-squares fitting	Analytic expression (Polynomial, exponential)	Gaussian + numerical tail correction	Escape + pileup	[Wä,87; Ca,86; Va,77a; Va,77b]
GRP/GTP	Nonlinear least-squares fitting	Removed by top-hat filter	Gaussian	Escape + pileup + radiative auger	[Wä,87; Ca,86; Ma,84]
HEX	Linear and non-linear least-squares fitting	Analytic expression (Polynomial, exponential)	Gaussian + step	Escape + pileup	[Wä,87; Ca,86; Ka,77]
Los Alamos data reduction	Linear least-squares fitting with inequality constraints	Polynomial of adaptable order	Gaussian	Escape + pileup	[Wä,87; Ro,84]
NANOLEX	Linear least-squares fitting	Stripping of blank target + flat background	Stripping of step + tails, Gaussian fit	Escape	[Wä,87; Ar,84]
PIXAN	Nonlinear least-squares fitting	Polynomial or removed by iterative peak filing	Gaussian + exponential tails + steps	Escape + pileup	[Wä,87; Ca,86; Cl,81[a]; Cl,81[b]; Cl,83]
SESAMX	Linear least-squares fitting	Analytic expression (Polynomial + exponential) + background step	Gaussian + exponential	Escape + pileup	[Wä,87; Ca,86; Ha,77]
UC Davis data reduction (RACE)	Stripping of separately fitted peaks	Stripping of blank target + flat background	Gaussian	Escape + pileup	[Wä,87]
PIXASE	Linear (or non-linear) least-squares fitting	Polynomial or removed by iterative peak filing	Gaussian + exponential tails + step	Pileup	[Zo,88]

5.9. Summary

Fourier transform techniques (*FTT*) have been used as another approach for investigating the information content of high energy *PIXE* X-ray spectra. The problem of regularly varying widths of the peaks which is an intrinsic property of nearly all solid state silicon or germanium detectors was overcome by preconditioning the data. The preconditioning employed the translationally invariance of the system to provide peaks with constant line-widths and this was made possible by the transformation of the energy axis of X-ray spectra.

Application of *FTT* to the data allowed the subtraction of most of the background and suppressed the statistical noise component without resorting to the conventional fitting methods. The criteria for the design of a digital filter having two components to subtract background and remove noise have been discussed.

The major advantages of the method over conventional techniques are that the shape of the background function need not to be known explicitly and by using minimum number of free parameters, a decrease in physical intervention in the data extraction procedure can be affected. To illustrate this, all the peaks present in the *PIXE* X-ray spectrum, after removing the disinformative parts, were extracted and identified by employing the same technique.

5.10. Future Work

It was shown that the application of the filter function to the first six frequency points of the power spectrum of the measured data subtracted most of the background. However, considering the origins of continuous background, discussed in detail in chapter 2, it is noticed that the formation and production mechanism of background which is energy dependent varies under different conditions and operational parameters. Therefore, it is anticipated that the number of frequency points to be affected by the filtering functions as well as the values assigned to the filters in different circumstances will not be exactly those investigated in this work and that they should be modified to be applicable to other situations. While this can easily be done following the procedure discussed in this thesis, however, it will be quite useful if further investigation is made to cancel this step of operation.

The filtering function to subtract background in high energy *PIXE* spectrum, as was discussed in this thesis, is being tested on different types of spectra such as low energy *PIXE* spectra and Raman scattering spectroscopy. However, the key point towards decomposing the information content of a spectrum and solving the problem of background subtraction lies upon further investigating the power spectrum of the data. To illustrate this, Fig. 5.18 represents the power spectrum of background function fitted to the X-ray spectrum of the leaf sample. It is noticed that only the first four ν-points have large amplitudes and the amplitudes of the rest of the data are almost negligible. Fig. 5.20 shows the power spectrum of the first 300 ν-points of the spectrum of Fig. 5.19 which contains only one arbitrarily chosen peak of the leaf spectrum. Finally, Fig. 5.21 illustrates the power spectrum of the first 300 ν-points of the entire spectrum of the leaf sample. A careful study of these power spectra reveals some structure present in them and that there are different components each with different frequencies producing the so called beat phenomenon.

It is suspected that by investigating the power spectra of different *PIXE* X-ray spectra obtained under different operational parameters and relating their structures to the design criteria of the corresponding filters to subtract background, it would be possible to develop some semi-empirical relation for the design of filter functions to subtract background under universal conditions.

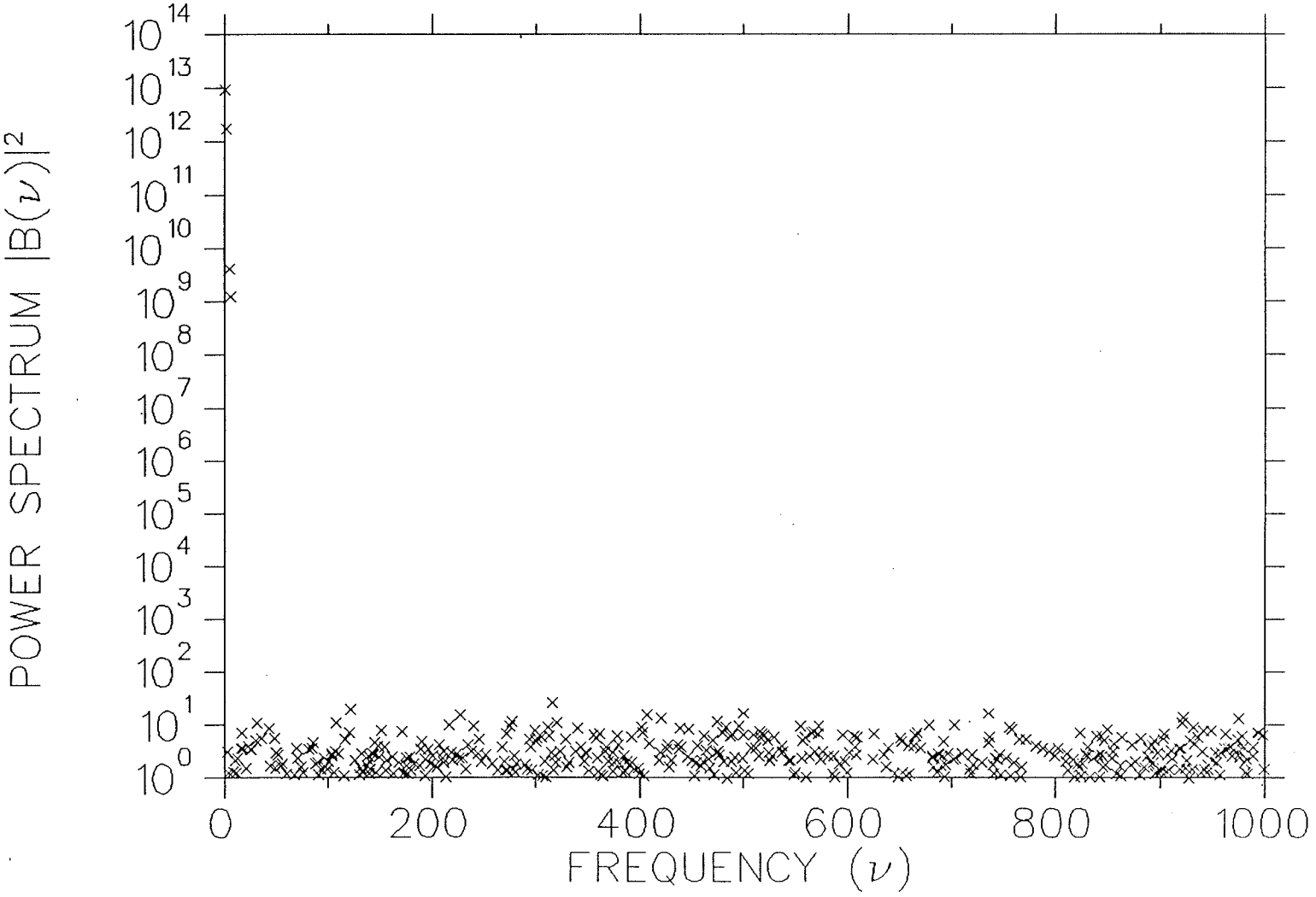

Fig. 5.18 Power spectrum of background function fitted to the X-ray spectrum of the leaf sample.

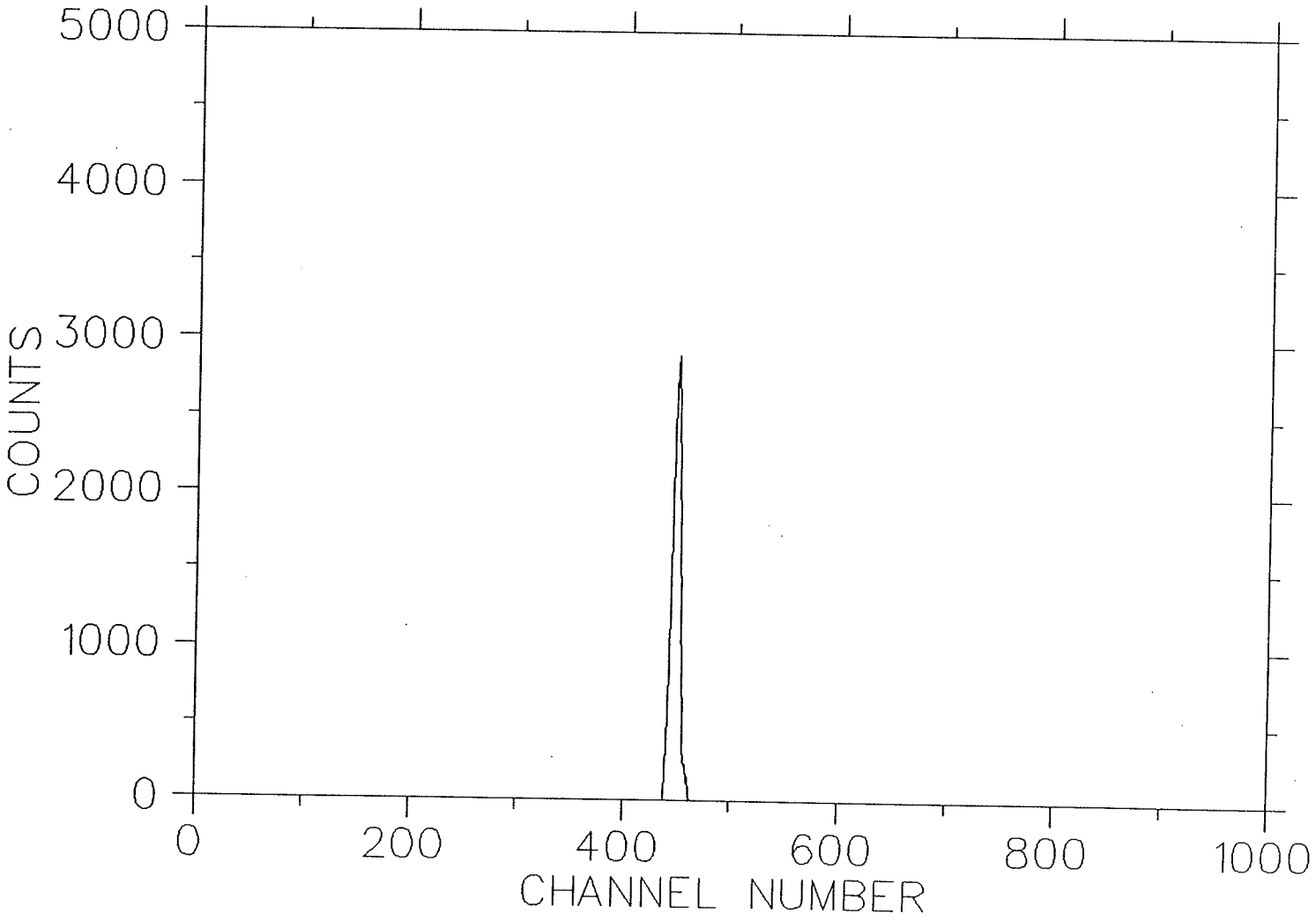

Fig. 5.19 An arbitrary peak of the leaf data to study its power spectrum.

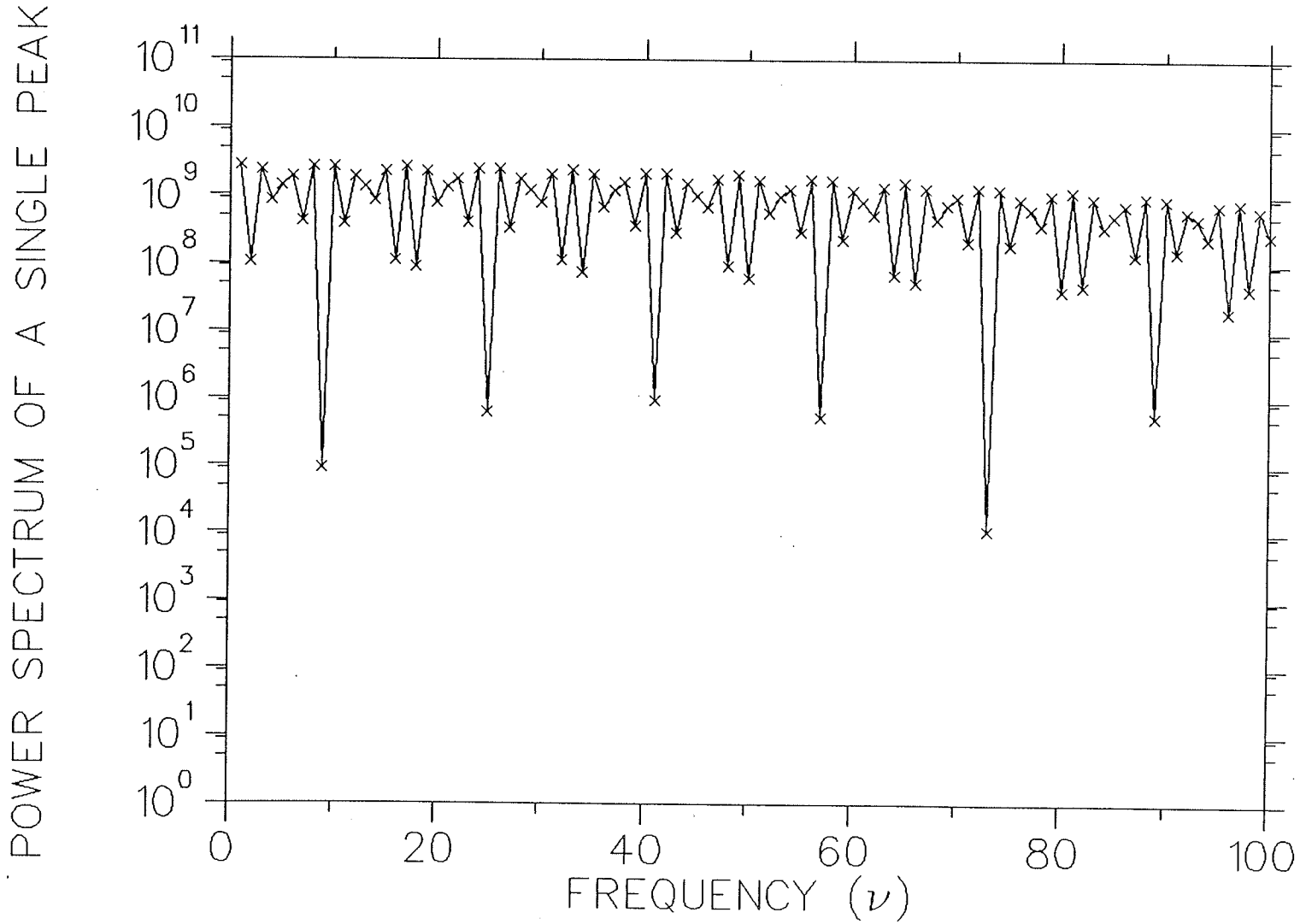

Fig. 5.20a) Power spectrum of the first 100 frequency points of the single peak of Fig. 5.19.

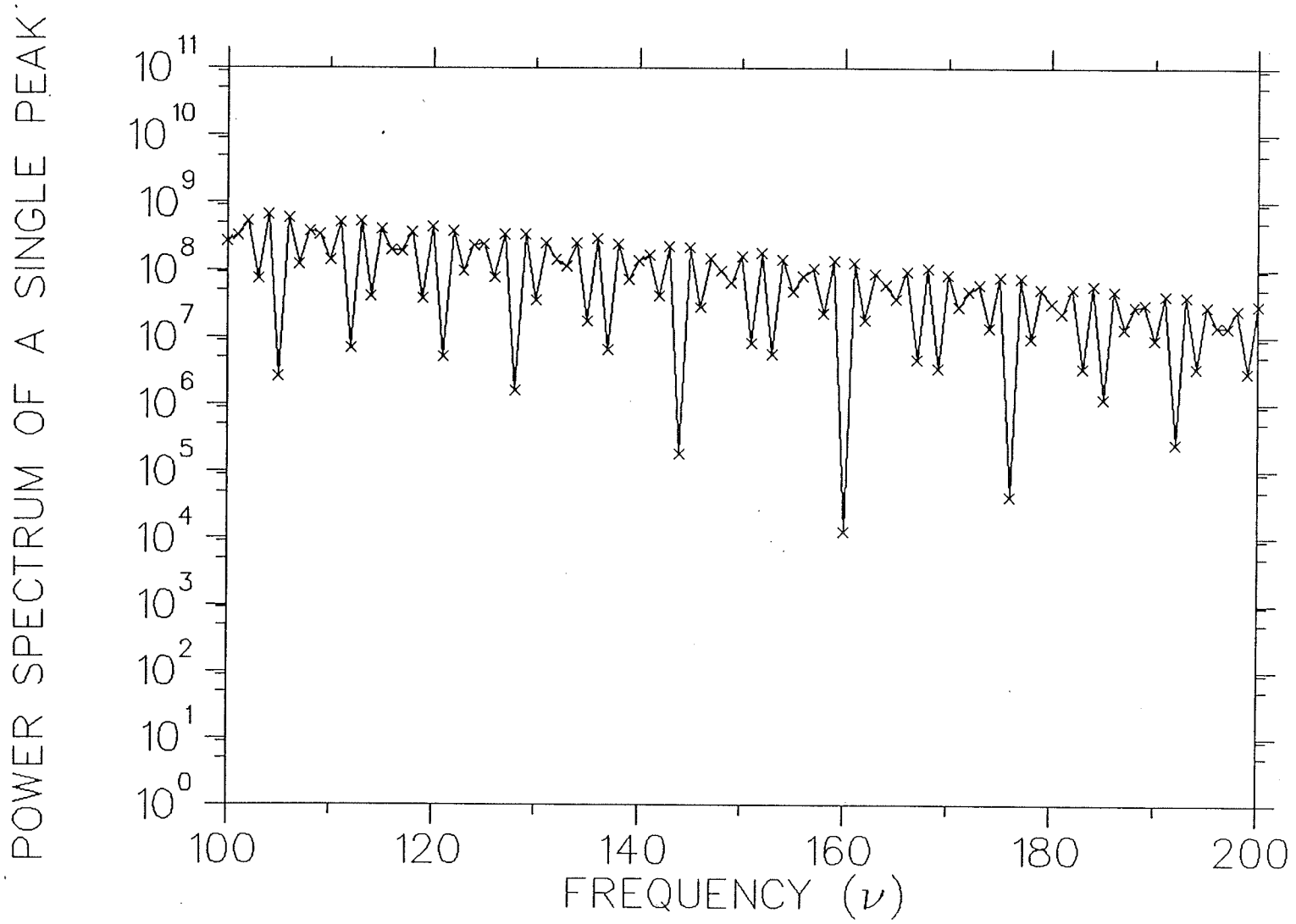

Fig. 5.20b) Power spectrum of the second 100 frequency points of the single peak of Fig. 5.19.

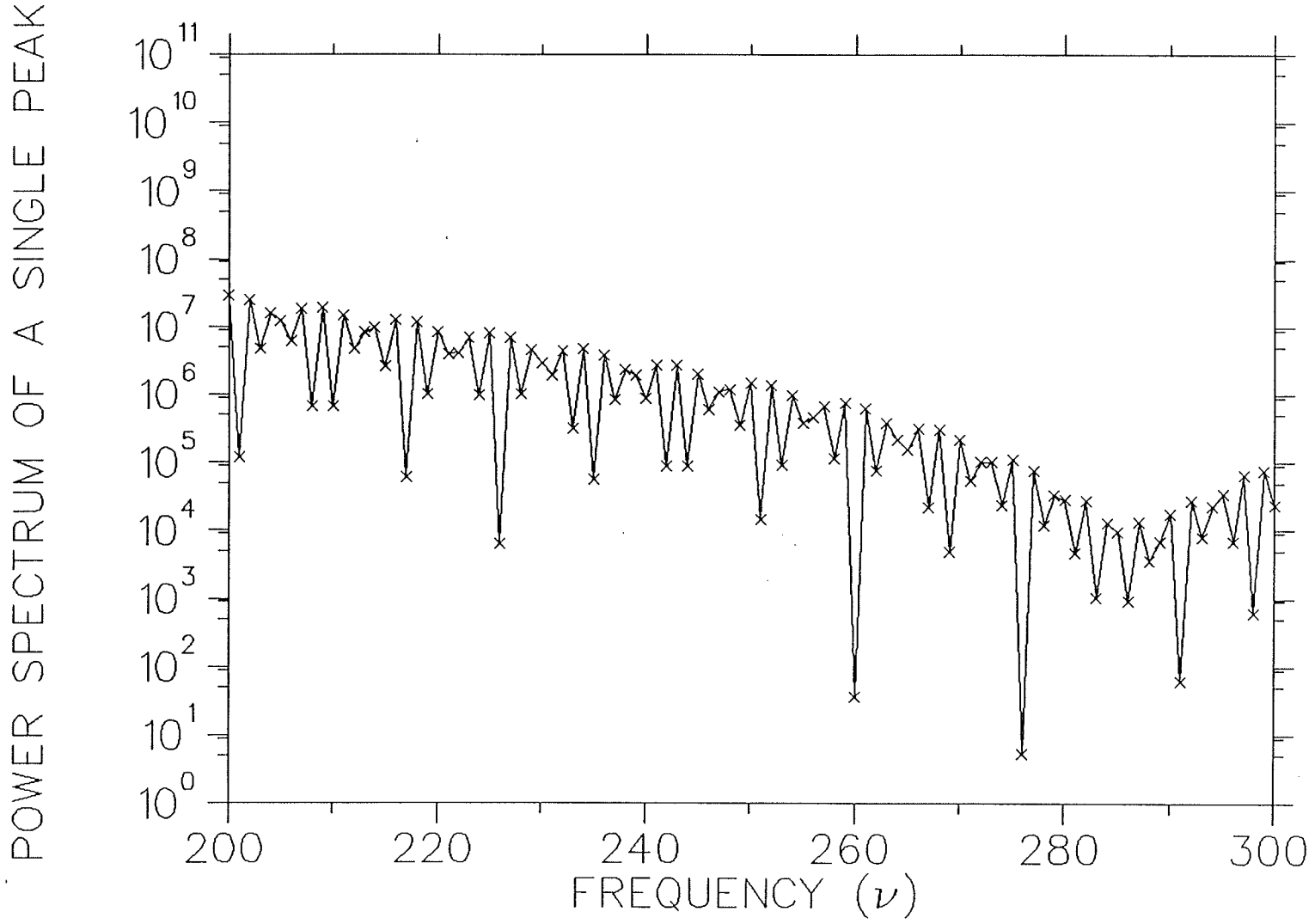

Fig. 5.20c) Power spectrum of the third 100 frequency points of the single peak of Fig. 5.19.

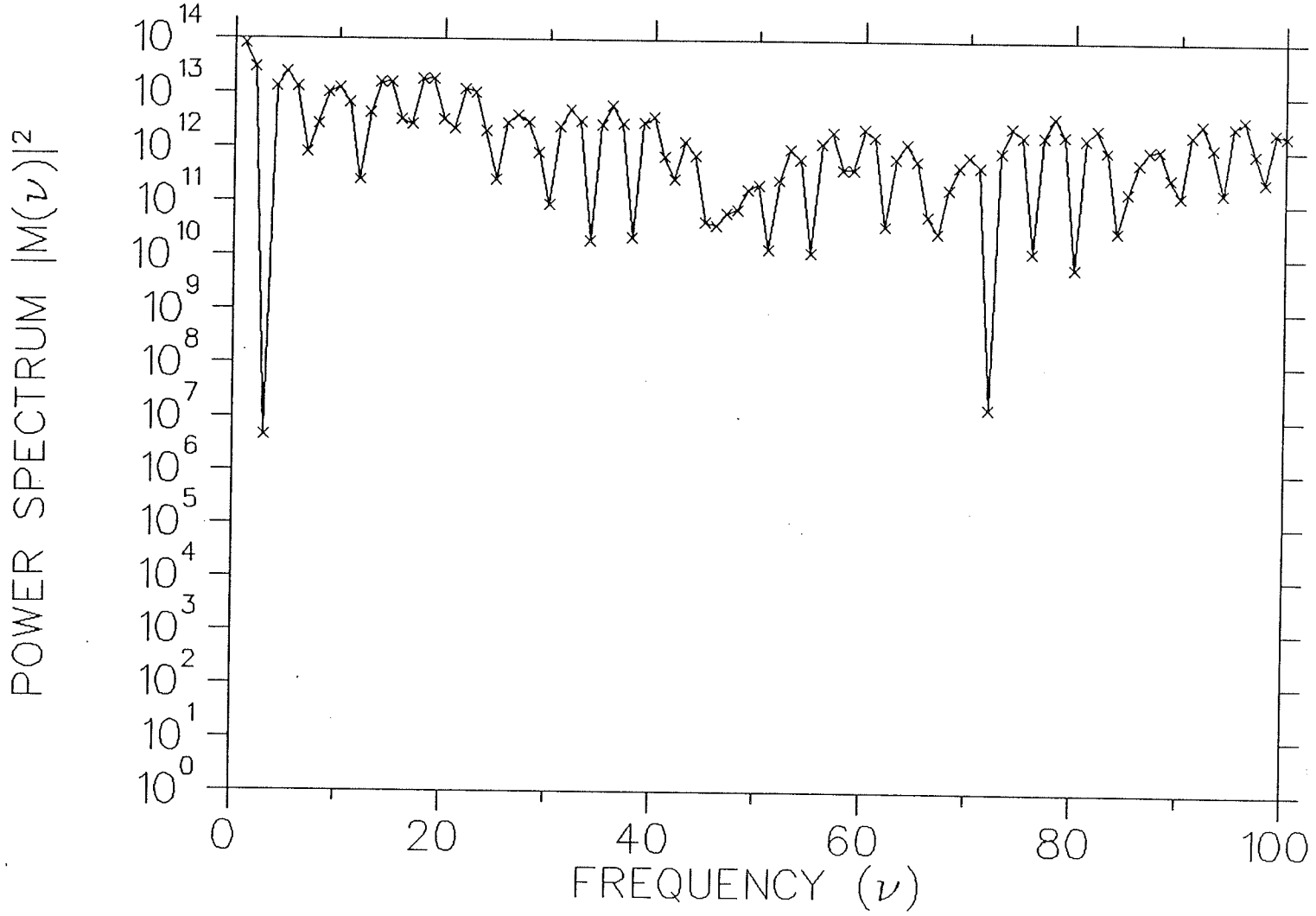

Fig. 5.21a) Power spectrum of the first 100 frequency points of the entire spectrum of the leaf sample.

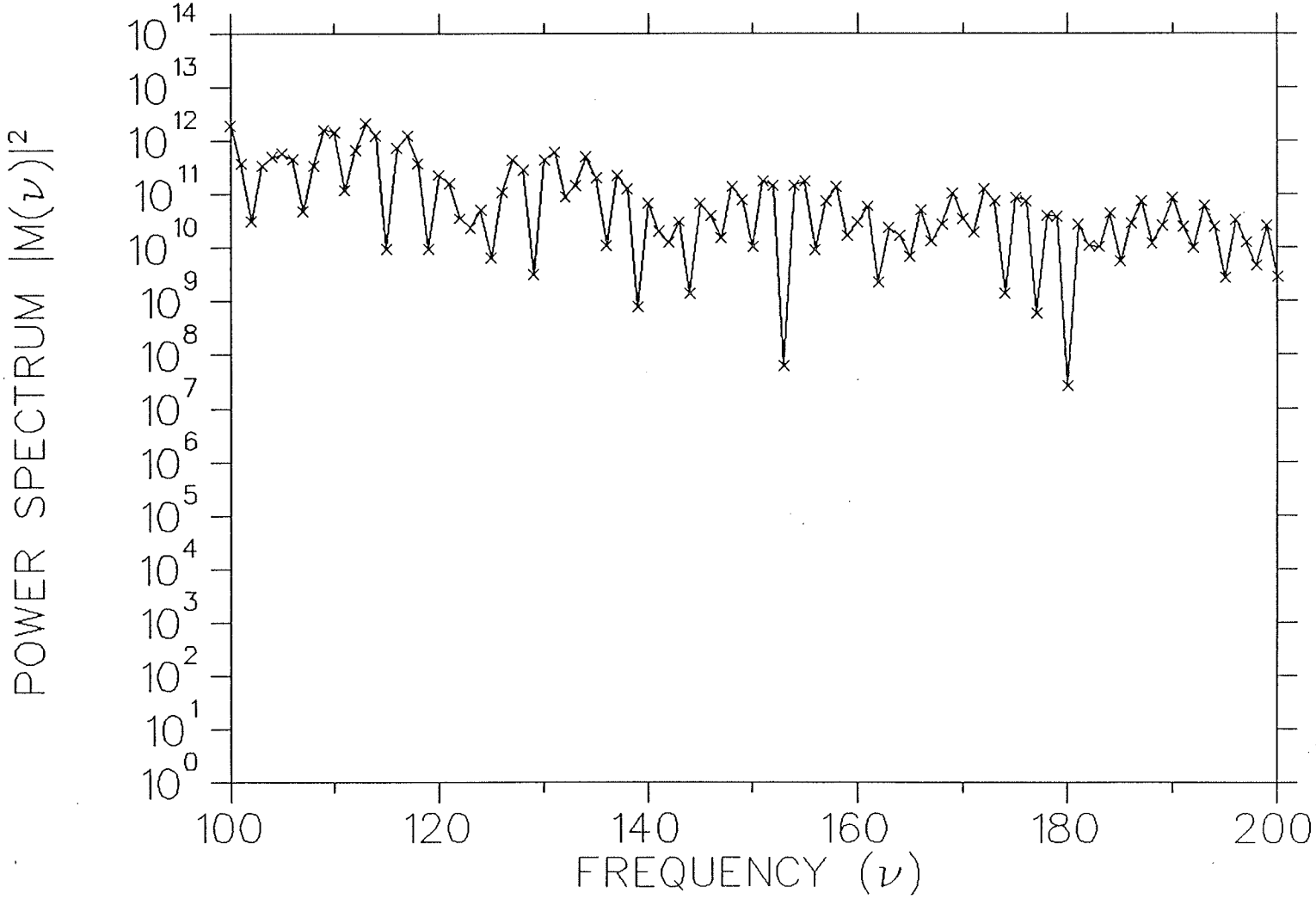

Fig. 5.21b) Power spectrum of the second 100 frequency points of the entire spectrum of the leaf sample.

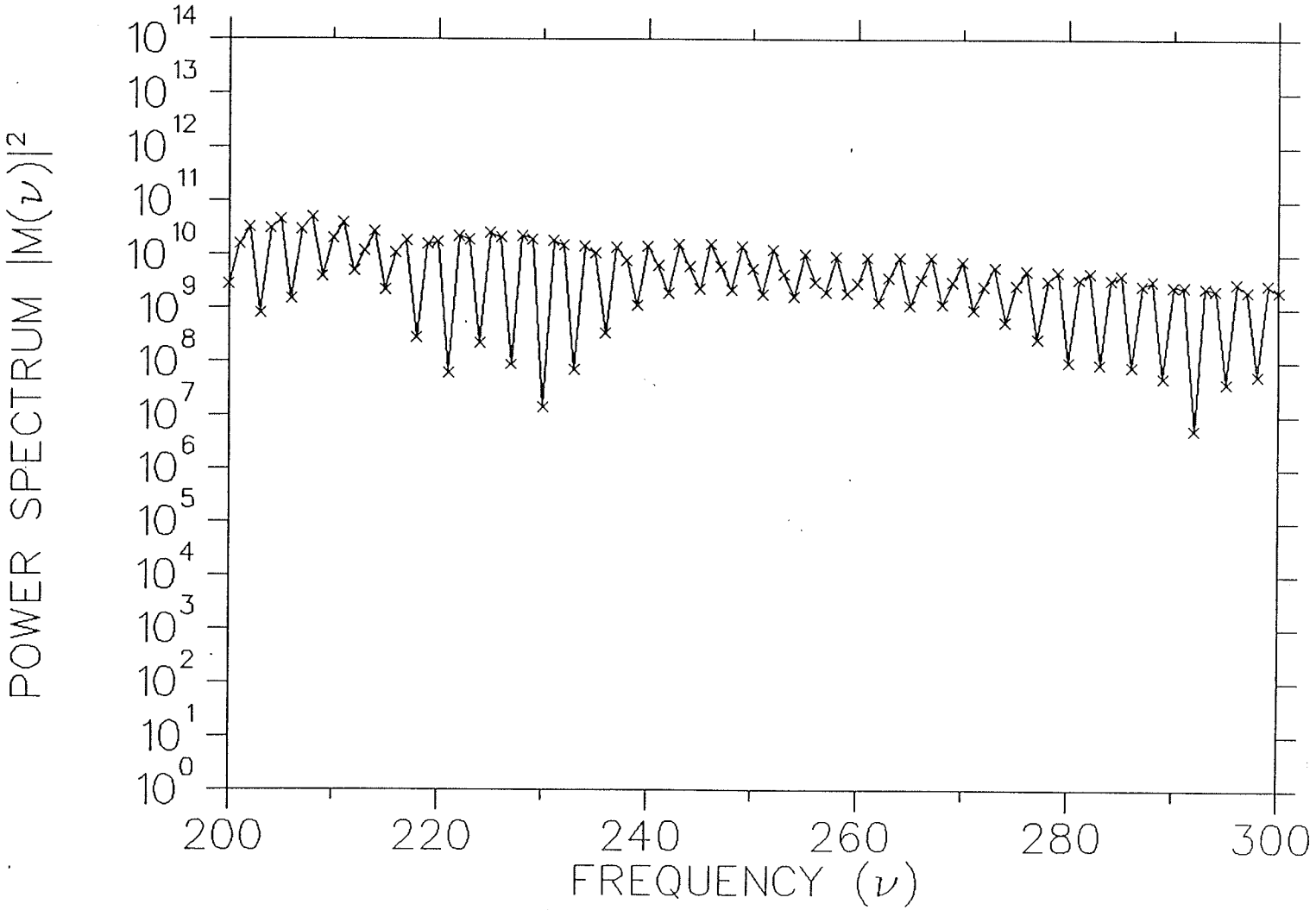

Fig. 5.21c) Power spectrum of the third 100 frequency points of the entire spectrum of the leaf sample.

References

- [An,90] H.J. Annegarn and S. Bauman, Nucl. Instr. and Meth. B49 (1990)264.
- [Ar,84] R.J. Arthur, M.W. Hill and N.F. Mangelson, Nucl. Instr. and Meth. B3(1984)305.
- [Be,69] P.R. Bevington, Data reduction and error analysis for the physical sciences (McGraw-Hill, New York, 1969).
- [Bi,72] Biology data book compiled and edited by Philip L. Altman and Dorothy S. Dittmer, Federation of American Societies for Experimental Biology, second edition, vol. 1(1972).
- [Bl,69] W.W. Black, Nucl. Instr. and Meth. 71(1969)317.
- [Bo,84] A.J.J. Bos, R.D. Vis, H. Verheul, M. Prins, S.T. Davies, D.K. Bowen, J. Makjanic and V. Valkovic, Nucl. Instr. and Meth. B3(1984)232.
- [B0,87] E. Bombelka, W. Koeing, F.W. Richter, and U. Watjen, Nucl. Instr. and Meth. B22(1987)21.
- [Bo,90] C. Boni, A. Caridi, E. Cereda, G.M. Braga Marcazzan and P. Redaelli, Nucl. Instr. and Meth. B49(1990)106.
- [Br,83] R.R. Brooks, Biological methods of prospecting for minerals (Wiley, New York, 1983).
- [Ca,84] J.L. Campbell and J.A. Cookson, Nucl. Instr. and Meth. B3 (1984)185.
- [Ca,86] J.L. Campbell, W. Maenhaut, E. Bombelka, E. Clayton, K. Malmqvist, J.A. Maxwell, J. Pallon and J. Vandenhaute, Nucl. Instr. and Meth. B14(1986)204.
- [Ca,90] J.L. Campbell, J.A. Maxwell, W.J. Teesdale and J.-X. Wang, Nucl. Instr. and Meth. B44(1990)347.

- [Ch,79] J. Chamberlain, 1979, the principles of interferometric spectroscopy (John Wiley & Sons, New York).
- [Cl,81a] E. Clayton, D.D. Cohen and P. Duerden, Nucl. Instr. and Meth. 180(1981)541.
- [Cl,81b] E. Clayton, Nucl. Instr. and Meth. 191(1981)567.
- [Cl,83] E. Clayton, Nucl. Instr. and Meth. 218(1983)221.
- [Cl,87] E. Clayton, P. Duerden and D.D. Cohen, Nucl. Instr. and Meth. B22(1987)64.
- [Cl,88] E. Clayton, Nucl. Instr. and Meth. B30(1988)303.
- [Co,70] A.L. Connelly and W.W. Black, Nucl. Instr. and Meth. 82(1970)141.
- [Co,90] David D. Cohen, Nucl. Instr. and Meth. B49(1990)1.
- [Du,87] C.J. Duffy, P.S.Z. Rogers and T.M. Benjamin, Nucl. Instr. and Meth. B22(1987)91.
- [Du,88] J.J.G. Durocher, N.M. Halden, F.C. Hawthorne and J.S.C. McKee, Nucl. Instr. and Meth. B30(1988)470.
- [En,90] Ch. Engelmann, Nucl. Instr. and Meth. B49(1990)33.
- [Fa,84] W.R. Falk, Nucl. Instr. and Math. 220(1984)473.
- [Fe,87] M.A.F. Fedikow, Results of a vegetation geochemical survey near Bisset, Southeastern Manitoba, Manitoba Energy and Mines, Geological Services(1987).
- [Fo,74] F. Folkmann, C. Gaarde, T. Huus and K. Kemp, Nucl. Instr and Meth. 116(1974)487.
- [Ga,69] J.D. Garcia, Phys. Rev. 177, 223(1969).
- [Ga,70] J.D. Garcia, Phys. Rev. A1(1970)280.
- [Gi,86] R.D. Giauque, J.M. Jaklevic and A.C. Thompson, Anal. Chem. 58(1986)940.
- [Go,77] R.C. Gonzalez and P. Wintz, 1977, Digital image processing (Addison-Wesley Publishing Company, London).

- [Go,81] J.I. Goldstein, D.E. Newbury, P. Echlin, D.C. Joy, C. Fiori and E. Lifshin, Scanning Electron Microscopy and X-ray Microanalysis, (Plenum Press, New York and London, 1981).
- [Ha,77] I. Hasselmann, W. Koenig, F.W. Richter, U. Steiner, U. Watjen, J. Chr. Bode and W. Ohta, Nucl. Instr. and Meth. 142(1977)163.
- [Ha,85] H.J. Hay, Nucl. Instr. and Meth. B10/11(1985)624.
- [Hn,76] V. Hnatowicz, Nucl. Instr. and Meth. 133(1976)137.
- [In,69] T. Inouye, T. Harper and N.C. Rasmussen, Nucl. Instr. and Meth. 67(1969)125.
- [In,90] International journal of PIXE, volume 1, number 1, March 1990 (World Scientific Publishing Company).
- [Is,76] K. Ishii, S. Morita, and H. Tawara, Phys. Rev. A13(1976)131.
- [Is,84] K. Ishii and S. Morita, Phys. Rev. A30(1984)2278.
- [Is,87] K. Ishii and S. Morita, Nucl. Instr. and Meth. B22(1987)68.
- [Is,88] K. Ishii and S. Morita, Nucl. Instr. and Meth. B34(1988)209.
- [Ja,62] J.D. Jackson, Classical electrodynamics (Wiley, New York).
- [Ja,70] D.F. Jackson, Nuclear reactions, 1970 (Chapman and Hall, London).
- [Jo,76] S.A.E. Johansson and T.B. Johansson, Nucl. Instr. and Meth. 137(1976)473.
- [Jo,84] K.W. Jones, B.M. Gordon, A.L. Hanson, J.B. Hastings, M.R. Howells, H.W. Kraner and J.R. Chen, Nucl. Instr. and Meth. B3 (1984)225.
- [Jo,87] S.A.E. Johansson, Nucl. Instr. and Meth. B22(1987)1.
- [Ka,77] H.C. Kaufmann, K.R. Akselsson and W.J. Courtney, Nucl. Instr. and Meth 142(1977)251.
- [Ka,80] Z. Kamal, J.S.C. McKee, W.D. Ramsay, M.S.A.L. Al-Ghazi, J. Birchall, J.J.G. Durocher and N. Videla, Phys. Lett. 75A(1980) 475.
- [Ka,81] K. Kaisla, T. Raunemaa and P. Paatero, Nucl. Instr. and Meth. 181(1981)77.

- [Ka,87] J. Kajfosz and W.M. Kwiatek, Nucl. Instr. and Meth. B22 (1987)78.
- [Ke,78a] T.J. Kennett, W.V. Prestwich and A. Robertson, Nucl. Instr. and Meth. 151(1978)285.
- [Ke,78b] T.J. Kennett, W.V. Prestwich and A. Robertson, Nucl. Instr. and Meth. 151(1978)293.
- [Ma,84] J.A. Maxwell, R.G. Leigh, J.L. Campbell and H. Paul, Nucl. Instr. and Meth. B3(1984)301.
- [Ma,87] W. Maenhaut, J. Vandenhaute and H. Duflou, Fresenius Z. Anal. Chem. 326(1987)736.
- [Ma,88] W. Maenhaut, Nucl. Instr. and Meth. B35(1988)388.
- [Ma,90] W. Maenhaut, Nucl. Instr. and Meth. B49(1990)518.
- [Mc,90a] J.S.C. McKee, J.J.G. Durocher, D. Gallop, N.M. Halden, M.S. Mathur, A.A. Mirzai, G.R. Smith and Y.H. Yeo, Nucl. Instr. and Meth. B45(1990)513.
- [Mc,90b] J.S.C. McKee, G.R. Smith, A.A. Mirzai, M.S. Mathur, N.M. Halden, C. Pinsky and R. Bose, Scanning Microscopy, Vol. 4, No. 4, 1990 (pages 843-851).
- [Mc,90c] J.S.C. McKee, D. Gallop, M.S. Mathur, A.A. Mirzai, Y.H. Yeo, C. Pinsky and R. Bose, Nucl. Instr. and Meth. B49(1990)225.
- [Mc,90d] J.S.C. McKee and G.R. Smith(1989) "Proton Microprobes and Their Applications", in Advances in Electronics and Electron Physics, P.W. Hawkes(ed), Academic Press, 93-132.
- [Mi,90] A.A. Mirzai, J.S.C. McKee, Y.H. Yeo, D. Gallop and J. Medved, Nucl. Instr. and Meth. B49(1990)313.
- [Mu,75] T. Mukoyama, Nucl. Instr. and Meth. 125(1975)289.
- [Na,78] M.J. Nass, A. Lurio and J.F. Ziegler, Nucl. Instr. and Meth. 154(1978)567.
- [Op,75] A.V. Oppenheim and R.W. Schafer, Digital signal processing ,1975 (Englewood Cliffs, New Jersey, Prentice Hall).

- [Pe,90] M. Peisach and C.A. Pineda, Nucl. Instr. and Meth. B49(1990)10.
- [Pr,89] W.H. Press, B.P. Flannery, S.A. Teukolsky, and W.T. Vetterling, Numerical recipe, 1989 (Cambridge University Press, New York).
- [Ra,75] L.R. Rabiner and B. Gold, 1975, Theory and applications of digital signal processing (Englewood Cliffs, New Jersey, Prentice Hall).
- [Ra,78] W.D. Ramsay, M.S.A.L. Al-Ghazi, J. Birchall and J.S.C. McKee, Phys. Lett. 69A(1978)258.
- [Ra,80] W.D. Ramsay, Ph. D. Thesis, 1980, University of Manitoba, Winnipeg, Manitoba, Canada.
- [Ro,72] A. Robertson, W.V. Prestwich and T.J. Kennett, Nucl. Instr. and Meth. 100(1972)317.
- [Ro,69] J.T. Routti, S.G. Prussin, Nucl. Instr. and Meth. 72(1969)125.
- [Ro,84] P.S.Z. Rogers, C.J. Duffy, T.M. Benjamin and C.J. Maggiore, Nucl. Instr. and Meth. B3(1984)671.
- [Sc,69] J.H. Scofield, Phys. Rev. 179(1969)9.
- [Sc,74] J.H. Scofield, Phys. Rev. A9(1974)1041.
- [Si,69] R.C. Singleton, IEEE Trans. Audio Electroacous. Au-17(1969)93.
- [St,77] P.J. Statham, Anal. Chem. 49(1977)2149.
- [Sw,90] C.P. Swann and S.J. Fleming, Nucl. Instr. and Meth. B49(1990)65.
- [Te,88] W.J. Teesdale, J.A. Maxwell, A. Perujo and J.L. Campbell, Nucl. Instr. and Meth. B35(1988)57.
- [Va,77a] P. Van Espen, H. Nullens and F. Adams, Nucl. Instr. and Meth. 142(1977)243.
- [Va,77b] P. Van Espen, H. Nullens and F. Adams, Nucl. Instr. and Meth. 145(1977)579.
- [Wä,87] Uwe Wätjen, Nucl. Instr. and Meth. B22(1987)29.
- [Wi,77] S.F.J. Wilk, J.S.C. McKee and C.P. Randell, Nucl. Instr. and Meth. 142(1977)33.

- [Wo,73] R. Woldseth, 1973, X-ray energy spectrometry, (Kevex Corporation, California).
- [Ya,81] A. Yamadera, K. Ishii, K. Sera, M. Sebata and S. Morita, Phys. Rev. A23(1981)24.
- [Zo,88] L. Zolnai and Gy. Szabo, Nucl. Instr. and Meth. B34(1988)118.